NASA-CR-203834

FINAL REPORT

MODELING OF DETACHED SOLIDIFICATION

NASA Grant NAG8-1063

Clarkson Account 375-565

Grant period: June 23, 1994 to December 22, 1996

Total funding: $108,000

Principal Investigator:

Dr. Liya L. Regel, Research Professor of Engineering and Director,
International Center for Gravity Materials Science and Applications
Clarkson University
Potsdam, NY 13699-5814
Phone: 315-268-7672; fax 3833
email: regel@agent.clarkson.edu
home page: http://www.clarkson.edu/~regel/center.html

Co-Investigator:

Dr. William R. Wilcox, Professor of Chemical Engineering
Clarkson University
Potsdam, NY 13699-5814
Phone: 315-268-7672; fax 3833
email: wilcox@agent.clarkson.edu

Research Assistant:

Dmitri Popov, Doctoral student
Interdisciplinary Engineering Science
Clarkson University
Potsdam, NY 13699-5814

SUMMARY

Our long term goal is to develop techniques to achieve detached solidification reliably and reproducibly, in order to produce crystals with fewer defects. To achieve this goal, it is necessary to understand thoroughly the physics of detached solidification. It was the primary objective of the current project to make progress toward this complete understanding.

The products of this grant are attached. These include 4 papers and a preliminary survey of the observations of detached solidification in space. We have successfully modeled steady state detached solidification, examined the stability of detachment, and determined the influence of buoyancy-driven convection under different conditions.

Directional solidification in microgravity has often led to ingots that grew with little or no contact with the ampoule wall. When this occurred, crystallographic perfection was usually greatly improved -- often by several orders of magnitude. Indeed, under the Soviet microgravity program the major objective was to achieve detached solidification with its resulting improvement in perfection and properties. Unfortunately, until recently the true mechanisms underlying detached solidification were unknown. As a consequence, flight experiments yielded erratic results. Within the past three years, we have developed a new theoretical model that explains many of the flight results. This model gives rise to predictions of the conditions required to yield detached solidification.

A. Observations of detached solidification in microgravity

Beginning with Skylab in 1974, many investigators have found that directional solidification in microgravity often yielded ingots that appear to have grown without being in intimate contact with their containers. These results are summarized in the table given in Attachment A. A wide range of surface features and behavior have been observed. We have classified these into the categories shown below. Note that a given ingot might display several of these features along its length, but not all of them.

1. The ingot easily slid out of its container, whereas sticking was observed when solidification was carried out on earth under otherwise identical conditions.
2. On its surface, the ingot had isolated voids or bubbles of various sizes, depths and contact angles with the ampoule wall. (Such surface bubbles are also frequently seen on terrestrially solidified materials.)
3. With a triangular or rectangular cross-section ampoule, the ingot had cylindrical detached surfaces in the corners and a flat surface in contact the wall over most of each face.
4. With an ampoule containing grooves machined in it, the ingot contacted only the peaks of the grooves.
5. After correcting for thermal contraction, there remained a gap of about 1 to 60 μm between the ingot and the ampoule wall around the entire periphery. Irregular narrow ridges maintained limited contact with the ampoule wall and were predominantly axial. A variety of features were seen in the detached regions, including microfacets and periodic waves or lines.

6. There was a gap of up to several mm between the ingot and the wall, typically with a wavy surface and sometimes forming an hourglass-shaped neck adjacent to the seed. Although this gap generally extended around the entire periphery, sometimes it was confined to a portion of the surface.

For semiconductors, the last portion of the ingot to freeze often replicated the surface of the ampoule, showing that contact had been intimate (as on earth).

Here, we are concerned primarily with 5 and 6 above, as these differ from all prior terrestrial experience and were completely unexpected prior to Skylab. Behaviors 1 and 2 often occur on earth. Behaviors 3 and 4 are not surprising, as one would not expect non-wetting (high contact angle) liquids to penetrate cavities.

Although detached solidification has been observed predominantly with semiconductors, Attachment A shows that it has also been observed with metals and inorganic compounds. This apparent predominance may reflect only the fact that most flight experiments on directional solidification have been performed on semiconductors.

Detached solidification has been observed at both fast and slow freezing rates. Sometimes it occurred with one type of dopant and not with others. The type of detachment, indeed even whether detachment occurred or not, has not been reproducible.

Some investigators have chosen to avoid detached solidification by using a spring to press a piston or plug tightly against the end of the melt. This strategy appears to have been successful. On the other hand, detachment has occurred nonetheless when a plug only lightly contacted the end of the feed ingot. We can explain these observations, in a fashion similar to that used to predict the influence of gravity on detached solidification (see Attachment G).

It has been claimed that detachment is sensitive to the residual acceleration. Unfortunately there have been so few measurements of residual acceleration, particularly the average value, that one cannot judge the validity of this claim from experimental evidence alone. Our theoretical treatment shown in Attachment G leads us to believe that acceleration can enhance detachment if it is of the correct direction and magnitude.

B. Influence of detachment on crystallographic perfection and compositional homogeneity

As with surface appearance, a wide variety of properties has been observed in ingots exhibiting detachment. These properties are also summarized in the table constituting Attachment A. It is interesting to note that there was seldom any correlation between the ridges and lines sometimes observed on the surface and any internal defects or composition variation.

Axial and radial variations in impurity doping ranged from that expected for diffusion-controlled solidification to that corresponding to vigorous convection. Sometimes there was a variation in composition near the detached surface. Although impurity striations were rare, they were

occasionally seen near the surface. Some detached surfaces were inadvertently coated with oxide, whereas even dissolved oxygen was not detected on others. An interesting result was obtained in Wilcox's Skylab experiments on GaSb-InSb alloys [1]. Large changes in composition occurred across twin boundaries only in the detached portions of the ingots.

Generally speaking, crystallographic perfection was much greater when detached solidification occurred. Very often, twins and grain boundaries nucleated only where the ingot contacted the ampoule wall. Dislocation etch pit densities were frequently orders of magnitude less when the solidification had been detached. In semiconductors, this higher perfection has led to substantial increases in charge carrier mobility.

C. Prior models for detachment

Over the past 22 years, several models have been proposed to explain detached solidification. We briefly review these below.

Ampoule de-wetting: When detached solidification was discovered in several Skylab experiments, it was generally thought that the melt had lost contact from the ampoule wall because of the high contact angles of the semiconductor melts. Indeed, the phenomenon is still called "de-wetting" by some investigators [e.g.,2-4]. This view persists, in spite of microgravity experiments [5,6] and theory [7] showing that liquids do not pull away from the ampoule wall, no matter what the contact angle. The implicit assumption underlying this model is that the solid took the same shape as the liquid from which it froze. This would be like a person examining a Czochralski-grown crystal and concluding it came from a cylindrical melt of the same diameter as the crystal! In reality, the edge of a growing crystal does not even begin to follow the melt's meniscus -- it deviates by the so-called growth angle.

It is relevant to note that the voids found on the surface of Bridgman-grown crystals do not have the same shape as the gas bubbles had on the wall in the melt before solidification. In a parabolic flight experiment with InSb, we found that gas bubbles on the wall moved when the freezing interface contacted them [8]. Such a bubble moved toward and partly onto the interface, so as to minimize the surface energy in the system. If one looks carefully at such cavities on a grown crystal, it can be seen that the contact angle to the ampoule changes as one moves around the cavity. This is a manifestation of the interaction between the growing crystal and the bubble.

Shrinkage: Some instances of detached solidification of metals in microgravity have been attributed to shrinkage during solidification. We believe this is erroneous. It is the inverse of the old discredited claim that one cannot grow semiconductor crystals by the vertical Bridgman technique because these materials expand when they freeze. To clarify the situation, let us consider the volume change that occurs as a semiconductor slowly freezes upward on earth. Solidification begins at the bottom of the ampoule, perhaps on a seed. If the density decreases upon freezing, then the top of the melt moves slowly upward to accommodate the increasing volume. Provided that enough head space remains for the entire volume change, solidification proceeds to completion without a problem. On the other hand, if the upward movement of the melt is blocked, then the ampoule breaks.

The reverse situation occurs for metals that contract when they freeze. The melt surface slowly moves downward during solidification, while the melt and the solid both remain in contact with the ampoule wall.

If the coefficient of thermal expansion is greater for the ampoule than for the ingot, then during cooling from the melting point, the ingot is put under tensile stress while the ampoule is under compression [9-13]. Depending on the mechanical properties and the degree to which the solid sticks to the ampoule, the ingot may break free from the ampoule wall and form a gap, it may remain stuck and plastically deform, or it may remain stuck and break the ampoule.

Rough ampoule wall: Duffar has attributed detached solidification to a rough ampoule wall [2-4]. The idea is that a non-wetting melt cannot penetrate into cavities, especially if some residual gas is present in them. The problem with this model is that the interior of quartz growth ampoules is typically very smooth. Often it has been coated with shiny pyrolytic carbon.

Duffar did find that artificially roughened ampoules yielded detached solidification between the peaks, while the solid was attached at the peaks [14-20].

Oxide coating: Another proposed model invokes an oxide coating that acts as a container smaller in diameter than the ampoule. While this may have been true in some flight experiments, it has been rare. Ampoules were sealed in an inert gas and/or vacuum, sometimes with a gas getter installed. In the case of GaSb, for example, electron channeling patterns on the detached surface were sharp and showed no oxide [21,22]. No oxygen was detected by Rutherford back scattering measurements.

D. Current model and results of theoretical development in this grant

Meniscus model: Our model of detached solidification is described in detail in Attachments D-G. Attachment D consists of the first paper dealing with our new model for detached solidification. A meniscus connects the edge of the ingot with the ampoule wall, similar to Czochralski growth but with much less distance between the ingot and the wall. Because of the curvature of the meniscus and the surface tension of the melt, the pressure in the gap must be greater than that in the adjacent melt. The gas filling this gap consists of one or more volatile constituents that are rejected by the growing solid. In most cases, this is the residual gas remaining in the ampoule that has dissolved in the melt. Although flight ampoules were generally sealed in a vacuum, outgassing would provide adequate gas to fill the gap. With only one known exception [15,17,19,20], the residual gas pressure has not been measured <u>after</u> flight experiments. In that one exception, it was about 10^{-2} Torr, in spite of the use of gas getters in the sealed cartridge.

One may draw an analogy between our mechanism of detached solidification and the formation of "worm holes" or gas tubes inside growing solids. Formation of such tubes is commonly observed in ice and organic compounds [e.g.,23-27]. The mechanism underlying tube formation is as follows. Residual gas dissolves in the melt, e.g. air in the case of water being converted to ice cubes. The dissolved gas is much less soluble in the solid, and so accumulates at the freezing interface. When its concentration becomes large enough, a gas bubble nucleates [28] and grows. If

conditions are right [29], it remains at the interface and blocks the solid from growing under it. The diameter and stability of the resulting tube depends on the transport of dissolved gas into the bubble [30]. One can regard detached solidification as the reverse geometry, i.e. the gas bubble surrounds the growing solid rather than vice versa.

We have thought of the following three mechanisms by which detached solidification could be initiated:

1. As described in Attachment D, the solid initially grows in contact with the ampoule wall. Because of the difference in thermal expansion between the ingot and the ampoule, stress builds up as the ingot cools from the melting point. Eventually this stress becomes large enough that the ingot pops loose of the ampoule. The resulting gap between the ingot and the ampoule rapidly fills with the volatile constituent that has been concentrating near the freezing interface. If the rate of transport of gas into the gap is sufficient, the gap widens and propagates along with the growing crystal.

2. The freezing interface encounters a gas bubble at the wall. If the contact angles are proper and the rate of transport of gas into the bubble is sufficient, this bubble propagates around the periphery to form a meniscus.

3. Normally the feed rod is smaller in diameter than the ampoule. If the rod is not completely melted, then a gap exists between the rod and the ampoule prior to the beginning of solidification. The peripheral gas bubble may even grow during the soak period by dissolution of residual gas into the melt at its hot end, diffusion down the melt, and discharge into the gap. The driving force for this transport could be the Soret effect (thermal diffusion) or the dependence of gas solubility on temperature. This phenomenon may have been responsible for the pronounced neck that resulted from some flight experiments (see Attachment A).

The ridges observed in experiments with a small gap width may be visualized as equivalent to several gas bubbles spaced around the periphery. The most probable cause is an instability in a highly curved meniscus that entirely surrounds a growing crystal. This should be investigated theoretically. Another possibility, which we consider less likely, is that the crystal remains stuck to the wall at several locations when it first pops loose, and these propagate down the crystal.

Detachment on only one side of an ingot may be understood via 1 or 2 above. It could be that the crystal pops free from the ampoule on only one side. This would be more likely for a crystal that deforms easily near its melting point. Alternately, partial detachment could be caused by a bubble/meniscus that simply doesn't propagate around the periphery. Another possibility is that the residual acceleration is transverse to the axis and deforms the meniscus sufficiently to make it unstable on one side. Although theoretical analysis of this possibility is needed, we can say that such deformation would only be significant for a relatively large gap width (for which the curvature of the meniscus is small and the resulting pressure change is small).

Over the last two years, we have been developing our theoretical model for detached solidification. Numerical calculations were performed for InSb, which has exhibited detached solidification in

numerous microgravity experiments. Attachment E is a manuscript for steady state in the absence of buoyancy-driven convection. For the calculation, we first selected a value for the gap width. The flow field and concentration field were calculated for an assumed freezing rate. A new gap width was calculated from these results. New values were assumed for the freezing rate and the calculations repeated until the calculated gap width equaled the value used for the calculations. This gave the correct freezing rate for that gap width. This process was repeated for a series of gap widths. We found that detached solidification in microgravity is favored by a low freezing rate, increased concentration of volatile constituent, large contact angle for the melt on the ampoule wall (poor wetting), low surface tension for the melt, and a large growth angle.

In our steady state model, we considered the influence of Marangoni convection arising from the dependence of surface tension on temperature along the meniscus. The flow pattern caused by Marangoni convection is a circulating cell with a size on the order of the gap width. Although this convection had a large effect on the local concentration field, it did not strongly influence the total flux of gas into the gap.

One would expect Marangoni convection to influence the axial and radial variation in impurity doping in the crystal. As summarized in Attachment A, flight experiments with detachment yielded a wide spectrum of results. In some cases, axial and radial concentration profiles corresponded to diffusion-controlled conditions. In other cases, there seemed to be clear evidence for Marangoni convection, ranging from gentle to vigorous. Why was Marangoni convection not always exhibited with detached solidification? If the gap is very narrow, our calculations show that the region of perturbed composition should also be very narrow. Thus, one might still achieve an axial concentration profile expected in the absence of convection, particularly if the freezing rate is not low.

Another possible explanation for diffusion-controlled segregation with detached solidification involves a surface-active impurity that concentrates on the meniscus surface. One would expect, for example, that dissolved oxygen would concentrate on the surface of semiconductor and metal melts. Such impurities strongly inhibit the movement of a free liquid surface. For example, surfactant can stop Marangoni motion of a gas bubble in a temperature gradient and retard its rise velocity in a gravitational field [e.g.,31]. The influence of a surfactant increases as the bubble size decreases. Thus, for a given oxygen concentration in a semiconductor melt, we would expect Marangoni convection to manifest itself only for large gap widths during detached solidification.

A third possibility, that we consider unlikely, is the formation of an oxide film on the surface of the meniscus. Although such as solid film would indeed stop convection, we do not believe such a film can be stable. In our mechanism of detached solidification, the meniscus must move along the ampoule surface during growth. An oxide film would tend to stick to the ampoule surface and either prevent motion of the meniscus or break in the process.

In Attachment F, we examine the stability of steady-state detached solidification in microgravity. We find that the shape of the meniscus is destabilizing in a fashion similar to Czochralski growth. If, for example, the crystal begins growing toward the wall, the meniscus shape tends to acceleration the change in diameter. Thus, if only the meniscus is taken into account, one predicts

that both Czochralski growth and detached solidification are unstable. Since this is contrary to experimental observations, other factors must stabilize the growth. Here, we considered gas transport and heat transfer as stabilizing mechanisms for detached solidification. We found that while gas transport into the gap is necessary for detached solidification, it is sufficient to stabilize detachment only for a short distance, on the order of the gap width. On the other hand, heat transfer strongly stabilizes detached solidification, as it does in Czochralski growth.

In Attachment G, we consider the influence of gravity on detached solidification. We show that in the usual vertical Bridgman configuration, we must add the melt's hydrostatic head to the gas pressure in the gap required to maintain the meniscus shape. Increased transport of gas into the gap is required to maintain this increased pressure. Buoyancy-driven convection can provide this increased transport, provided that the convection is gentle and is directed outward along the freezing interface. On earth, one would expect such convection for a very slightly convex interface shape. Thus, it is interesting to note that detached solidification was recently observed on earth for germanium with a slightly convex interface [32-34]. Use of a mirror furnace enabled observation of the ampoule in the neighborhood of the freezing interface. The appearance was exactly as expect from our model. Unfortunately, detachment is very sensitive to the degree of convection, making its achievement on earth a lucky and rare event.

REFERENCES

1. R.A. Lefever, W.R. Wilcox, K.R. Sarma and C.E. Chang, "Composition Variations in Directionally Solidified InSb-GaSb Alloys," Mat. Res. Bull. 13 (1978) 1181-1191.
2. T. Harter, T. Duffar and P. Dusserre, "Use of the 'De-Wetting' Phenomenon for High Quality Semiconductor Growth in Space," in: Proceedings of the VIIth European Symposium on Materials and Fluid Sciences in Microgravity, Oxford, ESA SP-295 (1990) 69-73.
3. T. Duffar and I. Harter, "Consequence of Wetting Phenomena on the Growth of Semiconductor Crystals on Earth and in Space: Two Examples," Ann. Chim. Fr. 16 (1991) 123-131.
4. T. Duffar, I. Paret-Harter and P. Dusserre, "Crucible De-Wetting during Bridgman Growth of Semiconductors in Microgravity," J. Crystal Growth 100 (1990) 171-184.
5. R. Sen and W.R. Wilcox, "Behavior of a Non-Wetting Melt in Free Fall: Experimental," J. Crystal Growth 74 (1986) 591-596.
6. R.J. Naumann, "Marangoni Convection in Closed Containers (MCCC)," in: Proceedings of the Joint L+1 Science Review for USML-1 and USMP-1 with the Microgravity Measurement Group, Huntsville, NASA (1993) 601-608.
7. R. Sen and W.R. Wilcox, "Behavior of a Non-Wetting Melt in Free Fall: Theoretical," J. Crystal Growth 78 (1986) 129-134.
8. R. Derebail, W.R. Wilcox and L.L. Regel, "The Influence of Gravity on the Directional Solidification of Indium Antimonide," J. Spacecraft & Rockets 30 (1993) 202-207.
9. D.J. Larson, Jr., L.G. Casagrande, D.D. Marzio, A. Levy, F.M. Carlson, T. Lee, D. Black, J. Wu and M. Dudley, "Producibility improvements suggested by a validated process model of seeded CdZnTe vertical Bridgman growth," in: Producibility of II-VI Materials and Devices, Proc. SPIE - Int. Soc. Opt. Eng. 2228 (1994) 11.
10. R. Shetty, W.R. Wilcox and L.L. Regel, "Influence of ampoule coatings on cadmium telluride solidification," J. Crystal Growth 153 (1995) 103.
11. T. Lee, "Finite Element Analysis of the Thermal and Stress Fields during Directional Solidification of Cadmium Telluride," Ph.D. Dissertation, Clarkson University (1996).

12. T. Lee, J.C. Moosbrugger, F.M. Carlson and D.J. Larson, Jr., "The role of thermal stress in vertical Bridgman growth of CdZnTe crystals," in: L.L. Regel and W.R. Wilcox (eds.), Materials Processing in High Gravity, Plenum Press, New York (1994) 111-122.
13. W. Rosch and F. Carlson, "Computed stress fields in GaAs during vertical Bridgman growth," J. Crystal Growth 109 (1991) 75.
14. T. Duffar, C. Potard and P. Dusserre, "Growth Analysis of the InSb Compound by a Calorimetric Method in Microgravity; Results of the SpaceLab-D1 Experiment," J. Crystal Growth 92 (1988) 467-478.
15. T. Duffar, P. Dusserre and J. Abadie, "Crucible-Semiconductor Interactions during Crystal Growth from the Melt in Space," 30th COSPAR Scientific Assembly, Hamburg, (1994); Adv. Space Res. 16 (1995) 199-203.
16. T. Duffar, P. Dusserre and M.D. Serrano, "Bridgman Solidification of GaSb. Results of EURECA AMF-118 Experiment," Adv. Space Res. 16 (1995) 101-104.
17. M.D. Serrano *et al.*, "Segregation in space GaInSb crystals," ELGRA meeting, Madrid (1994).
18. T. Duffar, seminar, Clarkson University, Potsdam, New York (1995).
19. T. Duffar and J. Abadie, "Convective Effects in the Growth of GaInSb Crystals," in: Preliminary Results of the D2 Mission, Norderney, European Space Agency, Paris (1994).
20. T. Duffar *et al.*, "Segregation during GaInSb solidification in space and on earth," in: 9th European Symposium on Gravity Dependent Phenomena in Physical Sciences, Berlin (1995).
21. E. Lendvay, M. Harsy, T. Gorog, I. Gyuro, I. Pozsgai, F. Koltai, J. Gyulai, T. Lohner, G. Mezey, E. Kotai, F. Paszti, V.T. Hryapov, N.A. Kultchitsky and L.L. Regel, "The Growth of GaSb Under Microgravity Conditions," J. Crystal Growth 71 (1985) 538-550.
22. I. Gyuro, E. Lendvay, M. Harsy, T. Gorog, I. Pozsgai, K. Somogyi, F. Koltai, J. Gyulai, T. Lohner, J. Gyilai, M. Kanky, J. Giber, L. Bori, L.L. Regel, V.T. Khryapov and N.A. Kultchitsky, "Crystal Growth of GaSb Under Microgravity Conditions," Acta Astronautica 11 (1984) 361-368.
23. Ya. E. Geguzin and A.S. Dzuba, "Gas Inclusions during Crystallization from the Melt," in: eds. E.I. Givargizov and S.A. Grinberg, Growth of Crystals, Consultants Bureau, New York 17 (1991) 193-204.
24. K.F. Vasconcellos and J. Beech, "The Development of Blowholes in the Ice/Water/Carbon Dioxide System," J. Crystal Growth 28 (1975) 85-92.
25. S.A. Bari and J. Hallett, "Nucleation and Growth of Bubbles at an Ice-Water Interface," J. Glaciology 13 (1974) 489-520.
26. M.J. Krasinski, D. Michalski and J. Karniewicz, "Observation of the Boundary Layer on the Top of Ice Growing from the Melt," Cryst. Res. Technol. 25 (1990) 625-632.
27. H. Jambotchian, R. Trivedi and B. Billia, "Interface Dynamics and Coupled Growth in Directional Solidification in Presence of Bubbles," J. Crystal Growth 134 (1993) 181-195.
28. W.R. Wilcox and V.H.S. Kuo, "Gas Bubble Nucleation during Crystallization," J. Crystal Growth 19 (1973) 221-228.
29. R. Cole, J.M. Papazian and W.R. Wilcox, "Bubble Departure Radii at Solidification Interfaces," Int. J. Heat Mass Transfer 23 (1980) 219-224.
30. V.A. Tatarchenko, "Cylindrical Pores in a Growing Crystal," J. Crystal Growth 143 (1994) 294-300.
31. D.A. Saville, "The Effects of Interfacial Tension Gradients on the Motion of Drops and Bubbles," Chem. Eng. J. 5 (1973) 251-259.
32. F. Szofran and P. Dold, Private Communication, NASA Marshall Space Flight Center (1996).
33. F. Szofran, K.W. Benz, A. Cröll, P. Dold, S.D. Cobb, S.L. Lehoczky, M.P. Volz, D.A. Watring and S. Motakef, "Magnetic Damping of Solid Solution Semiconductor Alloys," in: NASA Microgravity Materials Science Conference, NASA Conference Publication 3342, Huntsville (1996).
34. Microgravity News, IntoSpace, Germany, 3 (summer 1996) 7.

Attachment A. **Directional solidification experiments performed in space that appear to have shown detachment**

Material	Ampoule or crucible	Dimensions of feed rod	Freezing rate	Thermal conditions	Mission, hardware	Results: surface	Results: interior (EPD = etch pit density)	Authors
Ag	TiO_2/Ni skin, square ampule	49 mm long	6 mm/hr	Grad 200-300 K/cm	Shuttle SL-1 & TEXUS - 9	Gap between alloy and skin. Sometimes ingot separated into two parts. Contact angle 150^0.		Sprenger [42]
Ag-Cu (79% Ag)	Al_2O_3 crucible 750 torr Ar	5 mm dia.		No soak; Cool 1800 K/hr		Detached from the metal substrate. Large faceted zones on free surfaces.		Barbieri [43]
Al	Quartz, ~ 0.1 torr Ar	6.5 mm dia., 55 mm long	11 - 22.6 mm/hr translation	Soak 10 - 120 min; Cool 11.3 - 45 K/hr	Salyut-6, Bealutsa Kristall facility 1980	"Shrinkage" more in part of crystal with smaller diameter		Fuchs *et al.*, [45]
Al (+ 0.2-0.5wt% SiC & Al_2O_3 particles)	Graphite crucible, He	10 mm dia., 80 mm long		Soak 40 min, Cool 3600 K/hr	1 ES 315/1 1983	Many "shrinkage" voids and bubbles.	Distribution of SiC more homogeneous, microhard 20% higher, better adhesion of particles	Froyen [41]
Al (+ 4% Cu)	Quartz, ~ 0.1 torr Ar	11.5 mm dia, 100 mm long	11 - 22.6 mm/hr grad freeze	Soak 138-420 min, Gradient 30-40 K/cm, Cool 11.3-45 K/hr.	Salyut-6, Bealutsa Splav 1980	"Shrinkage" more in part of ingot with smaller dia.		Fuchs *et al.*, [45]
Al - Cu eutectic	Graphite	6.25 mm dia., 12.7 mm long	gradient freeze	Soak 1 hr., grad 45 K/cm, cool 144 K/hr	Skylab 3 Westinghouse furnace, 1974	Reduced diameter of hour glass shape in the regrowth region.	12 % lower average defect spacing, 20% lower average fault density.	Hasemeyer *et al.* [39]
Al - Cu eutectic	Graphite	6.25 mm dia., 12.7 mm long	gradient freeze	Soak 1 hr., grad 45 K/cm, cool 144 K/hr	Skylab 4 Westinghouse furnace, 1974	Very slight diameter reduction.	12 % lower average defect spacing, 20% lower average fault density.	Hasemeyer *et al.* [39]
Al - Ni eutectic (6.1wt% Ni)	graphite crucible $2x10^{-3}$ torr	7 mm dia., 70 mm long	20 or 200 cm/hr grad freeze	Cool 18 or 90 K/hr	Mir Cristallizator CSK-1 1987	Detached	$NiAl_3$ rods axially oriented from start, spacing 9% larger at 20 mm/hr, 13% at 200mm/h	Regel *et al.* [20a, 20b]
Al-Zn alloys	SiC crucible				Spacelab 1 ES 316	Detached ~3 - 5 mm	Microgravity samples not dendritic, 1-g samples are.	Potard and Morgand [44]
$(Bi_{1-x}Sb_x)_2Te_3$	quartz		10.8 mm/hr	Gradient 70 K/cm	Salyut-6 Halong-2&3, 1980	Pores, holes with smooth surfaces, pores with steps.		Zusman *et al.*, [34]
CdTe (+ 4% Zn)	quartz	15 mm dia.	1.6 mm/hr translation	Heat 2 K/min, soak 2 hr, cool 120 K/hr, gradient 33 K/cm	USML-1 Shuttle, Crystal Growth Furnace	~ 5 mm detachment on one side at end of cone region.	At detached region, no grain or twin nucleation, much lower stress and fewer dislocations.	Larson *et al.* [28]

Material	Ampoule or crucible	Dimensions of feed rod	Freezing rate	Thermal conditions	Mission, hardware	Results: surface	Results: interior (EPD = etch pit density)	Authors
Fe (alloy)	Al_2O_3 skin	49 mm long	6 mm/hr translation	Grad 200-300 K/cm	SL-1 Shuttle ES-325, TEXUS - 9	Gap between alloy and skin. Sometimes separation into two parts.		Sprenger [42]
GaAs (undoped)	Triangular cross section prism of pyrolytic BN	Non-cylindr cross section less than 3 mm dia.				Detached from the corners of triangular prism, in contact on faces.		Gatos *et al.* [48]
GaSb polycrystalline	Carbon-coated quartz, conical at front end, graphite spacer at tail end. ~10^{-6} torr	8 mm dia., 39 mm long	11.3 mm/hr translation	Soak 90 min, translate 5.5 hr	Salyut-6, Eötvös-7 Kristall facility ~ 1980	Detached except for ring near hemisphere front end. Ridges just after ring, some normal to growth, some zig-zag, some attached. Detached parts rough with some microfacets.	EPD 10X less, grain boundaries 15X fewer, mobility 40% higher than from earth. On surface, no oxide (electron channeling), <10^{16}O/cm^2 (Ruth. b.s.).	Lendvay, Regel *et al.* [19, 19a]
GaSb (+ 1at% Te) <111>Ga	Quartz, 5x10^{-3} torr	7 mm dia.	~ 10 mm/hr gradient freeze	Gradient 25 K/cm	Mir-Soyuz TM-3, Crystallizater CSK-1 furnace 1987	Asymmetric neck after seed, 7 mm long with max gap 1.1 mm & ridges mainly axial, intricate structure, not attached. Surface rough.	More uniform resistivity, higher perfection, no striations. Lamellar twins at shoulder. On earth, twins grew from interface where contacted wall.	Regel *et al.* [20, 20a, 20b]
GaSb (undoped) <111>B(Sb)	Sand blasted quartz, carbon cloth at ends, 10^{-6} torr	Feed rod 6 mm dia, 30 mm long. 10 mm ID amp.	10 - 20 mm/hr gradient freeze	Feed rod entirely melted prior to cooling to grow. 8 hr growth	China Returnable Satellite - 14 1992	Photo shows detached for at least 1/2 of length, with sharp variations in gap width.	Polycrystalline. Ground-based control stuck to ampoule wall.	Ge, Nishinaga *et al.* [21, 21a, 21b]
GaSb (Te-doped) <111>B(Sb)	Quartz, carbon cloth at ends, 10^{-6} torr	Feed rod 6 mm dia, 30 mm long. 10 mm ID amp.	10 - 20 mm/hr gradient freeze	All but 4 mm of feed rod melted before cooling to grow. 8 hr growth.	China Returnable Satellite - 14 1992	Dia < seed for 12.5 cm, ~3 mm gap and wavy, then attached. Photo appears to show irregular axial ridges and faint lines normal to axis. Shiny & metallic implies no oxide.	Single. No striations, diffusion-controlled axial conc. Twinning begins near attachment. EPD decreases to 0 in detached, increases steeply after attached.	Ge, Nishinaga *et al.* [21, 21a, 21b]
GaSb (undoped & + 1at% InSb)	Quartz with machined spiral groove	10 mm dia., 70 mm long	Translated out of furnace	Seeds accidentally entirely melted.	EURECA, Automatic Mirror Furnace 1992	No contact in beginning, then slight contact at sharp ridges at top of screw thread machined in crucible, attached at end.	Began poly, ended single. Quality increased where detached, degraged where attached. Diffusion-controlled segregation.	Duffar *et al.* [E, 22, 22a, 22b, 22c]

Material	Ampoule or crucible	Dimensions of feed rod	Freezing rate	Thermal conditions	Mission, hardware	Results: surface	Results: interior (EPD = etch pit density)	Authors
GaSb (5×10^{18} Te atom/cm^3 or 9at% In)	Quartz cruc., machined 1mm grooves, + gas getter. ~10^{-2} torr after expt.	Te-doped 120 mm long, In-doped 70 mm long.	Te 4.0-4.5 mm/hr, In 2.2-3.4 mm/hr, grad freeze	Te-doped gradient 18-28 K/cm, In-doped gradient 25-40 K/cm	Shuttle D2-WL Gradient Heating Facility - 03 1993	Detached except at 0.15 mm flats on top of screw thread machined into crucible surface and where In-doped was dendritic.	Grain and twin nucleation where attached and at silica dust accumulations on surface. Segregation indicates strong mixing.	Duffar *et al.* [E, 22, 22b, 23, 23a]
$Ga_{1-x}In_xSb$ (x = 0.1,0.3,0.5)	Carbon-coated quartz, 3 graph spacers sep'd by quartz wool at each end, 10 torr He.	8 mm dia., 90 mm long	~ 8 mm/hr increasing down ingot, gradient freeze	Soak 16 hr at 960 C melting back ~ 1/2, initial gradient ~ 80 K/cm, cool 36 K/hr for 8.3 hr.	Skylab 3 Westinghouse furnace 1974	Wavy surface with smaller diameter. Much smaller diameter in 2 areas for x = 0.1. (Attached in Skylab 4 experiments, performed under similar conditions.)	Mostly twin boundaries. 54% less boundaries than from earth. Twins seldom nucleate in space. Only where detached, large radial variation in comp'n. & ~2X changes across twin boundaries.	Wilcox *et al.* [E, 25, 25a, 25b, 25c, 25d, 25e]
Ge (8×10^{16} Ga/cm^3, 4×10^{14} Sb, or 2×10^{15} B) <111>	Graphite, 10^{-4} torr		18 mm/hr gradient freeze	Soak in gradient ~ 2 hr, cool 36 K/hr.	Skylab 3, Westinghouse furnace 1974	Smooth, necked in. Most pronounced for Ga-doped, ~ 1 cm long.	Resistivity fluctuations ~5X less from space. Less axial segregation. Higher resist. near surf.	Yue and Voltmer [2, 2a ,E]
Ge (+ 10^{19} Ga atom/cm^3) <111>	Quartz, graphite end cups for CID, quartz wool packing, 40 torr Ar.	8.43 mm dia., 95mm long	0 initially, approach ~36mm/hr. CID show no fluct'ns.	Heat 3.5 hr, soak 2 hr, gradient 50 K/cm, cool 144 K/hr.	Apollo-Soyuz T.P. Westinghouse gradient freeze furnace 1975	Random network of ridges 1-5 μm high, reducing contact to < 1% of surface.	Axial & radial variation in doping. Fluctuations on and near small (111) facet along one side. Many fewer grains & twins.	Witt *et al.* [1, 1a, 1b, 1c, 1d, 11c, E]
Ge (+ 0.7 - 1 at% Si + 1 - 2×10^{17} Sb/ cm^3) <111>	Carbon-coated quartz, 10^{-4} torr	38 mm long	gradient freeze	Gradient 30-40 K/cm	Apollo-Soyuz T.P. Westinghouse furnace 1975		No irregularities, cracks or bubbles; large radial variation in Si conc., with opposite variation in Sb.	Zemskov [3, 3A, 4]
Ge (+ 2×10^{17} Ga, 1.5×10^{18}Sb/cm^3)	Carbon-coated quartz, cylindr & ribbon	12 mm dia., 38-52 mm long	11.3 - 22.5 mm/hr translation	Soak 2 hr, gradient 70-80 K/cm	Salyut-6, Kristall facility ~ 1978 - 1982	Gap 40 - 60 μm wide, wavy, scattered peaks and ridges in contact with wall.	EPD 10^2 - 10^3 cm^{-2}, striations; melt 130-150° contact angle.	[4]
Ge (+ 10^{18} / cm^3)	Carbon-coated quartz	9 mm dia., 39 - 47 mm long	11.3 mm/hr translation		Salyut-6, Kristall facility ~ 1978 - 1982	Detached over ~ 1/4 of surface of ingot.	Variation of resistivity 3-4 times larger in samples grown on earth.	Khryapov *et al.* [4, 6, 6a]
Ge (+ 10^{17} Ga/cm^3)	Carbon-coated quartz	9.1 mm dia., 60 mm long	11.3 mm/hr translation		Salyut-6, Kristall facility	Irregular lateral mounds and longitudinal ridges in contact with ampoule.	EPD 2×10^3 cm^{-2} compared to 2×10^5 cm^{-2} from earth. Axial segregation reduced.	Markov *et al.* [8, 8a]

Material	Ampoule or crucible	Dimensions of feed rod	Freezing rate	Thermal conditions	Mission, hardware	Results: surface	Results: interior (EPD = etch pit density)	Authors
Ge (+ 10^{20} In/cm^3) <111>	Carbon-coated quartz, graphite end supports. 10^{-5} torr	72 mm long, 14 mm melted	11.3 mm/hr translation	Soak 1 hr at 1100°C	Salyut-6, Caribe Kristall module ~ 1978 - 1982	Large caverns, many small bubbles, collar with decreased diameter and small crests perpendicular to growth in contact.	Gas bubble on axis near frontier of growth. EPD 10^4 cm^{-2}. Lower resistivity & higher perfection.	Calzadulla *et al.* [4, 10, 10a]
Ge (+ P or Zn)	Graphite-lined quartz or graphite crucbl, 10^{-5} torr	8 mm dia.	~420 mm/hr gradient freeze	100 s to heat, 80 s to melt, 400 s to freeze	MIR sound rocket, 10 min, BKT exothermic furnace, 1976 - 1980	Contacted walls only in separate small areas.	Gas inclusions. Single crystals compared to polycrst from earth. EPD 10^2-10^3 lower. Uniform doping.	Vlasenko *et al.* [4, 50]
Ge (p-type, Zn + Sb; p-type, P + Zn) <111>	quartz, 10^{-4} torr	4 cm, ~ 2 cm melted	~360 mm/hr gradient freeze	100 s to heat	Exothermic furnace, ~1983	Wavy with over 99% detached.	EPD reduced to 10^2 cm^{-2} from 10^5 - 10^6 cm^{-2} in seed. Single from space, poly from earth.	Chernov *et al.* [5]
Ge ($5x10^{18}$ Ga/cm^3) <100>	Part free, part coated with quartz or Pyrex, 760 torr Ar	6 mm dia., ~ 20 mm melted	gradient freeze	Gradients: 125 K/cm with quartz, 95 K/cm with Pyrex	MASER 2 rocket, 7 min, mirror furnace, 1990	Regular ridges in growth direction with quartz, good contact with Pyrex. Cracks in uncoated parts, attributed to Ge oxide.	Reduced axial segregation in material grown detached.	Tilberg & Carlberg [7]
$Hg_{0.78}Cd_{0.22}Te$	quartz		2-50 mm/hr gradient freeze	Soak 2 hr (Syrena 1) & 4 hr 45 min (Syrena 2) at 500 - 900°C, gradient 30-40 K/cm.	Salyut-6, Syrena 1&2 Splav-01 furnace 1978	Detached.	Quality and grain size increase strongly as growth rate decreases. Skin enriched in CdTe.	Galazka, *et al.* [4, 26, 26a]
HgCdTe (~ 20% Cd)		8 mm dia., 15 - 30 mm long	gradient freeze	Soak, cool 11 K/hr (#1) and 2.8 K/hr (#2)	Salyut-6 Splav-01 furnace	Limited contacts with ampoule wall.	EPD 10^4 cm^{-2} compared to earth's 10^6 cm^{-2}, skin enriched in Cd.	Kurbatov *et al.* [4, 27]
$Hg_{0.84}Zn_{0.16}Te$		5.7 mm long regrown	0.15mm/hr translation	Heat up for 5hr, translate 5hr, soak 10hr, grow 39hr	Shuttle USML-1 1992	Mostly detached. Smooth with crinkles and some hills.	Asymmetric slightly concave interface.	Lehoczky, *et al.* [29]
InAs <111>	Carbon-coated quartz	9 mm dia., 40 - 50 mm long	11.3 mm/hr translation	Soak 2 hr	Salyut-6 Kristall facility	Detached for 1/3 to 1/2 of specimen length.		Khryapov, *et al.* [4, 17, 17a, 17b]
InSb (10^{14} - 5 x 10^{17} Te/cm^3)	Carbon-coated quartz	9 mm dia., 40 - 50 mm long	11.3 mm/hr translation	Soak 2 hr	Salyut-6 Kristall facility	Detached 1/3 to 1/2 of specimen length	EPD in detached regions ~2.5x10 cm^{-2} compared to earth's ≥5x10^4 cm^{-2}. Striations.	Khryapov *et al.* [4, 17, 17a, 17b]

Material	Ampoule or crucible	Dimensions of feed rod	Freezing rate	Thermal conditions	Mission, hardware	Results: surface	Results: interior (EPD = etch pit density)	Authors
InSb (+ 10^{18} Te/cm^3) <111>B in growth direction	Quartz, graphite spacers at end. 10^{-7} torr He	14.5 mm dia, 110 mm long, regrew 60 mm	~ 12 mm/hr gradient freeze	Heat up 120 min, soak 60 min, cool 70.2 K/hr for ~ 4 hr, power off.	Skylab 3 Westinghouse furnace 1973	Irregularly spaced ridges in growth direction, 25 μm avg height. Irreg. spaced lines normal to growth dir. attributed to vibrations.	Concave. Diffusion-controlled doping with no fluct'ns except on & near facet on one side, twins normal to growth direction.	Witt, Gatos *et al.* [E, 11, 11a, 11b, 11c]
InSb (+ 10^{18} Te/cm^3) <111>B in growth direction	Quartz, graphite spacers at end. 10^{-7} torr He	14.5 mm dia, 110 mm long, regrew 60 mm	~ 10 mm/hr before power off, then ~ 17 mm/hr	Soak 60 min, cool 70.2 K/hr for 140 min, soak 60 min, power off.	Skylab 4 Westinghouse gradient freeze furnace 1974	Reduced dia for 30 mm, then irregularly spaced ridges ~ 25 μm high. Similar appearance to Czochralski crystals.	Concave interface, diffusion-controlled doping with no fluct'ns, EPD 40% less than from earth.	Witt, Gatos *et al.* [E, 11, 11a, 11c]
InSb (≤ 10^{16} Zn/cm^3 or ~ 10^{19} Te cm^{-3}) <111>B	Carbon-coated quartz 10^{-5} torr	11 - 13 mm diameter, 20 - 30 mm long	3 - 9 mm/hr gradient freeze	Soak 2.3 hr, gradient 10K/cm, cool 11.3 K/hr.	Salyut-6 Splav-01 furnace	Necked in for ~ 20 mm to ~ 1.5 mm maximum gap.	Few inclusions, no striations, EPD reduced to 10 - 10^2 cm^{-2}	Zemskov *et al.* [12, 12a, 13, 13a, 13b]
InSb (undoped) <211>	Carbon-coated quartz 10^{-7} torr	8 mm dia, 60 mm long	11.3 mm/hr translation		Salyut-6 Kristall facility ~ 1978	Contact only on oblong mounds (hillocks), mat surface elsewhere.	EPD 250 cm^{-2}, particles mark seeding boundary, many twins.	Khashimov *et al.* [18]
InSb (7x10^{17}Te/cm^3) <211>	Carbon-coated quartz 10^{-7} torr	8 mm dia, 60 mm long	11.3 mm/hr translation		Salyut-6 Kristall facility ~ 1978	Spiral region free from contact, with hillocks & periodic bands, decreasing from 1/2 of perimeter to 1/5. Bubbles where attached.	Fewer grain boundaries, generally twins. No 5μm inclusions near seed as from earth. EPD 10^3-2x10^5/cm^2. Resist & mobility constant.	Khashimov *et al.* [18]
InSb (undoped & 9x10^{19} Sn/cm^3)	Unsealed quartz, machined inside, graphite caps.	10 & 14 mm dia, 100 mm long	0 to ~ 22 mm/hr from calorimetric technicque	Soak 2 hr, cool 4.3 hr, soak 2 hr	Shuttle D1 Gradient Heating Facility - 03 1987	Attached except where crucible had machining defects; wide bubble covering 22% at start of growth of Sn-doped.	Intensive segregation of Sn near bubble, attributed to Marangoni convection.	Duffar *et al.* [15]
InSb	Quartz and BN crucibles, C & BN end caps.	12 mm dia., 15 mm long.		Melted and cooled in 5 min.	TEXUS 31 TEM01-1	Kept shape of feed rods due to oxide coating, ~1μm thick & mostly Sb oxide.		Duffar *et al.* [22]
InSb	Quartz & C end caps; one smooth, one with grooves.	12 mm dia., 15 mm long.		Melted and cooled in 5 min.	TEXUS 32 TEM01-4	Both detached. Smooth ampoule gave irregular & larger facets. Machined gave cylindrical with rings.		Duffar *et al.* [22]
InSb <111> B	Quartz with large free space 10^{-3} - 10^{-4} torr	13 mm dia., 100 mm long	gradient freeze	Gradient 10 - 15 K/cm, cool 11.3 K/hr	Kosmos-1744 Splav-02 , 1986	Necked in ~ 10 mm, highly asymmetric, ~ 3 mm on one side, < 1 mm other.	No dopant striations and enhanced perfection.	Zemskov [14]

Material	Ampoule or crucible	Dimensions of feed rod	Freezing rate	Thermal conditions	Mission, hardware	Results: surface	Results: interior (EPD = etch pit density)	Authors
InSb <111> B	Quartz with large free space 10^{-3} - 10^{-4} torr	13 mm dia., 100 mm long	gradient freeze	Gradient 10-15 K/cm, cool 11.3 K/hr	Foton Splav-02, 1989	Detached ~ 1/2 of length on one side, much less on other side.	No dopant striations and enhanced perfection	Zemskov [14]
InSb (~ 10^{16} Zn/cm^3) <111>	Quartz ~ 10^{-5} torr		gradient freeze	Heat 90 min, then power off.	Recoverable Satellite Multi-purpose Crystal Processing Furnace, 1987	Smooth. Separated from container, while earth sample adhered tightly to quartz ampoule.	No dopant striations, 3.6% radial variation in resistivity compared to 34% from earth.	Zhang *et al.* [16, 16a]
NaF-NaCl (eutectic)	Graphite-lined teel tube	9.5 mm dia.	gradient freeze	Cool 36 K/hr, gradient 50 K/cm	Skylab, Westinghouse furnace, 1974			Yue and Yu [37]
$PbBr_2$ (+ 2% $PbCl_2$)	Quartz 10^{-5} torr				Sounding rocket TR-IA 3 1993	Traces of microscopic free surface. Contact angle with quartz 30-40°		Kinoshita *et al.* [35, 35a]
$PbCl_2$ - AgCl	Quartz	8 mm dia., 50 mm long	11.2 mm/hr translation	Gradient 15 K/cm	Salyut - 6 "Morava" Kristall facility	Partial detachment. Shape of the sample differs from that of the ampoule		Barta *et al.* [36]
PbTe (+ 0.41% In)	Quartz 10^{-5} torr	8 mm dia., ~ 30 mm long	11.3 mm/hr translation	Heat up 90 min, soak 4 hr, Gradient 90 K/cm	Salyut-6 Kristall facility	Many pores at ~ 21 mm, especially on one side, with surfaces of same morphology as detached parts.	The distribution of In in space sample is more homogeneous.	Abramov *et al.* [32]
$PbSe_{0.5}Te_{0.5}$	Quartz		2-50 mm/hr gradient freeze	Soak 2 hr (Syrena 1), 4 hr 45 min (Syrena 2)	Salyut-6, 1978 (Syrena 1, Syrena 2) Splav-01 furnace 1978	Detached	Quality strongly dependent on growth rate, at slow growth rates grains ~5mm.	Galazka *et al.* [26a]
$Pb_{0.8}Sn_{0.2}Te$	Quartz Ar	16 mm dia., ~ 40 mm long	< 3.5 mm/hr	Gradient 20 K/cm	Shuttle STS 61A 3-zone furnace 1985	Few small grains contacted the wall, the rest of the surface was detached and very near the wall.		Crouch, Fripp *et al.* [31]
Si (+ Sb or B)	Graphite-lined quartz, graph or Mo cruc, 10^{-5} torr	8 mm dia.	gradient freeze	100 s to heat, 80 s to melt, 400 s to freeze	MIR sound rocket, 10 min, BKT exothermic furnace, 1980	Contacted walls only in separate small areas. Surface enriched in Sb.	Single crystals grew at 7 - 10 mm/min compared to polycrst on earth. EPD 10^2-10^3 lower.	[4]
Zn (+ Zn^{65})	Graphite, Ar $5x10^{-6}$ torr	46.8 mm long	gradient freeze	Soak 1 hr at 775°C, gradient 45 K/cm	Skylab 3 Westinghouse furnace, 1974	Wrinkled	Nonuniform distribution of isotope	Ukanwa [38]

Material	Ampoule or crucible	Dimensions of feed rod	Freezing rate	Thermal conditions	Mission, hardware	Results: surface	Results: interior (EPD = etch pit density)	Authors
Zn - Pb monotectic (15 vol% Pb)	Graphite crucible			Soak 15 min at 850°C, cool 1800 K/hr	Shuttle D1 IHF 01	Gap on cold side with Zn spheres flattened against ampoule wall.		Ahlborn, Lohberg [40]

Attachment B. **Some directional solidification experiments performed in space that did not appear to have shown detachment.**

Material	Ampoule or crucible	Dimensions of feed rod	Freezing rate	Thermal conditions	Mission, hardware	Results: surface	Results: interior (EPD = etch pit density)	Authors
Al-Cu eutectic (+ 33 wt.% Cu)	Ar	5 mm dia., 150 mm long		No soak	Spacelab 1 STS-9 1983	Spherical bubbles (0.5 to 2 mm) on the last third of the low-gravity samples.	No change in lamellar spacing or regularity.	Favier and De Goer [47,47a,47]
Bi (+ 1% Sb)	carbon-coated quartz		gradient freeze	Cool 3 K/hr for 24 hr, gradients 5 K/cm and 11 K/cm	Salyut-6, Berolina. Splav 01 furnace, 1978	Bubbles, with smooth surface between in contact with wall		Schneider *et al.* [49]
Fe-C-Si (3 - 4% C)	Al_2O_3 skin, ~ 80μm thick, cylindrical with neck	7 mm dia, 150 mm long	6-18 mm/hr	Heat to 1350°C, soak 5 min, gradient 200-300 K/cm	Shuttle D-1 IHF-07 1985	The cast iron sample was processed within the Al_2O_3 skin without any detachment.	Sample diameter increase, no free pores or cavities	Sprenger [46]
GaP <111>	quartz	9 mm dia.		Soak 1000 - 1060°C for 15 hr, gradient 20 - 40 K/cm	Salyut-6, Kristall facility, zone melting	Bubbles on surface (melt length 3-5 mm)	EPD 10^4-10^5 cm^2, electrophysical properties similar	Regel *et al.* [24, 24a]
$Ga_{1-x}In_xSb$ (x = 0.1,0.3,0.5)	Carbon-coated quartz, 3 graph spacers sep'd by quartz wool at each end, 10 torr He.	8 mm dia., 90 mm long	~ 8 mm/hr, increasing down ingot, gradient freeze	Soaked 16 hr at 1020°C to melt back ~1/2, initial gradient 80 K/cm, cooled 36K/hr	Skylab 4 Westinghouse furnace 1974	Shiny surface in contact with ampoule. Not detached.	Mostly twin boundaries. 37% fewer boundaries than from earth. Planar initial interface. Radially uniform composition. Axial seg'n diff. control.	Yee,Wilcox, *et al.* [E, 25, 25a, 25b, 25c, 25d, 25e]
Ge ($5x10^{18}$ Ga/cm^3) <100>	Part free, part Pyrex-coated, 760 torr Ar	6 mm dia., ~ 20 mm melted	gradient freeze	Gradient 95 K/cm	MASER 2 rocket, 7 min, mirror furnace, 1990	Good contact with Pyrex, cracks in uncoated part, attributed to Ge oxide.		Tilberg & Carlberg [7]
Ge	Quartz. Carbon sheets at ends of crystal.	7 mm dia., 100 mm long, 7 mm grown	360 mm/hr measured by CCD camera		TR-IA rocket, 6 min Transparent gold-coated furnace with Ta heating coil,1992	Strong sticking of crystal to ampoule and carbon sheets at ends. Crack in ampoule at end of growth.	Convex interface. EPD ~ $10^6/cm^2$. Slightly lower from earth.	Nishinaga *et al.* [9, 9a]
InSb (undoped & ~$10^{20}$$Sn/cm^3$) <111>B in growth direction	Quartz, graphite spacers at end. 10^{-7} torr He	14.5 mm dia, 110 mm long, regrew 60 mm	~ 12 mm/hr gradient freeze	Heat up 120 min, soak 60 min, cool 70.2 K/hr for ~ 4 hr, power off.	Skylab 3 Westinghouse furnace 1973	Smooth and shiny. Randomly distributed cavities, i.e. gas bubbles.		Witt, Gatos *et al.* [E, 11, 11a]

Material	Ampoule or crucible	Dimensions of feed rod	Freezing rate	Thermal conditions	Mission, hardware	Results: surface	Results: interior (EPD = etch pit density)	Authors
InSb (undoped & ~10^{20}Sn/cm^3) <111>B in growth direction	Quartz, graphite spacers at end. 10^{-7} torr He	14.5 mm dia, 110 mm long, regrew 60 mm	~ 10 mm/hr before power off, then ~17	Soak 60 min, cool 70.2 K/hr for 140 min, soak 60 min, power off.	Skylab 4 Westinghouse gradient freeze furnace, 1974			Witt, Gatos *et al.* [E, 11, 11a]
PbTe (+ 10^{18} Ag)	Quartz Ar	17 mm dia., 50 mm long	10 mm/hr gradient freeze	Gradient 30 K/cm, cool	Shuttle Spacelab-1 CNES gradient freeze	Many bubbles up to 4 mm in dia. on the surface. No evidence of detachment.		Rodot and Tottereau [30]
$Pb_{0.8}Sn_{0.2}Te$<111>	BN crucible in quartz + BN piston, spring <10^{-5} torr	15 mm dia., 58 mm long, 32 mm grown in space	5.5 mm/hr translation	Heat up 1 hr, soak 1 hr, gradient >40 K/cm	SL-J/FMPT Shuttle 1992	Large voids inside one portion. Interface shifted from concave to convex. No detachment.	EPD 5x10^5 cm^{-2} (space) vs 3x10^6 cm^{-2} (earth). Homogeneous in void-free section. Mobility & resistivity ~2X higher from space.	Kinoshita [33]

ATTACHMENT C
Literature citations for Attachments A and B

[E] Microgravity Data Base, European Space Agency via http://www.esrin.esa.it/htdocs/mgdb/mgdbh1.htm

[1] A.F. Witt, H.C. Gatos, M. Lichtensteiger and C.J. Herman, "Crystal Growth and Segregation under Zero Gravity: Ge," J. Electrochem. Soc. 125(1978)1832.

[1a] A.F. Witt, H.C. Gatos, M. Lichtensteiger and C.J. Herman, in: Apollo-Soyuz Test Project (ASTP), NASA Report TM-X-73360, MSFC, Section V (1977).

[1b] H.C. Gatos and A.F. Witt, "Interface Markings in Crystals, Experiment MA-060," NASA report (1976) 25-1.

[1c] H.C. Gatos, C.J. Herman, M. Lichtensteiger and A.F. Witt, "Quantitative Determination of Zero-Gravity Effects on Crystal Growth from the Melt (Experiment MA-060)," in: ESA Special Publication No. 114. (1976)181.

[1d] A.F. Witt, "Crystal Growth Experiments on ASTP - An Overview," in: ESA Special Publication No. 114. (1976) 34.

[2] J.T. Yue and F.W. Voltmer, "Influence of Gravity-Free Solidification on Solute Microsegregation," J. Crystal Growth 29(1975)329.

[2a] J.T. Yue and F.W. Voltmer, "Influence of Gravity-Free Solidification on Microsegregation," in: Proceedings of the Third Space Processing Symposium, Skylab Results, NASA M74-5, 1(1974)375-424.

[3] V.S. Zemskov, V.N. Kubasov, I.N. Belokurova, A.N. Titkov, I.L. Shulpina, V.I. Safarov, and N.B. Guseva, "Ge-Si Solid Solutions, Experiment MA-150," in: Apollo-Soyuz Test Project (ASTP), NASA Report TM-X-73360, MSFC, Section IX (1977).

[4] V.S. Avduevsky, editor, "Manufacturing in Space: Processing Problems and Advances," MIR Publishers, Moscow (1982).

[5] A.A. Chernov, S.N. Maksimovskii, L.A. Vlasenko, E.N. Kholina, V.P. Martovitskii and V.L. Levtov, "Growth of Germanium Crystals with Low Dislocation Density in a Condition of Weightlessness," Soviet Physics Crystallography 29(1984)222-225.

[6] V.T. Khryapov, V.A. Tatarinov, T.V. Kul'chitskaya, N.A. Kul'chitskiy, E.V. Markov and R.S. Krupyshev, "Growth of Ge Bulk Single Crystals by Directional Solidification in Microgravity," in: V.S. Avduevsky (ed.), Technological Processes in Low Gravity (UNTS AN SSSR, Sverdlovsk (1983)47-58.

[6a] E.V. Markov, and R.S. Krupyshev and Yu.N. Kuznetsov, "Growth of Ge Bulk Single Crystals by Directional Solidification and Segregation in Microgravity," in: Abstracts, VI International Conference on Crystal Growth (ICCG-6), Moscow, 2(1980)261.

[7] E. Tillberg and T. Carlberg, "Semi-Confined Bridgman Growth of Germanium Crystals in Microgravity," J. Crystal Growth 99(1990)1265-1272.

[8] E.V. Markov *et al.*, "The Influence of Space Conditions on Directional Crystallization of Germanium and its Properties," in: Proceedings of the 3rd European Symposium on Material Science in Space, ESA SP-142, Grenoble (1979)17-23.

[8a] E. V. Markov, R.S. Krupishev, Yu.N. Kuznetsov, T.V. Kulchitskaya, N.A. Kulchitsky, T.I. Markova, V.A. Tatarinov and V.T. Khryapov, "Growth of Bulk Germanium Single Crystals by Directional Crystallization and Segregation Processes in Microgravity," in: Abstracts, ICCG-6, Moscow (1980)273-274.

[9] T. Nishinaga, Y. Okamoto, S. Yoda, T. Nakamura, O. Saito, Y. Hisada, H. Ando and S. Anzawa, "Rapid Melt Growth of Ge by TR-IA Sounding Rocket," J. Jpn. Soc. Microgravity Appl.10(1993)212.

[9a] T. Nishinaga, "Utilization of Microgravity to Understand the Crystal Growth of Semiconductors," Microgravity Quart. 3(1993)109-113.

[10] O. Calzadilla, J. Fuentes, I. Shulpina and L. Sorokin, "Estudio de los Cristales de Germanio Dopados con Indio en el Experimento 'Carbibe'," IX SLAFES, Latin American Seminar on Solid State Physics, Mar de Plata, Argentina (1985).

[10a] O. Calzadilla, J. Fuentes, J. Vidal, P. Diaz, R. Romero, C. Arencibia, E. Hernandez, L.M. Sorokin, I.I. Shulpina and A.S. Trebugova, "Influencia de la microgravitacion en la estructura y distribucion del elemento indio en una aleacion de Ge-In," Ciencias Tecnicas, Fisicas y Matematicas (April 1984)17-21.

[11] A.F. Witt, H.C. Gatos, M. Lichtensteiger, M.C. Lavine and C.J. Herman, "Crystal Growth and Steady-State Segregation under Zero Gravity: InSb," J. Electrochem. Soc. 122(1975)276.

[11a] A.F. Witt, H.C. Gatos, M. Lichtensteiger, M.C. Lavine and C.J. Herman in: Proceedings of the Third Space Processing Symposium, NASA M74-5, 1(1974)275-299.

[11b] H.C. Gatos, A.F. Witt, C.J. Herman, M.C. Lavine and M. Lichtensteiger, "Crystal Growth and Segregation Behavior under Zero Gravity Conditions: InSb," in: Skylab Science Experiments, eds. G.W. Morganthaler and G.E. Simonson, American Astronautical Society, Tarzana (1975)7-25.

[11c] H.C. Gatos, "Semiconductor Crystal Growth and Segregation Problems on Earth and in Space," in: Materials Processing in the Reduced Gravity Environment of Space, ed. G.E. Rindone, Elsevier, NY (1982)355-371.

[12} I.L. Shulpina, L.M. Sorokin, M.R. Raukhman, V.S. Zemskov, A.S. Tregubova, G.N. Mosina and E.A. Kositsyna, "Structural Quality of InSb single crystals with p-n junctions grown under space flight conditions," Sov. Phys. Solid State 23(1981)1775-1778.

[12a] I.V. Barmin, V.S. Zemskov, I.T. Krutovertsev, N.P. Konovalova, A.V. Laptev and M.R. Raukhman, "The Features of Dopant Segregation in InSb Single Crystals Grown by Directional Solidification. The Dependence on Grown Conditions," in: Doped Semiconductor Materials, Nauka, Moscow, ed. V.S. Zemskov (1985)127-131 (in Russian).

[12b] I.L. Shulpina, L.M. Sorokin, A.S. Tregubova, G.N. Mosina, V.S. Zemskov, M.R. Raukhman and E.A. Kozitsina, "Osobennosti strukturi legirovannikh kristallov antimonida indiya s p-n-pereokhodami, virashchennikh v osloviyakh nevesomosti," in: Legirovanniye Polyprovodnikoviye Materiali, ed. V.S. Zemskov, Nauka, Moscow (1985)138-142.

[13] V.S. Zemskov, I.V. Barmin, M.R. Raukhman and A.S. Senchenkov, "Eksperimenti po virashchivaniyo legirovannogo antimonida indiya v usloviyakh orbitalnogo poleta kosmicheskogo kompleksa 'Salyut-6'-'Soyuz'," in: Technological Experiments in Zero Gravity, Ural Scientific Center of the USSR Academy of Science, Sverdlovsk (1983)30-46.

[13a] V.S. Zemskov *et al.*, in: "K.E. Tsiolkovski and Problems of Production in Space," IIET, USSR Academy of Science, Moscow (1982)38-56.

[13b] V.S. Zemskov *et al.*, "Solidification of doped indium antimonide alloys in low gravity," Fiz. Khim. Obrab. Mater. 5(1983)56-65.

[14] V.S. Zemskov, M.R. Raukhman, E.A. Kozitsina, I.V. Barmin and A.S. Senchenkov, "Experiments on Directional Crystallization of Indium Antimonide on 'FOTON' Automatic Satellites," in: Proceedings of AAIA/IKI Microgravity Science Symposium, American Institute of Aeronautics and Astronautics, Washington DC (1991)124-129.

[15] T. Duffar, C. Potard and P. Dusserre, "Growth Analysis of the InSb Compound by a Calorimetric Method in Microgravity; Results of the SpaceLab-D1 Experiment," J. Crystal Growth 92(1988)467-478.

[16] F. Zhang, L. Zhang, G. Chen, M. Shen, G. Yan, D. Da, L. Huang, X. Xie and X. Tan, "InSb Crystal Growth under Microgravity Conditions," Chinese Science Bulletin 34(1989)1529-1532.

[16a] D.Y. He, Private Communication, Lanzhou University, China (1997).

[17] V.T. Khryapov, Ye.V. Markov, *et al.*, "Studies into Semiconductor Material Science Made with a Kristall Facility," in: eds. S.D. Grishin and L.V. Leskov, Prospects and Problems of Space Manufacturing, IIET AN SSSR, Moscow (1983)24-31.

[17a] V.T. Khryapov, Ye.V. Markov, N.A. Kulchitsky and Ye.T. Solomin, "Technology of Space Semiconducting Materials Science and the Development of Specialized Processing Equipment," Elektron. Promyshl. 1(1983)77-80.

[17b] V.T. Khryapov, Yu.N. Dyakov, Ye.V. Markov, N.A. Kulchitsky, *et al.*, "Technological Experiments on Space Materials Science with the Kristall Furnace on Salyut-6," in: Materials Science in Space, IIET AN SSSR, Moscow (1982)20-43.

[18] F.R. Khashimov, *et al.*, "Structural and Physical Characteristics of InSb Single Crystals Grown Under Near-Zero Gravity Conditions," in: Proceedings of the Third European Symposium on Materials Science in Space, Grenoble (1979)9-15.

[19] E. Lendvay, M. Harsy, T. Gorog, I. Gyuro, I. Pozsgai, F. Koltai, J. Gyulai, T. Lohner, G. Mezey, E. Kotai, F. Paszti, V.T. Hryapov, N.A. Kultchitsky and L.L. Regel, "The Growth of GaSb Under Microgravity Conditions," J. Crystal Growth 71(1985)538-550.

[19a] I. Gyuro, E. Lendvay, M. Harsy, T. Gorog, I. Pozsgai, K. Somogyi, F. Koltai, J. Gyulai, T. Lohner, J. Gyilai, M. Kanky, J. Giber, L. Bori, L.L. Regel, V.T. Khryapov and N.A. Kultchitsky, "Crystal Growth of GaSb Under Microgravity Conditions," Acta Astronautica 11(1984)361-368.

[20] O.V. Shumaev and L.L. Regel, "GaSb Crystal Growth in Microgravity Conditions," in: Proceedings of AAIA/IKI Microgravity Science Symposium, American Institute of Aeronautics and Astronautics, Washington DC (1991)119-123.

[20a] L.L. Regel, O.V. Shumaev, I.V. Vidensky, I.M. Safonova, A.A. Vedernikov, I.V. Melikhov, V.F. Komarov, A.I. Ivanov and S. Suleiman, "Experiments on Crystallization of Semiconductor Materials, Eutectic Alloys and Crystal Growth from Water Solution in Microgravity," Acta Astronautica 21(1990)331-348.

[20b] L.L. Regel, private communication, Clarkson University, Postdam, NY (1996).

[21] P. Ge, T. Nishinaga, C. Huo, Z. Xu, J. He, M. Masaki, M. Washiyama, X. Xie and R. Xi, "Recrystallization of GaSb under Microgravity During China Returnable Satellite No. 14 Mission," Microgravity Q. 3(1993)161-165.

[21a] T. Nishinaga, P. Ge, C. Huo, Z. Xu, J. He, M. Masaki, M. Washiyama, X. Xie and R. Xi, "Bridgman Growth of GaSb under Microgravity," Annual Report of the General Experiment Station of the Department of Engineering of the University of Tokyo 52(1993)99-103.

[21b] T. Nishinaga, P. Ge, C. Huo, J. He and T. Nakamura, "Melt Growth of Striation and Etch Pit Free GaSb under Microgravity," American Conference on Crystal Growth - 10, Vail (1996).

[22] T. Duffar, P. Dusserre and J. Abadie, "Crucible-Semiconductor Interactions during Crystal Growth from the Melt in Space," 30th COSPAR Scientific Assembly, Hamburg, (1994); Adv. Space Res. 16(1995)199-203.

[22a] T. Duffar, P. Dusserre and M.D. Serrano, "Bridgman Solidification of GaSb. Results of EURECA AMF-118 Experiment," Adv. Space Res. 16(1995)101-104.

[22b] M.D. Serrano *et al.*, "Segregation in space GaInSb crystals," ELGRA meeting, Madrid (1994).

[22c] T. Duffar, seminar, Clarkson University, Potsdam, New York (1995).

[23] T. Duffar and J. Abadie, "Convective Effects in the Growth of GaInSb Crystals," in: Preliminary Results of the D2 Mission, Norderney (1994).

[23a] T. Duffar *et al.*, "Segregation during GaInSb solidification in space and on earth," in: 9th European Symposium on Gravity Dependent Phenomena in Physical Sciences, Berlin (1995).

[24] N.T. Ngi, T.I. Olkhovikova, L.L. Regel and F.R. Khashimov, "Study of the Morphological Characteristics of GaP Crystals Obtained in Weightlessness," in: Trudy VI. Scientific Conferences on Space Aeronautics Dedicated to the Memory of the Soviet Pioneers in Space. Sect. 'Space Research', Moscow (1982); Study of Materials in Space, pp.144-152.

[24a] L.L. Regel and N.T. Ngi, "Distribution of the Impurities in GaP Crystals Obtained in Weightlessness," in: Abstracts, 6th International Conference on Crystal Growth (ICCG-6), Moscow 2(1980)147.

[25] J.F. Yee, M.C. Lin, K. Sarma and W.R. Wilcox, "The Influence of Gravity on Crystal Defect Formation," J. Crystal Growth 30(1975)185-192.

[25a] W.R. Wilcox, J.F. Yee, M.C. Lin, K. Sarma and S. Sen, "Directional Solidification of InSb-GaSb Alloys," in: Skylab Science Experiments, eds. G.W. Morganthaler and G.E. Simonson, American Astronautical Society, Tarzana (1975)27-41.

[25b] J.F. Yee, S. Sen, W.R. Wilcox, et al., in: Proceedings of the Third Space Processing Symposium, Skylab Results, NASA M74-5, 1(1974)301-374.

[25c] R.A. Lefever, K.R. Sarma, C.E. Chang and W.R. Wilcox, "Microstructure and Composition of InSb-GaSb Ingots Directionally Solidified Aboard Skylab," paper 77-161, AIAA 15th AeroSpace Sciences Meeting, Los Angeles (1977).

[25d] R.A. Lefever, W.R. Wilcox and K.R. Sarma, "Orientation,Twinning and Orientation-Dependent Reflectance in InSb-GaSb Alloys," Mat. Res. Bull. 13(1978)1175-1180.

[22e] R.A. Lefever, W.R. Wilcox, K.R. Sarma and C.E. Chang, "Composition Variations in Directionally Solidified InSb-GaSb Alloys," Mat. Res. Bull. 13(1978)1181-1191.

[26] R.R. Galazka, T. Warminski, J. Bak, J. Auleytner, T. Dietl, A.S. Okhotin, R.P. Borovikova and I.A. Zubritskij, "Directional Crystallization of CdHgTe in Microgravity Conditions," J. Crystal Growth 53(1981)397-408.

[26a] R.R. Galazka, T. Warminski, J. Bak, J. Auleytmer, A. Jedrzejczak, A. Szcserbakow, A.S. Okhotin, R.P. Borovikova, I.A. Zubritskij, V.T. Khryapov, E.V. Markov and I.V. Barmin, "Experiment SYRENA 1,2,3 - Space Processing of CdHgTe, CdHgSe and PbSeTe," in: Proceedings of the 3rd European Symposium on Material Science in Space, Grenoble, European Space Agency SP-142, Paris (1979)47-51.

[27] L.N. Kurbatov, B.N. Golovin, A.V. Izyurov and N.V. Komarov, "Experiments on the preparation of solid solutions of Cd-Hg-Te," in: V.S. Avduevsky, V.S. Polezhayev (eds.), Fluid Mechanics and Heat and Mass Transfer in Low Gravity, Nauka, Moscow (1982)218-221.

[28] D.J. Larson, Jr., J.I.D. Alexander, D. Gillies, F.M. Carlson, J. Wu and D. Black, "Orbital Processing of High-Quality CdTe Compound Semiconductors" in: Proceedings of the Joint Launch + One Year Science Review of USML-1 and USMP-1 with the Microgravity Measurement Group, Huntsville, NASA Conference Publication 3272, 1(1993)129-161.

[29] S.L. Lehoczky, F.R. Szofran, D.C. Gillies, S.D. Cobb, C.-H. Su, Y.-G. Sha and R.N. Andrews, "Crystal Growth of Selected II-VI Semiconducting Alloys by Directional Solidification," in: Proceedings of the Joint Launch + One Year Science Review of USML-1 and USMP-1 with the Microgravity Measurement Group, Huntsville, NASA Conference Publication 3272, 1(1993)163-222.

[30] H. Rodot and O. Tottereau, in: Proceedings of the 5th European Symposium on Material Science in Space, ESA SP-222, Bordeaux (1987)135-139.

[31] R.K. Crouch, A.L. Fripp, W.J. Debnam, G.A. Woodell, I.O. Clark, F.M. Carlson and R.T. Simchick, "Results from a Compound Semiconductor Crystal Growth Experiment in a Low Gravity Environment," in: SAMPE Electronic Materials & Processes Conference, Santa Clara (1987).

[32] O.V. Abramov, A.S. Okhotin, Zh.Yu. Chashechkina, I.P. Kazakov, O.I. Rakhmatov and S.A. Zver'kov, "The Results of the Study of $Pb_{1-x}In_xTe$ Crystals, Grown by Bridgman Method on Board Salyut-6," in: V.S. Avduevsky (ed.), Technological Processes in Low Gravity, UNTS AN SSSR, Sverdlovsk (1983)47-58.

[32a] O.V. Abramov, Zh.Yu. Chashechkina, I.P. Kazakov and G.E. Ignatjev, "Structural Studies of PbTe Crystals and Te-Se Solid Solutions Obtained under Different Gravity Conditions in the 'Crystal' Furnace," in: Abstracts of ICCG-6, Moscow (1980)262-264.

[33] K. Kinoshita and T. Yamada, "$Pb_{1-x}Sn_xTe$ Crystal Growth in Space," J. Crystal Growth 147(1995)91-98.

[34] H. Zusmann, K. Stekker, V. Aihler, S. Langhammer, N.H. Huen, N.V. Vuong, C.S. Hoai, V.M. Truzhenikov and M.B. Scherbina-Samoilova, "Results of the Experiments 'Halong-2,-3' on Directional Crystallization of $(Bi_{1-x}Sb_x)_2Te_3$ Solid Solutions in 'Kristall' Facility on Board 'Salyut-6' Space Station," in: Salyut-6 - Soyuz - Materials Science and Technology, Nauka, Moscow (1985)37-51.

[35] K. Kinoshita, S. Yoda, T. Nakamura, H. Sameshima, H. Ando, S. Anzawa, and Y. Arai, "Video-Imaging of the Melting and Solidification Processes of the $PbBr_2$-$PbCl_2$ System Under Microgravity," in: Proceedings of the International Conference on Crystal Growth, Holland (1995).

[35a] K. Kinoshita, S. Yoda, T. Nakamura, H. Sameshima, H. Ando, S. Anzawa and Y. Arai, "In-Situ Observation of Melting and Solidification Processes in the $PbBr_2$-$PbCl_2$ System under Microgravity," J. Jpn. Soc. Microgravity Appl. 12(1995)134-143.

[36] C. Barta, J. Trnka, A. Triska, V.I. Khrjapov, A.S. Okhotin and I.A. Zubritsky, "Experiment Morava on the Board of Salyut 6," in: Proceedings of the Third European Symposium on Materials Science in Space, Grenoble (1979)215-219

[38] A.O. Ukanwa, in: Proceedings of the Third Space Processing Symposium, Skylab Results, NASA M74-5, 1(1974)425-456.

[39] E.A. Hasemeyer, C.V. Lovoy and L.L. Lacy, in: Proceedings of the Third Space Processing Symposium, Skylab Results, NASA M74-5, 1(1974)457-467.

[40] H. Ahlborn and K. Lohberg, in: Proceedings Norderney Symposium on Scientific Results of the German SpaceLab Mission D1, Norderney (1986)297-304.

[41] L. Froyen and A. Deruyttere, "Melting and Solidification of Metal Matrix Composites under Microgravity," in: 5th European Symposium on Material Science under Microgravity, Schloss Elmau, ESA SP-222 (1984)69-78.

[42] H. Sprenger, "Skin Casting of Alloys and Composites - Results of SL-1 and TEXUS experiments," in: 5th European Symposium on Material Science under Microgravity, Schloss Elmau, ESA SP-222 (1984)87-94.

[43] F. Barbieri, C. Patuelli, P. Gonndi and R. Montanari, "Melting and Solidification in 0-g of Sintered Alloys Experiments ES311 A&B 'Bubble Reinforced Materials'," in: 5th European Symposium on Material Science under Microgravity, Schloss Elmau, ESA SP-222 (1984)101-107.

[44] C. Potard and P. Morgand, "Directional Solidification of a Vapor Emulsion Aluminum-Zinc in Microgravity," in: 5th European Symposium on Material Science under Microgravity, Schloss Elmau, ESA SP-222 (1984)121-125.

[45] E.G. Fuks, A. Roos and G. Buza, "Metallurgical Studies in Space: Program 'Bealutsa'," in: Salyut-6 - Soyuz - Materials Science and Technology, Nauka, Moscow (1985)101-115.

[46] H.J. Sprenger, "Skin Technology - Directional Solidification of Multiphase Alloys," in: Scientific Results of the German Spacelab Mision D1, Proceedings of Norderney Symposium (1986)342-349.

[47] J.J. Favier, J.P. Morlevat and J. Duvernoy, "Method of analysis of the regularity of lamellar eutectic structures by diffraction of a laser beam," Met. Trans. B 14-B(1983)105-108.

[47a] D. Camel and J.J. Favier, "Thermal convection and longitudinal macrosegregation in horizontal Bridgman crystal growth," J. Crystal Growth 67 (1984)42-67.

[47b] J.J. Favier and J. De Goer, "Directional Solidification of Eutectic Alloys," ESA SP-222 (1984)127.

[48] H.C. Gatos, J. Lagowski, I.M. Pawlowicz, F. Dabkowski and C.J. Li, "Crystal Growth of GaAs in Space," Results of Spacelab-1, Schloss Elmau, European Space Agency, Paris (1984).

[48] H.C. Gatos, J. Lagowski, L.M. Pawlowicz, F. Dabkowski, and C-J Li, "Crystal Growth of GaAs in Space," in: Results of Spacelab-1, 5-th European Symposium on Materials Science Under Microgravity, Schloss, FRG, 1984, pp.221-225.

[49] G. Schneider, R. Herrmann, H. Kruger, P. Rudolph, R. Kuhl and R. Rostel, "Results of Crystal Growth of Bismuth-Antimony Alloys ($Bi_{100-x}Sb_x$) in a Microgravity Environment," Crystal Res. & Technol. 18 (1983) 1213-1224.

[49a] P. Rudolph, Private Communication, Institute of Crystal Growth, Berlin (1997).

[50] L.A. Vlasenko, B.N. Golovin, L.N. Kurbatov, S.N. Maksimovskii, R.A. Khazieva, E.N. Kholina and B.I. Yurushkin, "Crystallization of Germanium in Microgravity at High Rates," in: V.S. Avduevsky and V.S. Polezhayev, eds., Fluid Mechanics and Heat and Mass Transfer in Low Gravity, Nauka, Moscow (1982) 221-230.

ATTACHMENT D

Authors run-on-prints of the journal

MICRO GRAVITY SCIENCE AND TECHNOLOGY

International Journal for Microgravity Research and Applications

dimension. These were difficult to measure because they had clumped together after the flight and could not be separated without breakage. Since the purpose of this initial flight experiment was the evaluation of the technique, no provision was made for in-flight retrieval of the grown crystals from the growth cells. Crystal retrieval will be required on subsequent flights to provide crystals suitable for post-flight analysis. A total of 4.34 g of crystals were recovered from the cell after it was returned to the laboratory. The third planned run could not be performed because of time constraints.

5 Conclusion

This experiment successfully demonstrated the value of our new method of initiating nucleation in a solution in microgravity in providing significantly better control over nucleation and growth processes than conventional techniques. A predetermined volume of nucleating solution was deployed in the desired location in a growth solution-filled cell. Nucleation was restricted to this well-defined region near the center of the cell, and crystallites were grown. The nucleation onset time was much shorter than expected based on the results of ground control experiments using the same concentrations. In these experiments a series of solutions of various concentrations were prepared and loaded into test tubes which were then sealed and allowed to cool to room temperature. These tubes were inspected periodically, and the time of the appearance of visible nucleation was noted. Nucleation onset times were typically hours to days. The reason for the difference between ground-based and flight onset times has not yet been determined, but turbulence in the nucleating solution during injection, and the high cooling rate may have been important factors. Further experiments will emphasize the optimization of the solution concentrations to improve control of the nucleation rate. With finer control over nucleation, this method will permit more precise control over growth parameters which control crystal characteristics.

References

1 *Nyvlt, J., Sohnel, O., Matuchova, M., Kroul M.:* The Kinetics of Industrial Crystallization, Elsevier, NY, p. 35 (1985)
2 U.S. Patient No. 5.173.087, Crystal Growth in a Microgravity Environment, December 22 (1992)

W. R. Wilcox and L. L. Regel

Detached Solidification

Many directional solidification flight experiments have produced ingots with smaller diameters than their containing ampoules, a wavy surface, and sometimes thin ridges that were in contact with their ampoule walls. Two hypotheses have been advanced in the literature to explain this unexpected phenomenon, but these hypotheses do not correspond to all of the experimental conditions and observations. We present here a new model for detached solidification that explains the results of all flight experiments. The first step is a sudden detachment of the crystal from the wall because of the stress from differential thermal contraction. This detachment propagates down to the growth interface, causing a meniscus to form that bends inward from the edge of the detached interface. The subsequent growth tracks this meniscus, causing the growth interface to move farther and farther away from the ampoule wall. This contraction of the ingot diameter continues until the meniscus contacts the edge of the interface at the angle required for constant diameter growth. The requirements for this model to operate are weak sticking of the solid to the ampoule, poor wetting of the ampoule by the melt, rejection of a volatile impurity (such as dissolved gas) by the freezing interface, and liberation of this volatile impurity through the meniscus into the gap between the crystal and the ampoule. We also discuss the advantages of detached solidification in improving crystallographic perfection.

1 Introduction

The first directional solidification experiments in space were conducted over 20 years ago in America's first space station, *Skylab*. Although some results were expected, others were a surprise and have yet to be satisfactorily explained. We consider here one set of observations from flight experiments, namely those having to do with reduced contact of the ingots with their containing ampoules.

Consider vertical Bridgman growth on earth. The melt is contained in an ampoule, which is placed in a furnace with a higher temperature on top than below. Solidification is caused to proceed slowly upward by translation of the ampoule downward, translation of the furnace upward, or programming down of the furnace temperature. Except for the effects of differential thermal contraction, the resulting ingot has the same diameter as the containing ampoule. Furthermore the ingot surface incorporates the surface morphology of the ampoule.

Directional solidification in space has often yielded very different results from those realized on earth. In particular, ingots from flight experiments often had a smaller diameter than the containing ampoule. (This phenomenon has been avoided in some flight experiments by arranging for a spring-loaded piston to press against one end of the column of melt and force it against the ampoule wall.)

Skylab contained a gradient freeze furnace constructed by *Westinghouse*. In each run, three samples were heated at one end and cooled passively at the other. Programming down the heater caused solidification, with the temperature gradient in the material decreasing with time and the freezing rate increasing with time. In one set of experiments, *Wilcox* et al. [1–7] obtained three InSb-GaSb alloy ingots smaller in diameter than their carbon-coated quartz ampoules. The ingots' surfaces were wavy. A second set of experiments gave only smooth surfaces in contact with the ampoule walls. This second set was run with a higher initial heater temperature. The residual acceleration levels were unknown.

Witt et al. [8, 9] directionally solidified Te-doped InSb in the *Skylab* furnace built by *Westinghouse*. A single crystal rod was melted partially back and refrozen. Over a distance of about two diameters, the resolidified ingot necked in from the seed crystal. The diameter then expanded to nearly fill the ampoule. There were irregular ridges on the surface of the crystal, like miniature walls of China. These ridges were about one-thousandth of an inch high and contacted the ampoule wall. The width of the ridges increased down the crystal. In the last centimeter, the ridges became irregular and branched out.

Similar results to those described above were obtained by others in *Skylab*, the *Apollo-Soyuz* Test Project, in various Soviet spacecraft, and in the Space Shuttle [10–47]. In some of these experiments the detached portions of the ingots also had ridges that were in contact with the ampoule walls. There was no apparent relation of these ridges to grain boundaries, other defects in the crystals, or crystallographic orientation. It is also interesting to note that all but one of these flight results were obtained on semiconductors. The exception is a set of experiments on aluminum containing some copper in an asbestos-coated quartz ampoule [46].

The explanation generally put forth for reduced contact was that the melt did not wet the ampoule wall and so pulled away from the wall. It appears to have been assumed that the ingot took the same shape as the melt, so that the melt was imagined to have been floating with little or no contact with the ampoule wall.

Mail address: Prof. William R. Wilcox, Dr. Liya L. Regel, International Center for Gravity Materials Science and Applications, Clarkson University, Box 5700, Potsdam, NY 13699-5700, USA, fax: (1)-315-268-3841.
Paper submitted: November 2, 1994
Submission of final revised version: February 6, 1995
Paper accepted: February 17, 1995

Unfortunately all of the above experiments were performed in typical tube furnaces, in which one cannot see inside the ampoule being processed. Thus the actual behavior of the melt and its interaction with the freezing interface were unknown.

Sen and *Wilcox* made the first observation of the behavior of non-wetting liquids inside a cylindrical ampoule at low gravity [48, 49]. Experiments were performed in the *KC-135* aircraft during parabolic flight maneuvers giving about 20 s of low gravity. The liquid never lost contact with the ampoule walls. Sometimes large gas bubbles formed at the surface of the ampoule walls, and sometimes the liquid separated into two or more columns. Similar observations were made by *Naumann* in an USML-1 glove box experiment [50]. *Sen* and *Wilcox* theoretically derived the limit of stability of gas bubbles before the liquid breaks into separate columns [51].

Derebail, *Wilcox*, and *Regel* [52, 53] solidified InSb in a transparent furnace in the *KC-135*. They neither observed the melt pulling away from the ampoule wall nor an ingot with reduced contact. Two interesting features were observed:

(1) The solid detached from the ampoule wall some distance behind the freezing interface, due to thermal contraction. This detachment propagated to the freezing interface, but not beyond.
(2) Gas bubbles on the wall moved slightly toward the freezing interface when it contacted them. This was attributed to the bubble moving partly over onto the freezing interface.

Lagowski, *Gatos*, and *Dabkowski* [54] advocated solidification of non-wetting melts in ampoules with triangular cross sections in space. They predicted that this would yield cylindrical crystals contacting the ampoules only along thin lines in the middle of each triangular face. *Bostrup* and *Rosen* [55] did obtain approximately cylindrical ingots of CdTe by solidification in triangular cross-section ampoules in the *KC-135*. However a non-wetting liquid did not form a liquid column in triangular ampoules in the *KC-135* [48, 49]. The liquid pulled away from the ampoule only in the corners. In agreement with theory [51], the liquid continued to contact each triangular face over about half of its width. *Duffar* [56] reported that he was shown GaAs crystals with this cross section that had been solidified by *Markov* using triangular boron nitride ampoules in the furnace CRATER on board MIR.

Another possible explanation for detached solidification is that the solid feed rods were covered with oxide. This oxide skin could be strong enough to contain the melt in space and prevent it from contacting the ampoule. Contrary evidence is the radial variation in composition of InSb-GaSb alloy that corresponded, qualitatively at least, to that predicted for thermocapillary convection [6]. (Thermocapillary convection would not occur in the presence of a strong oxide skin.) Similarly the large contraction in diameter observed in InSb [8, 9] was much more than would be expected in the presence of an oxide layer.

Avduyevsky et al. [57, 58] claimed that detached solidification was obtained only when the g-level was low. They furthermore stated that crystallographic perfection was greatly improved when ampoule contact was reduced. On the other hand, when large accelerations were present in flight experiments there was good contact with the ampoule, and crystal perfection was no better than when solidification was performed on earth. *Larson*'s recent results [43, 44] support these claims of improved perfection resulting from detached solidification.

Rather than the melt losing contact with the ampoule wall, it seems more likely that detached solidification arises from an interaction between the freezing interface, the melt, and the ampoule. One such mechanism was proposed by *Avduyevsky* [57] and by *Duffar*, *Paret-Harter*, and *Dusserre* [59]. A vital component of this mechanism is a rough surface on the interior of the ampoule. The melt contacts the wall only at the peaks, and does not penetrate into the pits in space[1]. However the roughness of the ampoules used for the cited flight experiments was not sufficient to correspond to this model. Fused silica ampoules were used with smooth interiors. Furthermore, the interior surface of most ampoules was coated with a shiny layer of carbon in order to reduce sticking of the ingot to the ampoule wall.

We conclude that none of the mechanisms proposed previously for detached solidification are able to explain all of the experimental observations. On the following pages we describe a new mechanism that is able to explain everything.

2 New Model for Detached Solidification

Following is a description of our new model for detached solidification.

When solidification first begins, the melt is in contact with the ampoule wall, and the solid that forms is also in contact with the wall, as shown in fig. 1. The thermal expansion coefficient for the solid is greater than that of the ampoule. Consequently, as more solid is formed and cools from the growth temperature, stress builds up between the solid and the ampoule. Eventually this stress is sufficient for the solid to detach from the wall, as observed in our *KC-135* flights on InSb [53]. This detachment propagates to the growth interface, producing the geometry shown in fig. 2. Notice that the meniscus bends inward toward the melt at the growth interface, and contacts the ampoule wall at the equilibrium contact angle. For convenience, let us assume that the solid surface propagates in the direction at which the meniscus contacts the growth interface, even

[1] *Duffar* et al. [59–61] used ampoules with artificially roughened surfaces to demonstrate that detached solidification can be produced by such a mechanism. The peaks had to be sharp in order for the mechanism to be operative.

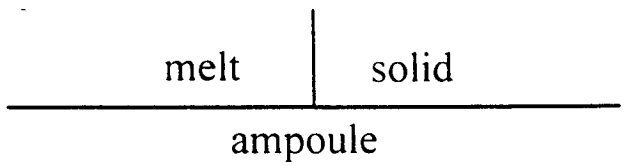

Fig. 1. Schematic diagram of the region near the ampoule wall during the initial solidification while the melt and the solid are both in contact with the wall

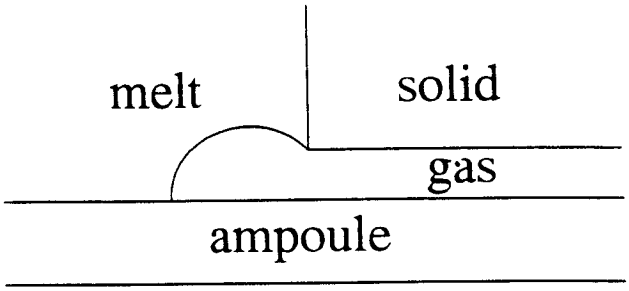

Fig. 2. Melt and solid configuration immediately following gap formation due to differential thermal contraction between solid and ampoule. Note that the angle at which the meniscus contacts the solid causes subsequent growth to enlarge the gap

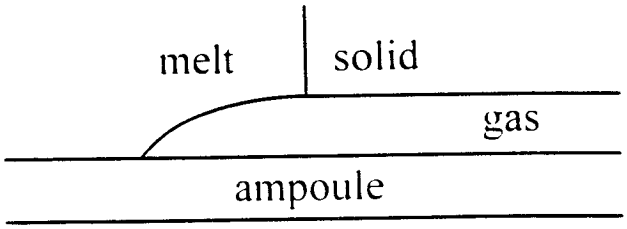

Fig. 3. Steady state configuration of the gap and meniscus assuming zero growth angle

though it has been observed empirically than there is a small angle between the two (usually referred to as the growth angle). In this way, the growth interface moves farther and farther away from the ampoule wall. The gap between the solid and the ampoule increases until the meniscus is parallel (for zero growth angle) to the ampoule wall at the point where the meniscus contacts the growth interface. If nothing else changes, the gap width remains constant, as shown in fig. 3.

In our model, several conditions are required for detached growth:

(1) The thermal expansion coefficient for the solid must be greater than that for the ampoule, which is true for semiconductors in quartz.
(2) The solid must not adhere strongly to the ampoule wall.
(3) The melt must not wet well the ampoule wall, i.e. the contact angle of the melt on the ampoule must be large.
(4) The pressure of the gas in the gap must exceed that in the melt at the meniscus. The pressure difference across the meniscus is related to its curvature by the Laplace equation[2].

We believe these conditions are often satisfied in semiconductor crystal growth in space. If the solid continues to adhere to the ampoule wall over part of the circumference, we will not observe detached solidification over that section. This is what we believe gave rise to the ridges observed in some flight experiments. If the ingot remains stuck to the ampoule at one point, this attachment leads to formation of a ridge that meanders down the ingot as it propagates.

Let us now discuss the shape and behavior of the meniscus. In space, the hydrostatic pressure is very small compared to the pressure difference across the meniscus caused by surface tension. For example, for an acceleration of 10^{-6} of earth's gravity and a 3 cm long column of InSb, the value of ϱgh is only 0.0019 Pa ($1.4 \cdot 10^{-5}$ Torr), which is negligible. Because of this and because the ampoule radius is much larger than the meniscus radius, the meniscus curvature must be nearly constant. That is, the meniscus is very nearly an arc of a circle. The meniscus contacts the ampoule wall at the equilibrium contact angle. The meniscus angle at the corner of the growth interface is arbitrary, but determines the growth direction through the growth angle.

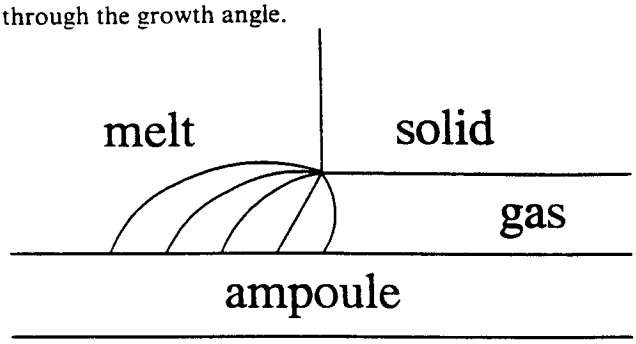

Fig. 4. Dependence of the meniscus shape on the pressure difference between the melt and the gas in the gap. The gas pressure is lower for the meniscus shape on the right, equal to the melt pressure for the straight meniscus, and increasing larger as one moves to the shapes on the left

Fig. 4 shows schematically the dependence of the meniscus shape on the pressure difference between the gas in the gap and the melt. The curve on the right would be expected when the pressure in the melt is larger. In such a case, the solid would immediately grow back to the ampoule surface and detached growth would not be realized. The meniscus with a straight line is for equal pressures. Those to the left of the straight line are for increasing pressure in the gap. Only with the meniscus on the far left would the gap increase in width (for zero growth angle).

In order for the gap pressure to exceed that melt pressure, there must be a source of gas flowing into the gap. This source is one or more volatile impurities in the melt. A likely source of such impurities is the gas the ampoule is backfilled with prior to sealing, typically an inert or reducing gas. This gas dissolves in the melt when the melt is produced. Another source of volatile impurity would be reaction of the melt with moisture to form oxide and hydrogen.

As with most other solutes, a volatile impurity would be expected to be rejected by the growing solid and accumulate

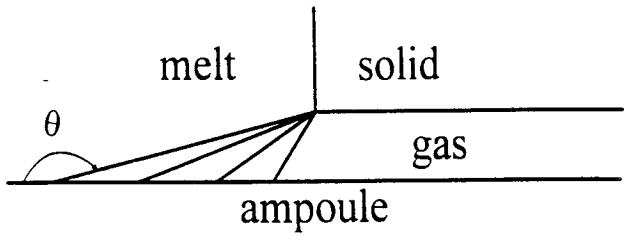

Fig. 5. Dependence of meniscus shape on contact angle of the melt with the ampoule wall, assuming the melt and the gas are at the same pressure.

[2] *Duffar* [56] derived the relationship between gap width, contact angle, growth angle, and pressure difference across the meniscus. For a gap width of 100 μm with InSb growing in silica, for example, he calculated a pressure difference of 2.267 Pa (17 Torr).

in the melt adjacent to the growth interface. Indeed, the concentration of rejection impurity may become large enough for gas bubbles to nucleate [62]. In the present case, the volatile impurity is liberated through the meniscus and into the gap. No matter how well the ampoule is evacuated prior to sealing, some gas will remain, dissolve in the melt, and subsequently be liberated in the gap.

Acceleration influences detached solidification in two ways, through the shape of the meniscus and through buoyancy-driven convention:

(1) Acceleration influences the hydrostatic pressure in the melt at the meniscus, and in this way influences the meniscus shape. This may explain why one does not observe detached growth on earth. As pointed out earlier, the hydrostatic pressure in orbiting spacecraft is probably too small to influence meniscus shape.

(2) Acceleration influences convective transport of the volatile impurity (dissolved gas). On earth, buoyancy-driven convection generally would be sufficient to prevent volatile impurity that had been rejected by the freezing interface from accumulating and being liberated at the meniscus. The residual acceleration in an orbiting spacecraft may be sufficient to influence the transport of volatile impurity, depending on the freezing rate, the acceleration level and direction, and the properties of the melt. Low acceleration levels may increase the transport of volatile impurity to the meniscus, while higher accelerations may prevent accumulation of impurity near the interface, as on earth. The waviness often observed on the surface of detached ingots may be attributed to variations in acceleration during solidification.

Another critical parameter is the contact angle θ of the melt on the ampoule wall. Fig. 5 shows how the contact angle influences the meniscus when there is no pressure difference between the gap and the melt. As the contact angle increases, one is more likely to have detached growth.

Although it is beyond the scope of this paper, we mention briefly the stability of the detached solidification. *Duffar* [56] pointed out that detached growth by our mechanism suffers from capillary instabilty when the growth angle is positive, as is typical for semiconductors. If we imagine the crystal growing with a steady state gap width, as in fig. 3 for zero growth angle, then any decrease in gap width leads to a still larger gap, and vice versa. The argument is nearly identical to *Surek*'s [63], which showed the capillary instability of the diameter in Czochralski growth. To the contrary, experience shows that Czochralski growth is very stable. Before the advent of automatic diameter control, little operator intervention was required. If the heater power and pull rate were kept constant, the diameter only slowly decreased as the melt level fell, because of reduced heat transfer from the growing crystal. This led to a carrot-shaped crystal. Czochralski growth was shown to be stabilized by heat transfer [64, 65]. Similarly the growth of gas tubes [66–69] during directional solidification was shown to be capillary unstable, but stabilized by the transport of volatile impurity to the bubble surface [70].

We have begun to develop a numerical model for the transport of volatile impurity to the meniscus during detached solidification, and expect to find that the gap width is stabilized by this transport. In this analysis we will also examine the influence of thermocapillary (Marangoni) convection generated by the temperature gradient along the meniscus, as well as buoyancy-driven convection due to the residual acceleration.

3 Benefits of Detached Solidification

In the early days of microgravity research, solidification in space was touted as a way to achieve compositional uniformity because of the supposed absence of convection. Over the years, we have come to realize that convection can occur in fluids in orbiting spacecraft, that materials solidified in microgravity are not always compositionally uniform, and that uniformity can sometimes be achieved on earth. A better reason for solidification in microgravity may be to achieve detached solidification. There are several possible benefits to growth with the solid having little or no contact with the ampoule wall. Following are some of these benefits:

(1) improved control of stoichiometry and doping,
(2) reduced contamination of the ingot by the ampoule,
(3) eliminated stress caused by differential thermal contraction between the ingot and the ampoule,
(4) reduced nucleation of grains and twins at the ampoule wall, and
(5) reduced heat transfer between the ingot and the furnace, leading to reduced temperature gradients in the solid, and lower thermal stress. (A more planar interface may also be produced, assisting in growing out of grain boundaries and dislocations.)

We now discuss each of these benefits of detachment.

One motivation for reduced contact is control of stoichiometry. For example, one usually wants to grow gallium arsenide slightly arsenic rich. On earth, the arsenic content can be controlled precisely throughout solidification only in the horizontal Bridgman method. The melt is contained in an open boat and an arsenic source is held at a controlled temperature. The melt and the solid are in direct contact with the arsenic vapor. However, cylindrical ingots are not produced in this growth technique. To produce the cylindrical crystals preferred for device fabrication, we use either vertical Bridgman growth or the *L*iquid *E*ncapsulated *C*zochralski technique (LEC). In LEC and the usual vertical Bridgman method, the melt becomes increasingly arsenic rich during solidification. Detached solidification in microgravity yields cylindrical ingots with the solid in contact with the vapor. Use of triangular ampoules also leaves three vapor passages along the melt and the resulting solid. In this way interaction with the arsenic source can be maintained throughout growth even while producing nearly cylindrical ingots.

For many materials, the ampoule is a source of contamination. In fact for some materials there is no ampoule material that is completely non-contaminating. If contact of the solid with the ampoule is greatly reduced, contamination will be reduced. (In our model, contamination of the melt would still occur.)

Rosch and *Carlson* [71] used a computer model to show that by far the largest contributor to stress in Bridgman growth is differential thermal contraction between the crystal and the ampoule. This stress is strongly influenced by the degree to which the crystal adheres to the ampoule wall. In extreme cases, such as silicon in quartz, sticking is so strong that the crystal breaks while cooling. Thus reduction or elimination of contact with the ampoule wall will greatly reduce stress during cooling from the melting point. Crystals of higher perfection can be produced. It may also be possible to directionally solidify materials in space that cannot be grown by the Bridgman technique on earth, such as silicon.

The ampoule wall can also act as a nucleation site for twins and grains. The recent USML-1 experiment of *Larson* is instructive [43, 44]. Zinc-doped CdTe was directionally solidified from a seed in a tapered ampoule. Seeding was successfully accomplished. Where the ampoule diameter was increasing, the ingot was not in contact with the ampoule wall. When the full diameter was reached, contact with the wall was established, but only on one side. Twins, a troublesome common defect in CdTe, formed only where the solid was in contact with the ampoule wall. The dislocation density in the microgravity-grown CdTe was 2 orders of magnitude lower than in material solidified on earth under otherwise identical conditions. The x-ray rocking curve was near the theoretical value for a perfect crystal.

Detachment of the ingot from the ampoule wall also should increase crystal perfection by decreasing thermal stress [32, 38, 72]. A gap between the ingot and the ampoule wall greatly increases the resistance to heat transfer between the solid and the furnace. This, in turn, decreases the axial and radial temperature gradients in the crystal, resulting in reduced thermal stresses and a more planar freezing interface. Reducing thermal stress decreases multiplication of dislocations. A more planar interface assists in grain selection and growing out of dislocations. Precipitate nucleation and growth are also influenced.

Experimental evidence for improved crystallographic perfection brought about by detached solidification in microgravity was obtained for GaSb [32]. The Hall mobility was significantly increased, the charge carrier concentration was decreased, the dislocation density was decreased, the grain size increased by solidification in space. Detached solidification of HgCdTe caused formation of a planar interface for the first time, and resulted in growth of a single crystal [47].

Acknowledgements

This research was supported by grant NAG8-1063 from NASA's Microgravity Science and Applications Division. We are grateful to T. Duffar and to the reviewer for stimulating and helpful comments.

References

1 *Wilcox, W. R., Yee, J. F., Sen, S., Sarma, K., Lin, M. C.:* Directional Solidification of InSb-GaSb Alloys. Proc. 3rd Space Proceeding Symp., Skylab Results, NASA Technical Report M-74-5, vol. 1, p. 301 (1974)

2 *Wilcox, W. R., Yee, J. F., Lin, M. C., Sarma, K., Sen, S.:* Directional Solidification of InSb-GaSb Alloys, in: Skylab Science Experiments, American Astronautical Society, Tarzana, California, p. 27 (1975)

3 *Yee, J. F., Lin, M. C., Sarma, K., Wilcox, W. R.:* The Influence of Gravity on Crystal Defect Formation in InSb-GaSb Alloys. J. Crystal Growth, vol. 30, p. 185 (1975)

4 *Lefever, R. A., Wilcox, W. R., Sarma, K. R., Chang, C. E.:* Composition Variations in Directionally Solidified InSb-GaSb Alloys. Mat. Res. Bull, vol. 13, p. 1181 (1978)

5 *Lefever, R. A., Wilcox, W. R., Sarma, K. R.:* Orientation, Twinning, and Orientation-Dependent Reflectance in InSb-GaSb Alloys. Mat. Res. Bull., vol. 13, p. 1175 (1978)

6 *Lefever, R. A., Chang, C., Wilcox, W. R.:* Surface Driven Convection in InSb-GaSb Melts Solidified Aboard *Skylab*-III. Bull. Am. Phys. Soc., vol. 20, p. 1511 (1975)

7 *Lefever, R. A., Sarma, K. R., Chang, C. E., Wilcox, W. R.:* Microstructure and Composition of InSb-GaSb Ingots Directionally Solidified Aboard *Skylab*. Oral presentation, AIAA 15th Aerospace Sciences Meeting, Los Angeles, CA, Preprint 77–161 (1977)

8 *Witt, A. F., Gatos, H. C., Lichtensteiger, M., Lavine, M., Herman, C. J.:* Proc. 3rd Space Processing Symp., *Skylab* Results, NASA Technical Report M-74-5, vol. 1, p. 275 (1974)

9 *Witt, A. F., Gatos, H. C., Lichtensteiger, M., Lavine, M. C., Herman, C. J.:* J. Electrochem. Soc., vol. 122, p. 276 (1975)

10 *Ukanwa, A. O.;* in: Proc. 3rd Space Processing Symp., Skylab Results, NASA Technical Report M-74-5, vol. 1, p. 425 (1974)

11 *Hasemeyer, E. A., Lovoy, C. V., Lacy, L. L.;* in: Proc. 3rd Space Processing Symp., Skylab Results, NASA Technical Report M-75-5, vol. 1, p. 457 (1974)

12 *Yue, J. T., Voltmer, F. W.:* Influence of Gravity-Free Solidification on Solute Microsegregation. J. Crystal Growth, vol. 29, p. 329 (1975)

13 *Gatos, H. C., Herman, C. J., Lichtensteiger, M., Witt, A. F.:* Quantitative Determination of Zero-Gravity Effects on Crystal-Growth from the Melt, in: ESA Special Publication no. 114 (1976)

14 *Witt, A. F.:* Crystal Growth Experiments on ASTP – an Overview, in: ESA Special Publication no. 114 (1976)

15 *Gatos, H. C., Witt, A. F., Lichtensteiger, M., Herman, C. J.;* in: *Apollo-Soyuz* Test Project – Composite, Section V, NASA TM X-77360, Marshall Space Flight Center (1977)

16 *Zemskov, V. S.,* et al.; in: *Apollo-Soyuz* Test Project – Composite, Section IX, NASA TM X-77360, Marshall Space Flight Center (1977)

17 *Witt, A. F., Gatos, H. C., Lichtensteiger, M., Herman, C. J.:* J. Electrochem. Soc., vol. 125, p. 1832 (1978)

18 *Galazka* et al.: Experiment "SYRENA" 1, 2, 3-Space Processing of CdHgSe, CdHgSe and PbSeTe. Proc. 3rd Europ. Symp. on Material Science in Space, ESA SP-142, p. 47 (1979)

19 *Khasimov, F. R.,* et al.; in: Proc. 3rd Europ. Symp. on Material Science in Space, ESA SP-142, Grenoble (1979)

20 *Markov, E. V.,* et al.: The Influence of Space Conditions on Directional Crystallization of Germanium and its Properties. Proc. 3rd Europ. Symp. on Material Science in Space, ESA SP-142, Grenoble (1979)

21 *Ivanov, L. I., Kubasov, V. N., Zemskov, V. S.:* Plavileniye Kristallizatsiya i Fazoobrazovaniye v Usloviyakh Nevesomosti, Nauka, Moscow (1979) (in Russian)

22 *Malinin, A. Yu.:* Eksperimenty po Vyrashchivaniyu Poluprovidnikovykh Materialov v Usloviyakh Kosmosa na Apparaturye *Kristall*. Elektronnaya Promyshlennost, no. 3 (1979) (in Russian)

23 *Markov, E. V.,* et al.: Growth of Bulk Germanium Single Crystals by Directional Crystallization and Segregation Processes in Microgravity. Oral presentation, 6th Int. Conf. on Crystal Growth, Moscow (1980)

24 *Avduyevsky, V. S., Grishin, S. D., Leskov, L. V.:* Problemy Kosmitcheskogo Proizvodstya. Mashinostroyeniye, Moscow (1980) (in Russian)

25 *Galazka, R. R.,* et al.: Directional Crystallization of CdHgTe in Microgravity Conditions. J. Crystal Growth, vol. 53, p. 397 (1981)

26 *Zemskov, V. S., Bolokyrova, I. N., Titkov, A. N., Shulpina, I. L.:* Naprevlenaya Kristallizatsiya Tverdikh Rastvorov Germanii-Kremnii-Surma v Eksperimente *Universalnaya Reck* Programmi *Soyuz-Appollon.* Protsessi Rosta Poluprovodnikovikh Kristallov i Plenok, *F. A. Kuznetzov* (ed.), Akademiya Nauk SSSR, p. 142 (1981) (in Russian)

27 *Avduyevsky, V. S., Grishin, S. D., Leskov, L. V.:* Some Physical Aspects of Unidirectional Crystallization in Microgravity. Acta Astronaut., vol. 9, p. 583 (1982)

28 *Schneider, G.*, et al.: Results of Crystal Growth of Bismuth-Antimony Alloys in a Microgravity Environment. Crystal Res. Techn., vol. 18, p. 1213 (1983)

29 *Zemskov, V. S.*, et al.: in: Proc. 4th European Symp. on Materials Science under Microgravity, ESA SP-191, Madrid (1983)

30 *Gyuroa, I.*, et al.: Acta Astronautica, vol. 11, p. 361 (1984)

31 *Chernov, A. A.*, et al.: Growth of Germanium Crystals with Low Dislocation Density in a Condition of Weightlessness. Soviet Physics Crystallogr., vol. 29, p. 222 (1984)

32 *Lendvay, E., Regel, L. L.*, et al.: The Growth of GaSb Under Microgravity Conditions. J. Crystal Growth, vol. 71, p. 538 (1985)

33 *Shulpina, I. L.*, et al.: Osobennosti Strukturi Legirovannikh Kristallov Antimonida Indiya c p-n Perekhodami. Virashchennikh v Usloviyakh Nevesomosti. in: Legirovanniye Poluprovodnikoviye Materiali, *V. S. Zenskov* (ed.), Nauka, Moscow (1985) (in Russian)

34 *Calzadilla, O., Fuentes, J., Shulpina, I., Sarokin, L.:* Estudio de los Cristales de Germanio Dopados con Indio en el Experimento 'Caribe'. IX SLAFES, Mar de Plata, Argentina (1985) (in Spanish)

35 *Zemskov, V. S.*, et al.: The Fundamental Achievements of Experiments under Zero Gravity Conditions and Various Problems. Izvestiya Akademii Nauk SSSR, Ser. Fizicheskaya, vol. 49, p. 673 (1985)

36 *Zemskov, V. S.*, et al.: Raspredeleniye Tellura v Kristallakh Antimonida Indiya Poluchennikh v Usloviyakh Nevesomosti. in: Legirovanniye Poluprovodnikoviye Materiali, *V. S. Zemskov* (ed.), Nauka, Moscow, p. 132 (1985) (in Russian)

37 *Zemskov, V. S., Raukhman, M. R.:* Influence of Gravity-Free Solidification on Solute Microsegregation. J. Crystal Growth, vol. 29, p. 329 (1975)

38 *Duffar, T., Potard, C., Dusserre, P.:* Growth Analysis of the InSb Compound by a Calorimetric Method in Microgravity – Results of the Spacelab-D1 Experiment. J. Crystal Growth, vol. 92, p. 467 (1988)

39 *Zhang, F. Q.*, et al.: InSb Crystal Growth under Microgravity Condition. Chinese Science Bulletin, vol. 34, p. 1529 (1989)

40 *Tillberg, E., Carlberg, T.:* Semi-Confined Bridgman Growth of Germanium Crystals in Microgravity. J. Crystal Growth, vol. 99, p. 1265 (1990)

41 *Zemskov, V. S., Raukhman, M. R., Kozitsina, E. A., Arsent'ev, I. M.:* Experiments on Directional Solidification in Indium Antimonide Ampuls on the Satellites *Kosmos-1744* and *Foton.* Fiz. Khim. Obrab. Mater., p. 46 (1991); through Chem. Abstr., vol. 115, no. 291482 (1991)

42 *Shumaev, O. V., Regel, L. L.:* GaSb Crystal Growth in Microgravity Conditions. Proc. AIAA/IKI Microgravity Science Symposium, American Institute of Aeronautics and Astronautics, Washington D.C., p. 119 (1991)

43 *Larson, D.:* Private Communications. Grumman Coroporation. Bethpage, NY (1993, 1994)

44 *Larson, D. J. Jr., Alexander, J. I. D., Gillies, D., Carlson, F. M., Wu, J., Black, D.:* Orbital Processing of High-quality CdTe Compound Semiconductors. Joint Launch and One Year Science Review of USML-1 and USMP-1 with the Microgravity Measurement Group, *N. Ramachandran, D. O. Frazier, S. L. Lehoczky, C. R. Baugher* (eds.), NASA Conference Publication 3272, vol. 1, p. 129 (1994)

45 *Duffar, T., Garandet, J. P.:* Convective Effects on the Growth of GaInSb Crystals – Main Experimental Results Obtained in GHF Facility during Spacelab-D2 Mission. Oral presentation, Int. Astronautical Federation Congress, IAF-94.J.3.241, Jerusalem (1994)

46 *Fuks, E. G., Roos, A., Buza, G.:* Metallurgicheskiye Issledovaniya v Kosmose po Programme *Bealutsa. Salyut-6-Soyuz* Materialovedeniye i Tekhnologiya, *Yu. A. Osipyan, L. L. Regel* (eds.), Nauka, Moscow, p. 101 (1985) (in Russian)

47 *Kurbatov, L. H., Golovin, B. I., Izyurov, A. V., Komarov, N. V.:* Nekotoriye Ocobennosti Eksperimentov po Polycheniyu Tverdikh Rastvorov Kadmii-Rtut Tellur. Provedennikh v Sostavye dos *Salyut-6.* Gidromekhanika i Templo-massoobmen v Nevesomosti, *V. S. Avduyevskii, V. I. Polezhayev* (eds.), Izdatel'stvo Nauka, Moscow, p. 219 (1982)

48 *Sen, R., Wilcox, W. R.:* Behavior of a Non-wetting Melt in Free Fall – Experimental. J. Crystal Growth, vol. 74, p. 591 (1986)

49 *Sen, R.:* Fluid Behavior in Non-wetted Ampoules and Formation of Twins in Dodecanedicarboxylic Acid. Ph.D. Thesis, Clarkson University (1985)

50 *Naumann, R. J.:* Marangoni Convection in Closed Containers. Joint Launch and One Year Science Review of USML-1 and USMP-1 with the Microgravity Measurement Group, *N. Ramachandran, D. O. Frazier, S. L. Lehoczky, C. R. Baugher* (eds.), NASA Conference Publication 3272, vol. 2, p. 601 (1994)

51 *Sen, R., Wilcox, W. R.:* Behavior of a Non-wetting Melt in Free Fall – Theoretical. J. Crystal Growth, vol. 78, p. 129 (1986)

52 *Derebail, R.:* Study of Directional Solidification of InSb under Low, Normal and High Gravity. M.S. Thesis, Clarkson University (1990)

53 *Derebail, R., Wilcox, W. R., Regel, L. L.:* Influence of Gravity on the Directional Solidification of Indium Antimonide. J. Spacecraft & Rockets, vol. 30, p. 202 (1993)

54 *Lagowski, J., Gatos, H. C., Dabkowski, F. P.:* J. Crystal Growth, vol. 72, p. 595 (1985)

55 *Rosen, G.:* Private Communication, Clarkson University (1991)

56 *Duffar, T.:* Private Communication, Centre D'Etudes Nucléaires, Grenoble (1994)

57 *Avduyevsky, V. S.* (ed), *Grishin, S. D., Leskov, L. V., Polezhayev, V. I., Savitchev, V. V.:* Scientific Foundations of Space Manufacturing. Mir Publishers, Moscow (1984)

58 *Avduyevsky, V. S.* (ed.), *Grishin, S. D., Leskov, L. V., Savitchev, V. V., Khryapov, V. T.:* Manufacturing in Space – Processing Problems and Advances. Mir Publishers, Moscow (1985)

59 *Duffar, T., Paret-Harter, I., Dusserre, P.:* Crucible De-wetting during Bridgman Growth of Semiconductors in Microgravity. J. Crystal Growth, vol. 100, p. 171 (1990)

60 *Duffar, T., Dusserre, P., Abadie, J.:* Crucible-Semiconductor Interactions during Crystal Growth from the Melt in Space. Adv. Space Research (in press)

61 *Duffar, T., Abadie, J.:* Convective Effects on the Growth of GaInSb Crystals, in: Scientific Results of the German Spacelab Mission D2, Norderney (in press)

62 *Wilcox, W. R., Kuo, V. H. S.:* Gas Bubble Nucleation during Crystallization. J. Crystal Growth, vol. 19, p. 221 (1973)

63 *Surek, T.:* J. Applied Physics, vol. 47, p. 4384 (1976)

64 *Surek, T., Coriell, S. R., Chalmers, B.:* The Growth of Shaped Crystals from the Melt. J. Crystal Growth, vol. 50, p. 21 (1980)

65 *Tatarchenko, V. A.:* Capillary Shaping in Crystal Growth from Melts. J. Crystal Growth, vol. 37, p. 272 (1977)

66 *Maeno, N.:* Air Bubble Formation in Ice Crystals. Physics of Snow and Ice, *H. Ôura* (ed.), vol. 1, p. 207 (1967)

67 *Vasconcellos, K. F., Beech, J.:* The Development of Blowholes in the Ice/Water/Carbon Dioxide System. J. Crystal Growth, vol. 28, p. 85 (1975)

68 *Zhdanov, V., Satunkin, G. A., Tatarchenko, V. A., Talyanskaya, N. N.:* Cylindrical Pores in a Growing Crystal. J. Crystal Growth, vol. 49, p. 659 (1980)

69 *Jamgotchian, H., Trivedi, R., Billia, B.:* Interface Dynamics and Coupled Growth in Directional Solidification in Presence of Bubbles. J. Crystal Growth, vol. 134, p. 181 (1993)

70 *Tatarchenko, V. A.:* Cylindrical Pores in a Growing Crystal. J. Crystal Growth, vol. 143, p. (1994)

71 *Rosch, W., Carlson, F.:* Computed Stress Fields in GaAs during Vertical Bridgman Growth. J. Crystal Growth, vol. 109, p. 75 (1991)

72 *Duffar, T., Bal, M.:* Thermal Effect of a Rough Crucible in Crystal Growth from the Melt. J. Crystal Growth (in press)

M. L. Fleet, S. J. Simske, A. Hoehn, T. A. Schmeister and M. W. Luttges†

An Autonomous Module for Supporting Mice during Spaceflight

The Animal Module for Autonomous Space Support (A-MASS) was developed to enable 30-day spaceflight for mice on the first Commercial Experiment Transporter mission. Because space hardware did not previously exist to support mice without astronaut intervention, the A-MASS presented considerable technical and animal care challenges. The technical challenges included maintaining a 42.5 l payload volume and 20-g structural conformance while providing 30 days of autonomous mouse support. Sensors, video, a pressurized oxygen supply system and an internal data logging system were incorporated. The A-MASS met NIH guidelines for temperature, humidity, food and water access, oxygen supply, air quality and odor control. These technical and animal care challenges, along with power and mass constraints, were addressed using a novel design which ensures a fresh food and water supply, a clean view path into the cage for the camera system, and removal of the wastes from the air supply. The payload was successfully tested in an enclosed chamber and passed animal health, vibrational, mechanical, and electrical tests. The physiological, tactical and animal support information gathered will be applicable to the development of mouse support modules for the Shuttle Middeck and Space Station Freedom Express Rack environments.

1 Introduction

Spaceflight effects on mammalian physiology are of considerable interest to biomedical researchers because

(1) the long-term habitation of space is jeopardized by the deleterious effects of spaceflight on, for example, the cardiovascular, immune and musculoskeletal systems, and
(2) the observed physiological effects mimic aspects of a variety of earth-bound disorders, such as osteoporosis, diabetes, and immunosuppression.

However, only a few flight programs currently exist which permit long-term experiments in space. An even lesser number of payloads exist which take advantage of these programs for long-term mammalian physiological studies. The COSMOS payload provides long-term, autonomous support of rats in space; however, none currently exist for the long-term support of mice (either autonomously or interactively).

Mice, because of their small size, relatively brief life spans, well-characterized genetic characteristics, and the availability of useful transgenic strains [1, 2], provide a useful animal model for the examination of long-term spaceflight effects on mammalian physiology [3, 4]. The *A*nimal *M*odule for *A*utonomous *S*pace *S*upport (A-MASS) is a payload designed and developed for the support of mice in an autonomous (earth orbit) environment for a nominal period of 30 days, the planned duration of the first *Com*mercial *E*xperiment *T*ransporter (COMET) mission. The hardware is designed to be readily amendable to other carriers, such as the Shuttle and Space Station.

The design and development of the A-MASS was complicated by its need to provide life support. Animal care and welfare concerns, in addition to the more typical payload concerns of safety, power, volume, and mass, impacted the A-MASS construction. The animal concerns included careful adherence to *N*ational *I*nstitutes of *H*ealth (NIH) [5] and *A*merican *V*eterinary *M*edical *A*ssociation (AVMA) [6] standards. Payload approval was obtained from the *A*nimal *C*are and *U*se *C*ommittee (ACUC) at the University of Colorado and at the NASA Ames Research Center. Adherence to these guidelines and protocol definitions ensured that the animals were not subjected to nonexperimental stress or health-endangering environmental factors within the A-MASS.

The developers of the Recovery System, *Space Industries*, Inc. (*SII*, Houston, TX, USA), specified additional design constraints to ensure compatibility with the COMET Recovery System. These included COMET mission safety, minimal vibrational and electrical interference with other COMET payloads, power draw and mass limitations, a specific volume, and structural constraints imposed by the forces placed on the payload during launch and during recovery (table 1).

2 A-MASS Design Approach

2.1 Food and Water

The A-MASS subsystems were designed to satisfy the animal care requirements while adhering to the engineering

Mail address: Mary Fleet, S. J. Simske, A. Hoehn, T. A. Schmeister, Bioserve Space Technologies, Department of Aerospace Engineering Sciences, University of Colorado, Campus Box 429, Boulder, CO 80309, USA, fax 001-1-303-492-8883.
Paper submitted: April 18, 1994
Submission of final revised version: September 1, 1994
Paper accepted: September 20, 1994

ATTACHMENT E.

Detached Solidification: 1. Steady-State Results at Zero Gravity

DMITRI I. POPOV[1], LIYA L. REGEL[1,a] and WILLIAM R. WILCOX[1]

1. International Center for Gravity Materials Science and Applications

Clarkson University, Potsdam, NY 13699-5814, USA

Tel: 315-268-7672, Fax: 315-268-3833

a. To whom correspondence should be addressed

Detached Solidification: Steady-State Results at Zero Gravity

Abstract

A new mechanism for detached solidification in space was described in a recent paper [1]. In this mechanism, a gap forms between the solid and the ampoule wall. The melt remains in contact with the ampoule wall, with a meniscus between the wall and the edge of the freezing interface. Dissolved gas is transported into the gap across the meniscus, affecting the pressure in the gap and the gap width. We have developed a steady state numerical model for convection in the melt and transport of dissolved gas. For steady-state detached solidification to occur, the freezing rate must be below a critical value, the residual gas pressure in the ampoule must exceed a certain level, the contact angle of the melt on the wall must exceed a critical value, and the melt-vapor surface tension should not be too large. A large growth angle favors detached solidification. Under some conditions, two different gap widths satisfy the governing equations.

Keywords: crystal growth, numerical modeling, gas diffusion.

1. INTRODUCTION

Numerous experiments on directional solidification of semiconductors in space yielded ingots with a diameter smaller than the inner diameter of the confining ampoule [1]. This phenomenon has been called "detached solidification" [1]. The early interpretation of the phenomenon was that poor wetting of the ampoule wall caused the melt to have little or no contact with it. However, this explanation failed to agree with experimental observations [2]. In the case of lead solidification [3], detachment was attributed to shrinkage upon freezing. This explanation is irrelevant to the present discussion; moreover, it cannot be applied to semiconductors since they expand on solidification. Another explanation of detached solidification was suggested in [4]. This model required considerable crucible roughness, which does not allow the melt to penetrate to the bottom of the cavities. Though the correlation between the crystal surface and crucible roughness obtained in [5] was obvious, the contraction of the crystal diameter in detached experiments was much larger than predicted by this model. Furthermore, the

surfaces were smooth for semiconductors solidified in space. Thus, all prior attempts to explain detached solidification met with difficulty when their predictions were compared with experimental observations.

A new model of detached solidification was proposed in [1]. An important feature of the model is the presence of one or more volatile components, such as dissolved gas, in the melt. Here, we assumed that gas remains in the ampoule after sealing due to residual or back-filled gas, such as argon or hydrogen. This gas dissolves in the melt. Its concentration increases near the freezing interface because of rejection by the growing solid (impurity segregation). When detachment takes place and the gap between the growing crystal and the ampoule wall appears, the dissolved gas diffuses into the gap across the liquid meniscus connecting the crystal with the ampoule. A steady-state gap width is reached when the transport of volatile species across the meniscus equals that required to maintain a gas pressure satisfying the condition of mechanical equilibrium across the meniscus (Fig.1).

The objective of this work was to understand steady-state detached solidification. Numerical modeling of detached solidification in zero gravity was carried out. Equations for momentum and mass balance were solved. The results of numerical modeling and the influence of various parameters on the steady-state gap width are presented here. Subsequent papers will examine the stability of the gap and the influence of buoyancy-driven convection.

2. MATHEMATICAL MODEL

2.1. Steady-State Numerical Modeling

Numerical calculations were carried out in the axisymmetric domain shown in Figure 2, using the physical properties of InSb (see Table 1), for which detached solidification has been observed [6-11]. Values used for the other parameters are given in Table 2. We chose a domain bounded by the axis of symmetry (r=0), the ampoule wall ($r=R_a$), the meniscus, the planar solidification interface (x=0), and a boundary at some distance L_a from the solidification interface. This distance L_a was chosen so that the velocity and concentration fields near the solidification interface do not depend on its precise value. The concentration of dissolved gas at $x=L_a$ had to be the

same as at the top of the melt column (melt free surface)[1]. We found that a sufficient condition is $L_a \geq 0.7R_a$, and so we used $L_a = 1.5\ R_a$ where the ampoule radius R_a was taken equal to 1 cm.

The velocity distribution in the melt is important for mass transport. When a free melt/gas surface (meniscus) exists near the solidification front, Marangoni convection, caused by the variation in surface tension along the meniscus, takes place even at zero gravity. We studied the influence of Marangoni convection on the dissolved gas distribution near the solidification interface and on gas transport from the melt into the gap.

Steady-state detached growth requires steady-state velocity distribution and gas concentration distribution in the melt. Therefore, we assumed axisymmetric, steady-state flow of an incompressible liquid with constant viscosity and density. The velocity field was obtained in the reference frame of the interface, which moves at constant freezing rate V_c. The steady-state Navier-Stokes and continuity equations were reduced to a well-known form [12] using the stream function formulation, where the velocity components are given by:

$$V_x = -\frac{1}{r}\frac{\partial \psi}{\partial r} \quad ; \quad V_r = \frac{1}{r}\frac{\partial \psi}{\partial x} \tag{1}$$

where ψ is the stream function. In this way the Navier-Stokes equation, combined with the incompressible continuity equation, takes the form:

$$-\frac{1}{r}\frac{\partial(\psi, E^2\psi)}{\partial(r,x)} - \frac{2}{r^2}\frac{\partial \psi}{\partial x}E^2\psi = \nu E^4\psi \tag{2}$$

where E^2 and E^4 are the operators:

$$E^2\psi = \frac{\partial^2\psi}{\partial r^2} - \frac{1}{r}\frac{\partial \psi}{\partial r} + \frac{\partial^2\psi}{\partial x^2}$$

$$E^4\psi = E^2(E^2\psi) \tag{3}$$

The boundary conditions for the axial and radial components of velocity, V_x and V_r, are:

[1] We should note that such a choice for the boundary conditions inside the melt is inappropriate for both the velocity and concentration fields at non-zero gravity. The convective vortices would be distributed over the whole melt region, providing global mixing.

$$At\ x = 0 \quad (\text{interface}): \qquad V_x = -V_c \quad ; \quad V_r = 0 \tag{4a}$$

$$At\ x = L_a >> e: \qquad V_x = V_c - 2V_c\left(1 - \frac{e}{R_a}\right)^2 + \frac{2V_c}{R_a^2}\left(\left(1 - \frac{e}{R_a}\right)^2 - 1\right)r^2 \quad ; \quad V_r = 0 \tag{4b}$$

$$At\ r = 0 \quad (ampoule\ axis): \qquad \frac{\partial V_x}{\partial r} = 0 \quad ; \quad V_r = 0 \tag{4c}$$

$$At\ r = R_a \quad (ampoule\ wall): \qquad V_x = -V_c \quad ; \quad V_r = 0 \tag{4d}$$

$$On\ the\ meniscus: \qquad V_n = 0 \quad ; \quad \frac{\partial V_s}{\partial n} = -\frac{1}{\mu}\tau_{ns} \tag{4e}$$

where V_c is the solidification rate, and x and r are the axial and radial coordinates. At $x=L_a$, the velocity profile shown is parabolic and satisfies the no-slip conditions at the wall as well as the total flux of melt into the freezing interface. Here V_n is the component of velocity normal to the meniscus, V_s is the component parallel to the meniscus surface, n is the distance into the melt normal to the meniscus, μ is the viscosity of the melt, and τ_{ns} is the shear stress on the surface of the meniscus. A shear stress could arise from the temperature-dependence of the surface tension, and result in a tangential dynamic boundary condition creating Marangoni flow in the melt[2].

For melt at the ampoule wall, near the line where the meniscus contacts the wall, a slip boundary condition was used for the axial component of the velocity. This was done to avoid a singularity for the radial component of the velocity at the contact line [13,14] and a discontinuity for the shear stress on the solid boundary. The slip length λ_c of the order 10^{-3} cm used in the calculations was larger than that suggested in [14] for the present melt viscosity and contact angle, but was limited by the finite difference mesh. Although the velocity field near the contact line is sensitive to the slip length parameter, the concentration field and gap width are not.

The combined continuity and Navier-Stokes equations were solved for the stream function ψ and vorticity ω by a central difference ADE method with overrelaxation [15]. A non-uniform mesh with 74 x 74 gridpoints was used, with a higher density of gridpoints near the meniscus. The same mesh was used for numerical solution of the mass transfer equation. The high density of grid points near the meniscus was used to provide accuracy in the gas flux determination. The finite difference representation of equations (1) to (3) is given in the Appendix.

[2] Marangoni convection does not necessarily occur at the meniscus. The presence of a surfactant species concentrated at the liquid-vapor interface can greatly retard or stop the motion. In semiconductor and metal melts, for example, oxygen might serve this role, at a concentration below that required to form a second-phase oxide film.

The concentration C of gas dissolved in the melt was assumed to satisfy the steady state mass transfer equation:

$$V_r \frac{\partial C}{\partial r} + V_x \frac{\partial C}{\partial x} = D \cdot \left[\frac{1}{r} \frac{\partial}{\partial r} \left(r \frac{\partial C}{\partial r} \right) + \frac{\partial^2 C}{\partial x^2} \right] \tag{5}$$

where D is the diffusion coefficient of gas in the melt. Following are the boundary conditions:

$$At\ x = 0\ (\text{int}erface): \quad D \frac{\partial C}{\partial x} = -V_c (1 - k) C \tag{6a}$$

$$At\ x = L_a >> e: \quad C = p_m \cdot K_{pm} \tag{6b}$$

$$At\ r = 0\ (ampoule\ axis): \quad \frac{\partial C}{\partial r} = 0 \quad - no\ flux \tag{6c}$$

$$At\ r = R_a\ (ampoule\ wall): \quad \frac{\partial C}{\partial r} = 0 \quad - no\ flux \tag{6d}$$

$$On\ the\ meniscus: \quad C = p_g \cdot K_{pg} \tag{6e}$$

where p_m and p_g are the gas pressure above the melt surface and in the gap, respectively. Here K_{pm} is the solubility of gas at the top of the melt column (hot zone temperature), K_{pg} is the solubility at the meniscus (at a lower temperature), and k is the segregation coefficient for the dissolved gas, i.e. the ratio of concentration in solid to that in melt at the freezing interface. The data for solubility of gases (especially oxygen) dissolved in semiconductor melts can be found in the literature, see references in [16]. The solubility of nitrogen at the temperatures of most III-V semiconductors melting points is less than of oxygen and argon. We used the following values of solubilities: $K_{pm} = 2.09*10^{-5}$ mol cm^{-3} atm^{-1} and $K_{pg} = 1.73*10^{-5}$ mol cm^{-3} atm^{-1} at 850 K and 800 K, respectively. As a rule, the solubility of gases in molten metals and semiconductors increases with temperature in this temperature range. This assumption gives higher solubility of dissolved gas at the top of the melt column than close to interface.

2.2. Gas Flux. Rate of Pressure Change in the Gap in the General Case

The volatile species (dissolved gas here) is segregated out at the freezing interface, diffuses to the meniscus, and is liberated as gas into the gap. The total molar gas flux across the meniscus depends on the gradient of concentration normal to the meniscus. The total molar flux J_{mol} into the gap was calculated from the concentration field near the meniscus by integrating the diffusion molar flux over the total surface of the meniscus:

$$J_{mol} = -D\iint_S \frac{\partial C}{\partial n} dS \tag{7}$$

where n is a unit vector normal to the meniscus and S is the area of the meniscus surface. Taking into consideration the axial symmetry of the physical domain, we used the diffusion molar flux j_{mol} :

$$j_{mol} = \frac{J_{mol}}{2\pi(R_a - \frac{e}{2})} \tag{8}$$

Therefore, recalling (8):

$$j_{mol} = -D\int_0^{l_a} \frac{\partial C}{dn} ds \tag{9}$$

where s is a direction tangential to the meniscus line and l_a is the length of the meniscus line (Figure 3).

We assumed that the pressure in the melt p_m equals that over the melt column and is constant. This assumption is equivalent to zero curvature of the melt/gas interface at the top surface. The pressure difference across the meniscus surface is:

$$\Delta p = p_g - p_m = \sigma\xi \tag{10}$$

where p_g is the pressure in the gap, σ is the gas/liquid surface tension, ξ is the mean curvature of the meniscus. Equation (10) is Laplace equation, which is applied here with regarding for the geometrical configuration of the meniscus. With these assumptions and using the Ideal Gas Law, the rate of pressure change across the meniscus in the general case equals to that in the gap and can be represented by three terms:

$$\frac{d\Delta p}{dt} = \frac{dp_g}{dt} = \frac{d}{dt}\left(\frac{NRT_{avg}}{V}\right) = \frac{RT_{avg}}{V}\frac{dN}{dt} + \frac{NR}{V}\frac{dT_{avg}}{dt} - \frac{NRT_{avg}}{V^2}\frac{dV}{dt} \tag{11}$$

Here N is the number of moles of gas in the gap, R is the ideal gas constant, T_{avg} is the average temperature of the gas in the gap, and V is the gap volume. The first term in (11) derives from dissolved gas diffusion to the meniscus and can be expressed in terms of the molar flux (7). The value and the sign of this term depend on the concentration field of dissolved gas in the melt. The second term derives from the rate of change of average gas temperature in the gap. Since the solid cools while growth proceeds, dT_{avg}/dt is negative. This term is small and was dropped here. The last term describes the increase in the gap volume due to growth. This term also gives a negative contribution to the rate of pressure change. The volume of the gap, from geometrical considerations is:

$$V = \pi e(2R_a - e)L \tag{12}$$

where L is the length of the gap. It should be noted that the contraction of crystal due to cooling is 2 to 3 orders of magnitude less than the values of the gap width used in the calculations. Consequently, this contraction was neglected in the derivation of equation (12). Neglecting the second term in (11), the rate of pressure change in the gap becomes:

$$\frac{dp_g}{dt} = \frac{RT_{avg}}{\pi e(2R_a - e)L} J_{mol} - \frac{p_g}{L}\frac{dL}{dt} - p_g \frac{2(R_a - e)}{e(2R_a - e)}\frac{de}{dt} \tag{13}$$

2.3. Steady-State Gap Width Calculation

Expression (13) is zero for steady-state detached solidification. The last term in (13) is also zero (de/dt = 0). Note that dL/dt is the solidification rate V_c. Therefore, at steady state:

$$\frac{dp_g}{dt} = \frac{RT_{avg}}{\pi e(2R_a - e)L} J_{mol} - \frac{p_g}{L} V_c = 0 \tag{14}$$

Expression (14) can now be rewritten using (8) as:

$$\frac{RT_{avg}}{e} j_{mol} - p_g V_c = 0 \tag{15}$$

As derived by Duffar [17] the gap width e for steady-state growth is given by:

$$e = \frac{2\sigma}{\Delta p} \cdot \cos\left(\frac{\alpha - \theta}{2}\right) \cdot \cos\left(\frac{\alpha + \theta}{2}\right) \tag{16}$$

where σ is the meniscus surface tension, α is the angle between the meniscus line and axial direction at the three-phase line, and θ is the contact angle (see Figure 3.) Here we considered that at steady state $\alpha = \alpha_0$, the growth angle. With the help of (16), the expression for the steady-state gap width e_{st} was found to be:

$$e_{st} = \frac{\frac{RT_{avg}}{V_c} j_{mol} - 2\sigma \cdot \cos(\frac{\alpha - \theta}{2}) \cdot \cos(\frac{\alpha + \theta}{2})}{p_m} \qquad (17)$$

3. RESULTS

Figures 4 and 5 illustrate typical results for the velocity field obtained by solving equations (1) to (3) with the boundary conditions (4). Figure 4a shows streamlines when surface tension driven convection is not taken into account, i.e. zero shear stress along the meniscus. Since the freezing interface and the meniscus were taken as fixed, the flow is due solely to solidification. The melt flows into the interface with velocity $-V_c$. The ampoule wall also moves at velocity $-V_c$. Intense convection takes place when the temperature dependence of the meniscus's surface tension is taken into account (Fig.4b). Convective vortices due to Marangoni convection are localized near the meniscus, with the maximum velocity being two to three orders of magnitude larger than in Figure 4a. (A constant axial temperature gradient of 10 $K*cm^{-1}$ is assumed). The maximum Reynolds number is 15 for Marangoni flow with Ma=187 and a gap width e=0.05 cm, whereas Re=0.03 for the flow without Marangoni convection.

The velocity field was used to solve the mass transfer equation (6). The calculation of the concentration field was carried out for a range of parameters: inverse diffusion length V_c/D, residual gas pressure p_m over the melt column, and segregation coefficient k of the dissolved gas at the solidification interface. There are no data available in the literature for segregation coefficient of gases in semiconductor melts. Consequently a range of segregation coefficient from 0.02 to 0.1 was used in the calculations.

Figure 6 shows the resulting concentration field at zero gravity with no Marangoni convection, with lines being constant concentration. Figure 7 shows that surface tension driven convection perturbs the concentration field locally, near the meniscus.

From our steady-state calculations the following qualitative conclusions were made:

- the concentration field depends on the inverse diffusion length V_c/D, as for one-dimensional segregation [18].

- the concentration at all points is proportional to the value of residual gas pressure p_m. With increase of that pressure, the concentration of dissolved gas along the solidification interface increases proportionally to p_m.

- the concentration of dissolved gas near the interface decreases as the segregation coefficient k increases (Fig.8).

The gas flux across the melt/gas interface (meniscus) was determined from the concentration gradient normal to the meniscus, equation (10). The concentration gradient varies along the meniscus and depends on the value of the inverse diffusion length V_c/D (Fig.9), residual gas pressure p_m, segregation coefficient k and gap width e. For large V_c/D, there is a steep positive concentration gradient at the meniscus near the freezing interface (s=0), where dissolved gas diffuses from the melt into the gap, and a large negative gradient at the ampoule wall ($s=l_a$), where gas diffuses back into the melt. For smaller values of V_c/D, the change of concentration gradient along the meniscus is less than for large V_c/D.

Figure 10 shows the dependence of the gas flux on the gap width for different values of V_c/D. For small gap width, the flux increases proportionally to e, due to an increase in the meniscus surface area S. In the limit of large gap width, the total flux begins to decrease because of back-diffusion of gas into the melt through the portion of the meniscus far from interface. This happens when the meniscus length l_a exceeds the diffusion length D/V_c. Figure 10 shows the decrease of the total gas flux for large gap width e and large solidification rate (V_c/D = 30 cm^{-1}.)

Surface tension driven convection does not change much the total gas flux into the gap, although it changes the distribution of gas flux along the meniscus (Fig.11).

The steady-state gap width was obtained by using equation (17). The value of the molar gas flux j_{mol} in (17) was found numerically for several assumed values of gap width e over the range of growth rate V_c and pressure p_m. The calculations were carried out for constant average temperature in the gap T_{avg}, meniscus surface tension σ, growth and contact angles. The correct steady state is found when the value of gap width calculated from (17) equals the assumed gap width. From our calculations, the gap width is on the order of 1 mm. This value agrees with experimental observations [7,8,11]. The results are shown in Figures 12 and 13. In the figures, the solid lines connect the points obtained from (17) with j_{mol} having been found numerically. The dotted lines

represent the assumed gap widths. The intersection of solid and dotted lines gives the correct value of steady-state gap width (solid squares). The heavy line connecting the squares in the figures shows the dependence of the correct gap width versus V_c/D and p_m.

One feature of these results is a maximum solidification rate, beyond which a steady-state gap width does not exist. The reason for this phenomenon in the existence of a maximum value of the gas flux (Fig.10). The attainable gas flux is insufficient to maintain a steady-state gap width for high solidification rate. Similarly, for small residual gas pressure, the gas flux cannot provide the necessary pressure difference Δp to maintain the meniscus curvature for a constant gap width.

The dependence of the steady-state gap width on segregation coefficient k for fixed V_c/D shows a maximum k at which steady state growth is still attainable (Figure 14). This result implies that only when dissolved gas is rejected well (low k) by the growing solid, can steady-state detachment be reached. The other feature seen in Figure 14 is the trend of k to decrease with increasing V_c/D in order to maintain steady-state detachment. Again, such behavior occurs because of back-diffusion of gas from the gap into the melt near the ampoule wall. With increasing V_c/D, the area of the meniscus surface, where back-diffusion takes place, broadens. The only way to maintain the same value of gas flux is to increase gas concentration near the freezing interface, i.e. to decrease the segregation coefficient.

It was also found that for small values of $V_c/D \sim 1$ cm^{-1}, the gap width becomes dependent on the length of the domain L_a. In other words, the use of the boundary conditions for the concentration field at $x=L_a$ becomes inappropriate for low solidification rates. In this case, the entire melt column must be considered. The influence of the domain length on the value of the gap width becomes less with increasing solidification rate V_c and melt column length. The length of the melt column turned out to be unimportant because a steady-state gap width on the order of 1 mm corresponds to larger values of V_c/D (> 1 cm^{-1}) (heavy line in Figure 12).

Marangoni convection makes little difference to the gap width, in spite of its dramatic influence on the velocity and concentration fields near the meniscus. In other words, it does not have a large influence on the integrated transport of volatile species from the freezing interface to the meniscus.

The dependence of the steady-state gap width on the growth angle α, contact angle θ, and surface tension σ was established by varying one of the aforementioned parameters and using equation (17) for values of the gap width around a steady-state value of 0.05 cm, with $V_c/D = 10.4\ cm^{-1}$ and the other parameters from Table 2 held constant. The dependence of the molar gas flux j_{mol} on gap width e can be approximated for $V_c/D = 10.4\ cm^{-1}$ by:

$$j_{mol}/D = j^{o}{}_{mol}/D - \frac{a_1}{e/R_a} - a_2 \ln\frac{e}{R_a} + a_3\frac{e}{R_a} \qquad (18)$$

with $j^{o}_{mol} = 0.246*10^{-12}$ mol cm^{-1} s^{-1}, $a_1 = 0.762*10^{-9}$, $a_2 = 0.109*10^{-7}$, $a_3 = 0.510*10^{-7}$ mol cm^{-3} found from the numerical calculations. The value of the gap width e used in (18) was found by substituting the parameters (α, θ, and σ) into (16). It follows from this analysis that the value of steady-state gap width increases with increasing α and θ, see Fig.15 and Fig.16, and decreases with increasing σ (Fig.17). The numerical values of a_1, a_2, and a_3 are valid only for small deviations of α, θ, and σ from the values used for the numerical calculations (Table 2) since (18) was derived for constant α, θ, and σ. In changing those parameters, not only the gap width e but the area of the meniscus surface also changes. In spite of weak dependence of the meniscus surface area on these parameters, the values of the constants in (18) would be different.

In addition, it should be noted that if the solubility of gas in the melt is less from that used in the calculations, this would decrease the gas flux and decrease the steady-state gap width, according to (17). To obtain the same values of gap width, either an increase of solidification rate or partial gas pressure would be necessary.

4. CONCLUSIONS

A study of steady-state detached solidification was carried out. The numerical analysis shows that a steady-state configuration can be achieved over a range of processing parameters; it gives values of the steady-state gap width that are reasonable and agree with the experimental observations. Low solidification rates are favorable to the existence of steady-state detached growth, whereas a low pressure of residual gas in the ampoule can be insufficient to achieve steady-state detached growth. The required values of V_c and p_m depend on the value of the diffusion coefficient of gas in the semiconductor melt, on the segregation coefficient of gas at the freezing interface, on the gas/melt surface tension, and on the values of growth and contact angles.

Acknowledgment

The research was supported by NASA's Microgravity Science and Applications Division under grant NAG8-1063.

REFERENCES

1. W.R. Wilcox, and L.L. Regel, *Microgravity Sci. Technol.* **7**, 56-61(1995).

2. R. Sen, and W.R. Wilcox, *J. Crystal Growth* **74**, 591-596(1986).

3. H. Ahlborn and K. Lohberg, in: *Proceedings Norderney Symposium on Scientific Results of the German SpaceLab Mission D1* (ESA, 1986) p.268.

4. T. Duffar, I. Paret-Harter, and P. Dusserre, *J. Crystal Growth* **100**,171-184(1990).

5. T. Duffar, C. Potard, and P. Dusserre, *J. Crystal Growth* **92**,467-478(1988).

6. A.F. Witt, H.C. Gatos, M. Lichtensteiger, M.C. Lavine, and C.J. Herman, *J. Electrochem.Soc.* **122**,276 (1975).

7. V.S. Zemskov and M.R. Raukhman, *Fizika I Khiniya Obrabotki Materialov*, **21**, 63-67(1987).

8. V.S. Zemskov, L.I. Ivanov, E.M. Savitskii, M.R. Raukhman, B.P. Mikhailov, V.N. Pimenov, I.N. Belokurova, R.S. Torchinova, M.I. Bychkova, and V.N. Meshcheryakov, *Izvestiya Akademii Nauk SSSR. Seriya Fizicheskaya*, **49**, 673-680(1985).

9. V.S. Zemskov, M.R. Raukhman, A.V. Laptev, I.B. Barmin, A.S. Senchenkov, I.G. Smirnova, and S.M. Pchelintsev, in: *Doped Semiconductor Materials* (Nauka, Moscow, 1985), pp.132-138, in Russian.

10. I.L. Shulpina, L.M. Sorokin, A.S. Tregubova, G.N. Mosina, V.S. Zemskov, M.R. Raukhman, E.A. Kozitsina, in: *Doped Semiconductor Materials* (Nauka, Moscow, 1985), pp.138-142, in Russian.

11. F. Zhang, L. Zhang, G. Chen, M. Shen, G. Yan, D. Da, L. Huang, X. Xie, and X. Tan, *Chinese Science Bulletin*, **34**, 1529-1532(1989).

12. R.B. Bird, W.E. Stewart, and E.N. Lightfoot, *Transport Phenomena* (John Wiley & Sons, Inc., NY, 1966).

13. P.A. Durbin, *J. Fluid Mech.* **197**,157-169(1988).

14. P.A. Durbin, *Quart. J. Mech. Appl. Math.* **42**,99-113(1989).

15. P.J.Roache, *Computational Fluid Dynamics* (Hermosa Publisher, Albuquerque, NM, 1982).

16. Y. Austin Chang, K. Fitzner, and Min-Xian Zhang, *Progress in Materials Science*, **32**, #2-3(1988).

17. T. Duffar, Private Communication, 1995, Centre d'Etudes Nucleaires, 85 X. F-38041 Grenoble, Cedex, France.

18. J. Crank, *The Mathematics of Diffusion* (Clarendon Press, Oxford, 1956).

19. V.M. Glazov, S.N. Chizhevskaya, and N.N. Glagoleva, *Liquid Semiconductors* (Plenum Press, NY, 1969).

APPENDIX

Finite difference representation and boundary conditions for momentum equation.

The governing equation (2) can be expressed in terms of vorticity ω,

$$\omega = \frac{1}{r} E^2 \psi = \frac{1}{r}\left(\frac{\partial^2 \psi}{\partial x^2} + \frac{\partial^2 \psi}{\partial r^2} - \frac{1}{r}\frac{\partial \psi}{\partial r} \right) \tag{A.1}$$

as:

$$V_x \frac{\partial \omega}{\partial x} + V_r \frac{\partial \omega}{\partial r} - \frac{1}{r} V_r \omega = \nu \left[\frac{\partial^2 \omega}{\partial x^2} + \frac{\partial^2 \omega}{\partial r^2} + \frac{1}{r}\frac{\partial \omega}{\partial r} - \frac{\omega}{r^2} \right] \tag{A.2}$$

The boundary conditions (4) can be expressed using the stream function and vorticity as:

$$\begin{aligned}
&At\ x = 0\ (interface): \quad \psi = \frac{1}{2} V_c r^2 ; \quad \omega = \frac{\partial V_r}{\partial x} \\
&At\ x = L_a >> e: \quad \psi = -\frac{1}{2} V_c r^2 + V_c \left(1 - \frac{e}{R_a} \right)^2 r^2 - \frac{V_c}{2 R_a^2} \left(\left(1 - \frac{e}{R_a^2} \right)^2 - 1 \right) r^4 ; \\
&\qquad \omega = -\frac{4 V_c}{R_a^2} \left(\left(1 - \frac{e}{R_a} \right)^2 - 1 \right) r \\
&At\ r = 0\ (ampoule\ axis): \quad \psi = 0 ; \quad \omega = 0 \\
&At\ r = R_a\ (ampoule\ wall): \quad \psi = \frac{1}{2} V_c (R_a - e)^2 ; \quad \omega = -\frac{\partial V_x}{\partial r} \\
&On\ the\ meniscus: \quad \psi = const. = \frac{1}{2} V_c (R_a - e)^2 ; \quad \omega = -\frac{\partial V_s}{\partial n} = -\frac{1}{\mu}\frac{\partial \sigma}{\partial s}
\end{aligned} \tag{A.3}$$

Equations (A.1), (A.2) and (1) were solved simultaneously using a finite difference representation on a nonuniform mesh. By designating:

$$\begin{aligned}
h_i &= \Delta x_{i-1,i} & h_j &= \Delta r_{j-1,j} \\
\varepsilon_i &= \frac{\Delta x_{i,i+1}}{\Delta x_{i-1,i}} & \varepsilon_j &= \frac{\Delta r_{j,j+1}}{\Delta r_{j-1,j}}
\end{aligned} \tag{A.4}$$

the first derivatives for the vorticity were taken as:

$$\frac{\partial \omega}{\partial x} = \frac{-\varepsilon_i^{\,2}\omega_{i-1,j} + (\varepsilon_i^{\,2} - 1)\omega_{i,j} + \omega_{i+1,j}}{h_i \varepsilon_i (1+\varepsilon_i)}$$
$$\frac{\partial \omega}{\partial r} = \frac{-\varepsilon_j^{\,2}\omega_{i,j-1} + (\varepsilon_j^{\,2} - 1)\omega_{i,j} + \omega_{i,j+1}}{h_j \varepsilon_j (1+\varepsilon_j)} \qquad \text{(A.5)}$$

and the second derivatives were found to be:

$$\frac{\partial^2 \omega}{\partial x^2} = \frac{2\left[\varepsilon_i \omega_{i-1,j} - (1+\varepsilon_i)\omega_{i,j} + \omega_{i+1,j}\right]}{h_i^{\,2} \varepsilon_i (1+\varepsilon_i)}$$
$$\frac{\partial^2 \omega}{\partial r^2} = \frac{2\left[\varepsilon_j \omega_{i,j-1} - (1+\varepsilon_j)\omega_{i,j} + \omega_{i,j+1}\right]}{h_j^{\,2} \varepsilon_j (1+\varepsilon_j)} \qquad \text{(A.6)}$$

The same equations have been used for finite difference representation of the stream function.

The finite difference representation of the first derivative used at the boundary was:

$$\left.\frac{\partial \psi}{\partial x}\right|_{x=bound.} = \frac{-3\psi_{0,j} + 4\psi_{1,j} - \psi_{2,j}}{2h_1}$$
$$\left.\frac{\partial \psi}{\partial r}\right|_{r=bound.} = \frac{-3\psi_{i,0} + 4\psi_{i,1} - \psi_{i,2}}{2h_1} \qquad \text{(A.7)}$$

The same form was used for the representation of the velocity components' derivatives at the boundaries. The boundary conditions for the velocity components at the meniscus were derived in the (x,r)-coordinate system using the angle ϕ between the positive direction of r-axis and the tangent to the meniscus (see Figure 3):

$$V_n = V_r \sin\phi - V_x \cos\phi = 0$$
$$\frac{\partial V_s}{\partial n} = \frac{\partial V_r}{\partial r}\sin\phi\cos\phi + \frac{\partial V_x}{\partial r}\sin^2\phi - \frac{\partial V_r}{\partial x}\cos^2\phi - \frac{\partial V_x}{\partial x}\sin\phi\cos\phi = \frac{1}{\mu}\frac{\partial \sigma}{\partial s} \qquad \text{(A.8)}$$

Finite difference representation of the diffusion equation.

The same finite difference forms as for vorticity and stream function (equations (A.5) to (A.7)) were applied for the concentration C of gas dissolved in the melt.

At the freezing interface (x=0), the material balance boundary condition was solved simultaneously with mass transfer equation (5) with $V_x = -V_c$ and $V_r=0$. This was done in order to use the usual finite difference representation for the second derivative at the boundary and to avoid imaginary finite difference points outside the computational domain. It should be noted that diffusion along the freezing interface has been incorporated here. The expression used for the concentration at the freezing interface in finite difference representation is:

$$C_{0,j} = \frac{C_{1,j}\left[\frac{2D}{h_i^{\,2}}\right] + C_{0,j-1}D\left[\frac{2}{h_j^{\,2}(1+\varepsilon_j)} - \frac{\varepsilon_j}{r_j h_j (1+\varepsilon_j)}\right] + C_{0,j+1}D\left[\frac{2}{h_j^{\,2}\varepsilon_j(1+\varepsilon_j)} + \frac{1}{r_j h_j \varepsilon_j (1+\varepsilon_j)}\right]}{\left(\frac{2D}{h_i^{\,2}} - \frac{2V_c(1-k)}{h_i} + \frac{V_c^{\,2}(1-k)}{D} + \frac{2D}{h_j^{\,2}\varepsilon_j} - \frac{(\varepsilon_j - 1)D}{r_j h_j \varepsilon_j}\right)} \qquad \text{(B.1)}$$

Table 1. Parameters and physical properties of InSb used in the numerical calculations.

Parameters	Symbol	Value	Reference
Gas-melt surface tension (at the melting point)	σ	430 dyne/cm	13
Temperature dependence of the surface tension	$d\sigma/dT$	$-8*10^{-2}$ dyne/cm K	5
Contact angle	θ	112 degrees	15
Growth angle	α_0	25 degrees	4
Kinematic viscosity	ν	$3.6*10^{-3}$ cm^2/s	18

Table 2. Estimated or assumed parameters used in the numerical calculations.

Parameters	Symbol	Value
Diffusion coefficient of dissolved gas	D	10^{-5} cm^2/s
Solubility (meniscus), 800 K	K_{pg}	$1.73*10^{-5}$ mol cm^{-3} atm^{-1}
Solubility (top of melt column), 850 K	K_{pm}	$2.09*10^{-5}$ mol cm^{-3} atm^{-1}
Segregation coefficient of dissolved gas at the solidification interface	k	0.02 - 0.1
Average temperature of gas in the gap	T_{avg}	800 K
Solidification rate	V_c	$2*10^{-5}$ - $5*10^{-4}$ cm/s
Pressure of gas over the melt column	p_m	$5*10^{2}$ - $2.5*10^{3}$ dyne/cm^2 ($5*10^{-4}$ - $2.5*10^{-3}$ atm)

NOMENCLATURE

Latin letters

a_1, a_2, a_3 - Coefficients defined by equation (18), [mol cm^{-3}];

C - Concentration of dissolved gas in the melt [mol cm^{-3}];

D - Diffusion coefficient of dissolved gas in the melt [cm^2 s^{-1}];

e - Gap width [cm];

h - Finite difference spacing, defined by eq.(A.4) [cm];

j_{mol} - Molar flux in the axisymmetric case (Equation (10)) [mol s^{-1} cm^{-1}];

J_{mol} - Molar flux of gas into the gap (Equation (8)) [mol s^{-1}];

k - Segregation coefficient of dissolved gas between solid and melt; ratio of concentration in solid to that in the melt at the freezing interface;

K_{pg}, K_{pm} - Solubility of gas dissolved in the melt at the interface (meniscus and over the melt column respectively) [mol cm^{-3} atm^{-1}];

l_a - Length of the meniscus line [cm];

L - Gap length [cm];

L_a - Length of the column of melt analyzed (from the planar interface) [cm];

n - Normal direction at the meniscus, inward toward the melt (Fig.3) [cm];

N - Number of moles of gas in the gap;

p_m - Pressure over the column of melt, assumed to be the same at L_a [dyne cm^{-2}];

p_g - Pressure of gas in the gap [dyne cm^{-2}];

Δp - Pressure difference across the meniscus between the gap and the adjacent melt, p_g-p_m [dyne cm^{-2}];

r - Radial direction [cm];

R - Ideal gas constant, $8.314*10^7$ [erg mol^{-1} K^{-1}];

R_a - Inner ampoule radius [cm];

R_m - Meniscus radius of curvature [cm];

s - Tangential direction at the meniscus [cm];

S - Area of the meniscus [cm^2];

T_{avg} - Average temperature in the gap [K];

V - Gap volume [cm^3];

V_x, V_r - Velocity components in the melt [$cm\ s^{-1}$];

V_c - Solidification rate [$cm\ s^{-1}$];

x - Axial direction [cm].

Greek letters

α - Angle between the meniscus line and the axial direction at the three-phase line [rad];

α_0 - Growth angle [rad];

θ - Contact angle of the melt at the ampoule wall [rad];

ξ - Mean curvature [cm^{-1}];

λ_c - Slip length [cm];

μ - Dynamic viscosity of the melt [$g\ cm^{-1}\ s^{-1}$];

ν - Kinematic viscosity of the melt [$cm^2\ s^{-1}$];

σ - Surface tension of meniscus [$dyne\ cm^{-1}$];

τ_{sn} - Shear stress at the meniscus [$dyne\ cm^{-2}$];

ψ - Stream function [$cm^3\ s^{-1}$];

ω - Vorticity [s^{-1}];

ε - Ratio defined by eq.(A.5);

ϕ - Angle between the positive direction of r-axis and the tangent to the meniscus, defined in Fig.3 [deg];

Subscripts

g - In the gap/gas;

m - Over the melt column ;

st - Steady-state.

FIGURE CAPTIONS

Fig.1. Model of detached solidification.

Fig.2. Physical domain used in the numerical calculations. Gap width is exaggerated. Here α_0 is growth angle and θ is contact angle.

Fig.3. Meniscus geometry.

Fig.4. Computed streamlines in the absence of Marangoni convection at zero gravity. Difference between the stream function for adjacent lines is $\Delta\psi=2*10^{-6}$ cm^3/s. The flow is into the solid/melt interface at velocity $-V_c=10^{-4}$ cm/s. Gap width is e=0.05 cm.

Fig.5. Computed streamlines with Marangoni convection at the meniscus at zero gravity, $\Delta\psi=2*10^{-5}$ cm^3/s. The flow is into the solid/melt interface at velocity $-V_c=10^{-4}$ cm/s. The axial temperature gradient is 10 K/cm. Gap width is e=0.05 cm.

Fig.6. Computed lines of constant concentration corresponding to the velocity field in Fig.4 without Marangoni convection. The concentration difference between adjacent lines is $\Delta C=2*10^{-8}$ mol/cm^3. Diffusion coefficient of dissolved gas in the melt is $D=10^{-5}$ cm^2/s, segregation coefficient is k=0.03, residual gas pressure is $p_m=10^3$ $dyne/cm^2$.

Fig.7. Computed lines of constant concentration corresponding to the velocity field in Fig.5 with Marangoni convection, $\Delta C=2*10^{-8}$ mol/cm^3. Diffusion coefficient of dissolved gas in the melt is $D=10^{-5}$ cm^2/s, segregation coefficient is k=0.03, residual gas pressure is $p_m=10^3$ $dyne/cm^2$.

Fig.8. Concentration along the solidification interface for different values of segregation coefficient k without Marangoni convection. Diffusion coefficient of gas in the melt is $D=10^{-5}$ cm^2/s, solidification rate $V_c = 10^{-4}$ cm/s, residual gas pressure is $p_m=10^3$ $dyne/cm^2$.

Fig.9. The distribution of the normal gradient of gas concentration along the meniscus when surface tension driven convection is not taken into account. A positive value corresponds to diffusion into the gap, a negative value produces back-diffusion from the gap into the melt. Gap width e=0.05 cm, k=0.03, $p_m = 10^3$ $dyne/cm^2$.

Fig.10. The dependence of the gas flux j_{mol} (equation (10)), normalized by the diffusion coefficient D, on the gap width. The values of the gap width are assumed and are not the steady-state values. Steady-state gap widths corresponds to the values of the flux j_{mol} satisfying equation (18).

Fig.11. Comparison of the distribution of the normal gradient of gas concentration along the meniscus without and with surface tension driven convection, corresponding to the velocity fields in Fig. 4 and Fig.5 respectively. $V_c/D = 10\ cm^{-1}$, e=0.05 cm, k=0.03, $p_m = 2.5*10^3$ dyne/cm^2.

Fig.12. The dependence of the steady-state gap width on inverse diffusion length V_c/D. Each thin solid line connects points obtained from the numerical calculations for an assumed value of gap width; the dotted lines indicate when the calculated gap width equals the assumed value. The thick solid line connects solutions for steady-state gap width with fixed segregation coefficient k=0.03 and residual gas pressure $p_m = 10^3$ dyne/cm^2.

Fig.13. The dependence of the steady-state gap width on residual gas pressure p_m. Each thin solid line connects points obtained from the numerical calculations for an assumed value of gap width; the dotted lines indicate when the calculated gap width equals the assumed value. The thick solid line connects solutions for steady-state gap width with fixed segregation coefficient k=0.03 and $V_c/D=10\ cm^{-1}$.

Fig.14. The dependence of the steady-state gap width on segregation coefficient k. Each dotted line indicates the assumed value of the gap width. The thick solid line connects solutions for steady-state gap width with fixed residual gas pressure $p_m = 10^3$ dyne/cm^2 .

Fig.15. The dependence of the steady-state gap width on the value of growth angle α, with other parameters as shown in Tables 1 and 2. The dotted line shows the value of the gap width, for which the solution of (17) is exact with the value of gas flux obtained in the numerical calculation. The solid line is the solution of (17) for different α, approximating the value of molar gas flux by (18).

Fig.16. The dependence of the steady-state gap width on the value of contact angle θ, with other parameters as shown in Tables 1 and 2. The dotted line shows the value of the gap width, for which the solution of (17) is exact with the value of gas flux obtained in the numerical calculation. The solid line is the solution of (17) for different θ, approximating the value of molar gas flux by (18).

Fig.17. The dependence of the steady-state gap width on the value of surface tension σ, with other parameters as shown in Tables 1 and 2. The dotted line shows the value of the gap width, for which the solution of (17) is exact with the value of gas flux obtained in the numerical calculation. The solid line is the solution of (17) for different σ, approximating the value of molar gas flux by (18).

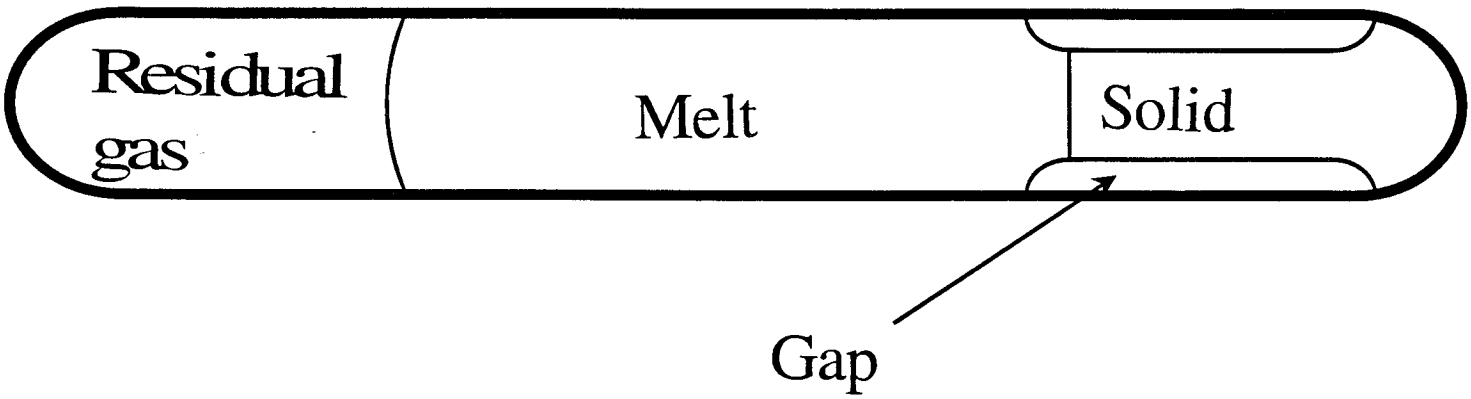

Fig. 1

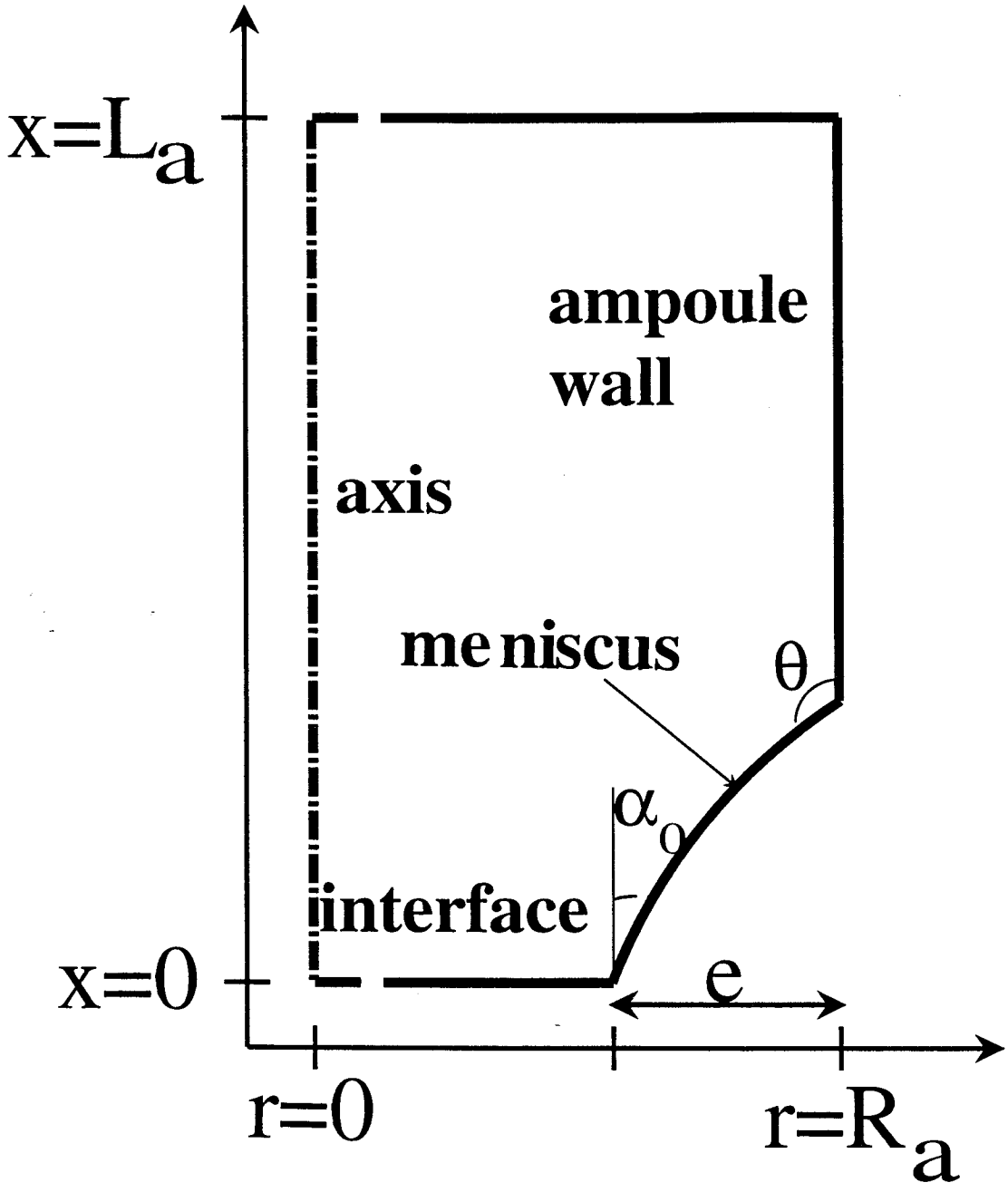
x=L_a
ampoule
wall
axis
meniscus
θ
α_0
interface
x=0
e
r=0
r=R_a

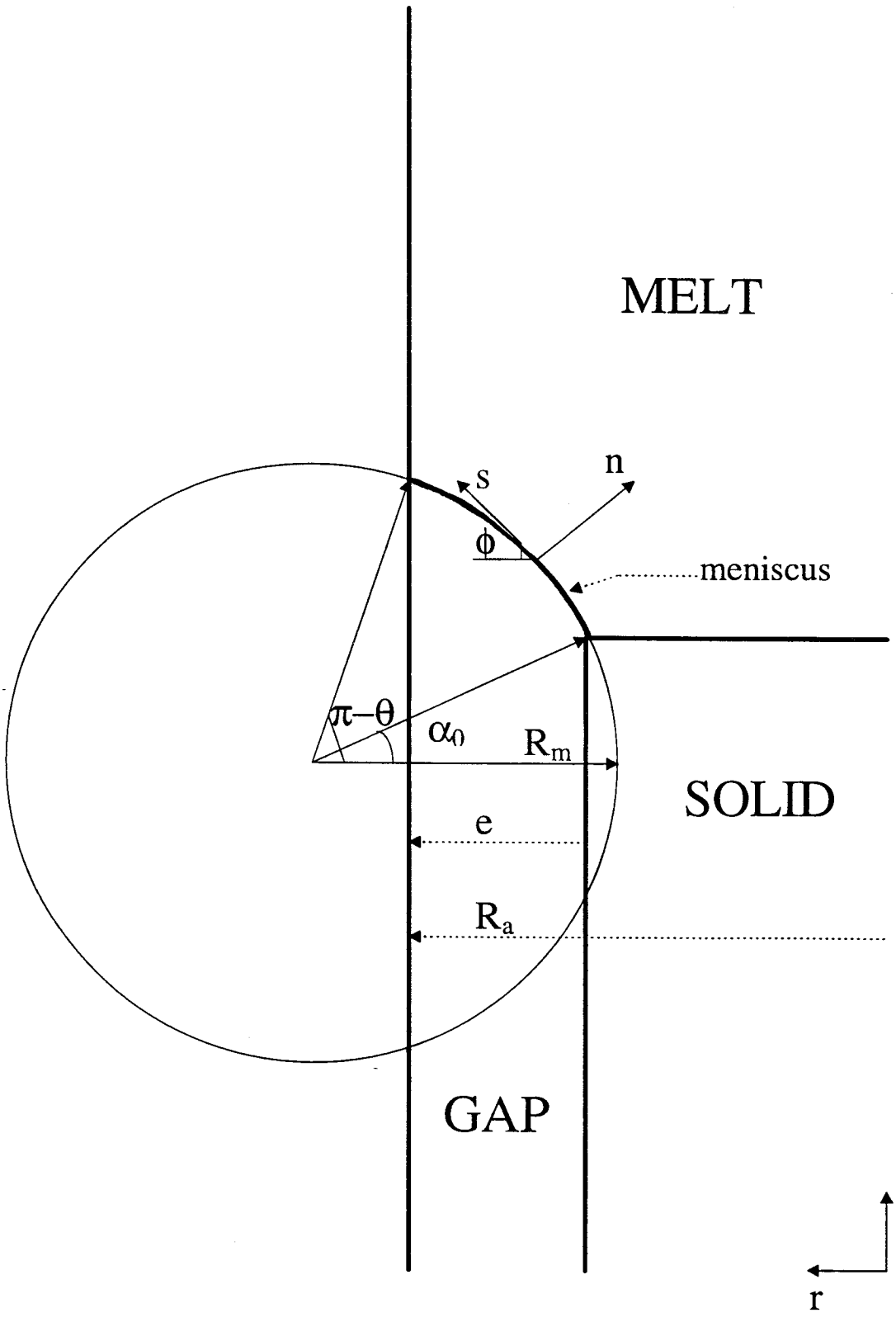
MELT
n
s
ϕ
meniscus
π–θ
α0
Rm
SOLID
e
Ra
GAP
x
r

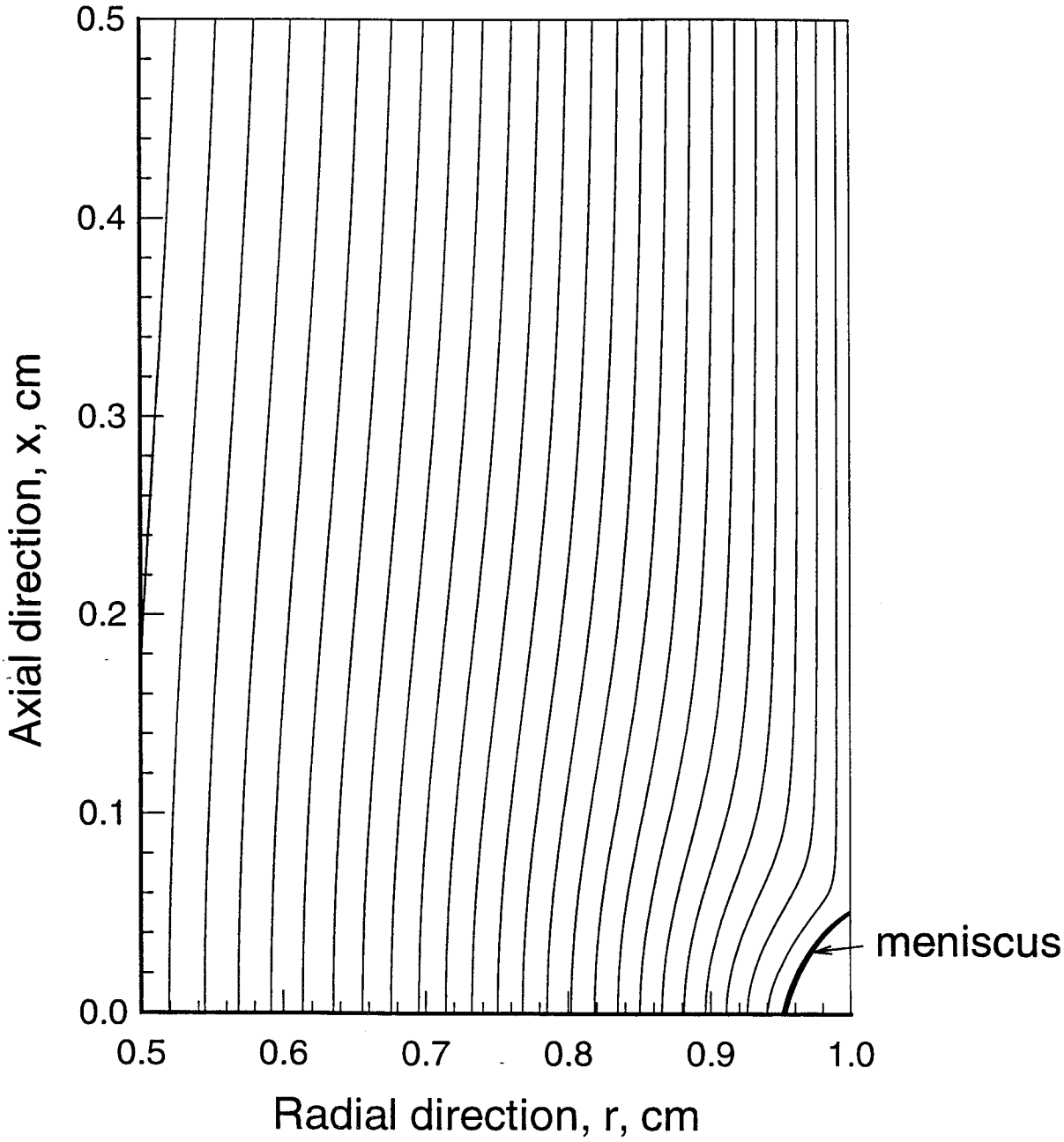
0.5
0.4
0.3
0.2
0.1
0.0
Axial direction, x, cm
0.5
0.6
0.7
0.8
0.9
1.0
Radial direction, r, cm
meniscus

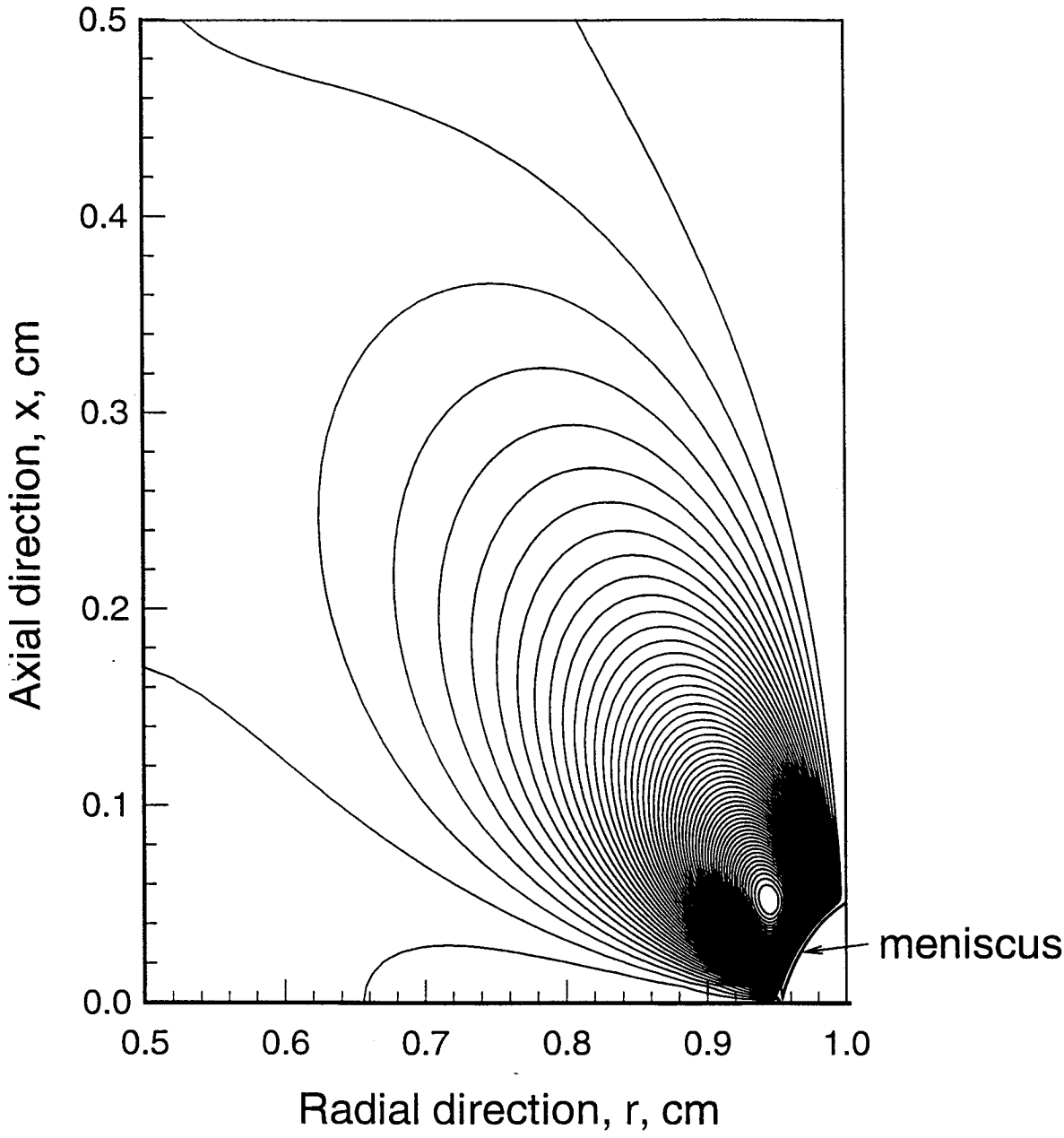
0.5
0.4
0.3
0.2
0.1
0.0
Axial direction, x, cm
0.5
0.6
0.7
0.8
0.9
1.0
Radial direction, r, cm
meniscus

Fig. 5

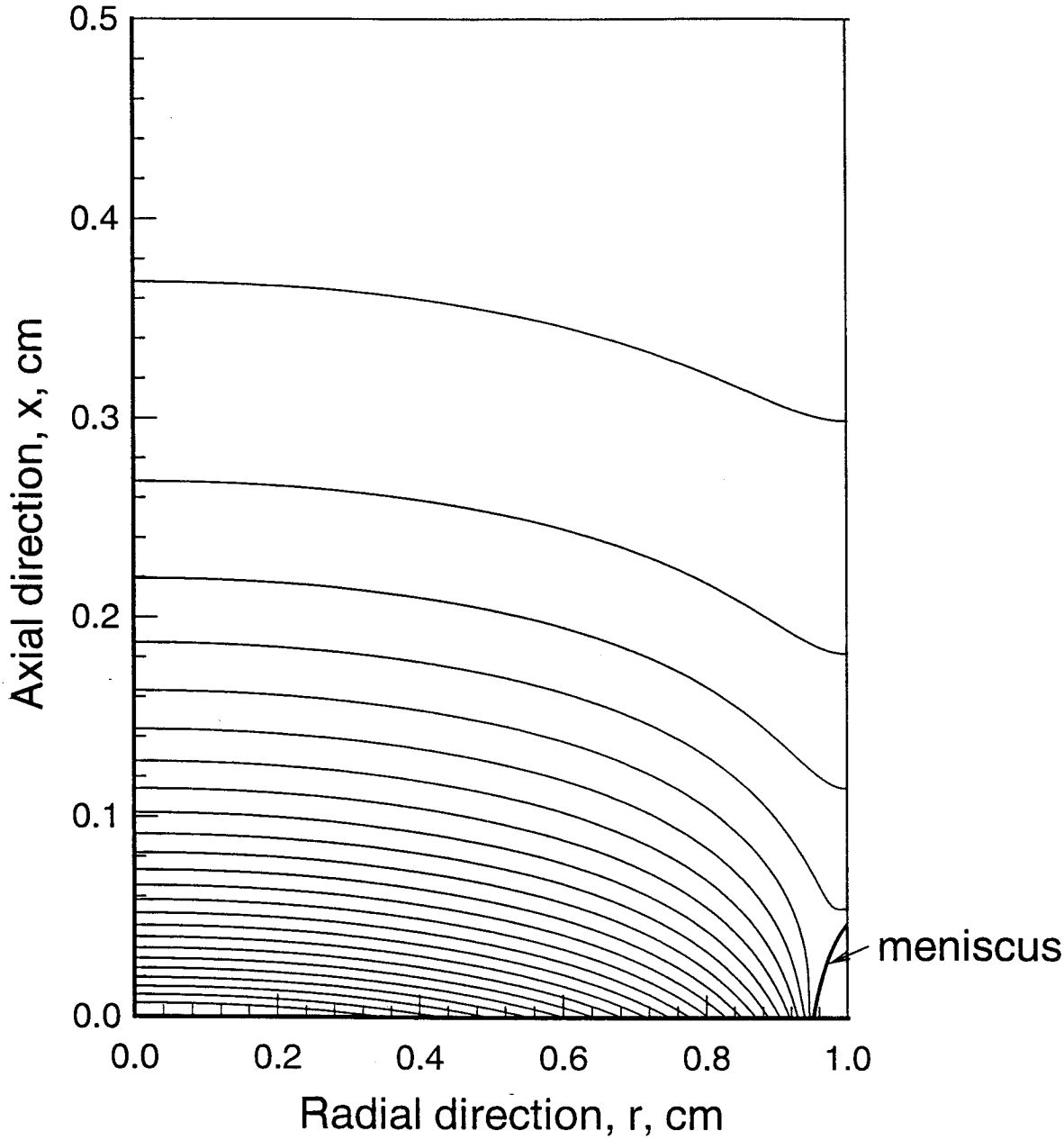
0.5
0.4
0.3
0.2
0.1
0.0
Axial direction, x, cm
0.0
0.2
0.4
0.6
0.8
1.0
Radial direction, r, cm
meniscus

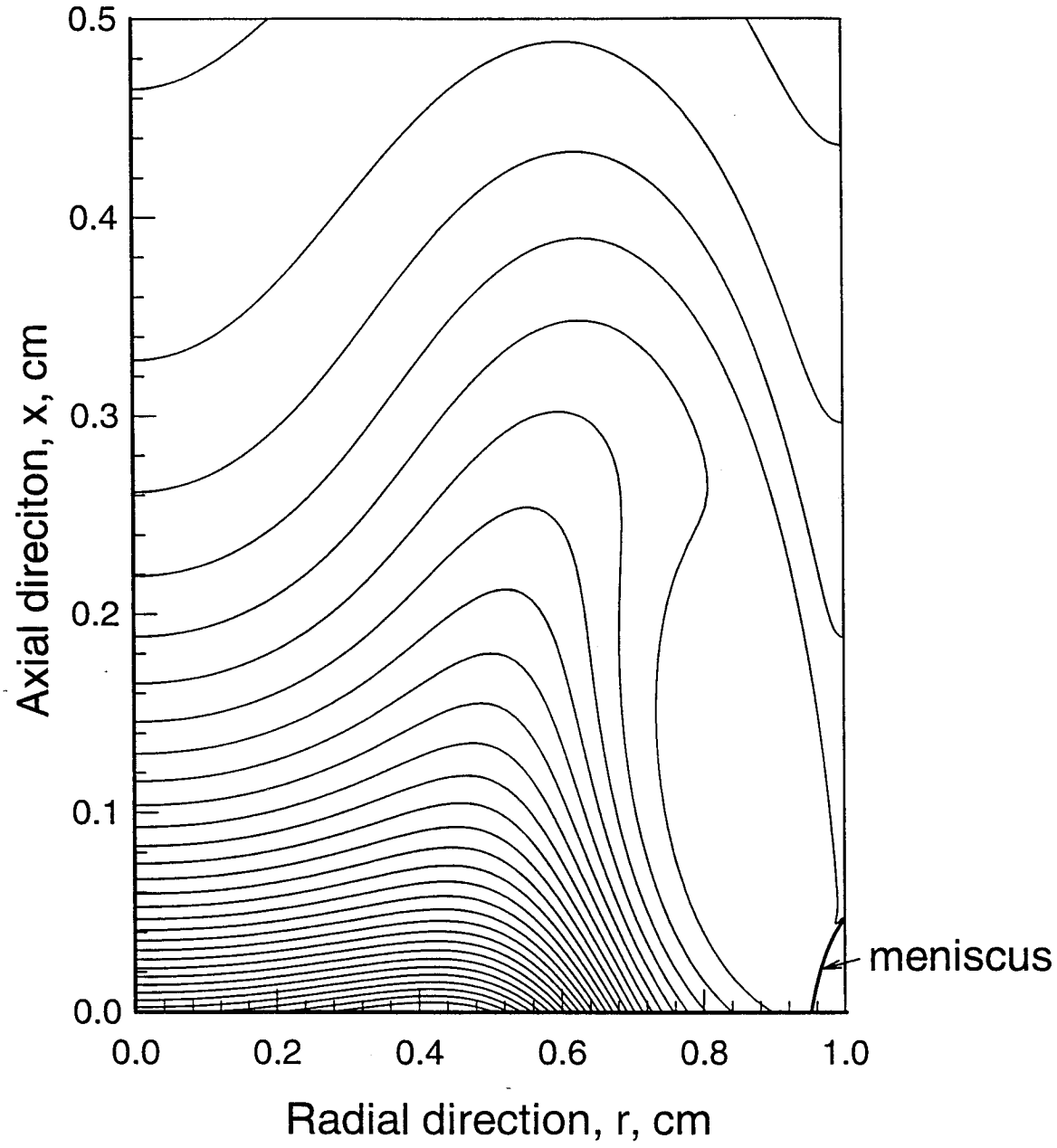
0.5
0.4
0.3
0.2
0.1
0.0
Axial direciton, x, cm
0.0
0.2
0.4
0.6
0.8
1.0
Radial direction, r, cm
meniscus

Fig. 7

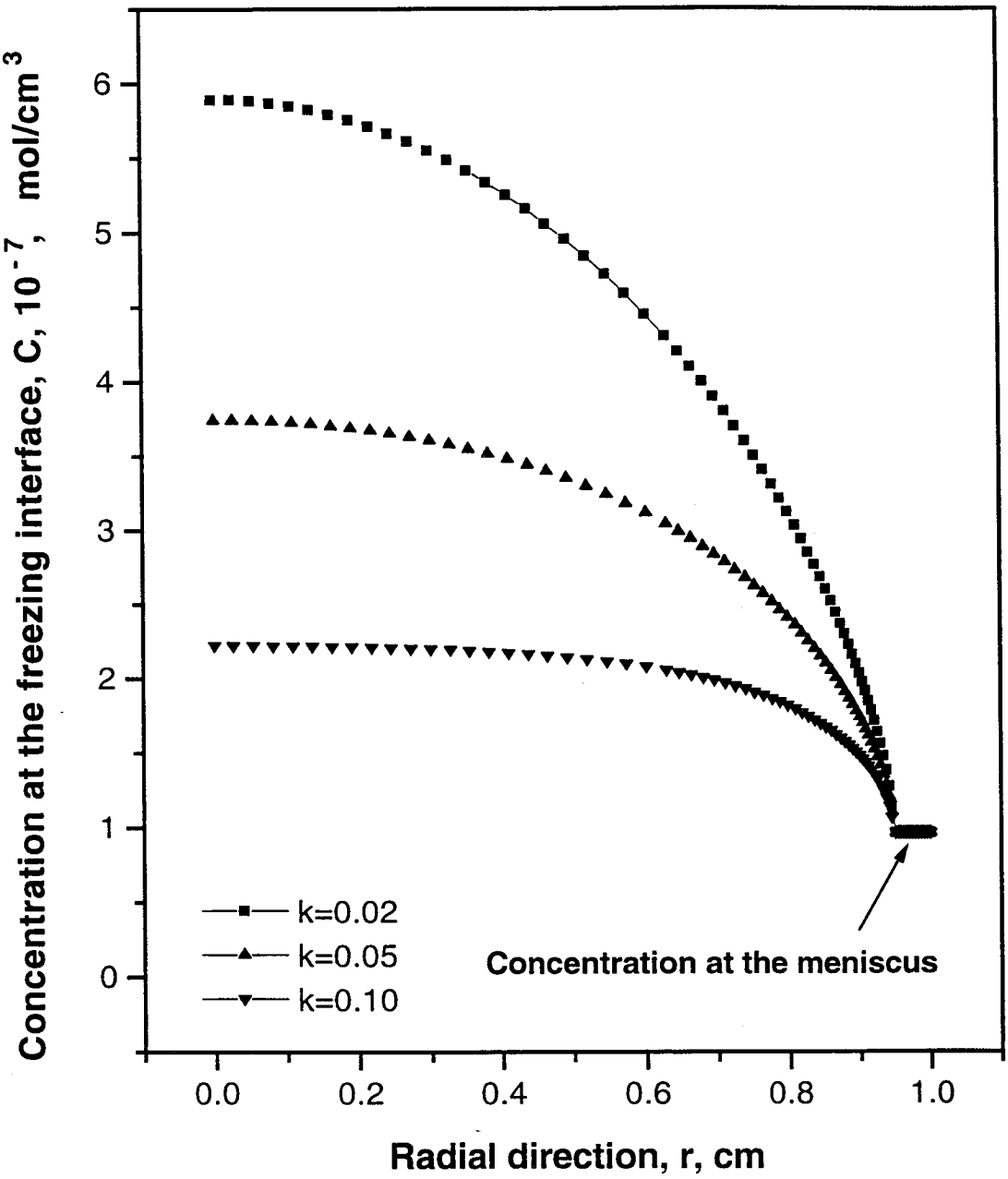
Concentration at the freezing interface, C, 10^{-7}, mol/cm^3
6
5
4
3
2
1
0
0.0
0.2
0.4
0.6
0.8
1.0
Radial direction, r, cm
k=0.02
k=0.05
k=0.10
Concentration at the meniscus

Fig. 9

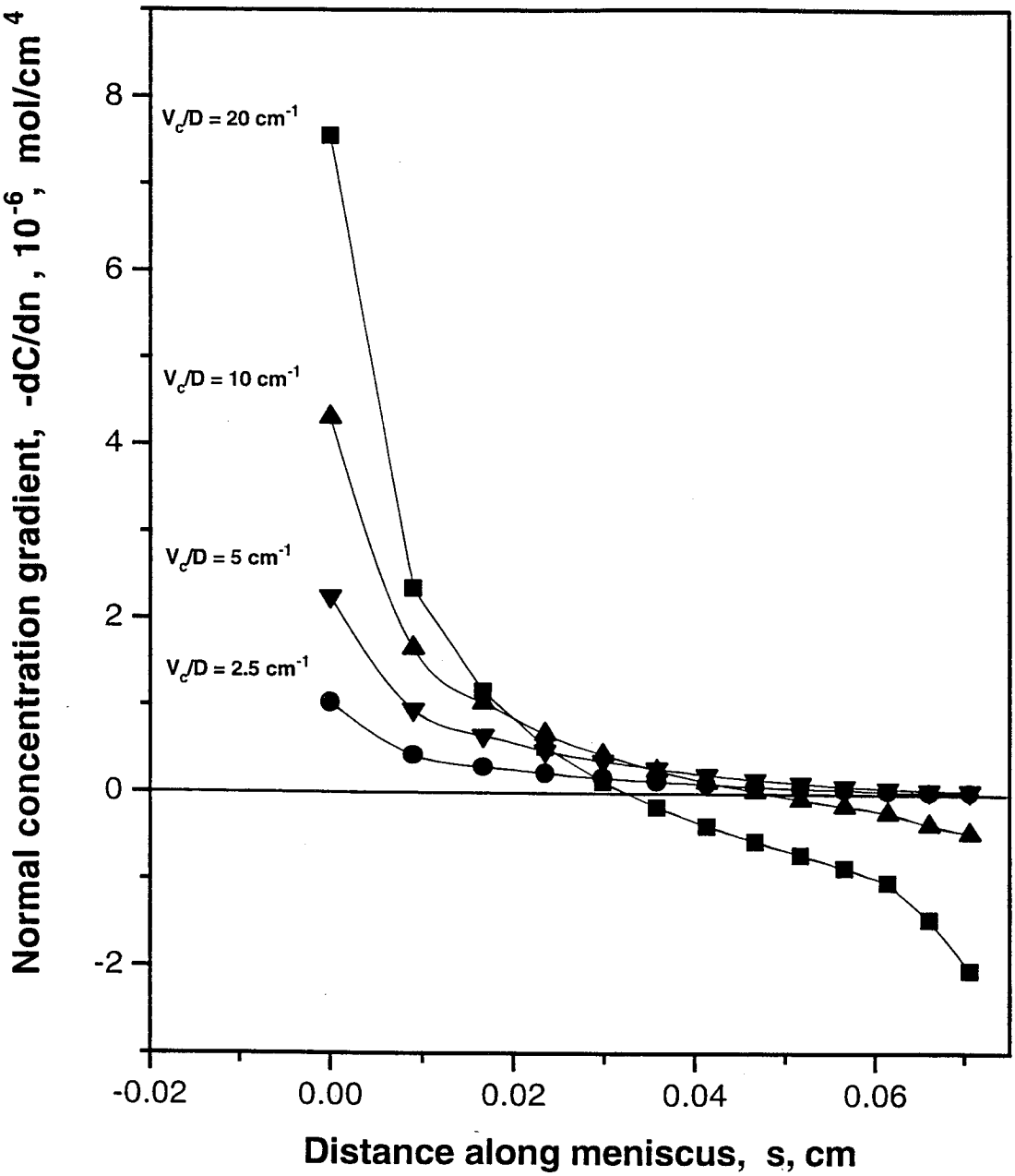
Normal concentration gradient, -dC/dn , 10^-6, mol/cm^4
8
6
4
2
0
-2
V_c/D = 20 cm^-1
V_c/D = 10 cm^-1
V_c/D = 5 cm^-1
V_c/D = 2.5 cm^-1
-0.02
0.00
0.02
0.04
0.06
Distance along meniscus, s, cm

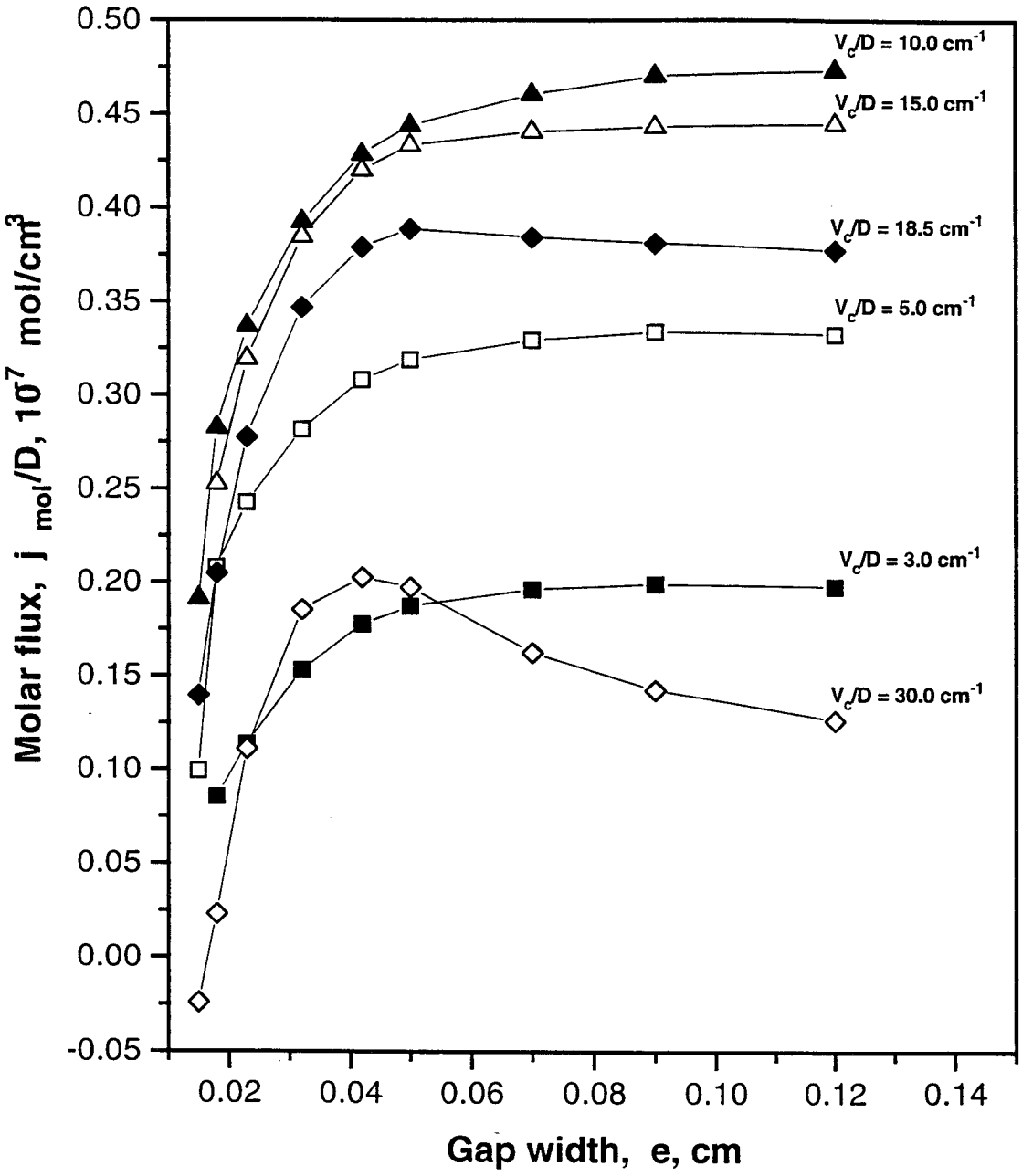
0.50
0.45
0.40
0.35
0.30
0.25
0.20
0.15
0.10
0.05
0.00
-0.05
0.02
0.04
0.06
0.08
0.10
0.12
0.14
Molar flux, j mol/D, 10-7 mol/cm3
Gap width, e, cm
Vc/D = 10.0 cm-1
Vc/D = 15.0 cm-1
Vc/D = 18.5 cm-1
Vc/D = 5.0 cm-1
Vc/D = 3.0 cm-1
Vc/D = 30.0 cm-1

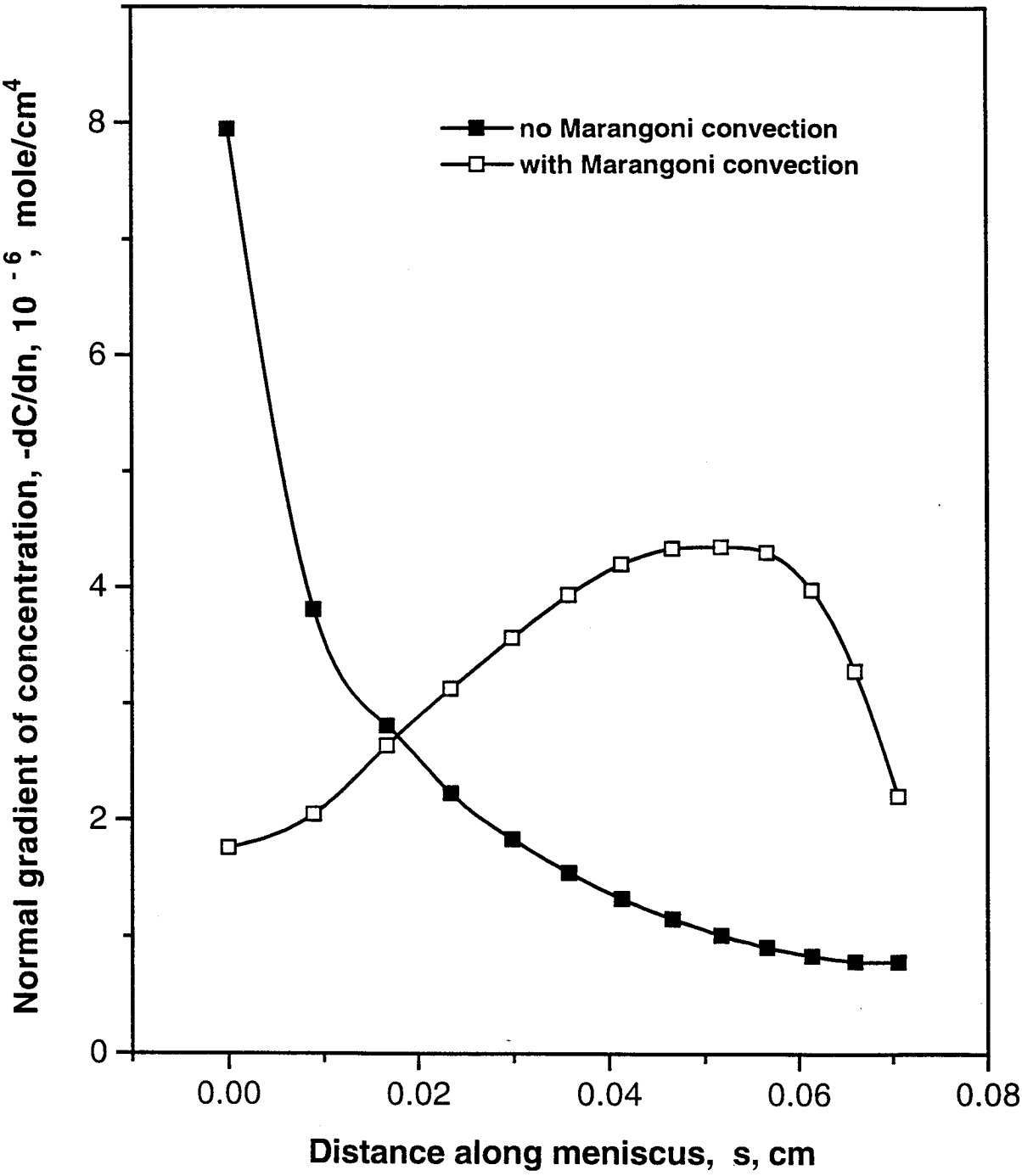
no Marangoni convection
with Marangoni convection
Normal gradient of concentration, -dC/dn, 10 -6; mole/cm4
Distance along meniscus, s, cm
0
2
4
6
8
0.00
0.02
0.04
0.06
0.08

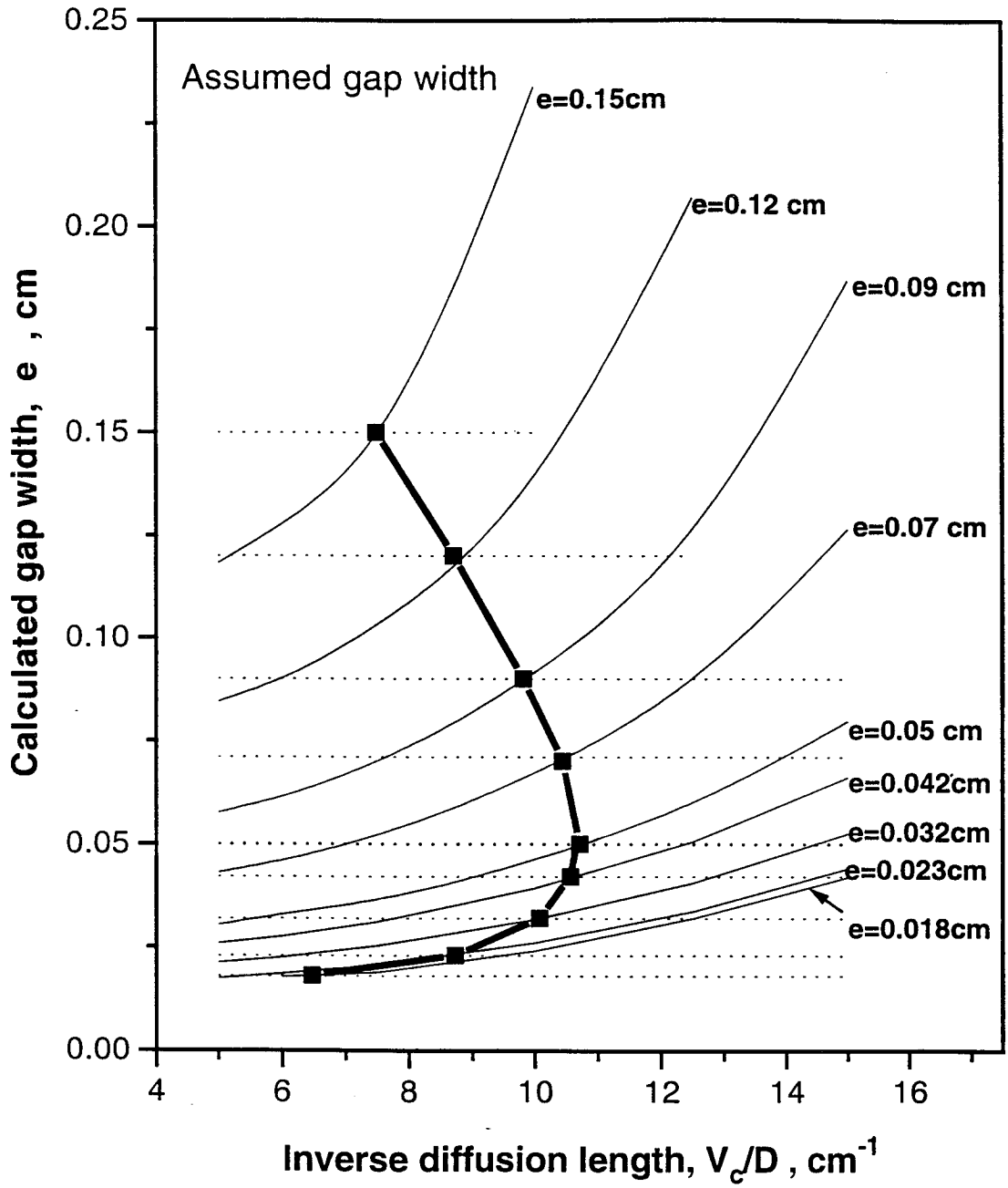
Assumed gap width
e=0.15cm
e=0.12 cm
e=0.09 cm
e=0.07 cm
e=0.05 cm
e=0.042cm
e=0.032cm
e=0.023cm
e=0.018cm
Calculated gap width, e , cm
Inverse diffusion length, V_c/D , cm^{-1}
0.25
0.20
0.15
0.10
0.05
0.00
4
6
8
10
12
14
16

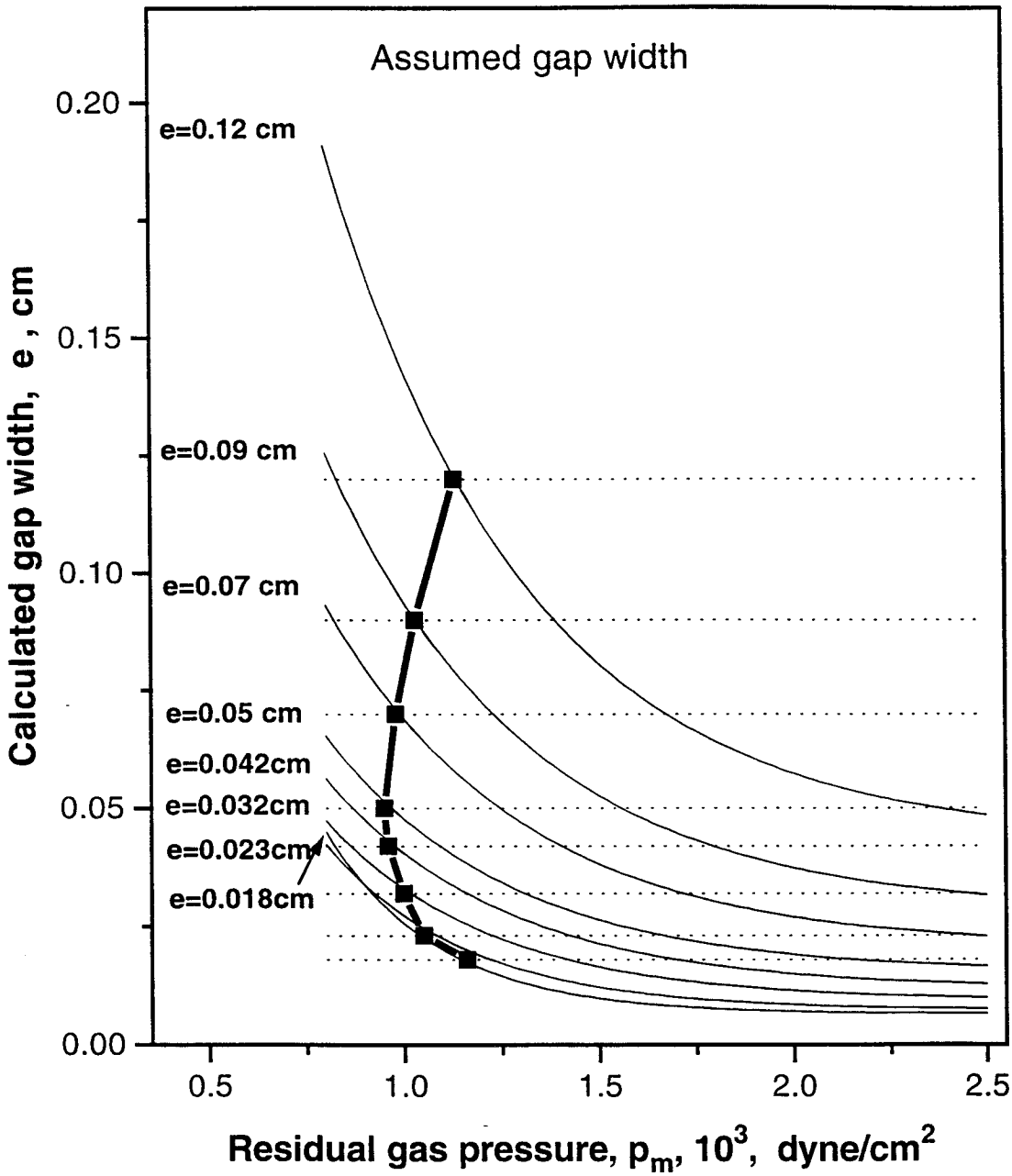
Assumed gap width
0.20
0.15
0.10
0.05
0.00
e=0.12 cm
e=0.09 cm
e=0.07 cm
e=0.05 cm
e=0.042cm
e=0.032cm
e=0.023cm
e=0.018cm
0.5
1.0
1.5
2.0
2.5
Calculated gap width, e , cm
Residual gas pressure, p_m, 10^3, dyne/cm^2

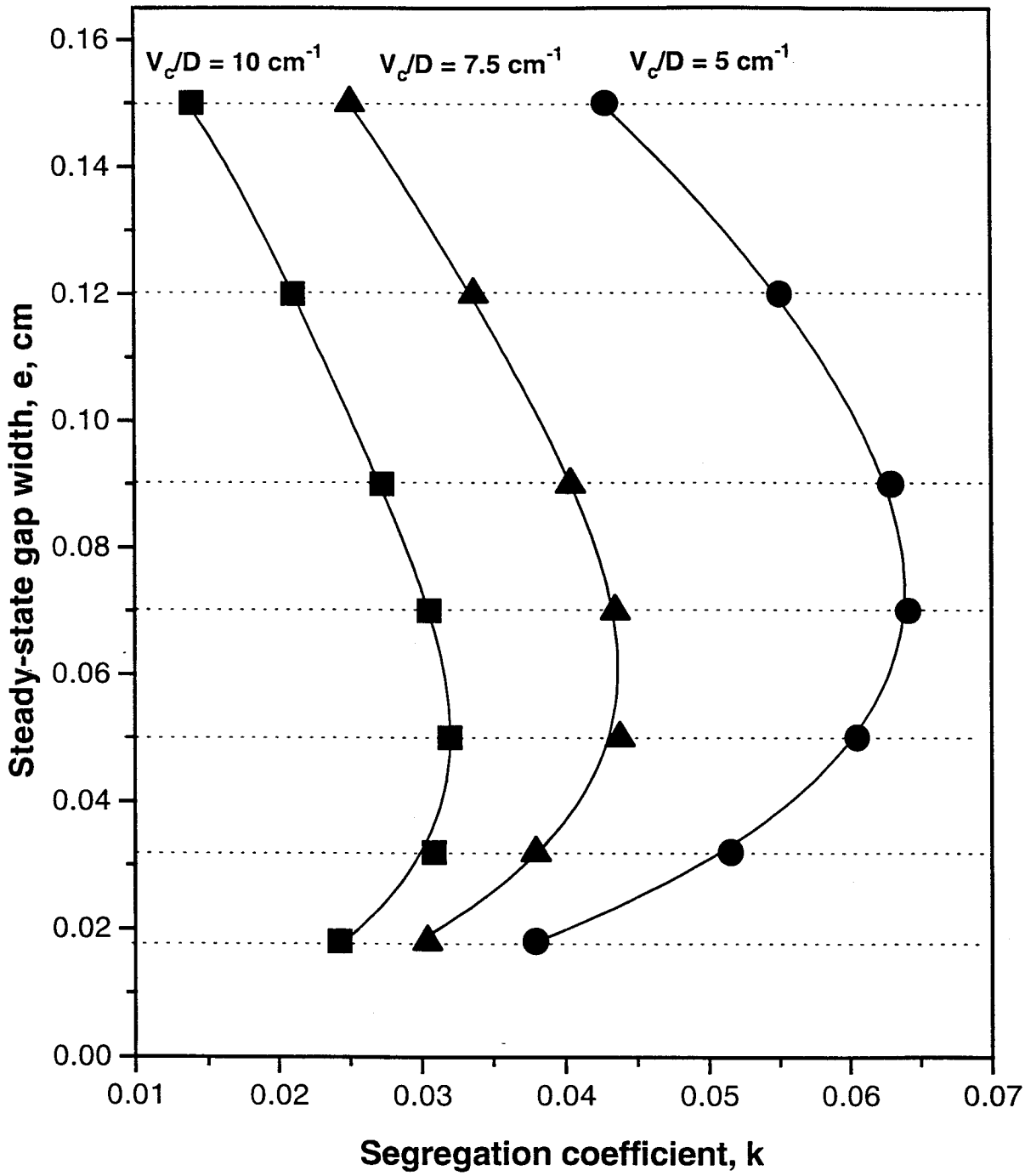
V_c/D = 10 cm^{-1}
V_c/D = 7.5 cm^{-1}
V_c/D = 5 cm^{-1}
Steady-state gap width, e, cm
0.16
0.14
0.12
0.10
0.08
0.06
0.04
0.02
0.00
0.01
0.02
0.03
0.04
0.05
0.06
0.07
Segregation coefficient, k

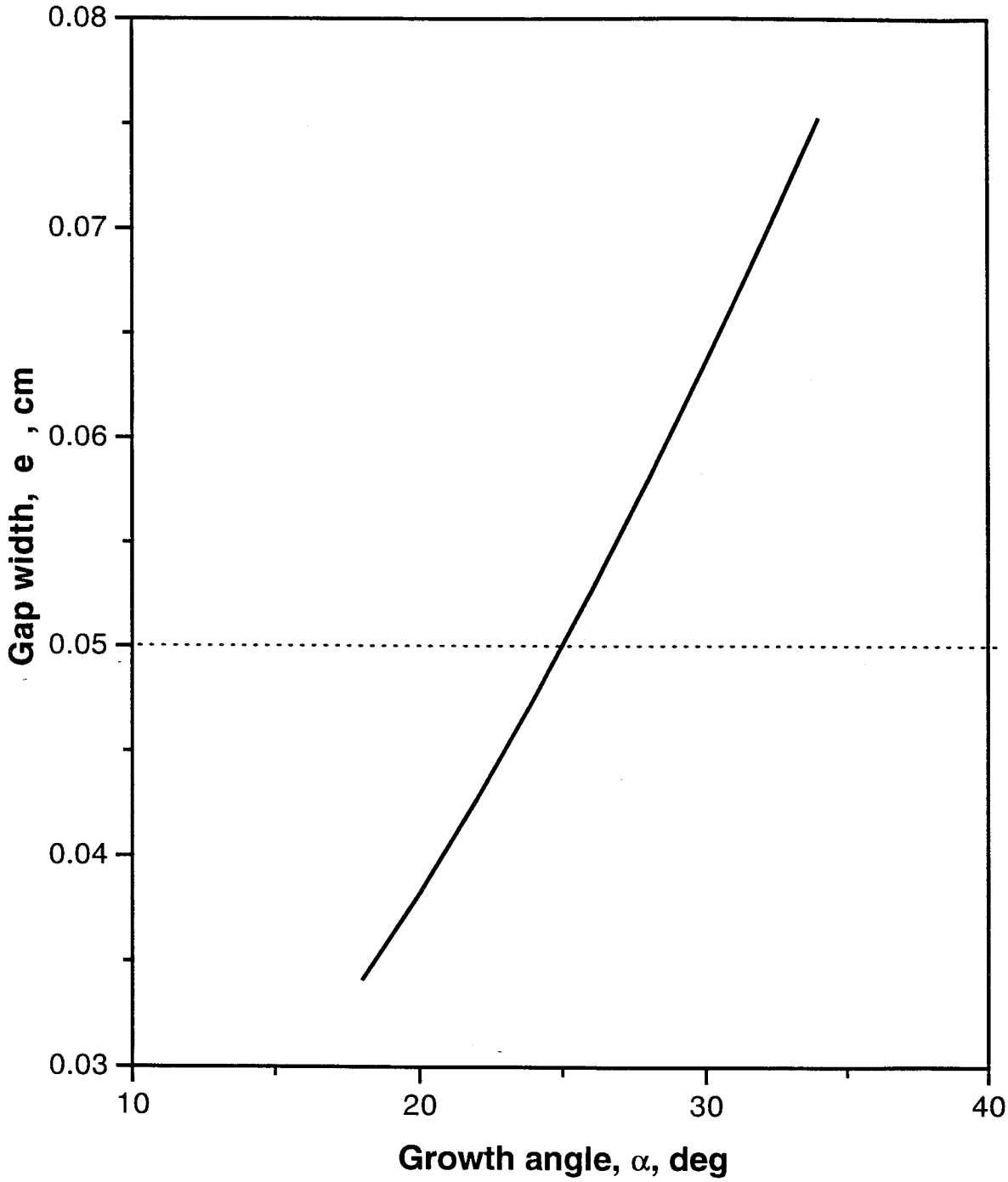
0.08
0.07
0.06
0.05
0.04
0.03
Gap width, e , cm
10
20
30
40
Growth angle, α, deg

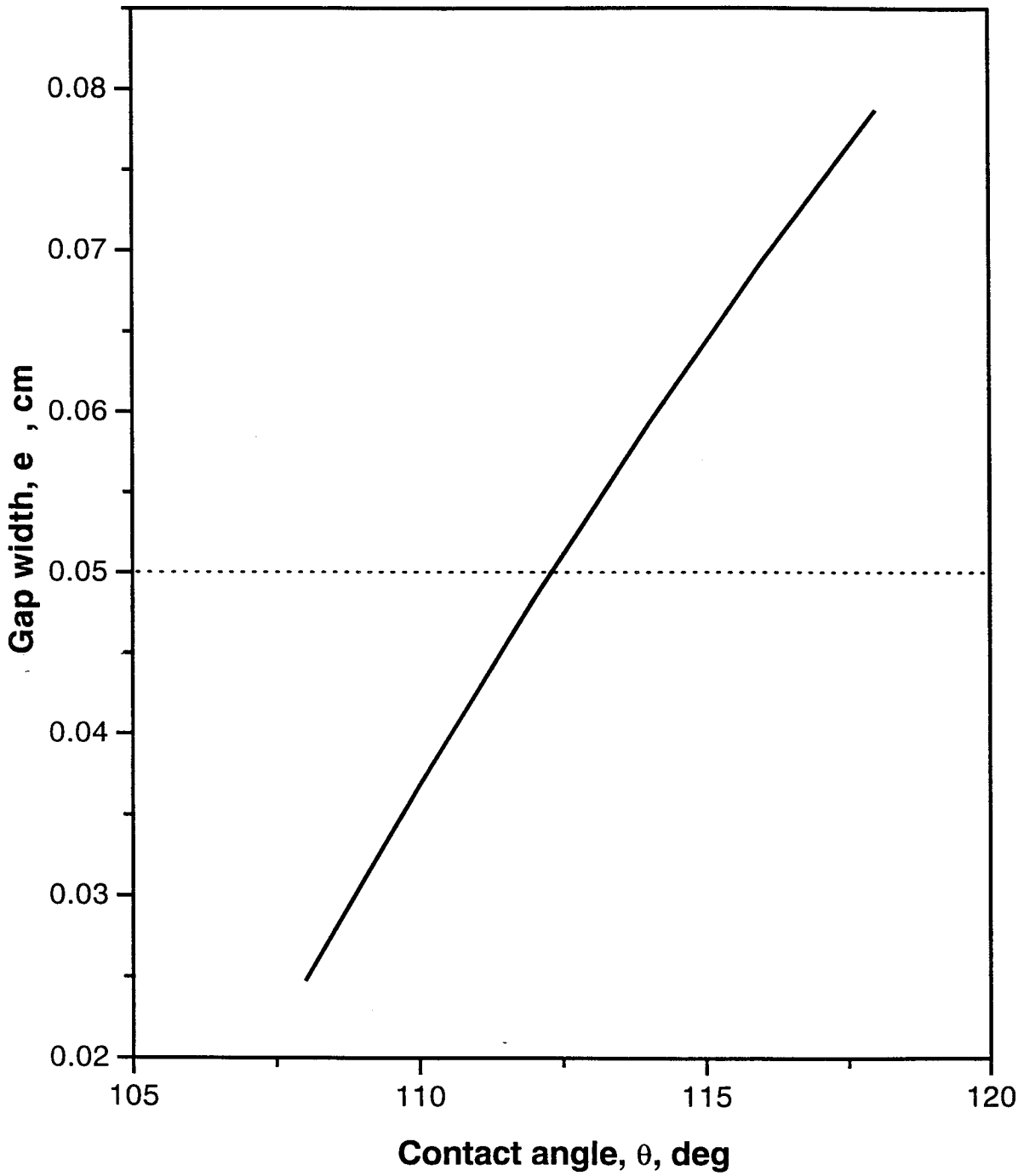
0.08
0.07
0.06
0.05
0.04
0.03
0.02
Gap width, e , cm
105
110
115
120
Contact angle, θ, deg

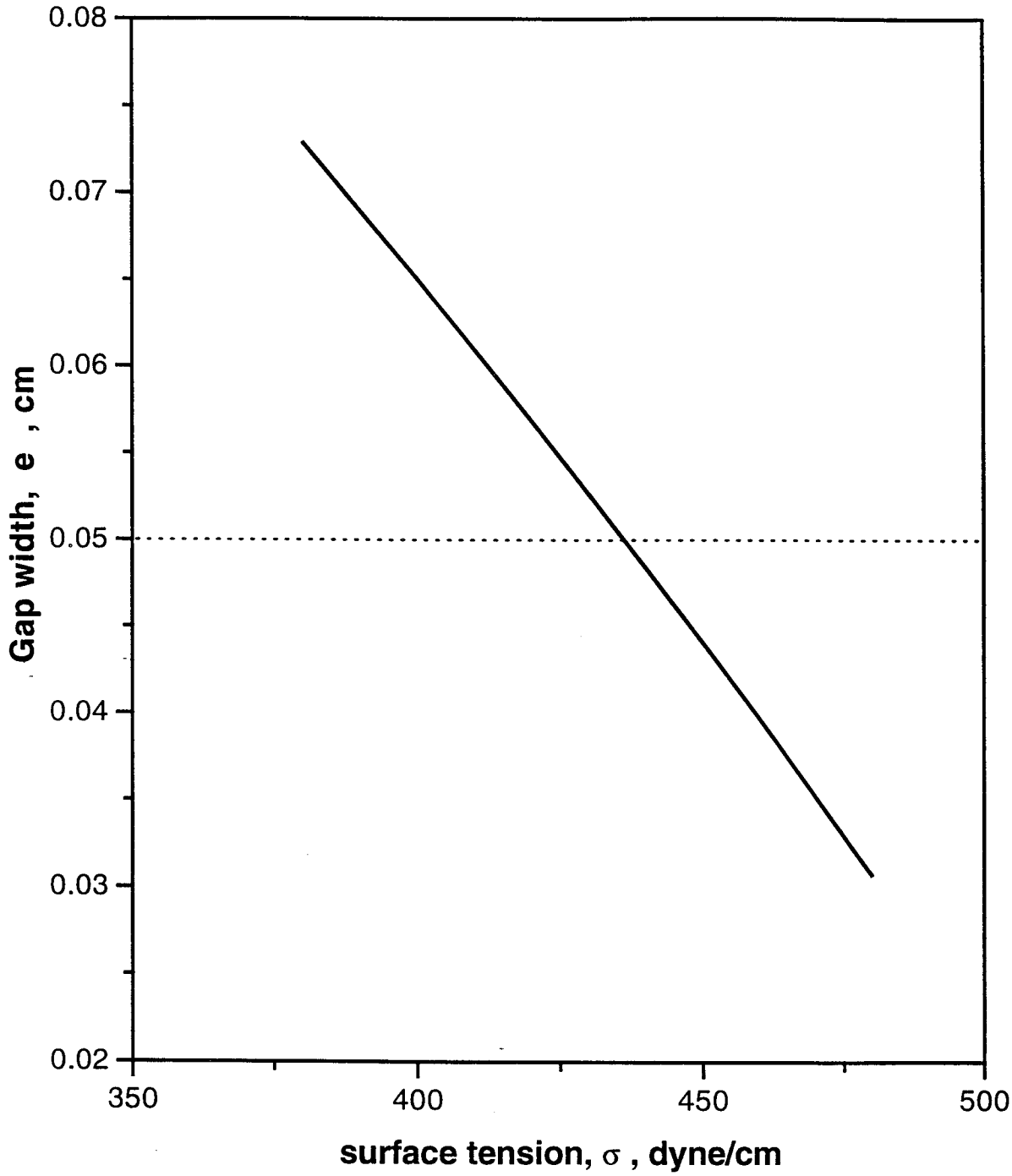
0.08
0.07
0.06
0.05
0.04
0.03
0.02
Gap width, e , cm
350
400
450
500
surface tension, σ , dyne/cm

ATTACHMENT F.

Detached Solidification: 2. Stability

DMITRI I. POPOV[1], LIYA L. REGEL[1,a] and WILLIAM R. WILCOX[1]

1. International Center for Gravity Materials Science and Applications

Clarkson University, Potsdam, NY 13699-5814, USA

Tel: 315-268-7672, Fax: 315-268-3833

e-mail: regel@agent.clarkson.edu

http://www.clarkson.edu/~regel/center.html

a. To whom correspondence should be addressed

Detached Solidification: Stability

Abstract

A new mechanism for detached solidification (Figure 1) in space was described in [1]. In [2] we presented a steady state numerical model for convection in the melt and transport of dissolved gas. In this paper the stability of the steady-state configuration was studied. Perturbations in pressure, gap width and solidification rate were considered. For this purpose, the concentration field of dissolved gas (found in [2]) was subjected to perturbations and the response was investigated. The temperature field in the system was found in the present work, and its changes due to perturbations in gap width and solidification rate were studied. It was assumed that small changes in pressure in the gap, and the gap length itself, do not affect the temperature field. The results show that at zero gravity, stable steady-state growth is possible. The analysis predicts stable detached solidification for some distance. This critical distance for the onset of instability is larger for larger gap widths. Dissolved gas transport into the gap stabilizes the steady-state detached configuration for short gap length. Heat transfer in the system influences the local solidification rate and acts as a stabilizing force for distances on the order of the sample diameter.

Keywords: crystal growth, gas diffusion, temperature field, stability.

1. INTRODUCTION

The stability of solidification processes involving a free melt surface has been studied in many papers. Most interest in stability has been for the Czochralski technique. For example, the shape and stability of the meniscus during Czochralski growth were studied by means of numerical methods by Mika & Uelhoff [3]. They determined the stability of the roots of the Euler equation describing the geometry of the meniscus. Surek [4] considered Czochralski, floating zone and EFG techniques in his paper, with excluded thermal effects from the stability analysis. It was pointed out that the stability of the diameter of the crystal growing with a free melt surface is related to the stability of the meniscus shape. If the perturbation in diameter is such that the angle α^1 approaches the crystal growth angle α_0 [2], the result is a new steady-state condition. On the other hand, if the change in

[1] The angle between the free melt surface and the x-axis at the three-phase line (see Figure 2).

[2] The angle between the free melt surface and the displacement line of the growing crystal.

diameter is such that α deviates even more from α_0, the crystal diameter is unstable. Padday & Pitt [5] treated the problem of stability based on an energy balance at the meniscus surface. The analysis of stability and control of Czochralski growth, based on a similar approach, was considered in [6],[7] and [8]. A dynamic model was obtained by means of a combined solution of thermal and capillary problems, based on conservation of mass and energy, and a constant growth angle α_0.

The diffusion of a volatile species (e.g. dissolved gas) across the free melt surface in Czochralski and EFG crystal growth is not important for stability of those systems because it has no effect on the pressure over the meniscus and, hence, the shape of the meniscus. Transport of a dissolved gas becomes important in the development of gas bubbles, gas pores, or a gap between the ampoule wall and the crystal in Bridgman growth (detached solidification.) The stability of a gas pore forming in a growing crystal was discussed in [9]. Thermal effects were neglected, while capillarity and gas diffusion were considered. Stability was studied for the response of the system to a deviation from the equilibrium growth angle and the concentration of volatile species at the gas/liquid surface of a pore. The rate of gas concentration change in the pore was found by taking into consideration the rate of gas flow across the melt/gas suraface and the rate of pore volume change. In the case of detached solidification (Figure 1), Duffar [10] claimed that the gap is unstable with respect to changes in the meniscus shape. Neither thermal effects nor the possibility of gas transport into the gap were taken into account.

Regel and Wilcox [1] proposed a model for detached solidification, which is shown schematically in Figure 1. The presence in the melt of one or more volatile components, such as dissolved gas, is an essential feature of this model. This gas concentrates near the freezing interface because of rejection by the growing solid (impurity segregation). At steady state, the dissolved gas diffuses into the gap across the liquid meniscus connecting the crystal with the ampoule at a constant rate. If the value of this flux is enough to maintain a constant pressure difference across the meniscus, the gap width is constant and we have steady-state detached solidification [2].

In the present paper, we show the significance of dissolved gas transport and heat transport for stability of the steady-state detached configuration. We carried out a dynamic stability analysis based on the system response to infinitesimal perturbations of system parameters. We formulated a set of dynamic equations, with respect to the

variations of the system parameters. For this purpose, the steady state energy equation was considered and the temperature field was obtained for a number of steady-state gap widths. The response of the temperature field to perturbations in parameters was determined from the change of interface position. The response of the concentration field of dissolved gas in the melt was related to the change of total gas flux across the meniscus surface.

2. MATHEMATICAL MODEL

The stability of this dynamic system was studied by the method of Liapunov [11]. This method deals with stability criteria on the basis of a variational approach. Consider a system that exhibits steady state behavior under some conditions. The question of stability arises when the conditions are perturbed. Stability analysis is concerned with the rate of change of perturbed behavior.

We consider a system described by:

$$\frac{d\vec{x}}{dt} = M(\vec{x}, \vec{f}, t) \tag{1}$$

where t is time, $\vec{f}$ is the vector of forcing functions, $\vec{x}$ is the vector of variables of interest. The goal is to analyze the deviations about some fixed trajectory $\vec{x}_0$. If the system is time invariant, it lacks an explicit time dependence. The superposition principle is valid for a dynamic system, when the system is linear and the function M($\vec{x}$, $\vec{f}$,t) is a linear function of $\vec{x}$. However, it is known that a non-linear system behaves similarly to a linear system in a sufficiently small neighborhood about equilibrium. So, it is always possible to determine the stability of a nonlinear system by applying linear methods. The linearized equation will be:

$$\frac{d\vec{x}}{dt} = \left(\frac{\partial M_j(t)}{\partial x_k}\right)\vec{x} + \left(\frac{\partial M_j(t)}{\partial f_k}\right)\vec{f} \tag{2}$$

If the system is time invariant, the matrices $\frac{\partial M_j}{\partial x_k}$ and $\frac{\partial M_j}{\partial f_k}$ are constant. Considering the autonomous case (no forcing functions), stability is observed when all the roots γ in the characteristic equation

$$\left| \frac{\partial M_j}{\partial x_k} - \gamma \delta_{jk} \right| = 0 \tag{3}$$

have negative real components [11]. Here δ_{jk} is the delta function.

3. PROBLEM FORMULATION

3.1. Gas Flux. Rate of Pressure Change.

The steady-state concentration field for gas dissolved in the melt and the gas flux for different values of processing parameters (growth rate, pressure of backfilled gas, gap width) were calculated in [2]. Taking into consideration the axial symmetry of the physical domain, we used the two-dimensional flux j_{mol} :

$$j_{mol} = \frac{J_{mol}}{2\pi (R_a - \frac{e}{2})} \tag{4}$$

where J_{mol} is the total gas flux. The dependence of j_{mol} on the gap width e for different diffusion lengths D/V_c was shown in Figure 6 of [2]. All of those results were obtained from the solution of the steady state diffusion equation in the melt. We showed in [2] that the rate of pressure change in the gap is:

$$\frac{dp_g}{dt} = \frac{RT_{avg}}{\pi e(2R_a - e)L} J_{mol} - \frac{p_g}{L}\frac{dL}{dt} - p_g \frac{2(R_a - e)}{e(2R_a - e)}\frac{de}{dt} \tag{5}$$

where R is the ideal gas constant, L is the gap length, e is the gap width, R_a is the ampoule radius, and T_{avg} is the average gas temperature in the gap. The value and the sign of the first term depend on the concentration field of dissolved gas in the melt. The second term describes the increase in the gap volume due to growth, while the third is due to the increase in gap width.

3.2. Temperature field

The time-independent axisymmetric form of the energy equation, assuming constant physical properties, used in the numerical calculations was:

$$k_i\left(\frac{1}{r}\frac{\partial}{\partial r}\left(r\frac{\partial T}{\partial r}\right)+\frac{\partial^2 T}{\partial x^2}\right)=0 \qquad (6)$$

where T is the temperature (K), and k_i (i=s.m,a,g) is the thermal conductivity (erg/(cm*s*K)) of crystal, melt, ampoule material or gas, respectively. We neglected convective heat transfer in the melt since the Prandtl number of semiconductor melts is low (for InSb, modeled in the calculations, $Pr=\nu/\alpha=0.04$ near the melting point). The physical domain used for the numerical calculations is shown in Figure 3.

The position and shape of the melt/crystal interface were determined from the following two boundary conditions at the solidification interface:

$$T|_{int} = T_f$$
$$k_s\left.\frac{\partial T}{\partial x}\right|_{int} - k_l\left.\frac{\partial T}{\partial x}\right|_{int} = Q V_c \qquad (7)$$

where T_f is the melting point of the material (K), Q is the latent heat of fusion per unit volume (positive for solidification and negative for melting), and V_c is the growth rate. The other boundary conditions are:

$$\text{At } r = R_s \text{ (outer ampoule wall)}, \quad k_a\frac{\partial T}{\partial r} = -h(T - T_0) \qquad (8)$$

where h is the heat transfer coefficient between the ampoule (quartz here) and the furnace wall, and T_0 is the furnace temperature, assumed to vary linearly from T_c to T_h (constant gradient). The value of the heat transfer coefficient used in the calculations is $2*10^6$ erg s^{-1} cm^{-2} K^{-1}.

At $r = R_a$ (inner ampoule wall), R_g ($R_g = R_a$-e), and the meniscus:

$$k_i\frac{\partial T}{\partial n} = k_j\frac{\partial T}{\partial n} \qquad (9)$$

where i,j refer to the two phases that meet at the boundary and n is the direction normal to the boundary.

$$\text{At } x = 0, \quad T = T_c \text{ (780 K), and at } x = L_a, \; T=T_h \text{ (820 K)} \qquad (10)$$

Equation (6) together with the thermal boundary conditions (7-10) were put into finite difference codes (see Appendix).

Heat transfer across the gap was assumed to be purely by conduction. This assumption is not a bad approximation at the melting point of InSb (525 ^{0}C). After the calculation had been done, the heat flux across the gap was estimated. It turned out that for e = 0.05 cm, the radiative heat flux is 10-20% of the conductive heat flux. For high melting point materials or larger gap widths it would be necessary to consider radiative heat transfer.

3.3. Analysis of the Stability of the Steady-State Detached Configuration

We applied the concepts described in Section 2 to study the stability of the steady-state detached configuration. Besides perturbations in the angle α, we also considered changes in the diffusion flux J_{mol} of gas from melt into the gap across the meniscus and perturbations in the temperature field. The perturbations in the angle α, the gas flux and the temperature field were related to the rate of change in the gap width e, the pressure p_g in the gap, and the gap length L. In a system with three degrees of freedom, small deviations from the steady value of the gap width e, pressure p_g in the gap, and gap length L were represented by equations (1) and (2) with time-independent $\frac{\partial M_j}{\partial x_k}$ and $\frac{\partial M_j}{\partial f_k} = 0$.

Let us consider the dynamic behavior of the gap width e, pressure p_g in the gap and gap length L, subjected to infinitesimal perturbations from their equilibrium values. The rate of change of a perturbation in gap width, $d(\delta e)/dt$, is governed by the change in solidification rate V_c near the three-phase line and the deviation of the angle α from the growth angle α_0. The rate of change of pressure perturbation, $d(\delta p_g)/dt$, depends on the change in gas flux J_{mol} across the meniscus and the change of gap volume. The rate of change of a perturbation in gap length, $d(\delta L)/dt$, depends on the change in solidification rate V_c. A change in V_c leads to a change of temperature field near the meniscus. The temperature field changes due to the resulting change in gap width and to the thermal balance at the freezing interface. So, the dynamic behavior of the system, describing the response to infinitesimal perturbations, can be described by internal perturbations only (no forcing function). Forcing functions would appear in response to an external influence on the system, e.g. a change in temperature gradient in the furnace, and are not considered here.

Taking into account the discussion above, the governing set of differential equations is:

$$d(\delta e)/dt = a_{ee}(\delta e) + a_{ep}(\delta p_g) + a_{eL}(\delta L)$$
$$d(\delta p_g)/dt = a_{pe}(\delta e) + a_{pp}(\delta p_g) + a_{pL}(\delta L)$$
$$d(\delta L)/dt = a_{Le}(\delta e) + a_{Lp}(\delta p_g) + a_{LL}(\delta L) \qquad (11)$$

where δe is the perturbation in gap width, δp_g is the perturbation in pressure in the gap, and δL is the perturbation in gap length.

The characteristic equation, which governs stability of the detached configuration, has the form:

$$f(\gamma) = \gamma^3 + b\gamma^2 + c\gamma + d = 0 \qquad (12)$$

where:

$$b = -(a_{ee} + a_{pp} + a_{LL})$$
$$c = a_{ee}a_{pp} + a_{ee}a_{LL} + a_{pp}a_{LL} - a_{eL}a_{Le} - a_{pL}a_{Lp} - a_{ep}a_{pe}$$
$$d = a_{ee}a_{pL}a_{Lp} + a_{pp}a_{eL}a_{Le} + a_{LL}a_{ep}a_{pe} - a_{ee}a_{pp}a_{LL} - a_{ep}a_{pL}a_{Le} - a_{eL}a_{pe}a_{Lp} \qquad (13)$$

The detached configuration is stable when all the roots of $f(\gamma)$ in the characteristic equation (12) have negative real components. The configuration is unstable if one or more of the roots of (12) has a positive real component. If the roots are purely imaginary, higher order terms are necessary [11] to provide further information about the eigenvalues γ of the characteristic equation.

3.4. Determination of a_{ij} coefficients

The rate of change of gap width can be derived from geometrical considerations (see Fig.2). It is given by:

$$de/dt = -V_c \cdot \tan(\alpha - \alpha_0) \qquad (14)$$

where de/dt is the rate of change of e. The variation of de/dt is:

$$\delta(de/dt) = -\delta(V_c \cdot \tan(\alpha - \alpha_0)) \approx -V_c \cdot \delta\alpha - \tan(\alpha - \alpha_0) \cdot \delta V_c \qquad (15)$$

The last term in (15) is zero to the first approximation, since $\alpha - \alpha_0$ is near zero. The previous expression can be rewritten as:

$$d(\delta e)/dt = -V_c \cdot \left(\frac{\partial \alpha}{\partial e}\delta e + \frac{\partial \alpha}{\partial p_g}\delta p_g \right) \qquad (16)$$

The partial derivatives in (16) are:

$$\frac{\partial \alpha}{\partial e} < 0 \qquad ; \qquad \frac{\partial \alpha}{\partial p_g} < 0 \tag{17}$$

The validity of the first inequality in (17) can be seen from Figure 2. The negative sign of that derivative indicates the capillary instability of the detached configuration, pointed out by Duffar [10]. The second inequality originates from the Laplace-Young equation when a perturbation in pressure occurs. The Laplace-Young equation for detached solidification is [10]:

$$e = \frac{\sigma}{\Delta p} \cdot (\cos\alpha + \cos\theta) \tag{18}$$

and is valid not only for the steady-state gap width e_{st} but for any e. In the general case, equation (18) relates e to the angle α, which is not necessarily equal to the growth angle α_0. The partial derivative $\partial\alpha/\partial e$ can be found by differentiating equation (18):

$$\frac{\partial \alpha}{\partial e} = -\frac{\cos\alpha + \cos\theta}{e \cdot \sin\alpha} \tag{19}$$

Carrying out partial differentiation with respect to p_g , we obtain:

$$\frac{\partial \alpha}{\partial p_g} = -\frac{e}{\sigma \sin\alpha} \tag{20}$$

The coefficients a_{pe} and a_{pp} can be found by applying the variation procedure to the equation for the rate of pressure change (equation (5)):

$$d(\delta p_g)/dt = \delta\left(\frac{RT_{avg}}{V} J_{mol} - \frac{p_g}{L} V_c - p_g \frac{2(R_a - e)}{e(2R_a - e)} \frac{de}{dt}\right) = \frac{RT_{avg}}{\pi e(2R_a - e)L}\left(\frac{\partial J_{mol}}{\partial e}\delta e + \frac{\partial J_{mol}}{\partial p_g}\delta p_g + \frac{\partial J_{mol}}{\partial V_c}\delta V_c\right)$$
$$-\frac{RT_{avg}}{\pi e(2R_a - e)L^2} J_{mol}\delta L - \frac{RT_{avg}}{\pi L} \cdot \frac{2(R_a - e)}{e^2(2R_a - e)^2} \cdot J_{mol}\delta e - \frac{V_c}{L}\delta p_g - \frac{p_g}{L}\delta V_c + \frac{p_g V_c}{L^2}\delta L - p_g \frac{2(R_a - e)}{e(2R_a - e)} d(\delta e)/dt \tag{21}$$

Recalling that V_c=dL/dt and using (16) we find that:

$$d(\delta p_g)/dt = \frac{RT_{avg}}{\pi e(2R_a - e)L}\left(\frac{\partial J_{mol}}{\partial e}\delta e + \frac{\partial J_{mol}}{\partial p_g}\delta p_g + \frac{\partial J_{mol}}{\partial V_c}\delta \dot{L}\right) - \frac{RT_{avg}}{\pi e(2R_a - e)L^2} J_{mol}\delta L$$
$$-\frac{RT_{avg}}{\pi L} \cdot \frac{2(R_a - e)}{e^2(2R_a - e)^2} \cdot J_{mol}\delta e - \frac{V_c}{L}\delta p_g - \frac{p_g}{L}\delta \dot{L} + \frac{p_g V_c}{L^2}\delta L - p_g \frac{2(R_a - e)}{e(2R_a - e)}\left[a_{ee}\delta e + a_{ep}\delta p\right] \tag{22}$$

The dependence of the rate of change of gap length on gap width (dL/dt(e)) and gap length (dL/dt(L)) was found by solving the temperature field near the moving solidification interface. With a change in gap width, the temperature field near the meniscus changes (Figure 5). The solidification interface either slows down or accelerates, affecting dL/dt. Furthermore, the change of position of the solidification interface is coupled to the change in solidification rate through the boundary condition for the temperature field at the freezing interface (equation (7)). The sensitivity of the gap length to perturbations in gap width and solidification rate can be written in the limit $\delta t \rightarrow 0$, where t is time. Therefore,

$$\delta L = \frac{\partial L}{\partial T}\frac{\partial T}{\partial e}\delta e + \frac{\partial L}{\partial T}\frac{\partial T}{\partial V_c}\delta V_c \tag{23}$$

A numerical calculation gives $\partial L/\partial e$ and $\partial L/\partial V_c$. Expression (23) can be rewritten as:

$$\delta L = \frac{\partial L}{\partial e}\delta e + \frac{\partial L}{\partial V_c}\delta\frac{dL}{dt} \quad \Rightarrow \delta\frac{dL}{dt} = -\frac{\partial L/\partial e}{\partial L/\partial V_c}\delta e + \frac{1}{\partial L/\partial V_c}\delta L \tag{24}$$

Substituting this expression into (24), we obtain:

$$\begin{aligned} d(\delta p_g)/dt = \{ & \frac{RT_{avg}}{\pi e(2R_a - e)L}\left(\frac{\partial J_{mol}}{\partial e} - \frac{\partial L/\partial e}{\partial L/\partial V_c}\frac{\partial J_{mol}}{\partial V_c}\right) + \frac{\partial L/\partial e}{\partial L/\partial V_c}\frac{p_g}{L} - \frac{RT_{avg}}{\pi eL}\cdot\frac{2(R_a - e)}{e^2(2R_a - e)^2}J_{mol} \\ & - p_g\frac{2(R_a - e)V_c}{e^2(2R_a - e)}\frac{\cos(\alpha)+\cos(\theta)}{\sin(\alpha)}\}\delta e + \{\frac{RT_{avg}}{\pi e(2R_a - e)L}\frac{\partial J_{mol}}{\partial p_g} - \frac{V_c}{L} \\ & p_g\frac{2(R_a - e)}{(2R_a - e)}\frac{V_c}{\sigma\sin(\alpha)}\}\delta p_g + \{\left(\frac{RT_{avg}}{\pi e(2R_a - e)L}\frac{\partial J_{mol}}{\partial V_c} - \frac{p_g}{L}\right)\frac{1}{\partial L/\partial V_c} + \frac{p_g V_c}{L^2}\}\delta L \end{aligned} \tag{25}$$

According to these calculations, the coefficients a_{ij} are given by:

$$a_{ee} = \frac{V_c}{e}\frac{\cos\alpha + \cos\theta}{\sin\alpha} \quad ; \quad a_{ep} = \frac{V_c e}{\sigma \sin\alpha} \quad ; \quad a_{eL} = 0 \quad ; \quad a_{Le} = -\frac{\partial L/\partial e}{\partial L/\partial V_c} \quad ; \quad a_{Lp} = 0 \quad ; \quad a_{LL} = \frac{1}{\partial L/\partial V_c} \quad ;$$

$$a_{pe} = \frac{RT_{avg}}{eL}\left[\frac{\partial j_{mol}}{\partial e} - \frac{\partial L/\partial e}{\partial L/\partial V_c}\frac{\partial j_{mol}}{\partial V_c} - \frac{2(R_a - e)}{e(2R_a - e)} j_{mol}\right] + \frac{\partial L/\partial e}{\partial L/\partial V_c}\frac{p_g}{L} - p_g \frac{2(R_a - e)}{e(2R_a - e)} a_{ee} \quad ;$$

$$a_{pp} = \frac{RT_{avg}}{eL}\frac{\partial j_{mol}}{\partial p_g} - \frac{V_c}{L} - p_g \frac{2(R_a - e)}{e(2R_a - e)} a_{ep} \quad ; \quad a_{pL} = \left[\frac{RT_{avg}}{eL}\frac{\partial j_{mol}}{\partial V_c} - \frac{p_g}{L}\right]\frac{1}{\partial L/\partial V_c} + \frac{p_g V_c}{L^2} \qquad (26)$$

Since we studied the stability of the steady state, with a gap length of the order of the crystal radius, we assumed that the temperature field does not change due to a small change in gap length, i.e. $a_{eL} = 0$. The partial derivatives dL/de and dL/dV_c were found from numerical calculations perturbing the gap width and solidification rate and studying the influence of the perturbation on the position of the freezing interface near the meniscus. Using the results in equation (26), several terms can be dropped in system (13) to yield:

$$\begin{aligned} b &= -(a_{ee} + a_{pp} + a_{LL}) \\ c &= a_{ee}a_{pp} + a_{ee}a_{LL} + a_{pp}a_{LL} - a_{ep}a_{pe} \\ d &= a_{ee}a_{pL}a_{Lp} - a_{ee}a_{pp}a_{LL} - a_{ep}a_{pL}a_{Le} \end{aligned} \qquad (27)$$

4. RESULTS

The stability analysis was done for different steady-state gap widths, solving equation (12) with the coefficients a_{ij} from (26). The partial derivatives $\partial j_{mol}/\partial e$ and $\partial j_{mol}/\partial p_g$ and $\partial j_{mol}/\partial V_c$ were determined numerically, solving the mass transfer equation near steady-state. The partial derivatives $\partial L/\partial e$ and $\partial L/\partial V_c$ were determined by solving for the temperature field and tracing the interface position near the meniscus with respect to infinitesimal perturbations in gap width e and solidification rate V_c. Table 1 shows the numerically calculated values of the gas flux j_{mol} and its three partial derivatives, together with the partial derivatives of the gap length.

Typical behavior of the characteristic function $f(\gamma)$ is shown in Figure 5 for two different values of the gap width, e_{st}=0.05 cm and e_{st}=0.15 cm. From the analysis of the behavior of $f(\gamma)$ we conclude that wider gaps are more stable than narrow ones. The conditions for stability are also sensitive to the value of the gap length L. Figures 6 and 7 show the dependence of the roots of $f(\gamma)$ on the gap length L for e_{st} = 0.05 cm and e_{st} = 0.15 cm, respectively.

The coefficient b in equation (12) is always positive. The stability criterion in this case is controlled by a 'feedback' coefficient, c (equation (27)). The terms $a_{ee}a_{LL}$ and $a_{pp}a_{LL}$ are on the order of 10^{-5} - 10^{-3} for large gap length (L > 0.1 cm). The value of the term $a_{ee}a_{pp}$ in (27) is smaller (~10^{-7} - 10^{-5}) than the other terms, and so it does not rule the stability criterion near the onset of instability. For e = 0.05 cm, the value of the gap length where stability fails is $L_{critical}$ = 0.77 cm; for e = 0.15 cm, $L_{critical}$ = 3.25 cm. Although the term $-a_{ep}a_{pe}$ is on the order of 10^{-5} to 10^{-4} for large gap length, it is critical near the onset of instability. The dependence of the three terms on the gap length L is shown in Figure 8. To have a stabilization effect, the term $-a_{ep}a_{pe}$ in equation (27) must be positive. Since a_{ep} is always positive, a_{pe} must have a negative value for stability. From analysis of the terms for a_{pe} in (26) it can be concluded that all the contributions to a_{pe} from gas flux perturbations have a negative sign and so are stabilizing. The pressure has a destabilizing character. Since a_{ep} does not depend on gap length L, according to (26), $-a_{ep}a_{pe} \sim 1/L$, whereas $a_{ee}a_{LL}$ is constant vs. L. The largest term in a_{pe} (equation (26)), which gives the largest contribution to stabilization, is the response of the dissolved gas flux to a perturbation in solidification rate. So, perturbations in solidification rate turn out to be more critical to the gas flux across the meniscus than perturbations in the gap width or pressure. The response of the system to perturbations in solidification rate are stabilizing. Now it is understandable, why wider gaps (large e) are stable over a longer distance (large $L_{critical}$) than narrower gaps. The equilibrium pressure p_g for narrower gaps is larger, according to (18). So, the destabilizing term in a_{pe} is larger than for wider gap width. The response of gas flux to perturbations in gap width and solidification rate is not so pronounced for narrow gaps as for wider ones, and cannot compensate for the rise of pressure due to a narrowing gap width.

With proceeding growth, the influence of gas transport on the rate of pressure change becomes less important with increasing gap volume, i.e. a_{pe} decreases with increasing L. Beyond a critical detached length $L_{critical}$ none of the mechanisms of gas transport are sufficient to stabilize steady-state growth. The response of the temperature field to perturbations in gap width and solidification rate is stabilizing, since the response of the interface position to a change in solidification rate gives a positive contribution to the b-coefficient in (27). Due to the large difference in thermal conductivity between a solid and a gas, a change in gap width changes the interface shape and position, thus affecting the solidification rate. The change in gap width causes the interface position to

decrease with increasing gap width, i.e. $\partial L/\partial e < 0$. This means that the temperature field does not allow the pressure in the gap to change drastically, since it preserves the gap volume to be nearly constant. Linear stability analysis in this case predicts $L_{critical}$ to be on the order of experimentally observed values [13-17], which is ~1- 3 cm for a gap width on the order of 0.05-0.1 cm. The trend of the critical value to increase with increasing gap width is seen from Figure 9. The deviation at small gap widths is probably due to numerical errors in calculating the gas flux and temperature field near the meniscus. This problem arises because for a smaller gap width, fewer gridpoints along the meniscus were used in the finite difference calculations. As a result, there was less accuracy in these numerical calculations.

5. CONCLUSIONS

A stability analysis of the steady-state detached configuration was carried out. Numerical analysis shows that a stable steady-state configuration can be achieved over a range of processing parameters. This analysis predicts stable detached solidification up to a critical gap length, which is larger for larger gap widths. With proceeding detached growth, the stability conditions deteriorate. Dissolved gas transport into the gap tends to stabilize the steady-state detached configuration, although no mechanism of gas transport is sufficient to provide stability for large gap length. Heat transfer in the system influences the local solidification rate at the three-phase line and, therefore, strongly affects the meniscus shape and stability. The variation in solidification rate due to a perturbation in the temperature field stabilizes the detached configuration. Therefore, heat transfer together with mass transfer act as stabilizing phenomena for detached solidification.

Acknowledgment

This research was supported by NASA's Microgravity Science and Applications Division under grant NAG8-1063.

REFERENCES

1. W.R. Wilcox and L.L. Regel, *Microgravity Sci. Technol.* **7**, 56-61(1995).

2. D.I. Popov, L.L. Regel and W.R. Wilcox, submitted to Journal of Materials Synthesis and Processing.

3. K. Mika and W. Uelhoff, *J. Crystal Growth*, **30** ,9-20 (1975).

4. T. Surek, *J. Appl. Phys.*, **47**,4384-4393(1976).

5. J.F. Padday and A.R. Pitt, *Phil.Trans.Royal Soc. London*, **A275**,489 (1973).

6. D.T.J. Hurle, *J. Crystal Growth*, **128**, 15- (1993).

7. D.T. Hurle, G.C. Joyce, M. Ghassempoory, A.B. Crowley, and E.J. Stern, *J. Crystal Growth* **100**,11-25(1990).

8. A.D. Myshkis, V.G. Babskii, N.D. Kopachevskii, L.A. Slobozhanin and A.D. Tyuptsov, in: Low-Gravity Fluid Mechanics, Springer, Berlin, 1987.

9. V.A. Tatarchenko, *J. Crystal Growth* **143**,294-300(1994).

10. T. Duffar, Private Communication, 1995, Centre d'Etudes Nucleaires, 85 X, F-38041, Grenoble, France.

11. D.D. Siljak, *Nonlinear Systems. The Parameter Analysis and Design* (John Wiley & Sons, Inc., NY, 1968.)

12. P.B. Kahn, *Mathematical Methods for Scientists & Engineers. Linear and Nonlinear Systems* (John Wiley & Sons Inc., NY, 1990).

13. A.F. Witt, H.C. Gatos, M. Lichtensteiger, M.C. Lavine, and C.J. Herman, *J. Electrochem.Soc.* **122**,276-283 (1975).

14. V.S. Zemskov and M.R. Raukhman, *Fizika I Khiniya Obrabotki Materialov*, **21**, 63-67(1987).

15. V.S. Zemskov, et.al., *Fiz. Khim. Obrab. Mater.* **5**(1983),56-65.

16. I.L. Shulpina, L.M. Sorokin, M.R. Raukhman, V.S. Zemskov, A.S. Tregubova, G.N. Mosina, and E.A. Kositsyna, *Sov. Phys.Solid State* **23**,#10(1981),1775-1778.

17. V.T. Khryapov, Yu.N. Dyakov, Ye.V. Markov, N.A. Kulchitsky, et.al., in: Materials Science in Space (IIET AN SSSR, Moscow 1982), pp.20-43.

18. L.N. Brush et al., *J. Crystal Growth* **102**(1990),725.

19. Y.S. Touloukian, R.W. Powell, C.Y. Ho, and P.G. Klemens, *Thermalphysical Properties of Matter*, V2-3, Thermal Conductivity, IFI/Plenum Data Corp., NY, 1970.

20. T. Duffar, I. Paret-Harter, and P. Dusserre, *J. Crystal Growth* **100**(1990),171-184.

21. I. Harter, P. Dusserre, T. Duffar, J.-Ph. Nabot, and N. Eustathopoulos, *J. Crystal Growth* **131**(1993),157-164.

APPENDIX

Finite-difference representation of the energy equation (6)

Equation (6) was solved using a finite difference representation on a nonuniform mesh. Having designated:

$$h_{i-1} = \Delta x_{i-1,i} \qquad h_{j-1} = \Delta r_{j-1,j}$$
$$h_i = \Delta x_{i,i+1} \qquad h_j = \Delta r_{j,j+1} \tag{A.1}$$

the finite difference representation of equation (6) was taken as:

$$T_{i,j} = \frac{\left(\frac{h_{i-1}}{h_i^2(h_{i-1}+h_i)}k_{i+\frac{1}{2},j} - \frac{(h_{i-1}-h_i)}{h_i^2(h_{i-1}+h_i)}k_{i,j}\right)\cdot T_{i+1,j} + \left(\frac{h_i}{h_{i-1}^2(h_{i-1}+h_i)}k_{i-\frac{1}{2},j} + \frac{(h_{i-1}-h_i)}{h_{i-1}^2(h_{i-1}+h_i)}k_{i,j}\right)\cdot T_{i-1,j} + \ldots}{\left(\frac{h_{i-1}}{h_i^2(h_{i-1}+h_i)}k_{i+\frac{1}{2},j} + \frac{h_i}{h_{i-1}^2(h_{i-1}+h_i)}k_{i-\frac{1}{2},j} - \frac{(h_{i-1}^2-h_i^2)}{h_i^2 h_{i-1}^2}k_{i,j} + \ldots\right.}$$

$$\frac{\ldots + \left(\frac{h_{j-1}}{h_j^2(h_{j-1}+h_j)}\frac{r_{j+\frac{1}{2}}}{r_j}k_{i,j+\frac{1}{2}} - \frac{(h_{j-1}-h_j)}{h_j^2(h_{j-1}+h_j)}k_{i,j}\right)\cdot T_{i,j+1} + \left(\frac{h_j}{h_{j-1}^2(h_{j-1}+h_j)}\frac{r_{j-\frac{1}{2}}}{r_j}k_{i,j-\frac{1}{2}} + \frac{(h_{j-1}-h_j)}{h_{j-1}^2(h_{j-1}+h_j)}k_{i,j}\right)\cdot T_{i,j-1}}{\ldots + \frac{h_{j-1}}{h_j^2(h_{j-1}+h_j)}k_{i,j+\frac{1}{2}} + \frac{h_j}{h_{j-1}^2(h_{j-1}+h_j)}k_{i,j-\frac{1}{2}} - \frac{(h_{j-1}^2-h_j^2)}{h_j^2 h_{j-1}^2}k_{i,j}\Big)} \tag{A.2}$$

where $i \pm \frac{1}{2}$ *and* $j \pm \frac{1}{2}$ are points in the mid-position between grid points (see Fig.A1). The thermal conductivity must be evaluated at those points. The position of the freezing interface was found by keeping the interface at constant temperature (first equality in (7)), and calculating the new interface position in each iteration cycle, using the second equality in (7) (see Fig.A2):

$$x_f = x_{i-1} + \frac{\tilde{Q} - \sqrt{\tilde{Q}^2 - 4QV_c\Delta x_{i-1,i}k_s(T_f - T_{i-1,j})}}{2QV_c} \tag{A.3}$$

where $\tilde{Q} = k_s(T_f - T_{i-1,j}) + k_l(T_{i,j} - T_f) + QV_c\Delta x_{i-1,i}$.

Outside the ampoule wall (in the furnace), a constant temperature gradient along the wall was assumed. The boundary condition used at that boundary was Newton's law of cooling with a heat transfer coefficient between quartz and gas. The finite difference representation of this boundary condition is:

$$T_{i,j_{max}} = \frac{\frac{4r_{j_{max}}}{\Delta r_{j_{max}-1,j_{max}}(2r_{j_{max}} + \Delta r_{j_{max}-1,j_{max}})}\cdot T_{i,j_{max}-1} + \frac{h}{k_a}\cdot T_0(x)}{\frac{4r_{j_{max}}}{\Delta r_{j_{max}-1,j_{max}}(2r_{j_{max}} + \Delta r_{j_{max}-1,j_{max}})} + \frac{h}{k_a}} \tag{A.4}$$

At the boundaries of different phases, continuity of heat flux was utilized.

The temperature at every boundary, where the constant temperature is not specified, was recalculated from the temperatures in the bulk of phases every iteration cycle.

Table 1. Parameters used in the stability analysis.

Parameters	Symbol	Value	Reference
Thermal conductivity of InSb melt	k_l	$1.3*10^6$ erg/(cm*K*s)	[18]
Thermal conductivity of InSb solid	k_s	$4.6*10^5$ erg/(cm*K*s)	[18]
Thermal conductivity of quartz	k_a	$3.1*10^5$ erg/(cm*K*s)	[19]
Thermal conductivity of gas in the gap	k_g	$2*10^4$ erg/(cm*K*s)	assumed
Heat transfer coefficient between ampoule wall and the furnace wall	h	$2*10^6$ erg/(cm^2*K*s)	assumed
Latent heat of solidification per unit volume of InSb	Q	$1.3*10^{10}$ erg/cm^3	[18]
Diffusion coefficient of dissolved gas	D	10^{-5} cm^2/s	assumed
Segregation coefficient of dissolved gas at the solidification interface	k	0.03	assumed
Average temperature of gas in the gap	T_{avg}	800 K	assumed to be at melting point
Meniscus surface tension	σ	430 erg/cm^2	[21]
Contact angle	θ	112 degrees	[21]
Growth angle	α_0	25 degrees	[20]

Table 2. Numerical values of the gas flux and partial derivative used in the stability analysis. Residual gas pressure, $p_m = 10^3$ dyne/cm^2.

Steady-state gap width, e_{st}, cm	Inverse diffusion length, V_c/D, cm^{-1} (calculated in [2])	Gas flux, j_{mol}/D mol/cm^3	$\left(\frac{\partial j_{mol}}{\partial e}\right)/D$ mol/cm^4	$\left(\frac{\partial j_{mol}}{\partial p_g}\right)/D$ mol/erg	$\left(\frac{\partial j_{mol}}{\partial V_c}\right)/D$ mol s/cm^4	$\left(\frac{\partial L}{\partial e}\right)$	$\left(\frac{\partial L}{\partial V_c}\right)$ s
0.018	6.2	$2.38*10^{-8}$	$-0.64*10^{-6}$	$-0.15*10^{-11}$	$2.88*10^{-4}$	-1.52	-9.5
0.032	10.0	$3.92*10^{-8}$	$-1.10*10^{-6}$	$-0.36*10^{-11}$	$0.80*10^{-4}$	-1.41	-9.5
0.05	10.4	$4.47*10^{-8}$	$-1.16*10^{-6}$	$-0.75*10^{-11}$	$0.43*10^{-4}$	-1.31	-9.5
0.084	10.0	$4.69*10^{-8}$	$-0.91*10^{-6}$	$-1.40*10^{-11}$	$0.60*10^{-4}$	-1.17	-9.5
0.12	8.6	$4.57*10^{-8}$	$-0.71*10^{-6}$	$-1.92*10^{-11}$	$1.51*10^{-4}$	-1.03	-9.5
0.15	7.5	$4.0*10^{-8}$	$-0.60*10^{-6}$	$-2.36*10^{-11}$	$2.83*10^{-4}$	-0.90	-9.5

NOMENCLATURE

Latin letters

a_{ij} - Coefficient in stability analysis (i,j = e,p_g,L);

C - Concentration of dissolved gas in the melt [mole cm^{-3}];

D - Diffusion coefficient of dissolved gas in the melt [cm^2 s^{-1}];

e - Gap width [cm];

f - Characteristic function (in equation 20);

h - Heat transfer coefficient between outer ampoule wall and furnace ambient [erg cm^{-2} s^{-1} K^{-1}];

j_{mol} - Molar flux in the axisymmetric case (Equation (10)) [mol s^{-1} cm^{-1}];

J_{mol} - Molar flux of dissolved gas into the gap (Equation (8)) [mol s^{-1}];

k - Segregation coefficient of dissolved gas between solid and melt;

k_l,k_g,k_s,k_a - Thermal conductivities of the phases (liquid, gas, solid, and ampoule material) [erg cm^{-1} s^{-1} K^{-1}];

l_a - Length of the meniscus line [cm];

L - Gap length [cm];

L_a - Length of the column of melt analyzed (from the planar interface) [cm];

M - Dynamic function, defined by (1);

n - Normal direction at the meniscus, inward toward the melt (Fig.3) [cm];

N - Number of moles of gas in the gap;

p_m - Pressure over the column of melt, assumed to be the same at L_a [dyne cm^{-2}];

p_g - Pressure of gas in the gap [dyne cm^{-2}];

Δp - Pressure difference across the meniscus between the gap and the adjacent melt, p_g-p_m [dyne cm^{-2}];

r - Radial direction [cm];

R - Ideal gas constant, $8.314*10^7$ [erg $mole^{-1}$ K^{-1}];

R_a - Inner ampoule radius [cm];

Q - Latent heat of solidification per unit volume [erg cm^{-3}];

s - Tangential direction at the meniscus [cm];

S - Area of the meniscus [cm^2];

T - Temperature [K];

T_{avg} - Average temperature in the gap [K];

V - Gap volume [cm^3];

V_c - Solidification rate [cm s^{-1}];

x - Axial direction [cm];

Greek letters

α - Angle between the meniscus line and the axial direction at the three-phase line (Fig.2) [rad];

α_0 - Growth angle [rad];

θ - Contact angle of the melt at the ampoule wall [rad];

σ - Surface tension of meniscus [dyne cm^{-1}];

Subscripts

a - Ampoule (within the wall);

c - Cold zone;

f - Freezing interface;

g - Gas;

h - Hot zone;

l - Melt(liquid);

s - Solid;

0 - Furnace

FIGURE CAPTIONS

Fig.1. Model of detached solidification.

Fig.2. Meniscus geometry.

Fig.3. Physical domain used in the numerical calculations of the temperature field.

Fig.4. Steady-state isotherms for different gap widths. With increasing gap width e, the freezing interface is closer to the cooler zone and becomes more planar. The temperature difference between the isotherms is 0.66 K.

Fig.5. The behavior of the characteristic function $f(\gamma)$ near zero for e = 0.05 cm and e = 0.15 cm. Gap length L = 0.7 cm.

Fig.6. Stability of a detached configuration, obtained by considering gas transport and heat transfer in the analysis. Points are numerical values of the largest real parts of the roots of characteristic equation (14). This gap is stable only when it is less than 0.77 cm long. The gap width is e = 0.05 cm, $V_c/D = 10.4\ cm^{-1}$, $p_m = 10^3$ dyne/cm^2, k = 0.03.

Fig.7. Stability of another detached configuration, obtained by considering gas transport and heat transfer in the analysis. Points are numerical values of the largest real parts of the roots of characteristic equation (14). This gap is stable only when it is less than 3.25 cm long. The gap width is e = 0.15 cm, $V_c/D = 7.5\ cm^{-1}$, $p_m = 10^3$ dyne/cm^2, k = 0.03.

Fig.8. Behavior of the components of the c-coefficient in equation (29) for e=0.05 cm. The critical gap length, when the instability first arises, is $L_{critical} = 0.77$ cm.

Fig.9. The dependence of the critical gap length $L_{critical}$, at which the onset of instability takes place, on e. The deviation from the trend at small e is probably due to numerical errors because of fewer mesh points at the meniscus.

Fig.A1. Grid points used for the finite difference representation of the energy equation (6).

Fig.A2. Finite difference grid near the freezing interface.

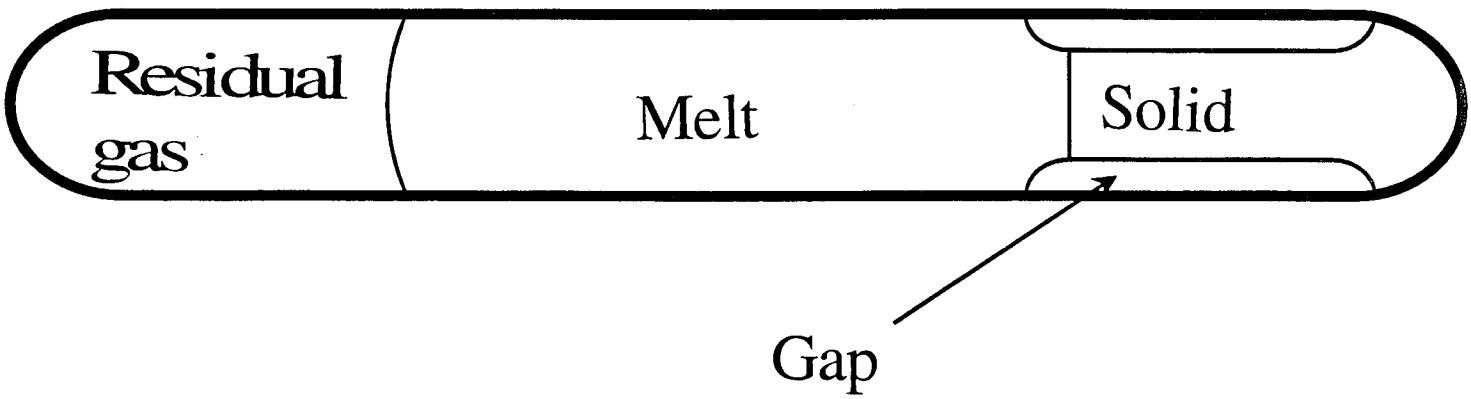

Fig. 1

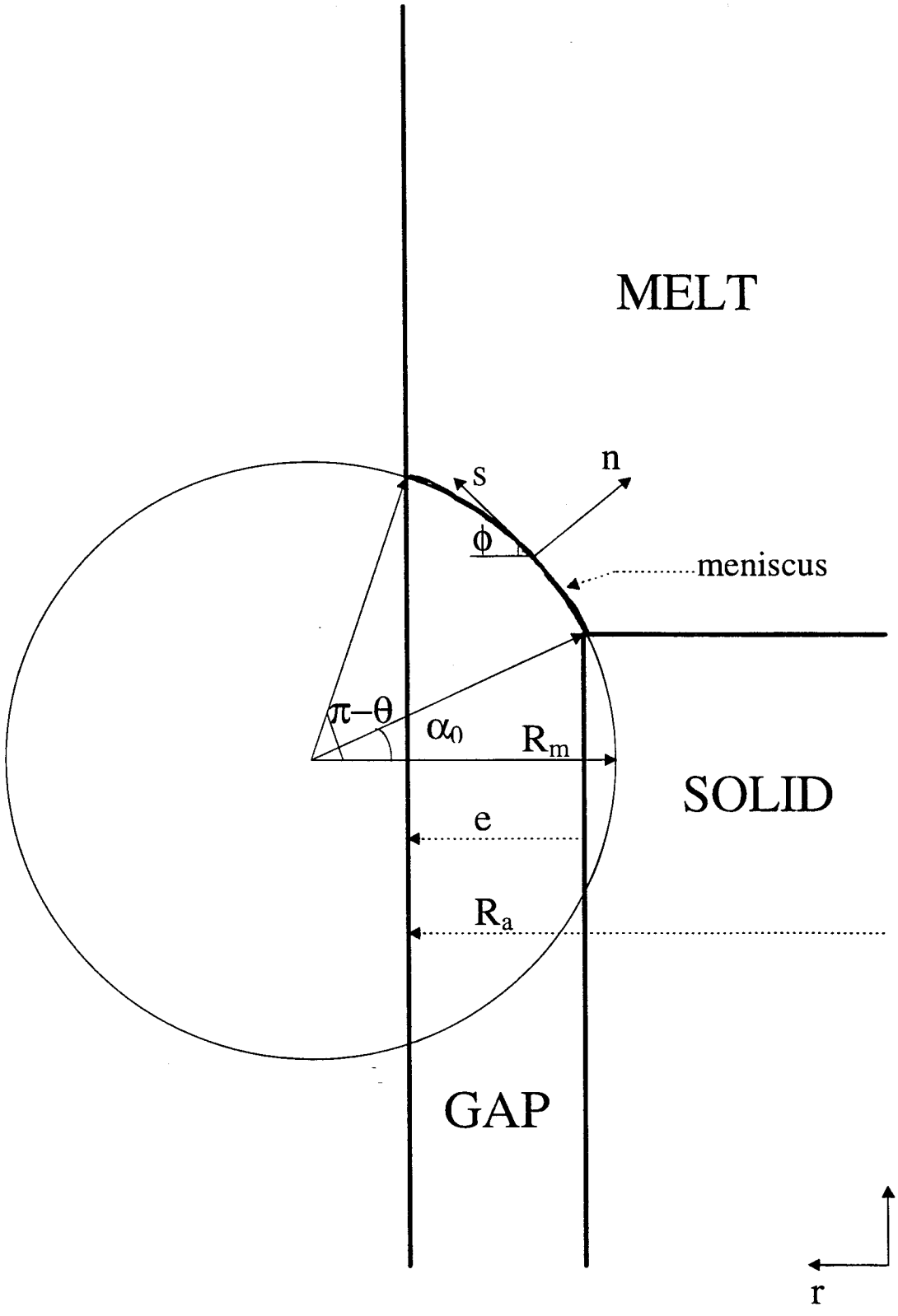

Fig. 2

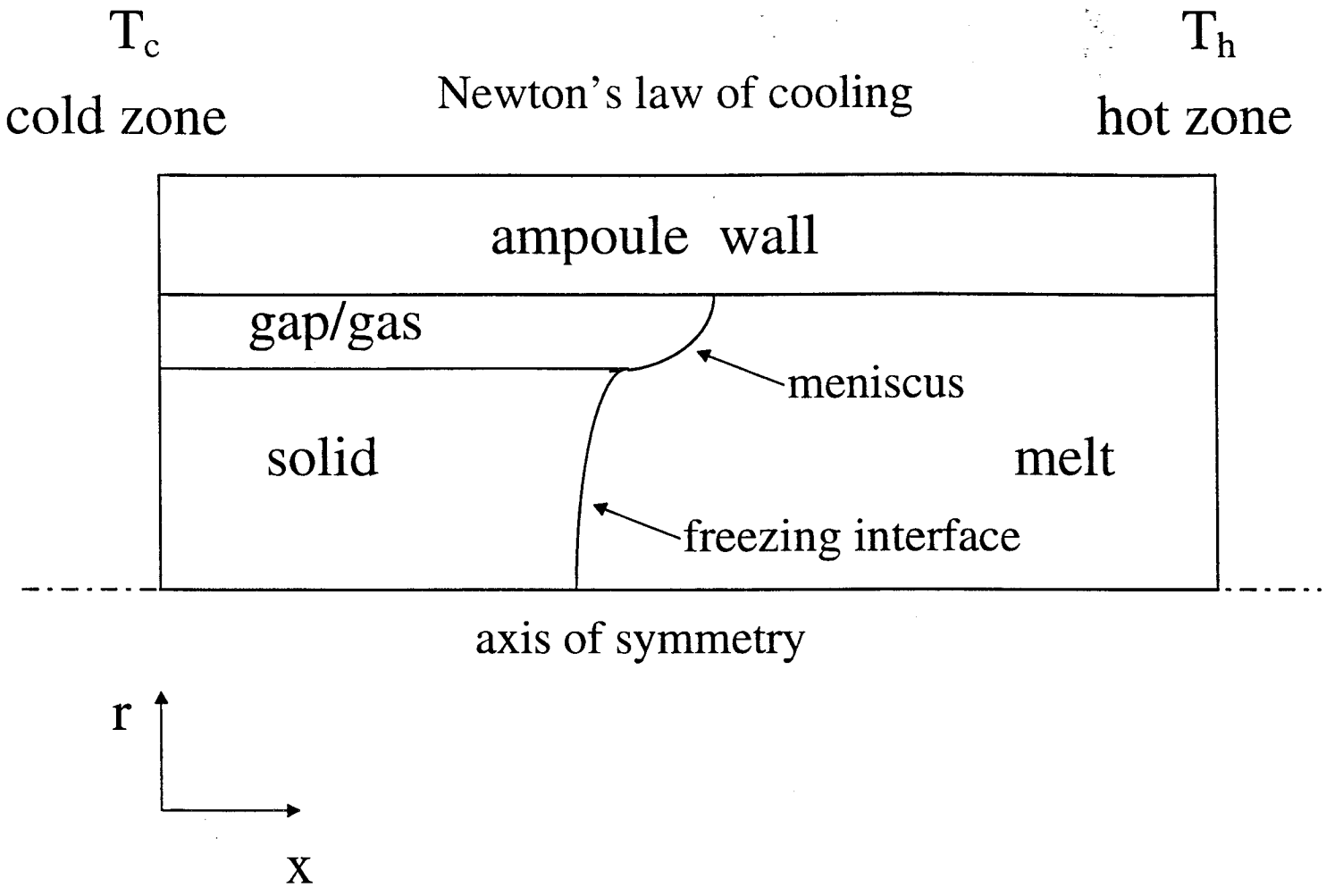
T_c
cold zone
Newton's law of cooling
T_h
hot zone
ampoule wall
gap/gas
meniscus
solid
melt
freezing interface
axis of symmetry
r
x

Fig. 3

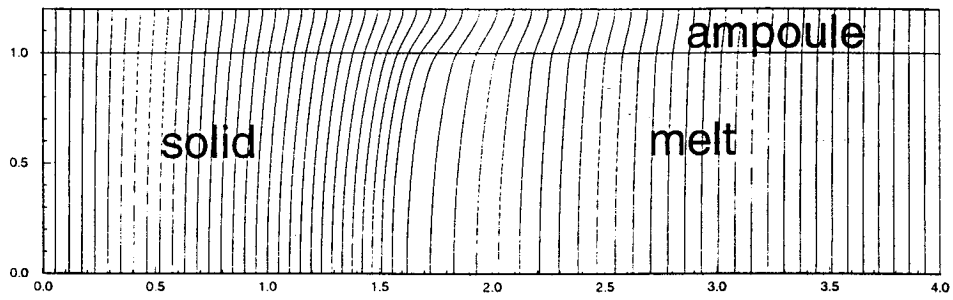

e=0.0 cm

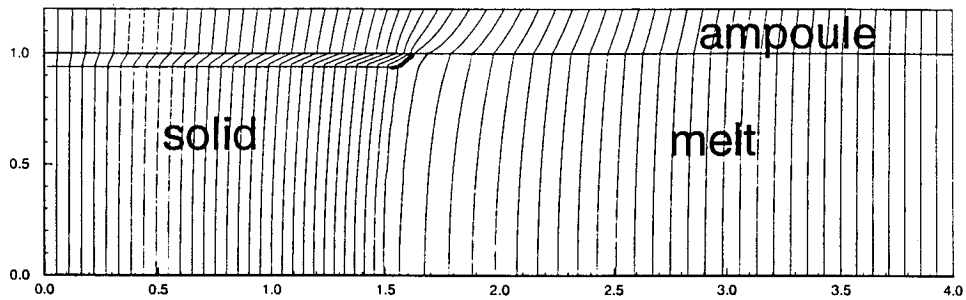

e=0.05 cm

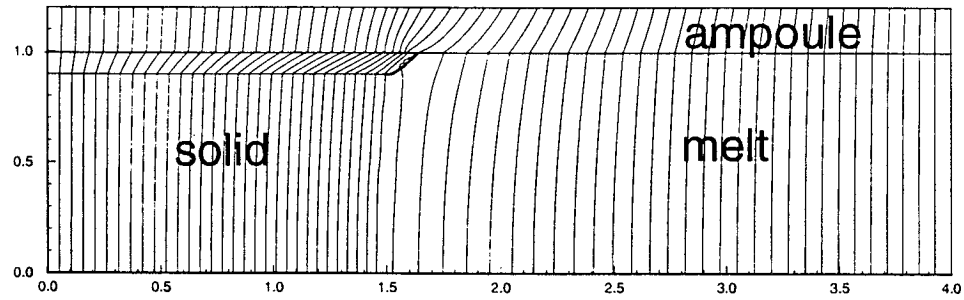

e=0.10 cm

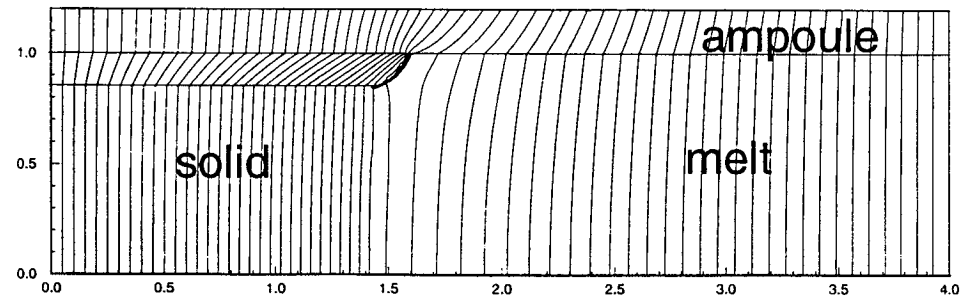

e=0.15 cm

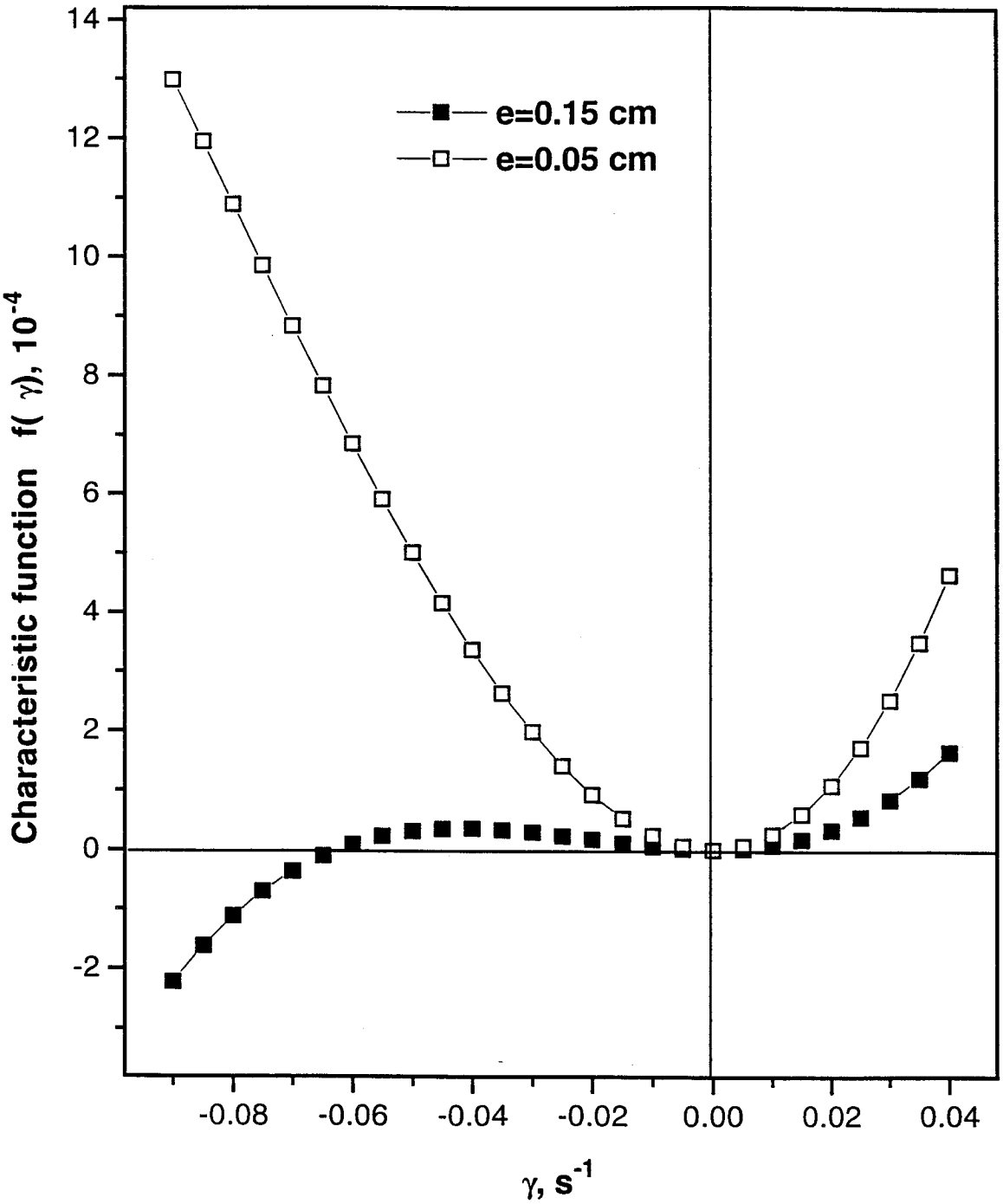
e=0.15 cm
e=0.05 cm
Characteristic function f(γ), 10^-4
γ, s^-1
14
12
10
8
6
4
2
0
-2
-0.08
-0.06
-0.04
-0.02
0.00
0.02
0.04

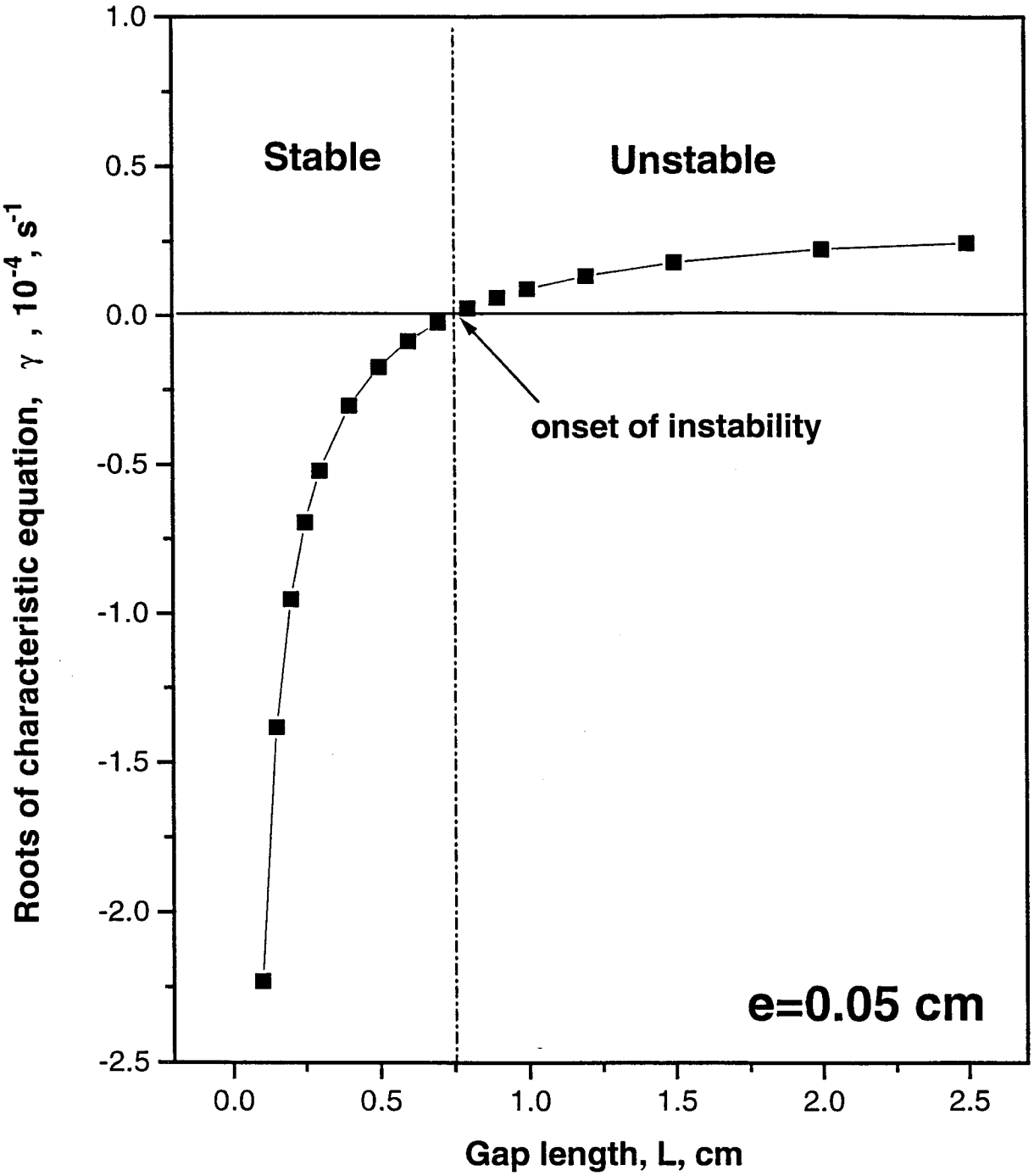
Stable
Unstable
onset of instability
e=0.05 cm
Roots of characteristic equation, γ , 10^-4, s^-1
Gap length, L, cm
1.0
0.5
0.0
-0.5
-1.0
-1.5
-2.0
-2.5
0.0
0.5
1.0
1.5
2.0
2.5

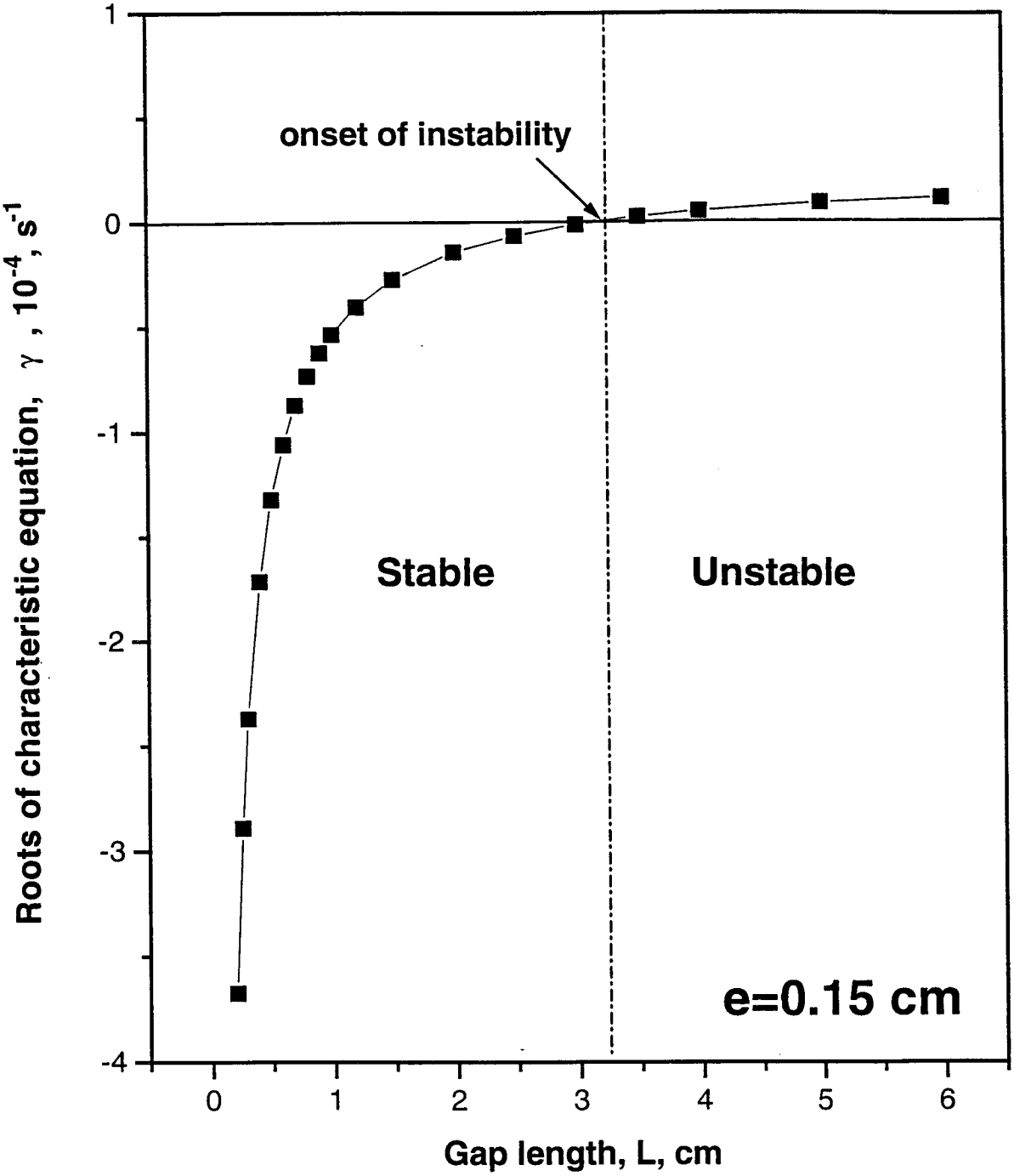
onset of instability
Stable
Unstable
e=0.15 cm
Roots of characteristic equation, γ , 10^-4, s^-1
Gap length, L, cm
1
0
-1
-2
-3
-4
0
1
2
3
4
5
6

Fig. 7

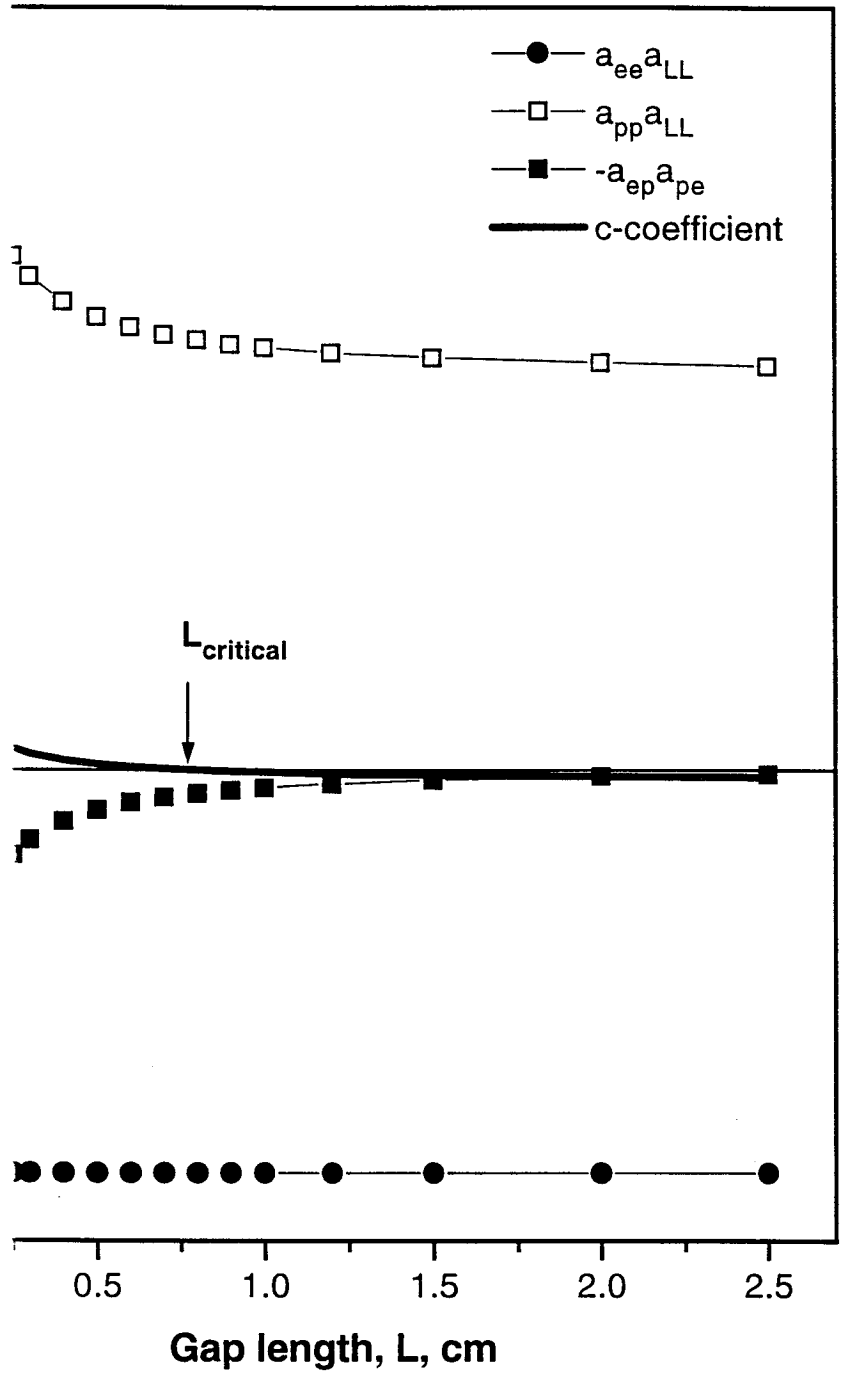
$a_{ee}a_{LL}$
$a_{pp}a_{LL}$
$-a_{ep}a_{pe}$
c-coefficient
$L_{critical}$
0.5
1.0
1.5
2.0
2.5
Gap length, L, cm

Fig 8

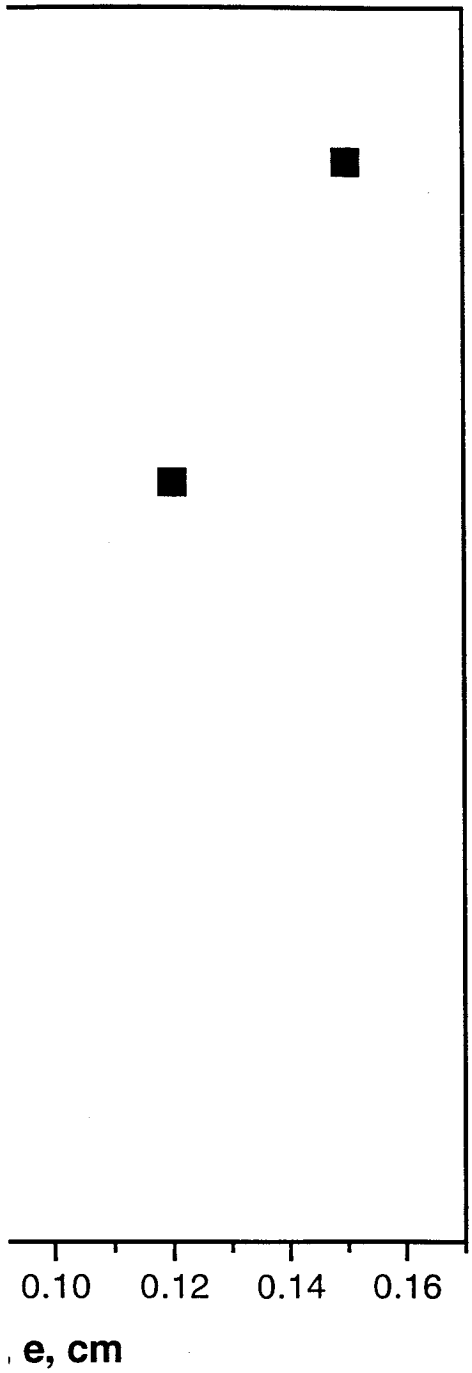
0.10
0.12
0.14
0.16
e, cm

Fig 9

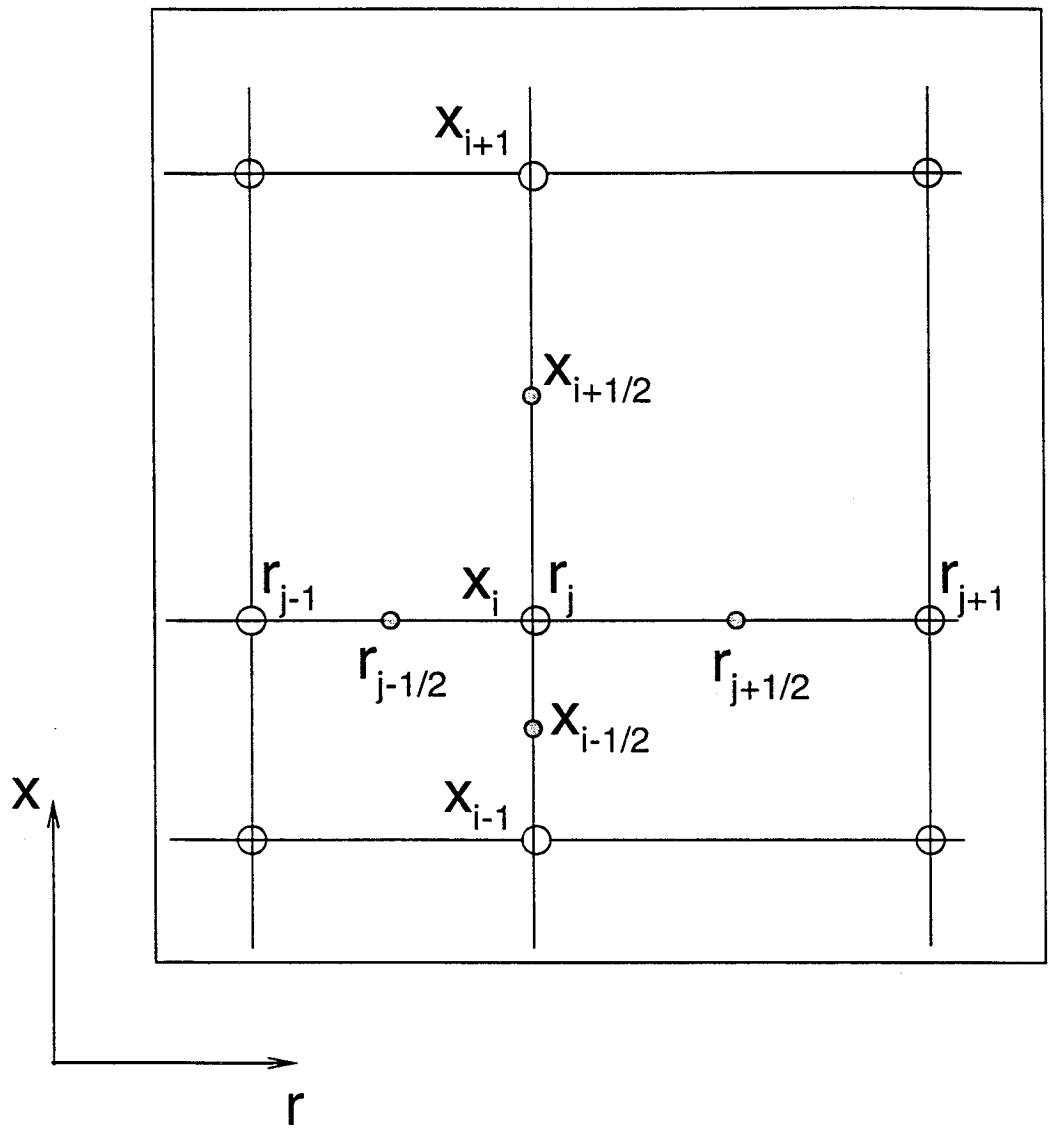
x_{i+1}
$x_{i+1/2}$
r_{j-1}
x_i
r_j
r_{j+1}
$r_{j-1/2}$
$r_{j+1/2}$
$x_{i-1/2}$
x_{i-1}
x
r

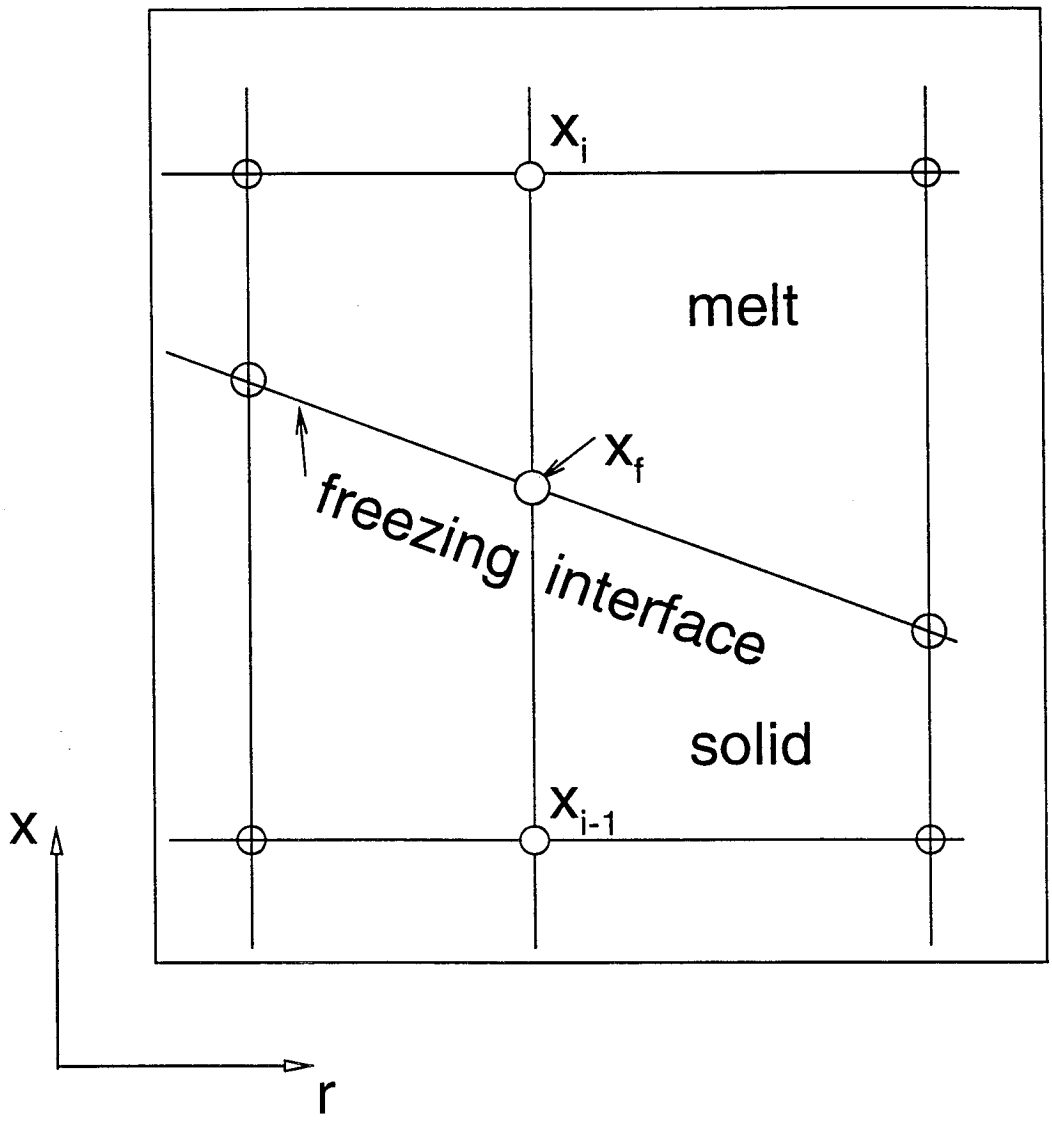
x_i
melt
x_f
freezing interface
solid
x_{i-1}
x
r

ATTACHMENT G

Detached Solidification: 3. Influence of Acceleration and Heat Transfer

DMITRI I. POPOV[1], LIYA L. REGEL[1,a] and WILLIAM R. WILCOX[1]

1. International Center for Gravity Materials Science and Applications

Clarkson University, Potsdam, NY 13699-5814, USA

Tel: 315-268-7672, Fax: 315-268-3833

e-mail: regel@agent.clarkson.edu

http://www.clarkson.edu/~regel/center.html

a. To whom correspondence should be addressed

Detached Solidification: Influence of Acceleration and Heat Transfer

Abstract

A new mechanism for detached solidification (Figure 1) in space was proposed in [1]. A model for the steady state was given in [2], and a linear stability analysis in [3]. Here we describe a numerical model for the two-dimensional flow and concentration fields in steady-state detached configuration for the vertical Bridgman-Stockbarger and Gradient Freeze growth techniques at accelerations from zero to g_0 (g_0 = earth's gravity). This modeling allowed us to gain insight on the influence of gravity on transport of a volatile species across the gas/melt meniscus. Transport into the gap is essential for detached solidification to persist. The possibility of detached solidification on earth is very important, since it would allow manufacture of crystals of higher perfection [1]. Even in microgravity, where the residual accelerations are considerable, buoyancy-driven convection is significant and should be taken into account. Different convection regimes are provided by different furnace configurations and thermal boundary conditions. Several of these were studied in order to find the most effective one for a sufficient amount of gas to be transported into the gap on earth. The results suggest that the most crucial parameter affecting the amount of gas transported into the gap is the shape of the freezing interface. Very gentle outward- directed convection can greatly increase the transport of the volatile species, and thereby enhance detachment. On the other hand, the usual levels of convection at earth's gravity cause mixing of the melt and thereby make detached solidification impossible.

Keywords: crystal growth, gas diffusion, buoyancy convection, gravity.

1. INTRODUCTION

The vertical Bridgman-Stockbarger (VBS) and vertical gradient freeze (VGF) methods are successfully used for growing semiconducting materials, both on earth and in microgravity. As described in [1], detached solidification yields improvements in crystallographic perfection. Until recently, detachment had been reported only in space experiments. One may ask, therefore, why is detached solidification so rare on earth? Figure 1 shows a schematic diagram of detached solidification as it would appear on earth. The gas pressure in the gap must equal the residual gas pressure over the melt, plus that due to the hydrostatic head of melt above the meniscus, plus that due to curvature of the meniscus. Increasing gravity from zero has three effects:

1. It causes the curvature of the meniscus to vary with height. For the usual small gap widths, this is negligible and is considered no further in the present paper.

2. If the gap width e is to be maintained at the same value, the flux of gas into the gap must be increased by the same amount by which the hydrostatic head increases the pressure in that gap.

3. It causes buoyancy-driven convection, which may provide the additional flux required in 2 if it is in the correct direction and of the correct magnitude.

The influence of convection on the transport of a volatile species is closely related to non-uniform doping in directional solidification. The influence of convection on axial and radial segregation of dopant has been studied numerically, analytically, and experimentally by many authors [e.g., 4-18]. It was shown that radial segregation depends on the magnitude of the convection compared to the freezing rate. Different controlling parameters have been considered, such as the temperature profile in the furnace. The majority of the models considered melts with a low Prandtl number, which is true for semiconductors and metals.

Convection in the melt can be induced by radial and axial temperature gradients. If the density of the melt decreases with height, then buoyancy-driven convection arises solely from the radial temperature gradient, which appears in the melt due to heat transfer between the ampoule and the furnace. The curvature of the interface reflects the radial temperature gradient at that position, since the interface is an isotherm for a single component system at low freezing rates. The curvature of the freezing interface has a strong influence on the impurity concentration distribution in the melt along this interface.

Chang and Brown [8] showed that in VBS growth with a stabilizing axial thermal gradient, convection arises from the radial temperature gradients and can cause considerable radial segregation. For a convex or planar freezing interface, the concentration of a dopant with a distribution coefficient $k<1$ is larger at the ampoule wall than at the axis. The opposite result was predicted for the VGF technique with a concave freezing interface [10]. Independent of the direction of the convective flow, the radial segregation has a maximum versus Rayleigh number, beyond which the melt becomes increasingly mixed and homogeneous in composition [16].

An essential feature of our model for detached solidification [1-3] is the presence in the melt of one or more volatile components, such as a dissolved gas. The concentration of this component near the freezing interface is higher than in the bulk of the melt because of rejection by the growing solid ($k<1$). The volatile species diffuses into the gap across the liquid meniscus connecting the crystal with the ampoule wall. The value of this flux is determined by the concentration field near the meniscus [2]. In the present paper, we study the significance of

convection induced by gravity on transport of the volatile component and the possible existence of steady-state detached solidification. We carried out numerical calculations for the axisymmetric steady-state velocity, temperature, and concentration fields for solidification in the VBS and VGF configurations. The equations were formulated in cylindrical coordinates with a reference frame of the moving interface. The diffusion coefficient, solubility of gas in the melt, and the segregation coefficient of dissolved gas at the freezing interface, though unknown, were assumed to be physically reasonable values.

As shown in [2], the pressure in the gap determines the gap width in steady-state detached solidification. Gas transport into the gap can be either enhanced or suppressed by convection arising from a non-zero acceleration. A decrease of gas transport into the gap would lead to a fall of pressure in the gap and an inability to sustain detachment. On the other hand, increased transport would favor detachment. The following conditions that influence buoyancy-driven convection are considered in this paper:

1. Acceleration direction and magnitude.

2. Growth method (furnace temperature profile).

3. For the VGF, a) heat transfer coefficient between the ampoule and the furnace wall; b) growth rate; c) direction of gravity.

4. For the VBS, a) temperatures of hot and cold zones; b) length of adiabatic zone; c) position of adiabatic zone, d) ampoule diameter, e) gap width.

2. HYDROSTATIC PRESSURE

The hydrostatic head due to a column of melt L_m high is given by:

$$\Delta p_h = \rho g L_m \tag{1}$$

It is instructive to consider an example. Let us consider a 10 cm column of molten InSb, the relevant properties for which are given in Table 1. Equation (1) yields a pressure of $6.3*10^4$ dyne/cm^2, or 47 torr.

The pressure change across the meniscus due to curvature is related to the steady-state gap width by [19]:

$$\Delta p_c = \frac{\sigma}{e}(\cos\alpha + \cos\theta) \tag{2}$$

where σ is the surface tension of the melt, α is the growth angle, and θ is the contact angle. Again, it is instructive to consider InSb as an example. For the properties shown in Table 1, a 10 cm height of melt gives the same pressure change as a gap width of 36 μm. Thus if the residual gas pressure p_m above the melt is much less than 47 torr, we would have to double the gas flux into the gap in order to maintain its width at 36 μm. The required increase in flux can be calculated by considering the rate of increase of gap volume:

$$\frac{required\ flux\ increase}{2\pi R_a} = \frac{V_c e(\rho g L_m)}{R T_{gap}} \tag{3}$$

where V_c is the growth rate, R is the ideal gas constant and T_{gap} is the average temperature in the gap.

It also follows that inversion of the furnace, so that the solid is above the melt, may reduce the pressure in the gap required to support detached solidification. The success of such a measure would depend on the force used to support the melt from below and the continued availability of a volatile species to be liberated into the gap.

3. MATHEMATICAL MODEL HEAT TRANSFER AND CONVECTION

Computations were carried out for InSb, as in our previous papers [2,3].

3.1. Temperature field

The numerical model for the steady-state temperature field was described in [3]. We applied the finite difference discretization scheme to describe the steady-state governing equation for heat transfer:

$$k_i\left(\frac{1}{r}\frac{\partial}{\partial r}\left(r\frac{\partial T}{\partial r}\right)+\frac{\partial^2 T}{\partial x^2}\right)=0 \tag{4}$$

In equation (4) k_i designates the thermal conductivity of the i^{th} phase (melt, crystal, ampoule material or gas in the gap). We neglected convective heat transfer in the melt since the Prandtl number of semiconductor melts is low (for InSb used in the calculations, $Pr = \nu/\kappa = 0.04$ near the melting point). The position and shape of the melt/crystal interface were determined from the following two boundary conditions at the solidification interface:

$$T|_{int} = T_f$$
$$k_s \frac{\partial T}{\partial x}\bigg|_{int} - k_l \frac{\partial T}{\partial x}\bigg|_{int} = Q V_c \tag{5}$$

where Q is the latent heat of fusion per unit volume, V_c is the growth rate, and T_f is the temperature of the freezing interface (here assumed to be equal to the melting point of InSb). At the ampoule outer wall, Newton's law of cooling was assumed. The heat transfer coefficient between the ampoule and the furnace wall was assumed to be temperature independent. Heat transfer across the gap was considered to be purely by conduction. At phase boundaries where no phase transition takes place, heat flux is equal on both sides of the boundary. The details of the finite difference discretization were given in the Appendix of [3].

The numerical calculations were carried out for VBS (Brid) and VGF (Grad) techniques as shown in Figure 2 under the conditions summarized in Table 2.

The following assumptions were made:

- hot and cold zone temperatures are constant and uniform;
- the insulation zone in VBS furnace is perfectly adiabatic;
- no heat transfer by natural convection in the melt;
- thermal properties are not temperature dependent;
- all transients are neglected.

3.2. Gravitational convection

The numerical method used for solving the Navier-Stokes equation was presented in [2]. Following [2], we assumed axisymmetric, incompressible and Newtonian flow of the melt in a cylindrical ampoule in the reference frame of the moving interface. The governing equation was expressed in terms of the stream function ψ and the temperature T as:

$$\frac{1}{r}\frac{\partial(\psi, E^2\psi)}{\partial(r,x)} + \frac{2}{r^2}\frac{\partial\psi}{\partial x}E^2\psi + \frac{\mu}{\rho_m}E^4\psi - \beta_T g r \frac{\partial T}{\partial r} = 0 \tag{6}$$

Here g is the acceleration of gravity, and β_T is the thermal volume expansion coefficient. E^2 and E^4 are the operators:

$$E^2\psi = \frac{\partial^2\psi}{\partial r^2} - \frac{1}{r}\frac{\partial\psi}{\partial r} + \frac{\partial^2\psi}{\partial x^2} \quad ; \quad E^4\psi = E^2(E^2\psi) \tag{7}$$

The radial and axial components of the velocity are:

$$V_x = -\frac{1}{r}\frac{\partial\psi}{\partial r} \qquad V_r = \frac{1}{r}\frac{\partial\psi}{\partial x} \tag{8}$$

Thus the velocity field becomes dependent on the acceleration and the radial temperature gradients in the melt. The boundary conditions on the velocity assume no-slip at the interface and the ampoule wall, and perfect slip at the meniscus. The validity of the boundary conditions on the melt free surface (far above the freezing interface) was discussed in [2]. It should be mentioned, that the velocity boundary conditions at the top free melt surface do not greatly affect the solute field in the melt, especially for small segregation coefficients and small diffusion length. Symmetry boundary conditions at the axis of the cylindrical ampoule were specified.

The convection calculations were carried out for the thermal configurations Grad-I, Grad-III, Brid-I, and Brid-II, shown in Table 2. The overrelaxation parameter for the central finite difference method was $\varepsilon = 1.7$ for both the vorticity and the stream function calculations.

3.3. Concentration field

The steady-state concentration field for the volatile species in the melt and its flux into the gap for different values of the processing parameters (growth rate, pressure of backfilled gas, gap width) were calculated in [2]. Zero gravity was assumed, so there was no gravity-induced convection. Even in the microgravity environment of space, buoyancy-driven convection can cause considerable convective mass transfer in liquid because the Schmidt number is very large.

The convective terms on the left-hand side of the mass transfer equation:

$$V_r\frac{\partial C}{\partial r} + V_x\frac{\partial C}{\partial x} = D\cdot\left[\frac{1}{r}\frac{\partial}{\partial r}\left(r\frac{\partial C}{\partial r}\right) + \frac{\partial^2 C}{\partial x^2}\right] \tag{9}$$

are known [20] to be the origin of the divergence of the finite difference solution of the elliptic PDE (9), where V_i are the components of the velocity, and D is the diffusion coefficient in the melt. The problem can be solved by using asymmetric weighting functions, still conserving the finite difference discretization [20]. The method for solving the two-dimensional problem using five finite-difference grid points is not as accurate as using nine points. However, achieving the high-order accuracy makes the discretization very laborious, especially in cylindrical coordinates with the explicit r-dependence of (9). A one-dimensional asymmetric weighting function was applied in both r- and x-directions. The values of the weighting coefficients were calculated from the local mass transfer Peclet number:

$$Pe_i^{loc} = \frac{V_i^{loc} \cdot h_i}{D} \tag{10}$$

where i=r,x; h_i is the local mesh size (Δx or Δr)[1], and 'loc' corresponds to the local grid point. The calculations were carried out according to [21]:

$$\xi = \coth\left(\frac{Pe_x^{loc}}{2}\right) - \frac{2}{Pe_x^{loc}} \quad ; \quad \eta = \coth\left(\frac{Pe_r^{loc}}{2}\right) - \frac{2}{Pe_r^{loc}} \tag{11}$$

which minimizes the numerical error. Therefore, the values of the weighting coefficients ξ and η were dependent on the local velocity and the grid size. The finer the grid (smaller h_i), the smaller values of ξ and η were required. Hence, the choice of ξ and η between 0 and 1 allowed us to avoid increasing the number of the grid points in order to have a convergent result. All of the details of the finite difference discretization using asymmetric weighting functions are given in the Appendix.

The boundary conditions used in the calculations were the same as described in [2]. At the ampoule wall and the axis of symmetry the radial gradient of concentration was set equal to zero. At the free melt surfaces (top of the melt and the meniscus), the gas concentration was assumed constant, and was related to the pressure over the melt through the temperature-dependent solubility coefficient. The boundary condition at the freezing interface for conservation of mass is:

$$D\frac{\partial C}{\partial x} = -V_c(1-k)C \tag{12}$$

[1] For the nonuniform grid used in the calculations, $h_x = (\Delta x_{j-1} + \Delta x_j)/2$, and $h_r = (\Delta r_{j-1} + \Delta r_j)/2$

where V_c is the growth rate, and k is the segregation coefficient of volatile species at the freezing interface. Diffusion in the solid phase was neglected.

4. GRADIENT FREEZE CONFIGURATION

4.1. Temperature field

The computed temperature fields for the gradient freeze technique are shown in Figures 3a and 3b for several conditions. In Figure 3a, the gap width is zero, i.e. there is no detachment. The interface is concave, as expected for the gradient freeze technique [22]. The deflection of the interface from planarity is large; 14 % of the ampoule radius (Figure 4a). For weaker heat transfer (Grad-III) between the ampoule and the furnace, the freezing interface is less concave than when the heat transfer coefficient is ten times larger (Grad-I). In Figure 3b, the gap width is 0.12 cm. The gas in the gap has a much lower thermal conductivity than the solid, and so improves the thermal isolation of the solid from the furnace, thus reducing the radial temperature gradient. A decreased radial temperature gradient is reflected in a decreased interface curvature (Figure 4b). One would expect that in this case there would be much less convection. Since the deflection $z/(R_a-e)$ of the interface is only about 3% for a heat transfer coefficient h of $2*10^6$ erg s^{-1} cm^{-2} K^{-1}, and about -0.5% for h = $2*10^5$ erg s^{-1} cm^{-2} K^{-1}, we did not consider the interface curvature in the convection calculations. The interface was assumed to be a non-isothermal planar boundary, which is a radial cut at the circumference where the meniscus contacts the freezing interface. The interface curvature was taken into account for a gap width e of 0.05 cm, for which the interface deflection is significant. It turned out that the assumption of a non-isothermal planar boundary is not bad for small deflections. Even for an interface deflection of 7% the velocity field near the meniscus does not differ for a planar non-isothermal boundary compared to the case when the interface curvature is incorporated in the discretisized equations.

In [3] it was found that the interface position shifts to the cold zone of the furnace with increasing gap width and with increasing solidification rate (all other parameters held constant). Here, we found that the deflection of the freezing interface shape from planarity decreases with increasing gap width, i.e. $dz/de < 0$. The

response of the interface shape to a change in solidification rate has the opposite trend. The interface becomes even more concave with increasing V_c, so $dz/dV_c > 0$. This result is similar to that reported in the literature [e.g.,17].

4.2. Buoyancy-driven convection

The radial temperature gradient near the freezing interface does not differ much for Grad-I and Grad-II (different hot zone and cold zone temperatures). In spite of the change in position of the freezing interface, the shape and the deflection of the interface from planarity do not change significantly. So, we do not expect much influence on convection. Hence, the velocity field was calculated only for the two thermal configurations that differ in the value of heat transfer coefficient between the ampoule and the furnace. The convective regimes are similar (Fig 5a and 5b), with a transition from linear flow (controlled by crystallization) to circulating flow as g is increased. This transition takes place at a higher g for the configuration with the lower heat transfer coefficient (Grad-III) than for the configuration with h one order of magnitude larger (Grad-I). For both configurations, this transition point is between 10^{-4} and 10^{-3} g_0. The radial temperature gradient is negative throughout the melt. This results in flow downward (toward the freezing interface) along the ampoule wall and upward along the axis.

The transition of the flow regime from linear to circulating (Figures 5 a,b) occurs at a particular Rayleigh number that depends on the thermal configuration. Here we define the Rayleigh number as:

$$Ra = \frac{\beta_T g (T_h - T_f)}{\alpha \nu} \frac{R_a^4}{L_m} \tag{13}$$

where β_T is the volumetric thermal expansion coefficient, T_h and T_f are the hot zone and the freezing interface temperatures, respectively, L_m is the length of the melt column, and α and ν are the thermal diffusivity and kinematic viscosity of the melt. As shown in Figure 6, a decrease of heat transfer coefficient between the ampoule and the furnace wall shifts the flow transition point to a higher Rayleigh number.

The effect of the interface shape was studied for a gap width e of 0.05 cm. Although the interface deflection is large for the Grad-I configuration, a secondary eonvective cell does not appear. This is because the radial temperature gradient does not change sign in the melt.

For g above 10^{-5}- 10^{-4} g_0, inversion of the furnace (growth down) causes the convective flow to change direction and slightly increase in magnitude.

4.3. Concentration field

The concentration field obtained for the gradient freeze configuration (Grad-I) at different gravity levels is shown in Figure 7. These results are similar to those in [10]. The maximum concentration at the interface remains at the axis of symmetry at all values of g, unless g is directed in the opposite direction from shown in Figure 1 (inverted furnace). In the inverted gradient freeze technique, gas accumulates near the meniscus.

Figure 7 shows the transition from a pure diffusion regime for mass transfer to a convective regime with mixing. This transition takes place at a Rayleigh number (in Figure 6 Ra~0.1) corresponding to the transition to circulating convection. For a lower heat transfer coefficient h, mixing starts at a larger Rayleigh number.

Gas mass transfer across the meniscus was calculated from the concentration field according to [2]:

$$j_{mol} = -D\int_0^{l_a} \frac{\partial C}{\partial n} ds \qquad (14)$$

where j_{mol} is the molar diffusion flux per unit length in the axisymmetric domain, l_a is the length of the meniscus line, and the integration is carried out along the meniscus line. The dependence of j_{mol} on the gap width e and diffusion length D/V_c at zero gravity was shown in [2]. Here, we compare the present results with the results in [2] for zero gravity.

Figures 8 shows the radial concentration profiles for the Grad-I thermal configuration. The slope of the curves at the meniscus (the very right end of the curves) determines, to a first approximation, the gas flux into the gap. Figures 9 shows the concentration gradient normal to the meniscus. With increasing gravity, the curves shift downward. The value of the total gas flux, which is proportional to the area under the curve, diminishes and even becomes negative for higher g with the gap width held constant.

The solidification rate does not influence the mass transfer across the meniscus as much as the acceleration does. This is shown in Figure 10, where the value of the gas flux drops slightly when V_c is increased from 10^{-4} cm/s to $2*10^{-4}$ cm/s (solid and open squares in the figure).

The effect of the heat transfer coefficient h on the concentration field is more pronounced than the effect of the growth rate. Decreasing h causes the gas flux into the gap to maintain its value to g.

Solidification with an inverted furnace changes the direction of buoyancy-driven convection relative to the freezing interface. As a result, there is an enhanced gas transfer into the gap with increasing convection, until bulk mixing lowers the concentration at the freezing interface. Thus, for example, detached solidification in microgravity would be enhanced by proper orientation of the furnace relative to the residual acceleration vector. Excessive g-jitter, on the other hand, could mix the melt and eliminate detached solidification.

5. VERTICAL BRIDGMAN-STOCKBARGER CONFIGURATION

5.1. Temperature field

The temperature field and the interface shape in the vertical Bridgman-Stockbarger (VBS) configuration are shown in Figures 11 and 12. Contrary to the tendency of the interface deflection in the gradient freeze technique to increase only slightly during solidification, the shape and deflection of the interface in VBS are changed drastically by freezing (Fig.12a for Brid-I and Fig.12b for Brid-II configurations). The position of the interface relative to the insulation zone is very critical to the temperature distribution near the interface. The shape of the freezing interface changes from convex to concave with translation of the ampoule down through the furnace.

Decreasing the length of the adiabatic zone causes the freezing interface to become more concave (Fig.12c), independent of the temperatures of the hot and cold zones.

Decreasing the gap width causes the freezing interface to become more concave, similar to the gradient freeze configuration (Fig.12d). Thus, it is likely that this trend does not depend on the furnace temperature profile.

A reduction in ampoule diameter causes the freezing interface to become more convex (Fig.12e for Brid-I and Fig.12f for Brid-II configurations). Quantitatively, the influence is more pronounced in the latter stages of solidification, especially for the Brid-II configuration with the lower temperatures.

5.2. Buoyancy-driven convection

The interface shape depends strongly on its position in the furnace. Here, the freezing interface is planar or slightly convex in the early part of the solidification. With the ampoule high in the furnace, the flow in the melt is directed downward along the axis of symmetry and upward along the ampoule wall. With continuing lowering of the ampoule, a change in the sign of the radial temperature gradient near the interface causes the convective flow to change its direction. First, the convective cell splits into two cells with opposite directions of rotation. Further, a new vortex appears close to the interface, spreads upward, and absorbs the old one. The resulting flow has a direction that is downward along the ampoule wall and upward along the axis. Figure 13a shows two cells for the growth ampoule in the middle of the furnace (see Figure 2). Lowering the temperature of both cold and hot zones leads to the appearance of the second cell at a later stage of solidification, i.e. when the upper part of the ampoule is in the insulation zone (see Figure 13b where the second cell has not yet appeared). On the other hand, since a shorter insulation zone results in a more concave interface, the transition of the flow (splitting into two cells) takes place at an earlier stage of solidification, i.e. for the bottom end of the ampoule nearer the insulation zone.

For the Bridgman configuration, the critical Rayleigh number (defined by (13)) for the transition to circulating convection is lower than for the gradient freeze furnace.

5.3. Concentration field

Contrary to the behavior in the gradient freeze configuration, the interface shape changes considerably with time as the ampoule is lowered. The resulting change in the convection pattern influences the solute concentration distribution. The concentration fields for different thermal configurations (Brid-Ib and Brid-IIb) are shown in Figures 14 a,b. The flow in a cell near a concave freezing interface has an upward direction along the axis of symmetry. Under these conditions, the maximum of gas concentration along the interface is near the axis of symmetry for all g, see Figure 15a (Brid-Ib configuration). The concentration gradient at the meniscus (see Fig.16a) decreases with increasing g, similar to the gradient freeze configuration. With lowering of the ampoule

position, one cell remains in the melt, with the direction of flow downward along the ampoule wall. In this case, the maximum of gas concentration remains at the axis.

Another behavior is observed for the Brid-II configuration. Corresponding to the flow field shown in Figure 13b, the maximum of gas concentration along the interface is near the meniscus (Figure 15b). Moreover, the concentration gradient at the meniscus increases with increasing g up to a certain level (Fig.16b). As shown in Figure 17, for g from 10^{-4} to 10^{-2} g_0, convection causes the total gas flux to increase from the value at 10^{-6} g_0, reach a maximum, and then decline. At the maximum, convection provides gas transfer *into* the gap at higher accelerations than all the others considered in this paper.

5. DETACHED SOLIDIFICATION ON EARTH

We have seen that detached solidification on earth should be possible. In addition to the requirements given in [1], we find here that convection must transport enough additional gas into the gap to counterbalance the hydrostatic head.

Recent experimental results at NASA's Marshall Space Flight Center corroborate this view [23]. Germanium was solidified upward in a mirror furnace, allowing the ampoule to be viewed in the neighborhood of the freezing interface. When a strong magnetic field was used, the solid was in contact with the quartz ampoule wall. On the other hand, without a magnetic field, detached solidification occurred in one experiment. The appearance corresponded to our model [1-3]. The gap was about 30 μm wide and 27 mm long, and the freezing interface was slightly convex.

Our interpretation of the MSFC experiments described above is as follows. Detached solidification in space has been realized with germanium several times [24-34]. With a magnetic field applied on earth, the transport of dissolved residual gas into the gap was too small to compensate for the hydrostatic head. On the other hand, with a slightly convex interface, the melt flowed outward along the interface toward the

wall. Convective mass transfer was, apparently, sufficiently high to increase the gas pressure in the gap and maintain the meniscus shape required for stable detached solidification.

6. CONCLUSIONS

In the presence of a hydrostatic head, the transport of a volatile species into the gap must be increased in order for detached solidification to occur with the same gap width.

The influence of gravity on steady-state dissolved gas transport in the melt was studied in this paper. From the numerical modeling it was found that the most critical indication of the gas flux from the melt into the gap is the shape of the freezing interface. A convex freezing interface provides convective mass transfer from the axis to the meniscus along the interface. This mechanism enhances mass transfer across the meniscus only up to a certain level of convection, at which it reaches a maximum value. Stronger convection causes bulk mixing and reduces the concentration along the entire freezing interface. Correspondingly, the normal gradient of concentration at the meniscus is reduced. Thus, for a convex interface, convective mass transport supports detachment only till a certain level of convection is reached.

On the other hand, a concave freezing interface causes the opposite direction of convective flow. In this case the mass transfer of gas into the gap decreases with increasing convection. All levels of convection weaken mass transport and, therefore, inhibit detachment.

Since a convex interface can be produced by solidification in VBS furnaces, this configuration is more favorable for reaching detached solidification at non-zero gravity than the gradient freeze configuration, where a convex interface is not normally attainable. In the VBS technique, the most favorable configuration is one with lower temperatures in the hot and cold zones. A longer adiabatic zone in the furnace keeps the freezing interface planar or slightly convex for a longer time during solidification, favoring detached solidification. So does a smaller ampoule diameter.

A lower freezing rate should cause detached solidification with a smaller value of the gap width [2]. The result is less influence of hydrostatic pressure. Therefore, a low solidification rate would favor the observation of detached solidification on earth.

Following are the means by which the proper convective flow can be established to aid in achieving detached solidification. The optimal flow rate would increase with increasing V_c/D.

I. Concave freezing interface.

A. Strong curvature of interface.

1. Microgravity with residual g vector up (inverted furnace).

2. Earth's gravity with rotation of ampoule about its axis just above the critical rotation rate for flow reversal [35].

3. Earth's gravity with inverted furnace and moderate magnetic field applied.

B. Slight curvature of interface.

1. Inverted furnace on earth.

2. Same as 2 above, with critical rotation rate lower.

3. Same as 3 above, with lower magnetic field.

II. Convex freezing interface

A. Strong curvature of interface.

1. Microgravity with residual g vector down.

2. Earth's gravity with moderate magnetic field applied.

B. Slight curvature of interface.

1. Earth's gravity.

In the VBS technique, the interface shape can be adjusted via the heater and cooler temperatures. Lower temperatures cause the interface to become more convex / less concave. In the gradient freeze technique, on the other hand, one has little control over the concave interface shape. In both techniques, increasing the freezing rate causes the interface to become more concave.

Acknowledgment

This research was supported by NASA's Microgravity Science and Applications Division under grant NAG8-1063.

REFERENCES

1. W.R. Wilcox and L.L. Regel, *Microgravity Sci. Technol.* **7**, 56-61(1995).

2. D.I. Popov, L.L. Regel and W.R. Wilcox, "Detached Solidification: 1.Steady-State Results at Zero Gravity," submitted to Journal of Materials Synthesis and Processing.

3. D.I. Popov, L.L. Regel and W.R. Wilcox, "Detached Solidification: 2.Stability," submitted to Journal of Materials Synthesis and Processing.

4. T. Jasinski, W.M. Rohsenow, and A.F. Witt, "Heat Transfer Analysis of the Bridgman-Stockbarger Configuration for Crystal Growth," *J. Crystal Growth* **61**, 339-354(1983).

5. V.I. Polezhaev, K.G. Dubovik, S.A. Nikitin, A.I. Prostomolotov, and A.I. Fedyushkin, "Convection during Crystal Growth on Earth and in Space," *J. Crystal Growth* **52**,465-470(1981).

6. S.A. Nikitin, V.I. Polezhaev, and A.I. Fedyushkin, "Mathematical Simulation of Impurity Distribution in Crystals Prepared under Microgravity Conditions," *J. Crystal Growth* **52**,471-477(1981).

7. A.I. Feonychev, "Numerical Investigation of Heat and Mass Transfer Processes Acompanying Crystallization under Conditions when Body Forces Produce Weak Accelerations," *Fluid Dynamics* **16**,155-161(1981).

8. C.J. Chang and R.A. Brown, "Radial Segregation Induced by Natural Convection and Melt/Solid Interface Shape in Vertical Bridgman Growth," *J. Crystal Growth* **63**,343-364(1983).

9. D.H. Kim and R.A. Brown, "Modelling of Directional Solidification: from Scheil to Detailed Numerical Simulation," *J. Crystal Growth* **109**,50-65(1991).

10. D.H. Kim and R.A. Brown, "Transient Simulations of Convection and Solute Segregation of GaAs Growth in Gradient Freeze Furnace," *J. Crystal Growth* **109**,66-74(1991).

11. S.R. Coriell and R.F. Sekerka, "Lateral Solute Segregation during Unidirectional Solidification of a Binary Alloy with a Curved Solid-Liquid Interface," *J. Crystal Growth* **46**,479-482(1979).

12. J.J. Favier and D. Camel, "Analytical and Experimental Study of Transport Processes during Directional Solidification and Crystal Growth," *J. Crystal Growth* **79**,50-64(1986).

13. D. Camel and J.J. Favier, "Scaling Analysis of Convective Solute Transport and Segregation in Bridgman Crystal Growth from the Doped Melt," *J. Physique* **47**,1001-1014(1986).

14. S. Motakef, "Interference of Buoyancy-Induced Convection with Segregation During Directional Solidification: Scaling Laws," *J. Crystal Growth* **102**,197(1990).

15. C.W. Lan and C.C. Ting, "Numerical Investigation on the Batch Characteristics of Liquid Encapsulated Vertical Bridgman Crystal Growth," *J. Crystal Growth* **149**,175-186(1995).

16. G.T. Neugebauer and W.R. Wilcox, "Experimental Observation of the Influence of Furnace Temperature Profile on Convection and Segregation in the Vertical Bridgman Crystal Growth Technique," *Acta Astronautica* **25**,357-362(1991).

17. P.S. Dutta, K.S. Sangunni, H.L. Bhat, and V. Kumar, "Growth of Gallium Antimonide by Vertical Bridgman Technique with Planar Crystal-Melt Interface," *J. Crystal Growth* **141**,44-50(1994).

18. R.A. Brown, "Theory of Transport Processes in Single Crystal Growth from the Melt," AIChE Journal 34(1988),881-911.

19. T. Duffar, Private Communication, 1995, Centre d'Etudes Nucleaires, 85 X, F-38041 Grenoble, Cedex, France.

20. T.M. Shih, *Numerical Heat Transfer*, Hemisphere Publishing Corporation, Springer-Verlag, 1984.

21. I. Christie, D.F. Griffiths, A.R. Mitchell, "Finite Element Methods for Second Order Differential Equations with Significant First Derivatives," *Int. J. Numerical Methods in Engineering* **10**(1976),1389-1396.

22. C.E. Chang and W.R. Wilcox, "Control of Interface Shape in the Vertical Bridgman-Stockbarger Technique," *J. Crystal Growth* **21**(1974),135-140.

23. F. Szofran, K.W. Benz and P. Doldt, Private communication, 1996. NASA Marshall Space Flight Center, Alabama.

24. A.F. Witt, H.C. Gatos, M. Lichtensteiger, and C.J. Herman, "Crystal Growth and Segregation under Zero Gravity: Ge," *J. Electrochem. Soc.* **125**(1978),1832.

25. J.T. Yue and F.W. Voltmer, "Influence of Gravity-Free Solidification on Solute Microsegregation," *J. Crystal Growth* **29**(1975),329

26. V.S. Zemskov, V.N. Kubasov, I.N. Belokurova, A.N. Titkov, I.L. Shulpina, V.I. Safarov, and N.B. Guseva, "Ge-Si Solid Solutions, Experiment MA-150," in: Appolo-Soyuz Test Project (ASTP), NASA Report TM-X-73360, MSFC, Section IX, 1977.

27. A.A. Chernov, S.N. Maksimovskii, L.A. Vlasenko, E.N. Kholina, V.P. Martovitskii, and V.L. Levtov, "Growth of Germanium Crystals with Low Dislocation Density in a Condition of Weightlessness," *Soviet Physics Crystallography* **29**(1984),222-225.

28. V.T. Khryapov, V.A. Tatarinov, T.V. Kul'chitskaya, N.A. Kul'chitskiy, E.V. Markov, and R.S. Krupyshev, "Growth of Ge Bulk Single Crystals by Directional Solidification in Microgravity," in: V.S. Avduevsky (ed.) Technological Processes in Low Gravity (UNTS AN SSSR, Sverdlovsk 1983),pp.47-58.

29. E.V. Markov, and R.S. Krupyshev, and Yu.N. Kuznetsov, "Growth of Ge Bulk Single Crystals by Directional Solidification and Segregation in Microgravity," in: Thesis of VI International Conference on Crystal Growth, Moscow 10-16 September 1980, vol.2, p.261.

30. E. Tillberg and T. Carlberg, "Semi-Confined Bridgman Growth of Germanium Crystals in Microgravity," *J.Crystal Growth* **99**(1990),1265-1272.

31. E.V. Markov et.al., "The Influence of Space Conditions on Directional Crystallization of Germanium and its Properties," in: Proceedings of the 3rd European Symposium on Material Science in Space, ESA SP-142, Grenoble (1979), pp.17-23.

32. E. V. Markov, R.S. Krupishev, Yu.N. Kuznetsov, T.V. Kulchitskaya, N.A. Kulchitsky, T.I. Markova, V.A. Tatarinov, and V.T. Khryapov, "Growth of Bulk Germanium Single Crystals by Directional Crystallization and Segregation Processes in Microgravity," in: Proceedings of ICCG-6, Moscow, 1980, pp.273-274.

33. T. Nishinaga, Y. Okamoto, S. Yoda, T. Nakamura, O. Saito, Y. Hisada, H. Ando, and S. Anzawa, "Rapid Melt Growth of Ge by TR-IA Sounding Rocket," *J. Jpn. Soc.Microgravity Appl.* **10**-4(1993),2-10.

34. T. Nishinaga "Utilization of Microgravity to Understand the Crystal Growth of Semiconductors," *Microgravity Q.* **3**(1993),109-113.

35. W.A. Arnold and L.L. Regel, "Thermal Stability and the Suppression of Convection in a Rotating Fluid on Earth," in: Materials Processing in High Gravity, L.L. Regel and W.R. Wilcox, eds., Plenum Press, New York, 1994.

Table 1. Parameters used in the numerical calculations. Some data are for InSb, while others were assumed.

Parameters	Symbol	Value
Thermal conductivity of melt	k_l	$1.3*10^6$ erg/(cm*K*s)
Thermal conductivity of solid	k_s	$4.6*10^5$ erg/(cm*K*s)
Thermal conductivity of quartz	k_a	$3.1*10^5$ erg/(cm*K*s)
Thermal conductivity of gas in the gap	k_g	$2*10^4$ erg/(cm*K*s)
Latent heat of solidification per unit volume	Q	$1.3*10^{10}$ erg/cm^3
Freezing rate	V_c	10^{-4} cm/s
Diffusion coefficient of dissolved gas in melt	D	10^{-5} cm^2/s
Segregation coefficient of dissolved gas at the solidification interface	k	0.03
Average temperature of gas in the gap	T_{avg}	800 K
Meniscus surface tension	σ	430 erg/cm^2
Contact angle of melt on quartz	θ	112 degrees
Growth angle	α_0	25 degrees
Density	ρ	6.4 g/cm^3
Volumetric thermal expansion coefficient	β_T	10^{-4} K^{-1}
Acceleration due to gravity	g_0	981 cm/s^2

Table 2. Thermal configurations used in the numerical analysis.

	T_c (K)	T_h (K)	Furnace temperature gradient (K/cm)	Length (L_a) and position of the insulated zone relative to the ampoule	Heat transfer coefficient between the ampoule wall and the furnace wall (erg s^{-1} cm^{-2} K^{-1})
Grad - I	780	830	12.5		$2*10^6$
Grad - II	765	815	12.5		$2*10^6$
Grad - III	780	830	12.5		$2*10^5$
Brid - I	780	830		L_a = 1/3 L ; a) from 1/9 L to 4/9 L; b) from 3/9 L to 6/9 L; c) from 5/9 L to 8/9 L	$2*10^6$
Brid - II	765	815		L_a = 1/3 L ; a) from 1/9 L to 4/9 L; b) from 3/9 L to 6/9 L; c) from 5/9 L to 8/9 L	$2*10^6$
Brid - III	780	830		L_a = 1/9 L ; from 4/9 L to 5/9 L (center)	$2*10^6$
Brid - IV	765	815		L_a = 1/9 L ; from 4/9 L to 5/9 L (center)	$2*10^6$

APPENDIX

Asymmetric Weighting Functions for Finite Difference Equation in Cylindrical Coordinates

Assuming that the operator L is:

$$L = \frac{\partial^2}{\partial x^2} + \frac{\partial^2}{\partial r^2} + \frac{1}{r}\frac{\partial}{\partial r} - \frac{V_x}{D}\frac{\partial}{\partial x} - \frac{V_r}{D}\frac{\partial}{\partial r} \tag{A.1}$$

the weak form of equation (7) is:

$$\left(W_{ij}, LC\right) = \iint_{\Omega}\left(W_{ij}\frac{\partial^2 C}{\partial x^2} + W_{ij}\frac{\partial^2 C}{\partial r^2} + \frac{W_{ij}}{r}\frac{\partial C}{\partial r} - W_{ij}\frac{V_x}{D}\frac{\partial C}{\partial x} - W_{ij}\frac{V_r}{D}\frac{\partial C}{\partial r}\right)dxdr \tag{A.2}$$

Here W_{ij} is an asymmetric weighting function, with the form:

$$W_{ij}(x,r) = \left(N_i(x) \pm \xi \cdot n_i(x)\right)\left(N_j(r) \pm \eta \cdot n_j(r)\right) \tag{A.3}$$

where (+) refers to $x \in [x_{i-1}, x_i]$ *and* $r \in [r_{j-1}, r_j]$, and (-) refers to $x \in [x_i, x_{i+1}]$ *and* $r \in [r_j, r_{j+1}]$.

According to equation (9), ξ and η are positive if the local velocities V_x and V_r are positive in the defined coordinate system, and are negative if the respective components of velocity are less than zero. Here N_j are linear weighting functions with the form:

$$N_i(x) = \frac{x - x_{i-1}}{x_i - x_{i-1}} \quad and \quad N_j(r) = \frac{r - r_{j-1}}{r_j - r_{j-1}} \text{ for } x \in [x_{i-1}, x_i] \quad and \quad r \in [r_{j-1}, r_j] \tag{A.4a}$$

$$N_i(x) = \frac{x_{i+1} - x}{x_{i+1} - x_i} \quad and \quad N_j(r) = \frac{r_{j+1} - r}{r_{j+1} - r_j} \text{ for } x \in [x_i, x_{i+1}] \quad and \quad r \in [r_j, r_{j+1}] \tag{A.4b}$$

The asymmetric parts of the weighting functions are represented as:

$$n_i(x) = -\frac{3(x - x_{i-1})(x - x_i)}{(x_i - x_{i-1})^2} \quad and \quad n_j(r) = -\frac{3(r - r_{j-1})(r - r_j)}{(r_j - r_{j-1})^2} \text{ for}$$

$$x \in [x_{i-1}, x_i] \quad and \quad r \in [r_{j-1}, r_j]; \tag{A.5a}$$

$$n_i(x) = -\frac{3(x - x_i)(x - x_{i+1})}{(x_{i+1} - x_i)^2} \quad and \quad n_j(r) = -\frac{3(r - r_j)(r - r_{j+1})}{(r_{j+1} - r_j)^2} \text{ for}$$

$$x \in [x_{i-1}, x_i] \quad and \quad r \in [r_{j-1}, r_j]. \tag{A.5b}$$

The integration in the space of weighting functions over x and r can be carried out at five points, corresponding to grid points in the finite difference scheme. In this case, the weighting function $W_{ij}(x,r)$ can be separated in such a way that it depends only on x for integration over x and depends only on r for integration over r. In the Galerkin method, weighting functions without asymmetric parts are also used for the representation of the unknown function in the nodal coordinates.

We use the finite difference discretization of the elliptic equation (7):

$$A_x C_{i-1,j} + A_r C_{i,j-1} + B C_{i,j} + E_x C_{i+1,j} + E_r C_{i,j+1} \tag{A.6}$$

where the coefficients in (A.7) are:

$$A_x = \int_{x_{i-1}}^{x_i} \left(\frac{1}{h_{i-1}} - 3\xi \frac{2x - x_{i-1} - x_i}{h_{i-1}^2} \right) \cdot \left(-\frac{1}{h_{i-1}} \right) dx + \frac{V_x}{D} \int_{x_{i-1}}^{x_i} \left(\frac{x - x_{i-1}}{h_{i-1}} - 3\xi \frac{(x - x_{i-1})(x - x_i)}{h_{i-1}^2} \right) \cdot \left(-\frac{1}{h_{i-1}} \right) dx$$

$$E_x = \int_{x_i}^{x_{i+1}} \left(-\frac{1}{h_i} + 3\xi \frac{2x - x_i - x_{i+1}}{h_i^2} \right) \cdot \left(\frac{1}{h_i} \right) dx + \frac{V_x}{D} \int_{x_i}^{x_{i+1}} \left(-\frac{x - x_{i+1}}{h_i} + 3\xi \frac{(x - x_i)(x - x_{i+1})}{h_i^2} \right) \cdot \left(\frac{1}{h_i} \right) dx$$

$$A_r = \int_{r_{j-1}}^{r_j} \left(\frac{1}{h_{j-1}} - 3\eta \frac{2r - r_{j-1} - r_j}{h_{j-1}^2} \right) \cdot \left(-\frac{1}{h_{j-1}} \right) dr + \int_{r_{j-1}}^{r_j} \left(\frac{V_r}{D} + \frac{1}{r} \right) \left(\frac{r - r_{j-1}}{h_{j-1}} - 3\eta \frac{(r - r_{j-1})(r - r_j)}{h_{j-1}^2} \right) \cdot \left(-\frac{1}{h_{j-1}} \right) dr$$

$$E_r = \int_{r_j}^{r_{j+1}} \left(-\frac{1}{h_j} + 3\eta \frac{2r - r_j - r_{j+1}}{h_j^2} \right) \cdot \left(\frac{1}{h_j} \right) dr + \int_{r_j}^{r_{j+1}} \left(\frac{V_r}{D} + \frac{1}{r} \right) \left(-\frac{r - r_{j+1}}{h_j} + 3\eta \frac{(r - r_j)(r - r_{j+1})}{h_j^2} \right) \cdot \left(\frac{1}{h_j} \right) dr$$

$$B = -A_r - A_x - E_r - E_x$$

(A.7)

Deriving the integrals:

$$A_x = -\frac{1}{2}(\xi + 1)\frac{V_x}{D} - \frac{1}{h_{i-1}} \qquad A_r = -\frac{1}{2}(\eta + 1)\frac{V_r}{D} - \frac{r_{j-1} \ln\left(\frac{r_j}{r_{j-1}}\right)}{h_{j-1}^2} + \eta \left(\frac{3}{2} \frac{r_{j-1} + r_j}{h_{j-1}^2} - \frac{3 \cdot r_{j-1} r_j \ln\left(\frac{r_j}{r_{j-1}}\right)}{h_{j-1}^3} \right)$$

$$E_x = -\frac{1}{2}(\xi - 1)\frac{V_x}{D} - \frac{1}{h_i} \qquad E_r = -\frac{1}{2}(\eta - 1)\frac{V_r}{D} - \frac{r_{j+1} \ln\left(\frac{r_{j+1}}{r_j}\right)}{h_j^2} + \eta \left(\frac{3}{2} \frac{r_j + r_{j+1}}{h_j^2} - \frac{3 \cdot r_j r_{j+1} \ln\left(\frac{r_{j+1}}{r_j}\right)}{h_j^3} \right)$$

(A.8)

These coefficients were used in the numerical calculations for discretization of (7) into (A.6).

NOMENCLATURE

Latin letters

C - Concentration of dissolved gas in the melt [mole cm^{-3}];

D - Diffusion coefficient of dissolved gas in the melt [$cm^2\ s^{-1}$];

e - Gap width [cm];

g - Acceleration of gravity [$cm\ s^{-2}$];

h - Heat transfer coefficient between outer ampoule wall and furnace ambient [$erg\ cm^{-2}\ s^{-1}\ K^{-1}$];

j_{mol} - Molar flux per length of the meniscus line in the axisymmetric case [$mol\ s^{-1}\ cm^{-1}$];

k - Segregation coefficient of dissolved gas between solid and melt;

k_l, k_g, k_s, k_a - Thermal conductivities of the phases (liquid, gas, solid, and ampoule material) [$erg\ cm^{-1}\ s^{-1}\ K^{-1}$];

l_a - Length of the meniscus line [cm];

L_m - Length of the column of melt [cm];

n - Normal direction at the meniscus, inward toward the melt (Fig.3) [cm];

p_m - Pressure over the column of melt, assumed to be the same at L_a [$dyne\ cm^{-2}$];

p_g - Pressure of gas in the gap [$dyne\ cm^{-2}$];

Δp_c - Pressure difference across the meniscus between the gap and the adjacent melt due to meniscus curvature, $p_g - p_m$ [$dyne\ cm^{-2}$];

Δp_h - Hydrostatic head over the meniscus, $\rho g L_m$, [$dyne\ cm^{-2}$];

r - Radial direction [cm];

R - Ideal gas constant, $8.314*10^7$ [$erg\ mol^{-1}\ K^{-1}$];

R_a - Inner ampoule radius [cm];

Q - Latent heat of solidification per unit volume [$erg\ cm^{-3}$];

s - Direction along the meniscus [cm]; s=0 is at the freezing interface;

S - Area of the meniscus [cm^2];

T_c - Temperature of the cold zone [K];

T_h - Temperature of the hot zone [K];

T_f - Temperature of the freezing interface [K];

T_{gap} - Average temperature of gas in the gap [K];

V_c - Solidification rate [cm s^{-1}];

W - Weighting function;

x - Axial direction [cm];

z - Interface deflection from planarity

Greek letters

α - Angle between the meniscus line and the axial direction at the three-phase line (Fig.2) [rad];

α_0 - Growth angle [rad];

β_T - Volumetric thermal expansion coefficient [K^{-1}];

θ - Contact angle of the melt at the ampoule wall [rad];

ρ - Density of the melt [g cm^{-3}];

ν - Kinematic viscosity of the melt [cm^2 s^{-1}];

κ - Thermal diffusivity of the melt [cm^2 s^{-1}];

σ - Surface tension of meniscus [dyne cm^{-1}];

ψ - Stream function [cm^3 s^{-1}];

ω - Vorticity [s^{-1}];

ξ - Coefficient in the representation of asymmetric weighting function (equation (9));

η - Coefficient in the representation of asymmetric weighting function (equation (9));

Subscripts

a - Ampoule (within the wall);

amb - Ambient (in the furnace);

c - Cold zone;

f - Freezing interface;

g - Gas;

h - Hot zone;

l - Melt(liquid);

s - Solid.

DIMENSIONLESS PARAMETERS

Pr $= \nu/\kappa$ - Prandtl number. Ratio of kinematic viscosity to thermal diffusivity (~ 0.04 for InSb at melting point);

Sc $= \nu/D$ - Schmidt number. Ratio of kinematic viscosity to diffusion coefficient (~ 360 for InSb at melting point);

Re^{loc} $= V^{loc}*R_a/\nu$ - local Reynolds number. Dependent on local velocity field;

Pe^{loc} $= Re^{loc}*Sc$ - local mass transfer Peclet number. Characterizes the ratio of convective mass transfer to diffusion mass transfer.

Ra $= \beta g(T_h-T_f)(R_a^4/L_m)/\nu\kappa$ - Rayleigh number

FIGURE CAPTIONS

Fig.1. Model of detached solidification with acceleration g.

Fig.2. Furnace configurations modeled here. Solidification is caused by slowly decreasing the temperature in the vertical gradient freeze technique (VGF), and by slowly lowering the ampoule in the vertical Bridgman-Stockbarger (VBS) method.

Fig.3a. Isotherms calculated for VGF without detachment. ΔT between the isotherms is 0.83 K. Freezing rate is 10^{-4} cm/s.

Fig.3b. Isotherms calculated for VGF with a gap width e of 0.12 cm. All parameters are the same as in Figure 3a.

Fig.4a. The interface shape in VGF without detachment. Note that the vertical scale is greatly magnified.

Fig.4b. The interface shape in VGF with a gap width e of 0.12 cm.

Fig.5a. Streamlines for the VGF Grad-I thermal configuration with acceleration g from 10^{-5} to 10^{-2} g_0. The spacing between streamlines $\Delta\psi$ is not constant, but increases with g. These figures depict the flow pattern only.

Fig.5b. Streamlines for the VGF Grad-III thermal configuration with acceleration g from 10^{-5} to 10^{-2} g_0. The spacing between streamlines $\Delta\psi$ increases with g.

Fig.6. The dependence of the maximum local mass transfer Peclet number on the Rayleigh number in VGF. The value of Pe begins to increase at the flow transition from linear to circulating convection.

Fig.7. The concentration field for the VGF Grad-I thermal configuration versus acceleration. Note that the horizontal scale is expanded by a factor of 2.9. The spacing between isoconcentration lines is $\Delta C=2*10^{-8}$ mol/cm^3.

Fig.8. Radial concentration profile at the freezing interface for different accelerations (VGF Grad-I thermal configuration).

Fig.9. Normal gradient of concentration along the meniscus for different accelerations (Grad-I). A positive value causes diffusion into the gap. A negative value produces back-diffusion from the gap into the melt.

Fig.10. The dependence on acceleration of the total gas flux j_{mol} into the gap (equation (14)), normalized by the diffusion coefficient D, for VGF Grad-I and Grad-III.

Fig.11a Isotherms calculated for the vertical Bridgman-Stockbarger (VBS) configuration Brid-I with a gap width e of 0.12 cm. The length of the insulation zone is 1/3 of the sample length.

Fig.11b Isotherms calculated for VBS Brid-II with a gap width e of 0.12 cm. The length of the insulation zone is 1/3 of the sample length.

Fig.12a. Interface shape in VBS Brid-I for different positions of ampoule relative to the insulation zone as given in Table 2. The gap width e is 0.12 cm. Note that the vertical scale is greatly magnified.

Fig.12b. Interface shape in VBS Brid-II for different position of the ampoule relative to the insulation zone as given in Table 2. The gap width e is 0.12 cm.

Fig.12c. Interface shape in VBS Brid-I and Brid-II for two different lengths of the adiabatic zone (see Table 2). The gap width e is 0.12 cm.

Fig.12d. Interface shape in VBS Brid-II for different positions of the ampoule. The gap width e is 0.05 cm. See Table 2 for a,b and c conditions.

Fig.12e. Interface shape in VBS Brid-I for different positions of the ampoule. The gap width e is 0.12 cm. The ampoule radius is 0.5 cm.

Fig.12f. Interface shape in VBS Brid-II for different position of the ampoule. The gap width e is 0.12 cm. The ampoule radius is 0.5 cm.

Fig.13a. Streamlines for VBS Brid-Ib thermal configuration with acceleration from 10^{-5} to 10^{-2} g_0. The spacing between streamlines $\Delta\psi$ increases with g.

Fig.13b. Streamlines for VBS Brid-IIb thermal configuration with acceleration from 10^{-5} to 10^{-2} g_0. The spacing between streamlines $\Delta\psi$ increases with g.

Fig.14a. The concentration field for VBS Brid-I thermal configuration versus acceleration. Note that the horizontal scale is expanded by a factor of 2.67. The spacing between isoconcentration lines is $\Delta C=2*10^{-8}$ mol/cm^3.

Fig.14b. The concentration field for VBS Brid-II thermal configuration versus acceleration. Note that the horizontal scale is expanded by a factor of 2.1. The spacing between isoconcentration lines is $\Delta C=2*10^{-8}$ mol/cm^3.

Fig.15a. Radial concentration profile at the freezing interface for VBS Brid-I thermal configuration at different accelerations.

Fig.15b. Radial concentration profile at the freezing interface for VBS Brid-II thermal configuration at different accelerations.

Fig.16a. The normal gradient of concentration along the meniscus for VBS Brid-I at different accelerations. A positive value corresponds to diffusion into the gap. A negative value produces back-diffusion from the gap into the melt.

Fig.16b. The normal gradient of concentration along the meniscus for VBS Brid-I at different accelerations. A positive value corresponds to diffusion into the gap. A negative value produces back-diffusion from the gap into the melt.

Fig.17. The dependence on acceleration of the total gas flux j_{mol} into the gap (equation (14)), normalized by the diffusion coefficient D, for VBS Brid-I and Brid-II.

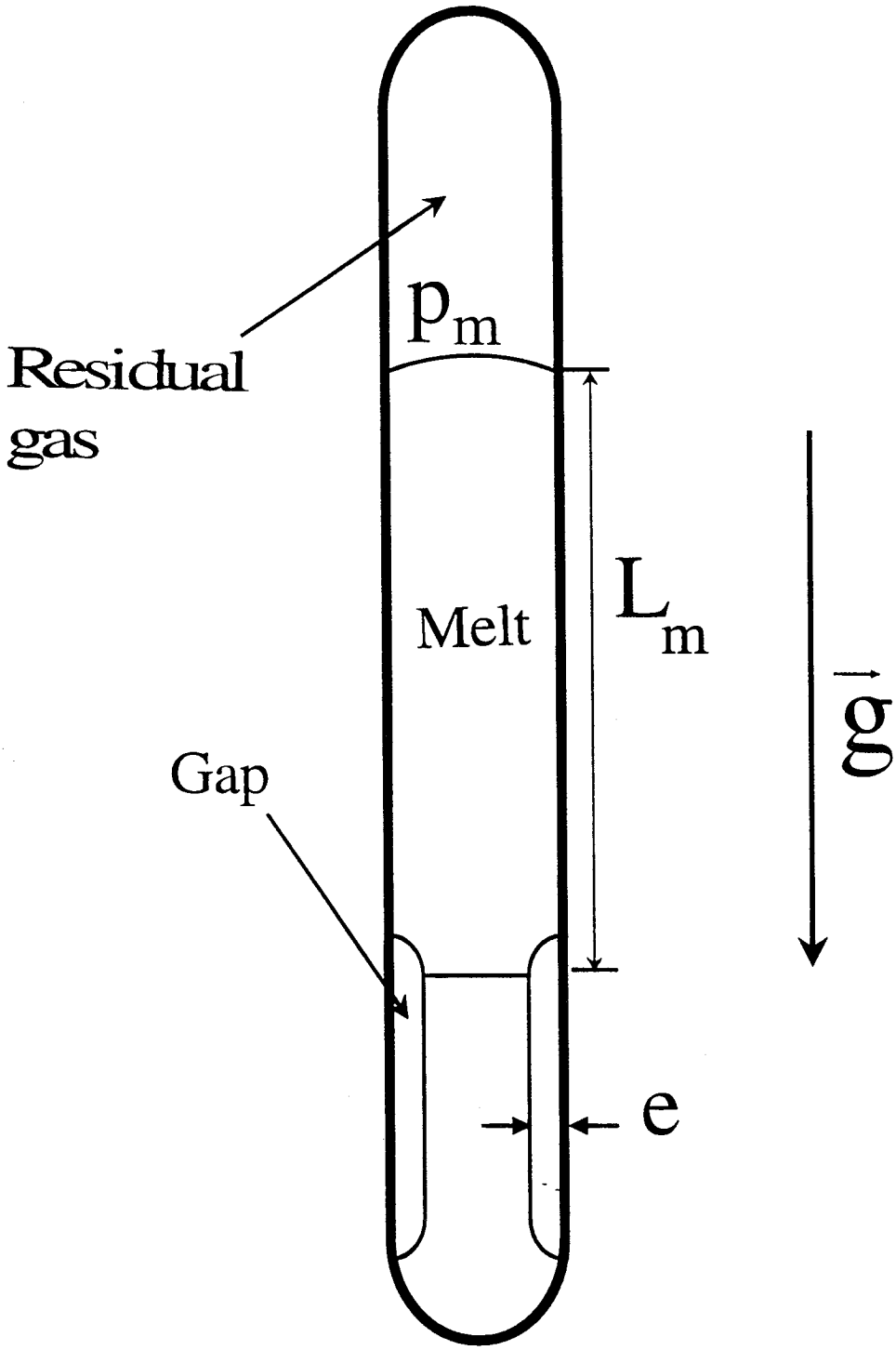

Fig. 1

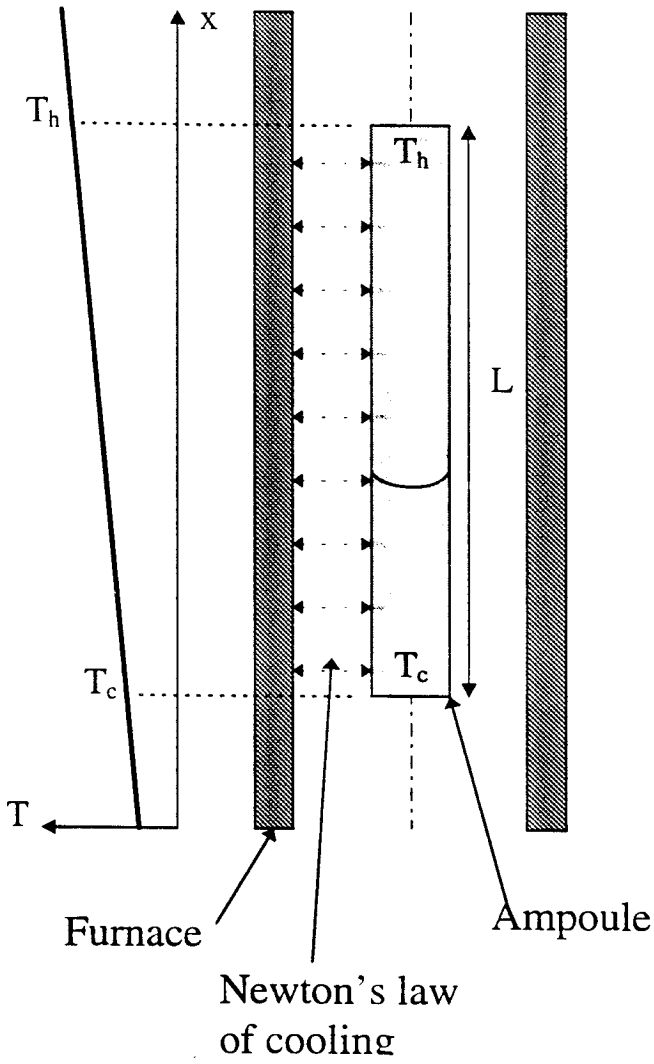

Gradient Freeze furnace

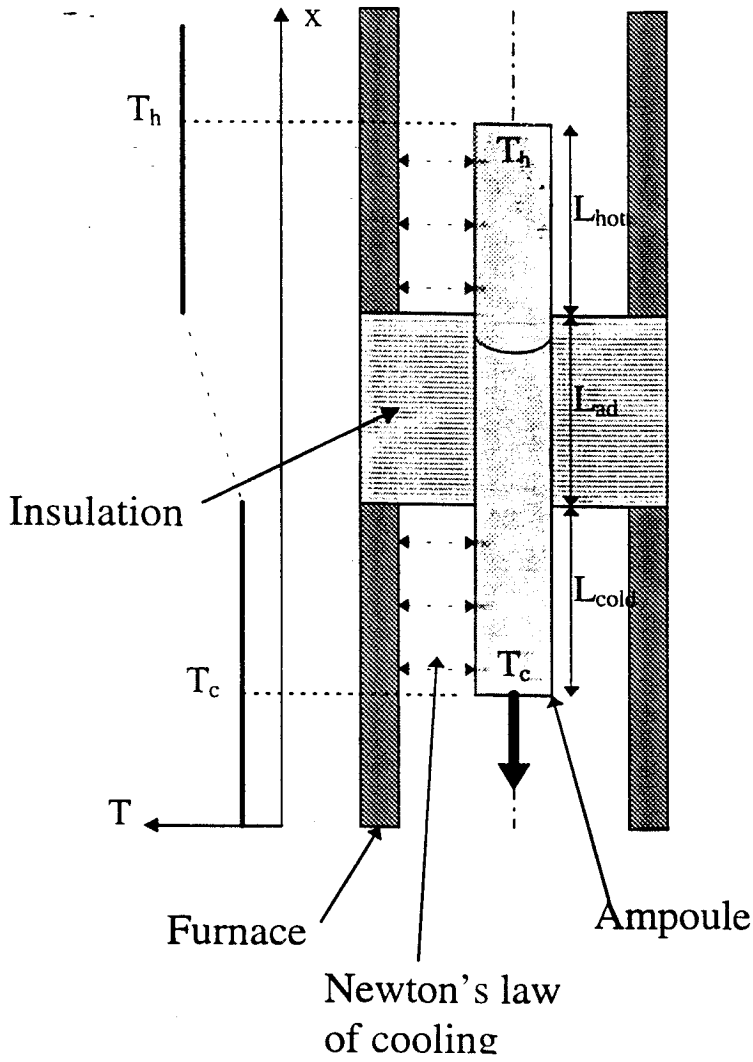

Bridgman furnace

Grad-I

$T_c = 780$ K $h = 2*10^6$ erg s^{-1} cm^{-2} K^{-1} $T_h = 830$ K

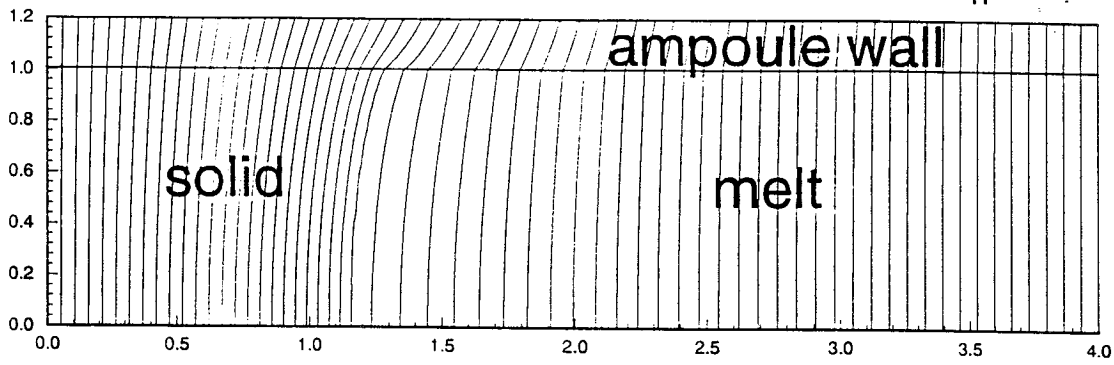

Grad-II

$T_c = 765$ K $h = 2*10^6$ erg s^{-1} cm^{-2} K^{-1} $T_h = 815$ K

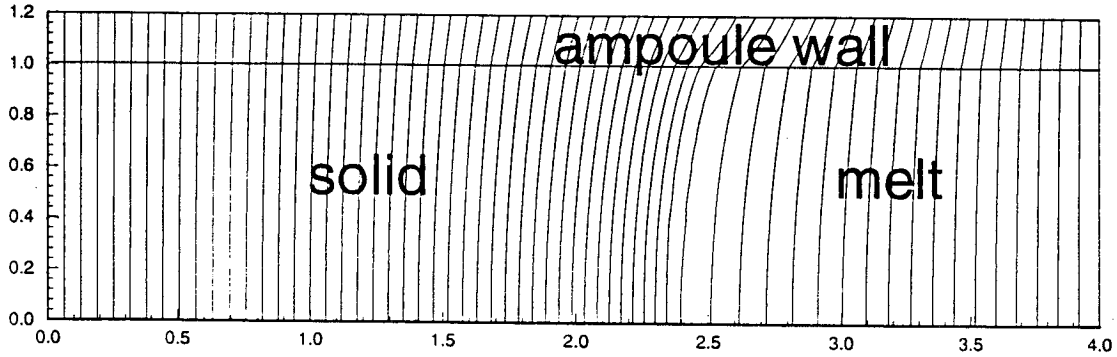

Grad-III

$T_c = 780$ K $h = 2*10^5$ erg s^{-1} cm^{-2} K^{-1} $T_h = 830$ K

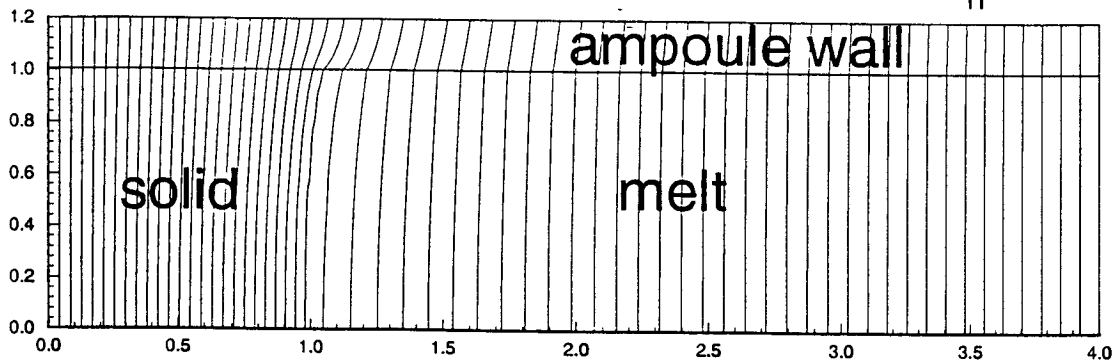

Grad-I

$T_c = 780$ K $T_h = 830$ K

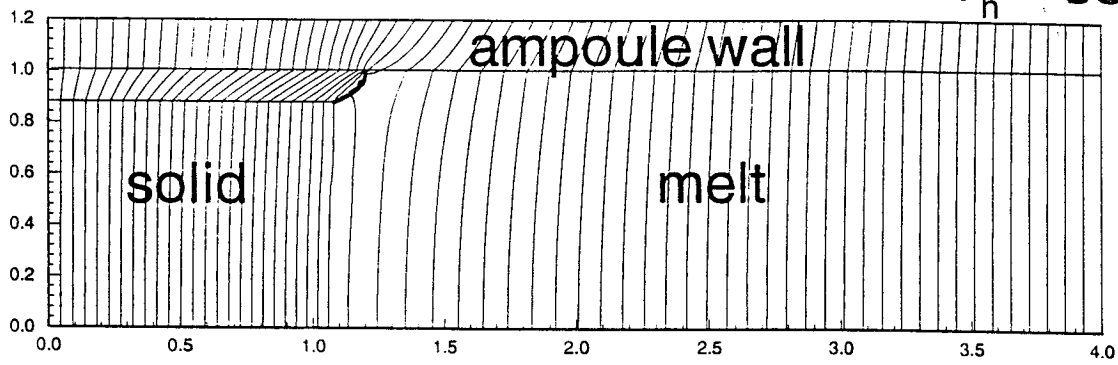

Grad-II

$T_c = 765$ K $T_h = 815$ K

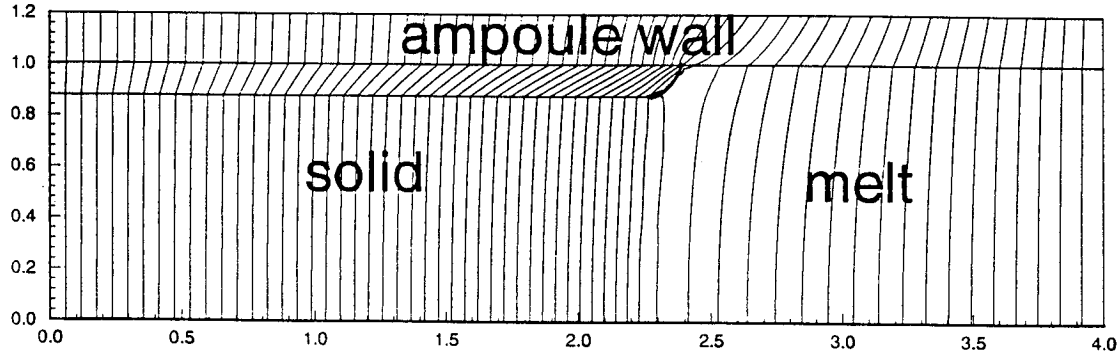

Grad-III

$T_c = 780$ K $T_h = 830$ K

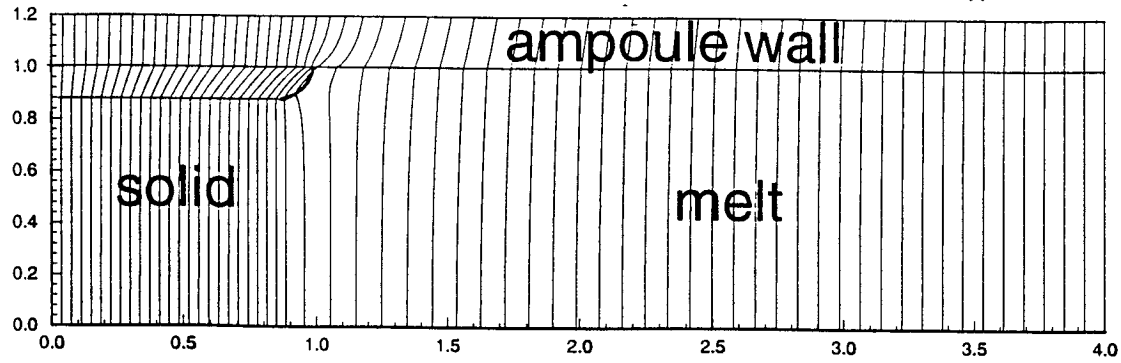

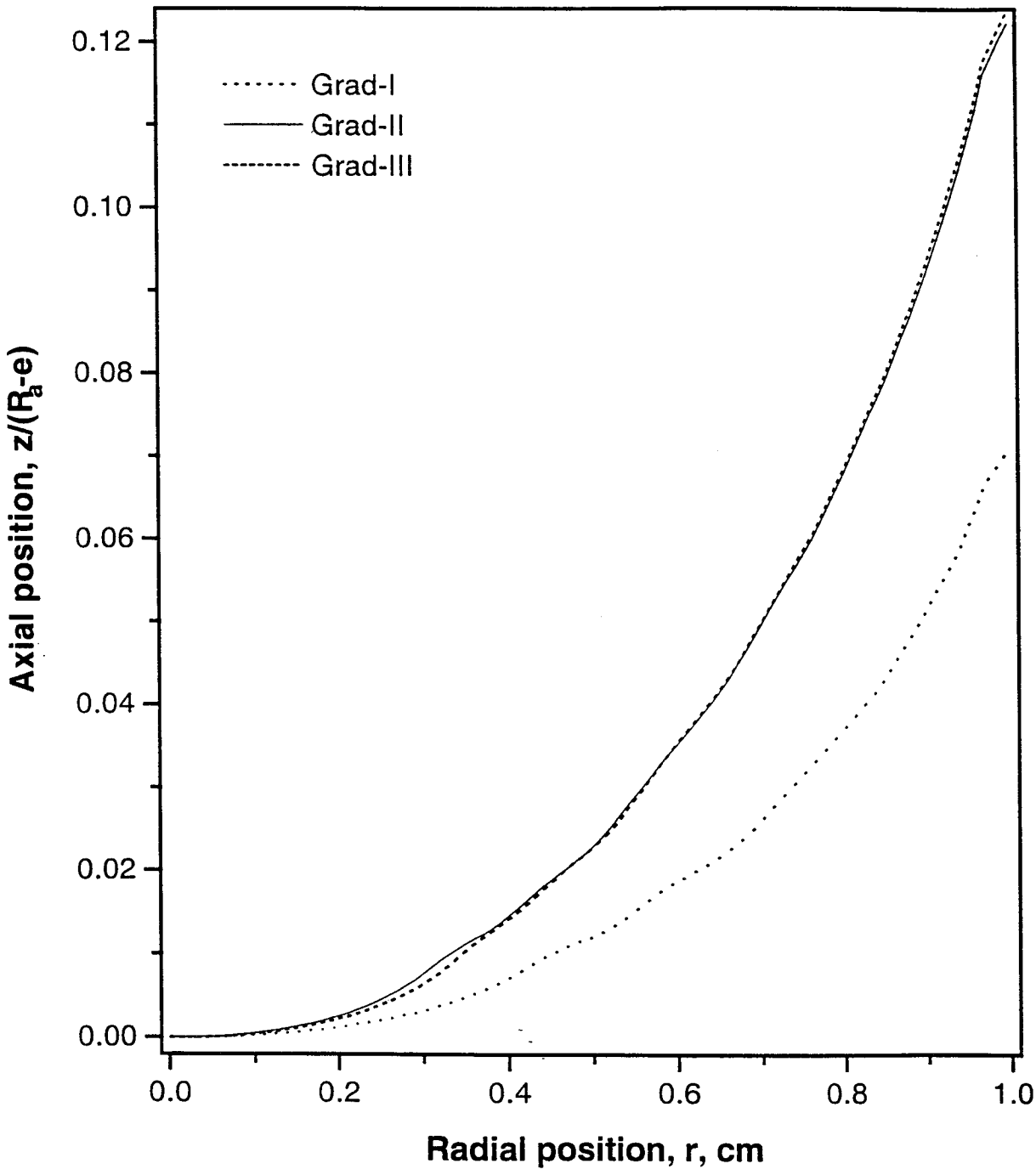
Grad-I
Grad-II
Grad-III
0.12
0.10
0.08
0.06
0.04
0.02
0.00
0.0
0.2
0.4
0.6
0.8
1.0
Axial position, z/(Ra-e)
Radial position, r, cm

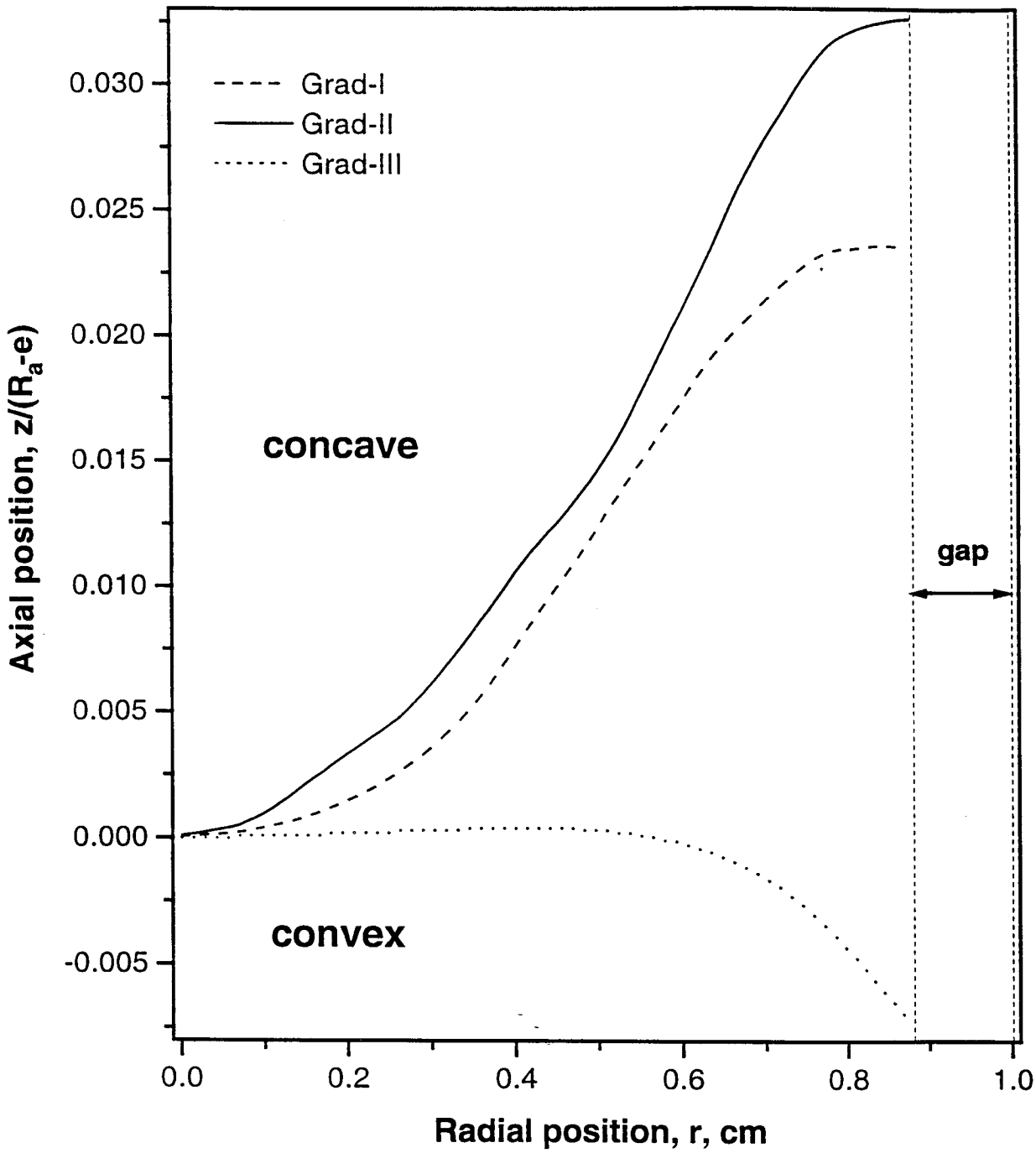
Grad-I
Grad-II
Grad-III
concave
convex
gap
0.030
0.025
0.020
0.015
0.010
0.005
0.000
-0.005
0.0
0.2
0.4
0.6
0.8
1.0
Axial position, z/(Ra-e)
Radial position, r, cm

Grad-I

$g = 10^{-5}\ g_0$

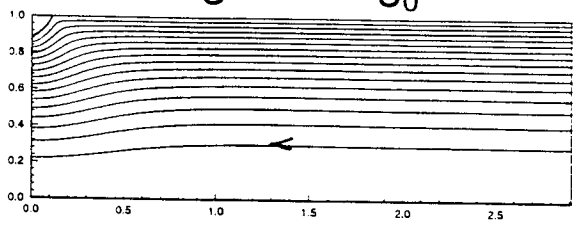

$g = 10^{-4}\ g_0$

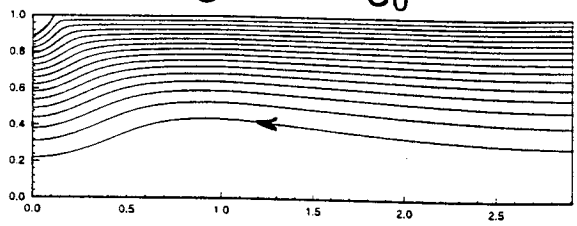

$g = 2*10^{-4}\ g_0$

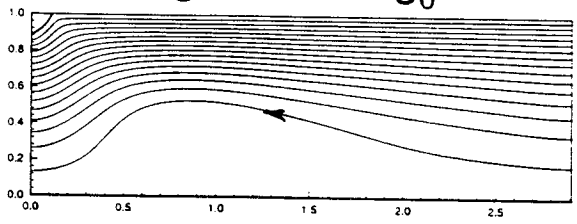

$g = 5*10^{-4}\ g_0$

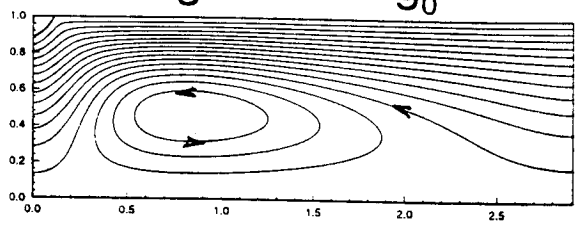

$g = 10^{-3}\ g_0$

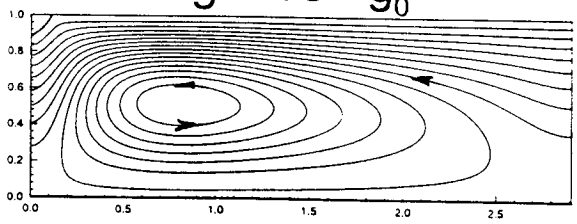

$g = 2*10^{-3}\ g_0$

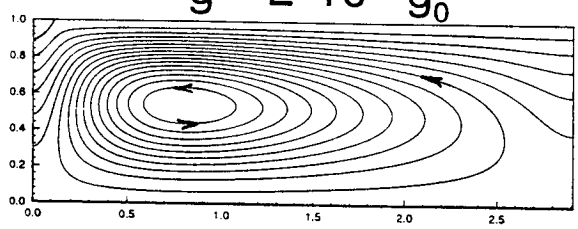

$g = 5*10^{-3}\ g_0$

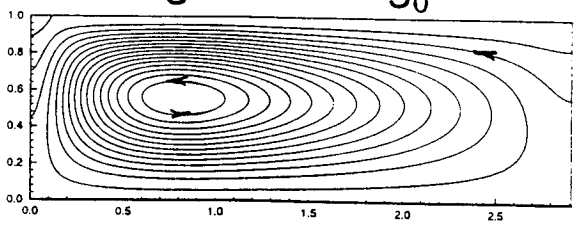

$g = 10^{-2}\ g_0$

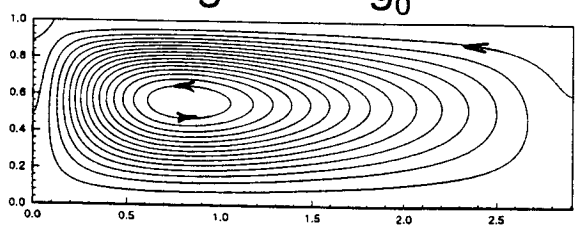

Grad-III

$g = 10^{-5}\, g_0$

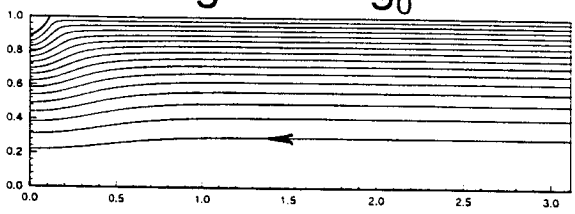

$g = 10^{-4}\, g_0$

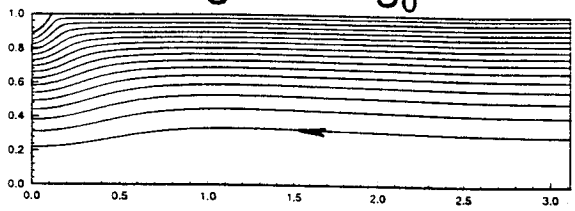

$g = 2*10^{-4}\, g_0$

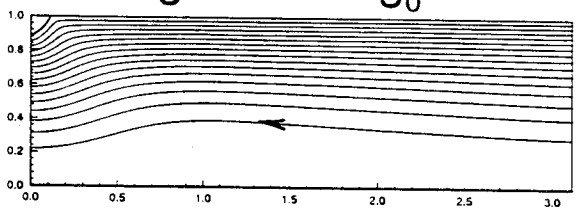

$g = 5*10^{-4}\, g_0$

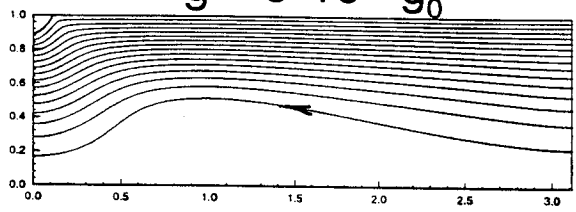

$g = 10^{-3}\, g_0$

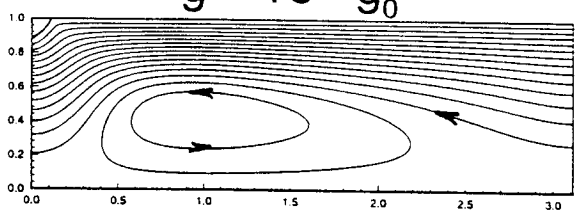

$g = 2*10^{-3}\, g_0$

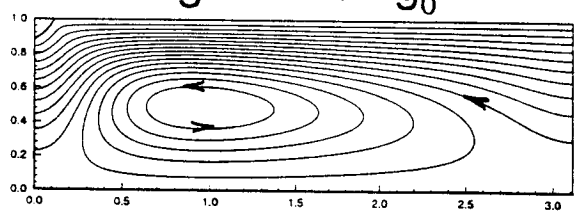

$g = 5*10^{-3}\, g_0$

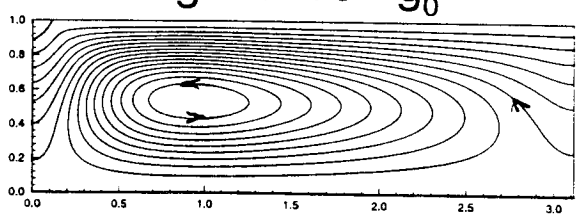

$g = 10^{-2}\, g_0$

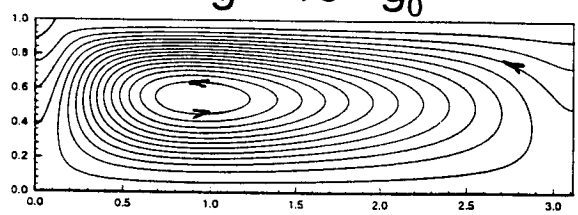

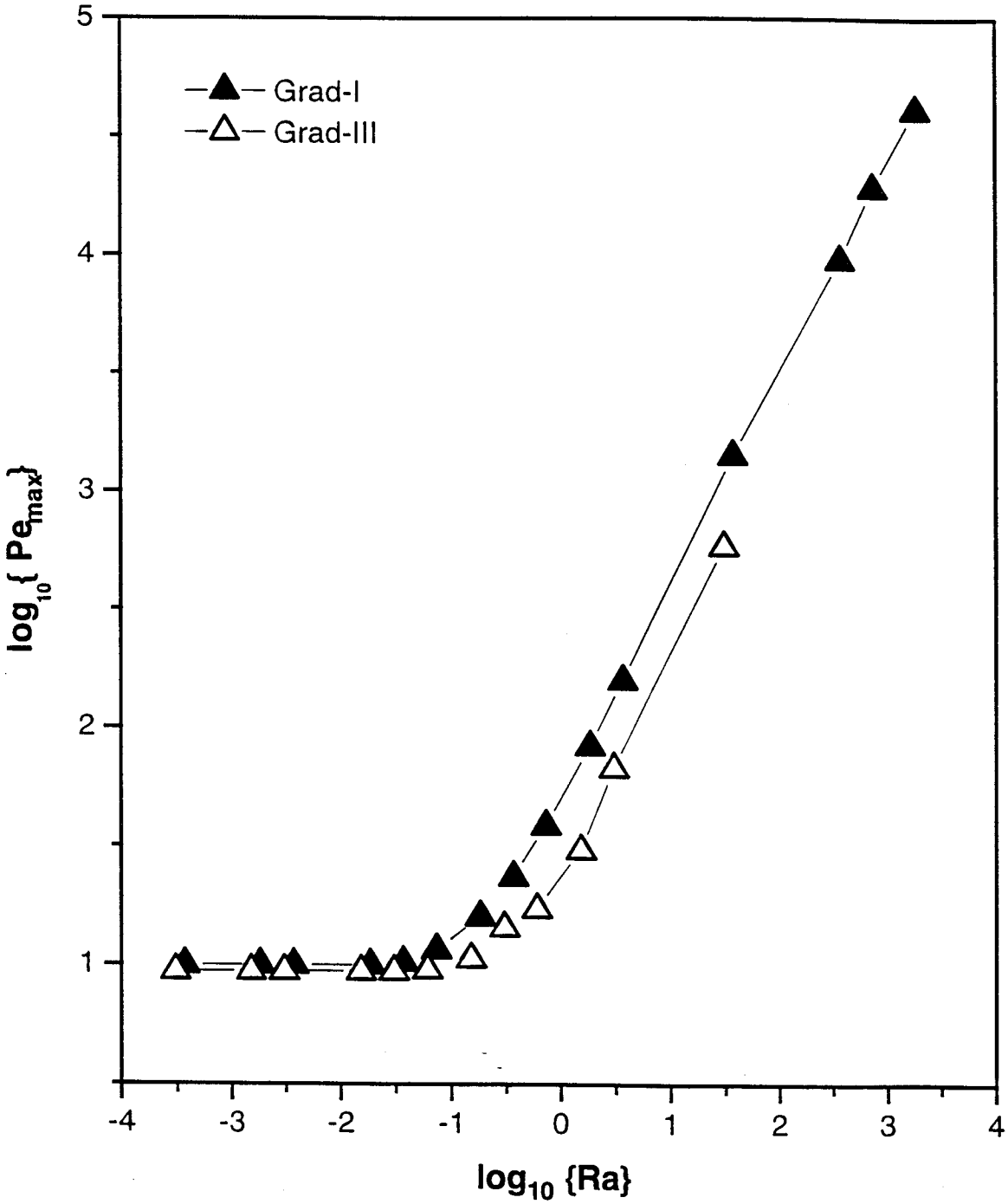
Grad-I
Grad-III
5
4
3
2
1
-4
-3
-2
-1
0
1
2
3
4
log10 { Pemax }
log10 {Ra}

Grad-I

$g = 10^{-5}\, g_0$

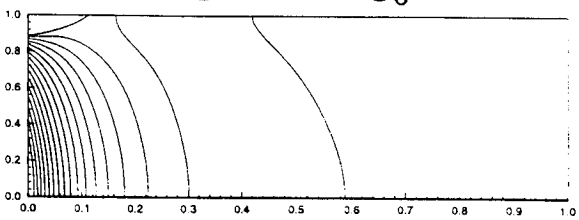

$g = 10^{-4}\, g_0$

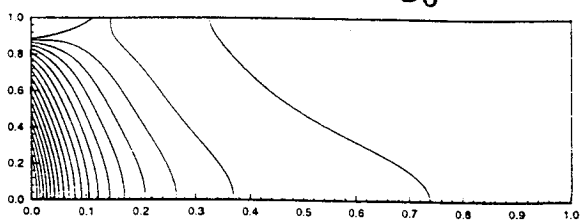

$g = 2*10^{-4}\, g_0$

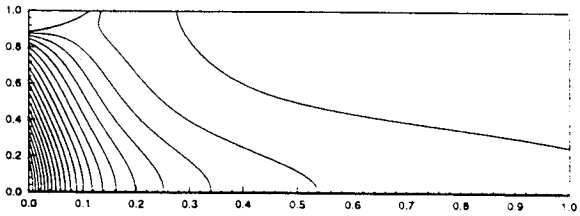

$g = 5*10^{-4}\, g_0$

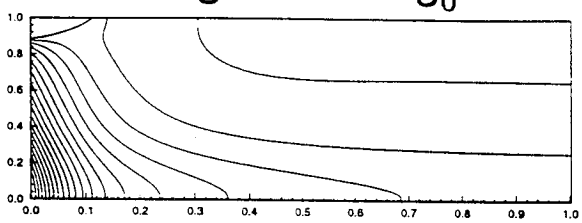

$g = 10^{-3}\, g_0$

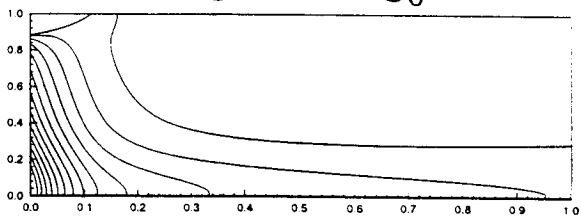

$g = 2*10^{-3}\, g_0$

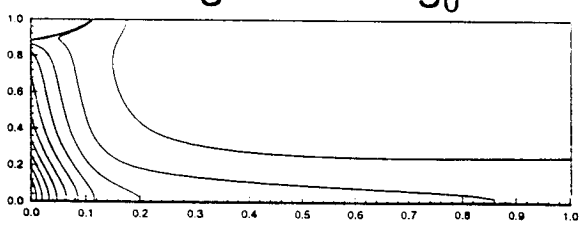

$g = 10^{-3}\, g_0$

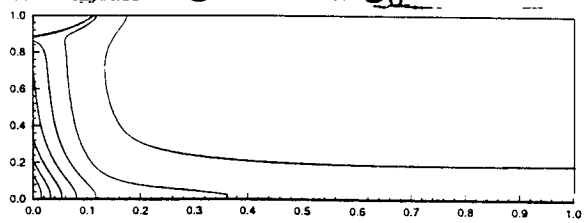

$g = 10^{-2}\, g_0$

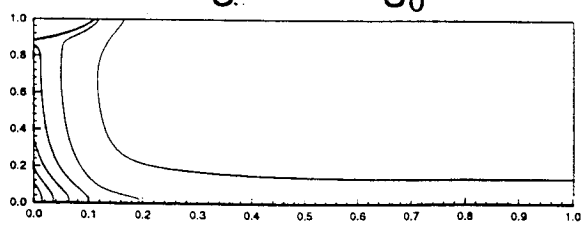

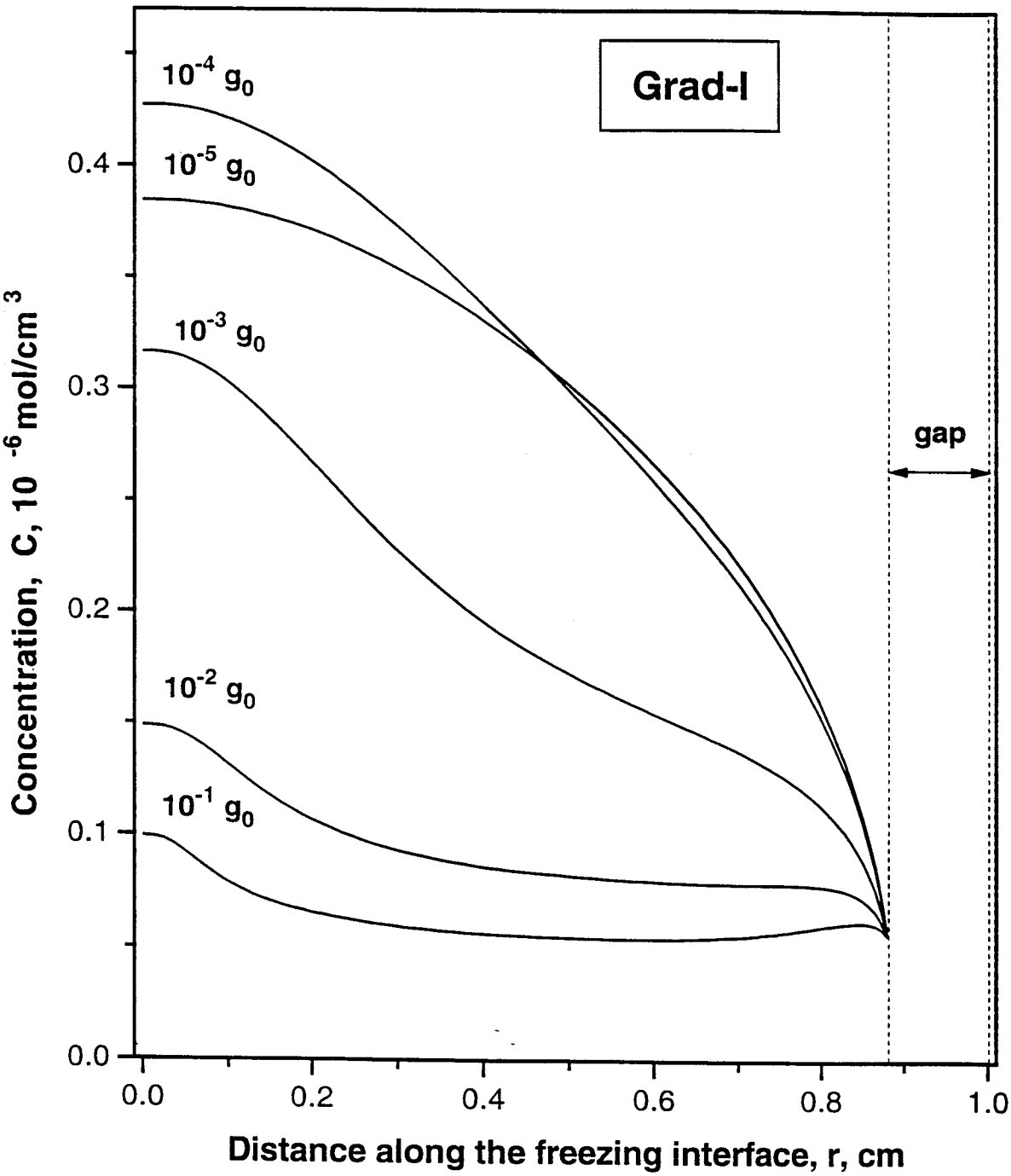
Grad-I
10^{-4} g_0
10^{-5} g_0
10^{-3} g_0
10^{-2} g_0
10^{-1} g_0
gap
Concentration, C, 10^{-6} mol/cm^3
0.0
0.1
0.2
0.3
0.4
0.0
0.2
0.4
0.6
0.8
1.0
Distance along the freezing interface, r, cm

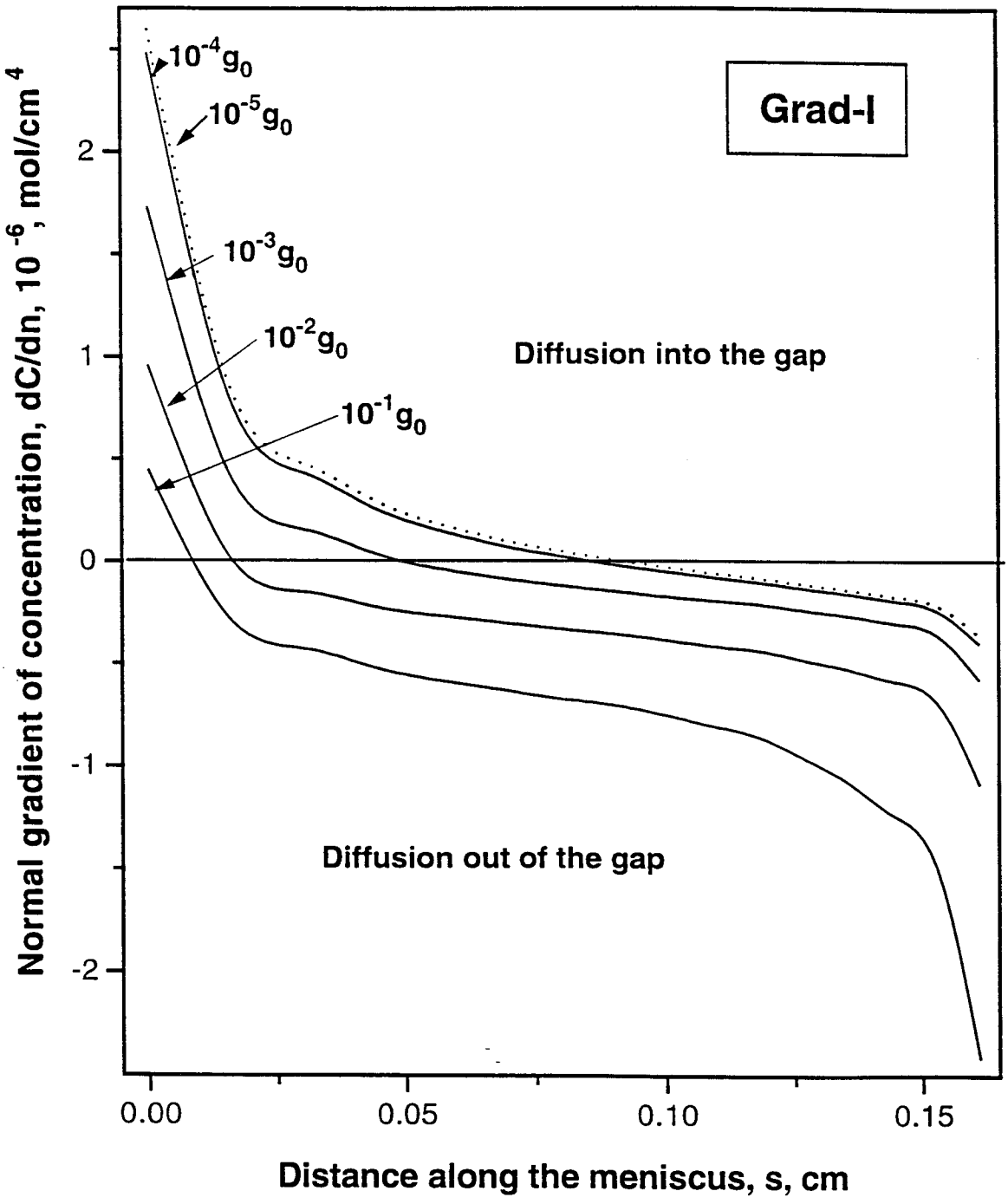
Grad-I
$10^{-4}g_0$
$10^{-5}g_0$
$10^{-3}g_0$
$10^{-2}g_0$
$10^{-1}g_0$
Diffusion into the gap
Diffusion out of the gap
Normal gradient of concentration, dC/dn, 10^{-6}, mol/cm^4
Distance along the meniscus, s, cm
2
1
0
-1
-2
0.00
0.05
0.10
0.15

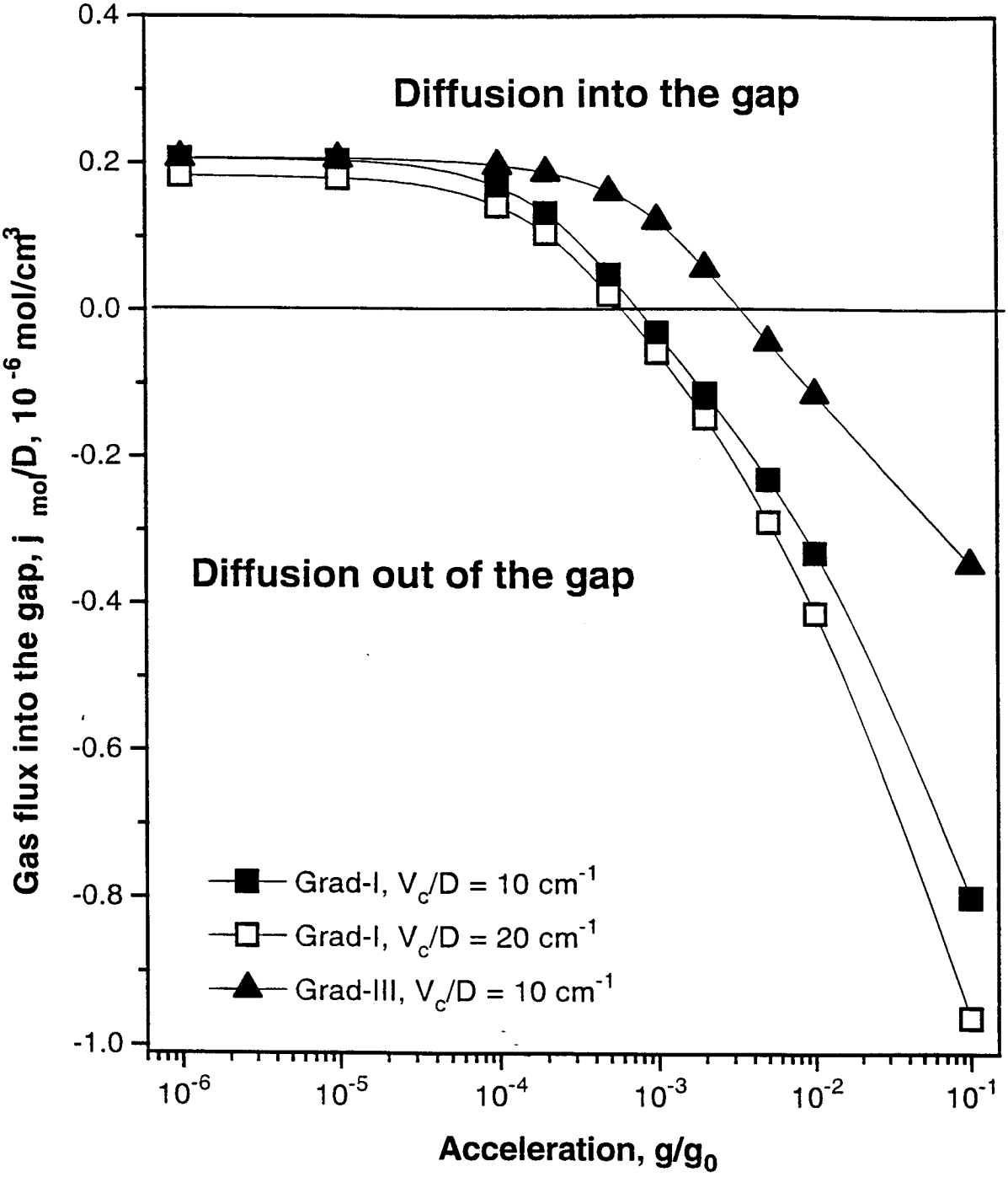
Diffusion into the gap
Diffusion out of the gap
Grad-I, V_c/D = 10 cm^{-1}
Grad-I, V_c/D = 20 cm^{-1}
Grad-III, V_c/D = 10 cm^{-1}
Gas flux into the gap, j_{mo}/D, 10^{-6} mol/cm^3
Acceleration, g/g_0
0.4
0.2
0.0
-0.2
-0.4
-0.6
-0.8
-1.0
10^{-6}
10^{-5}
10^{-4}
10^{-3}
10^{-2}
10^{-1}

Brid-Ia

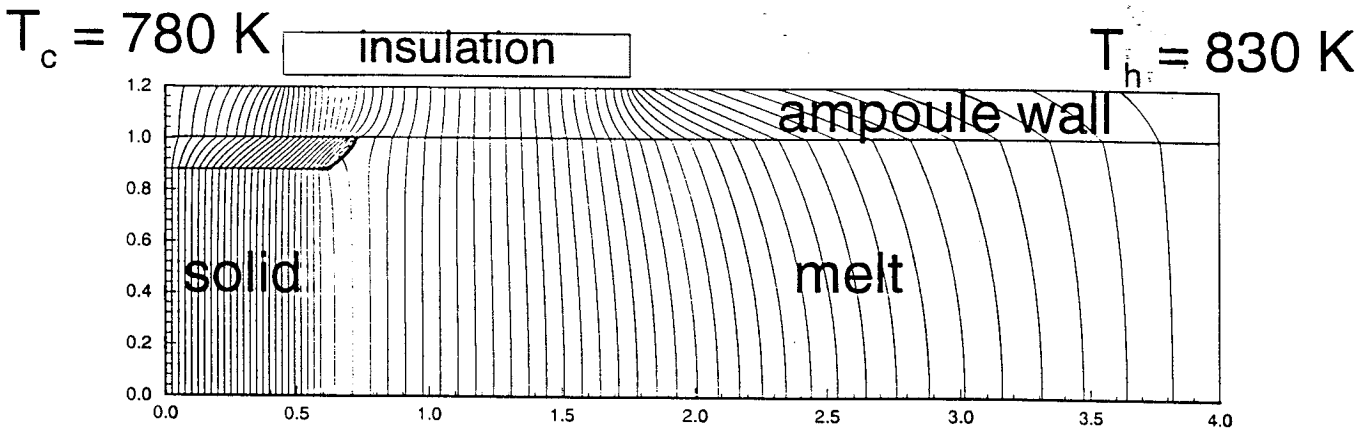

Brid-Ib

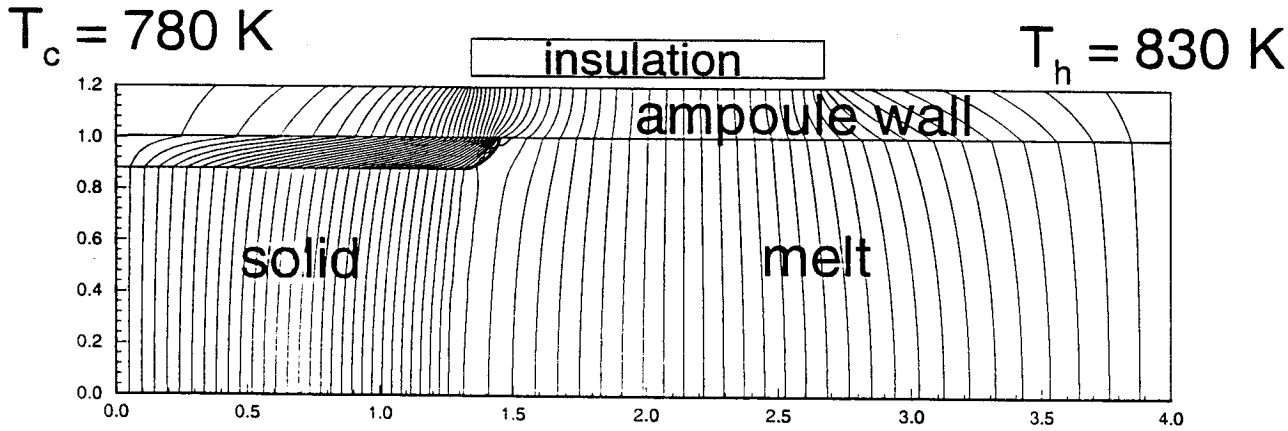

Brid-Ic

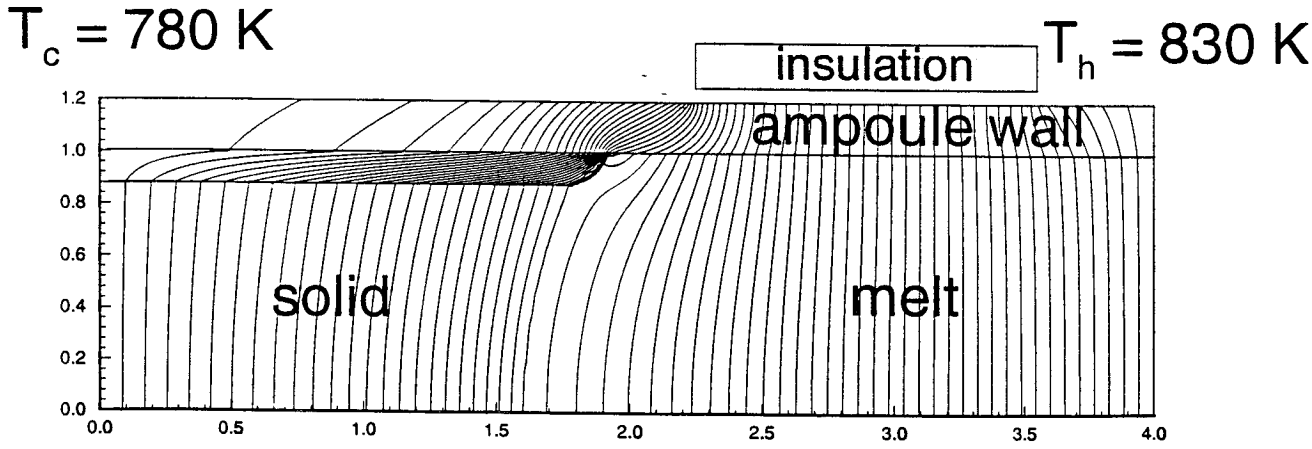

Brid-IIa

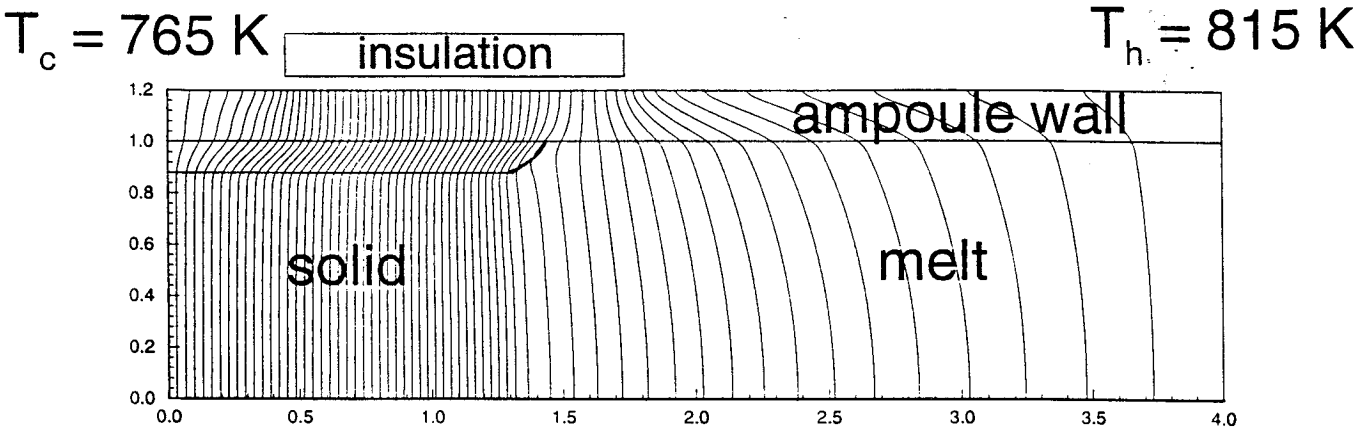

Brid-IIb

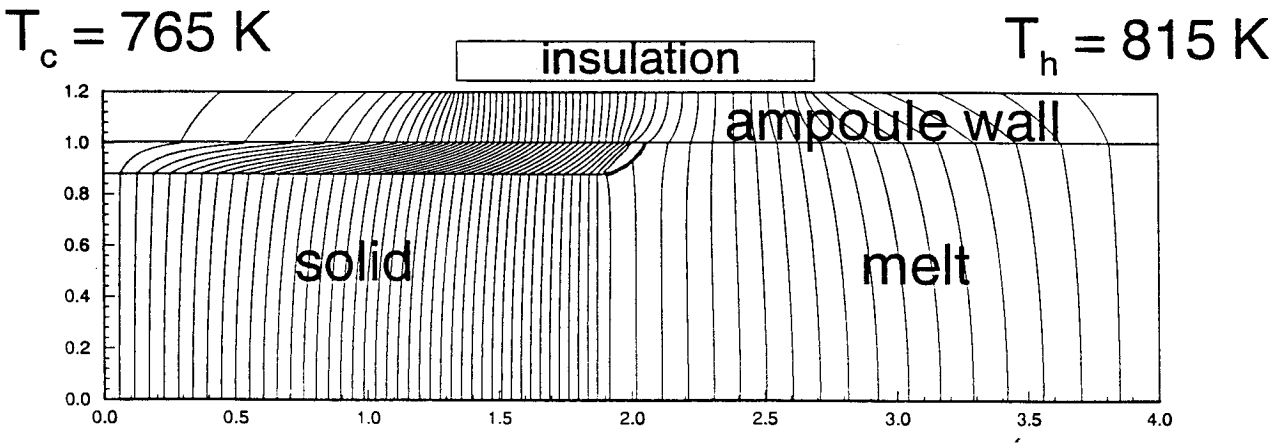

Brid-IIc

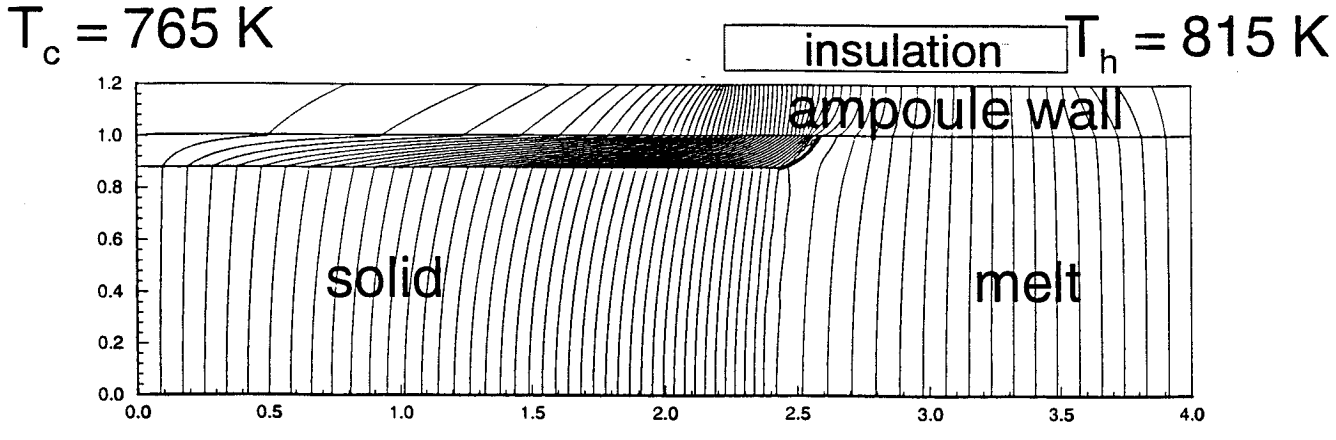

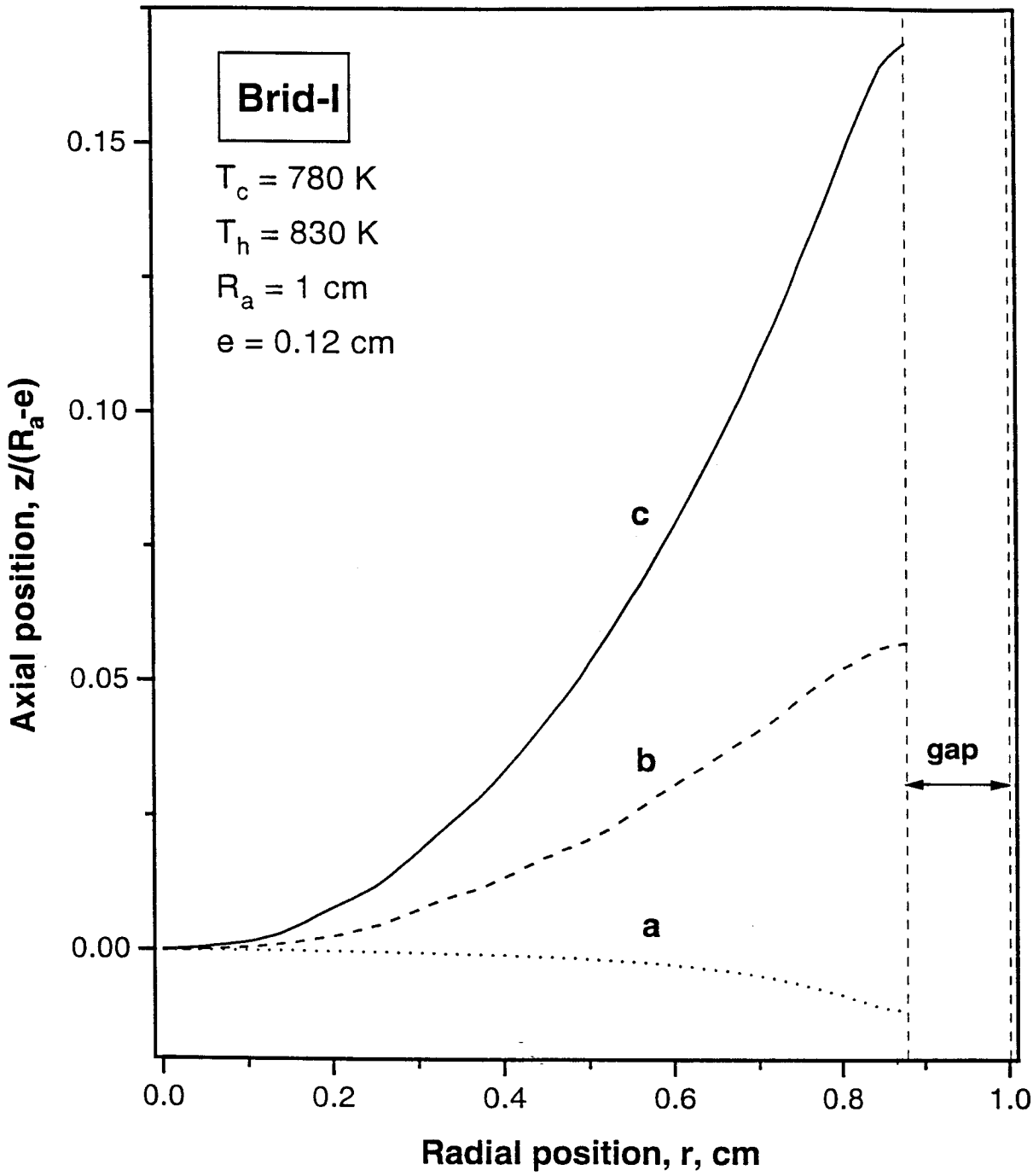
Brid-I
T_c = 780 K
T_h = 830 K
R_a = 1 cm
e = 0.12 cm
c
b
a
gap
0.15
0.10
0.05
0.00
0.0
0.2
0.4
0.6
0.8
1.0
Axial position, z/(R_a-e)
Radial position, r, cm

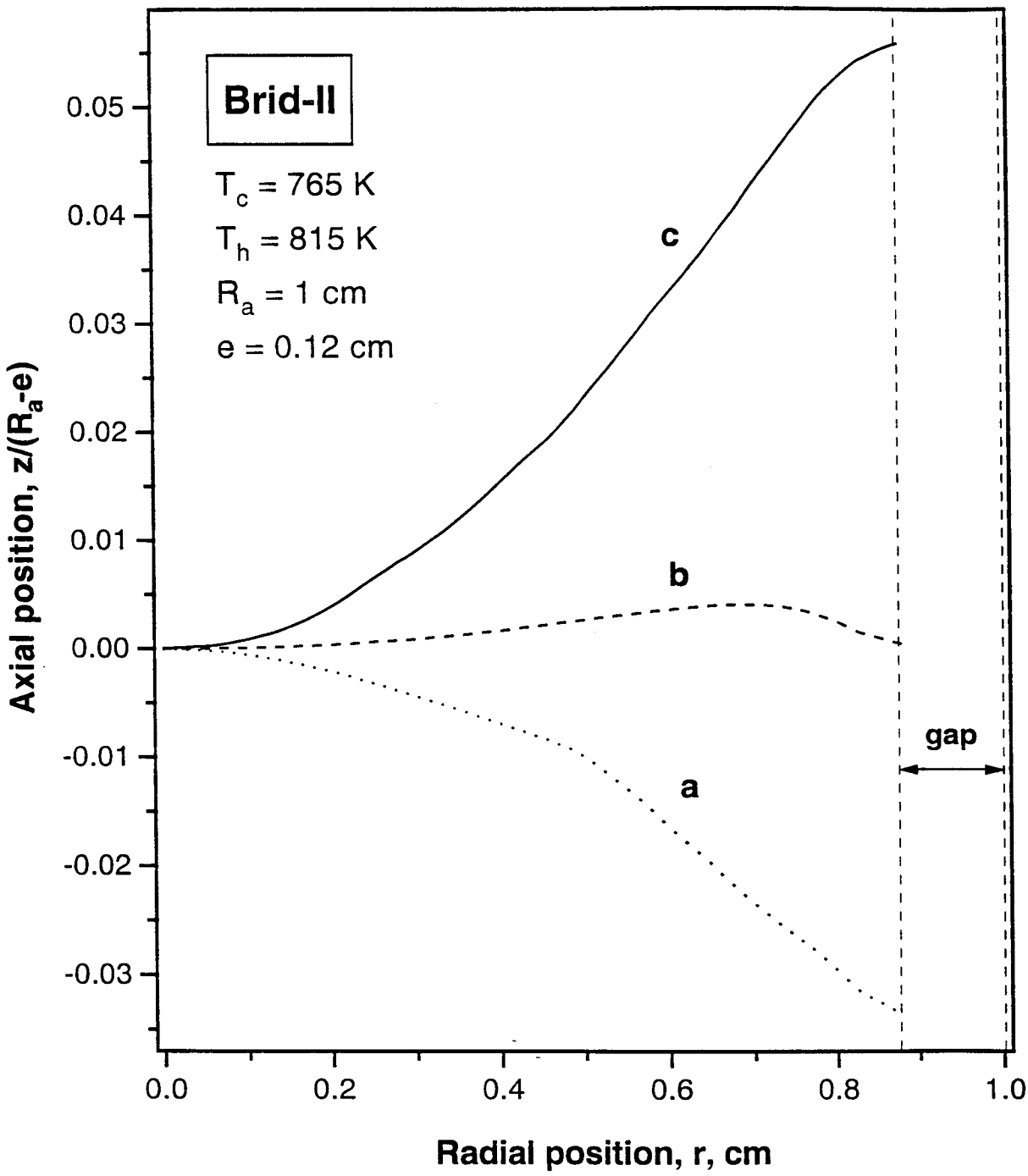
Brid-II
T_c = 765 K
T_h = 815 K
R_a = 1 cm
e = 0.12 cm
c
b
a
gap
0.05
0.04
0.03
0.02
0.01
0.00
-0.01
-0.02
-0.03
0.0
0.2
0.4
0.6
0.8
1.0
Axial position, z/(R_a-e)
Radial position, r, cm

Fig. 12

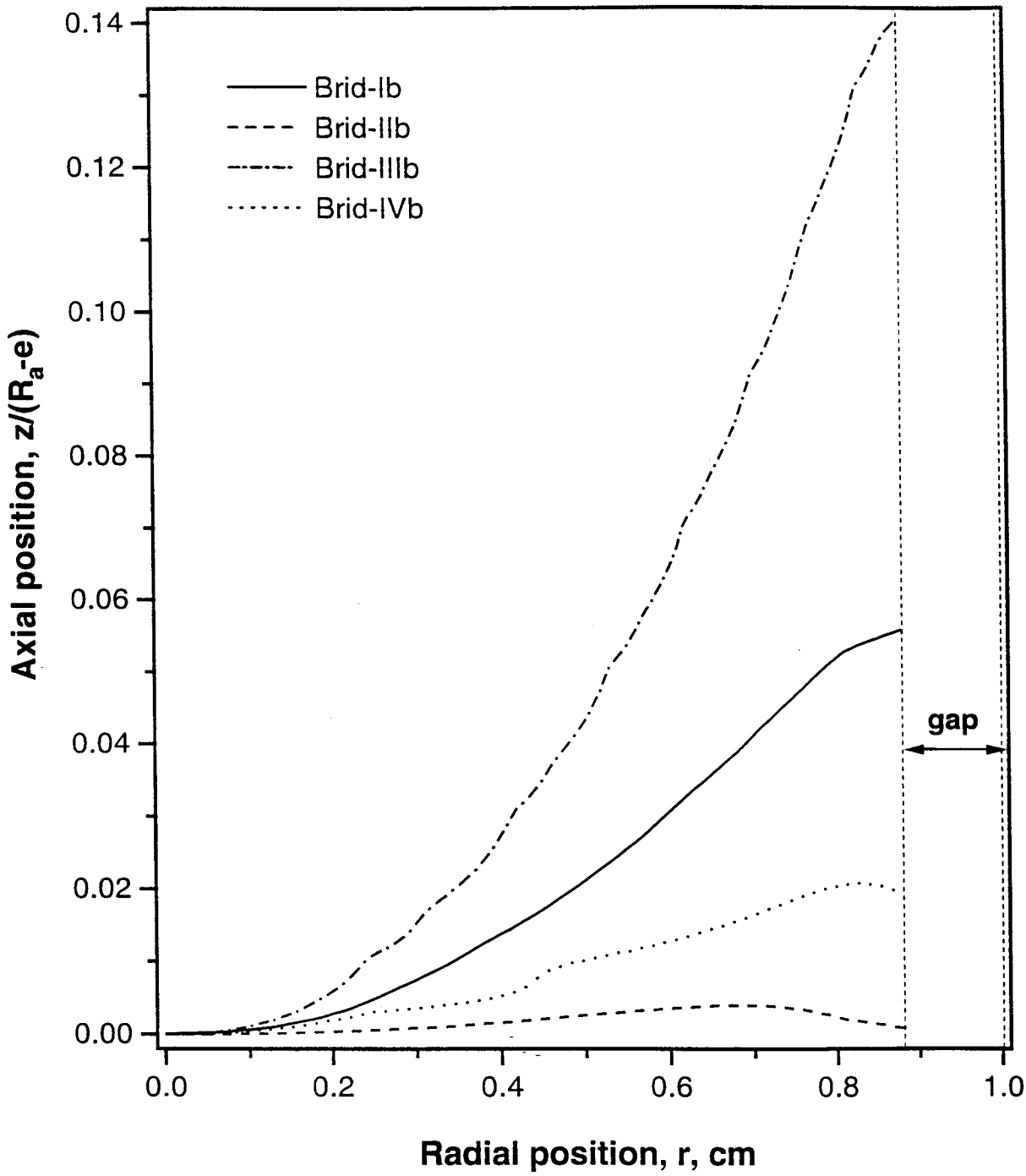
Brid-Ib
Brid-IIb
Brid-IIIb
Brid-IVb
gap
0.14
0.12
0.10
0.08
0.06
0.04
0.02
0.00
0.0
0.2
0.4
0.6
0.8
1.0
Axial position, z/(Ra-e)
Radial position, r, cm

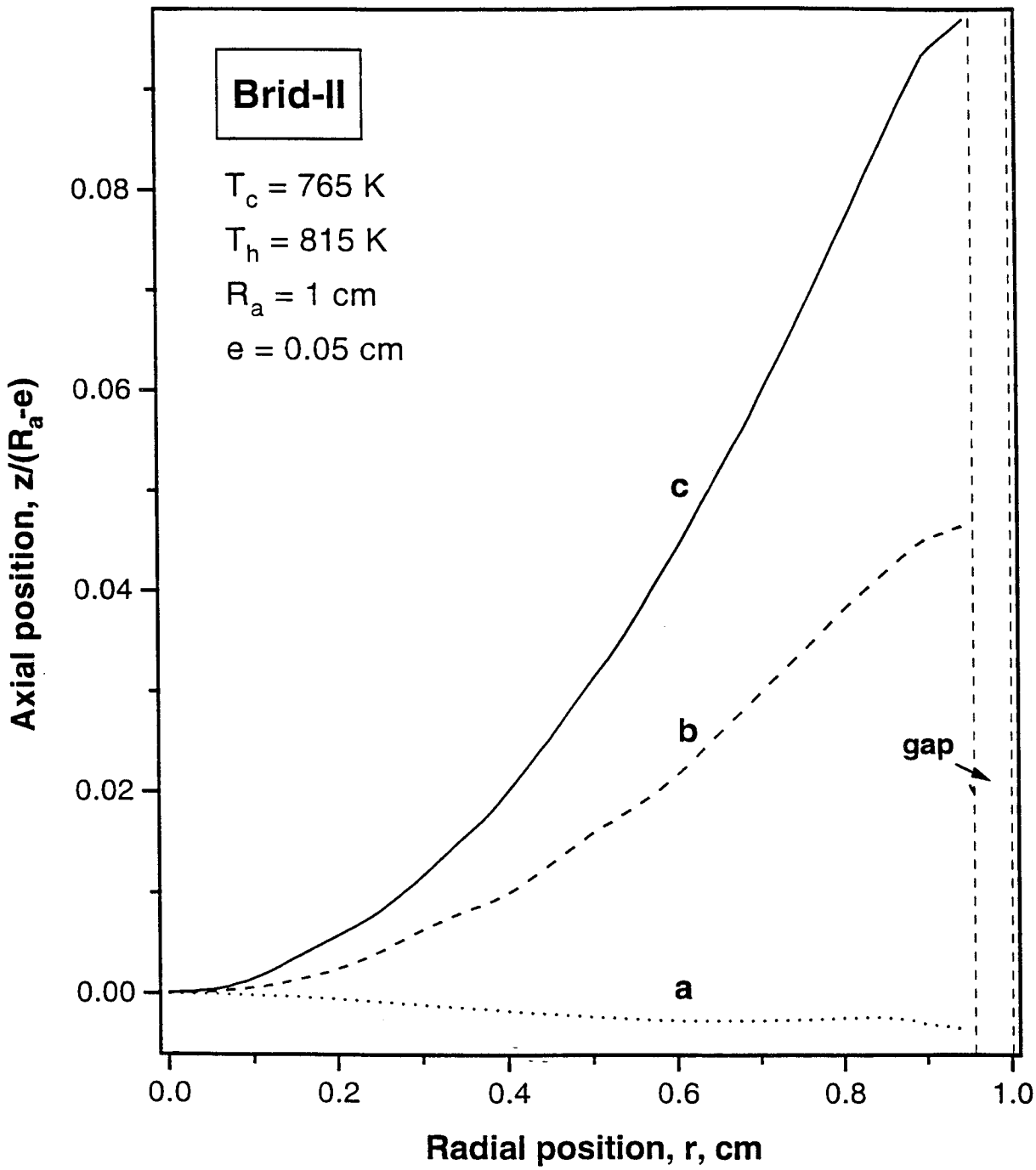
Brid-II
T_c = 765 K
T_h = 815 K
R_a = 1 cm
e = 0.05 cm
c
b
a
gap
0.08
0.06
0.04
0.02
0.00
0.0
0.2
0.4
0.6
0.8
1.0
Axial position, z/(R_a-e)
Radial position, r, cm

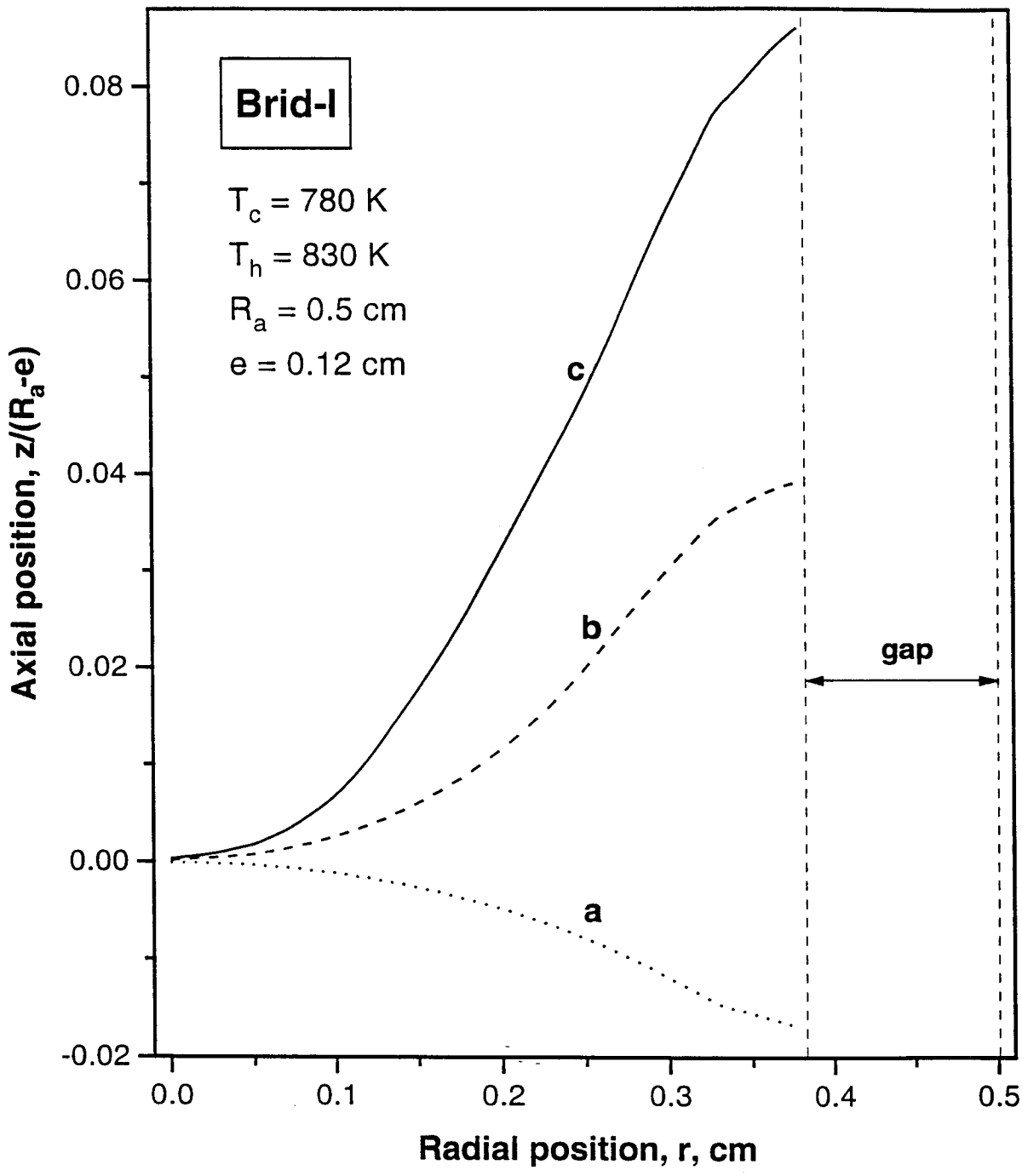
Brid-I
T_c = 780 K
T_h = 830 K
R_a = 0.5 cm
e = 0.12 cm
a
b
c
gap
Axial position, z/(R_a-e)
Radial position, r, cm
0.08
0.06
0.04
0.02
0.00
-0.02
0.0
0.1
0.2
0.3
0.4
0.5

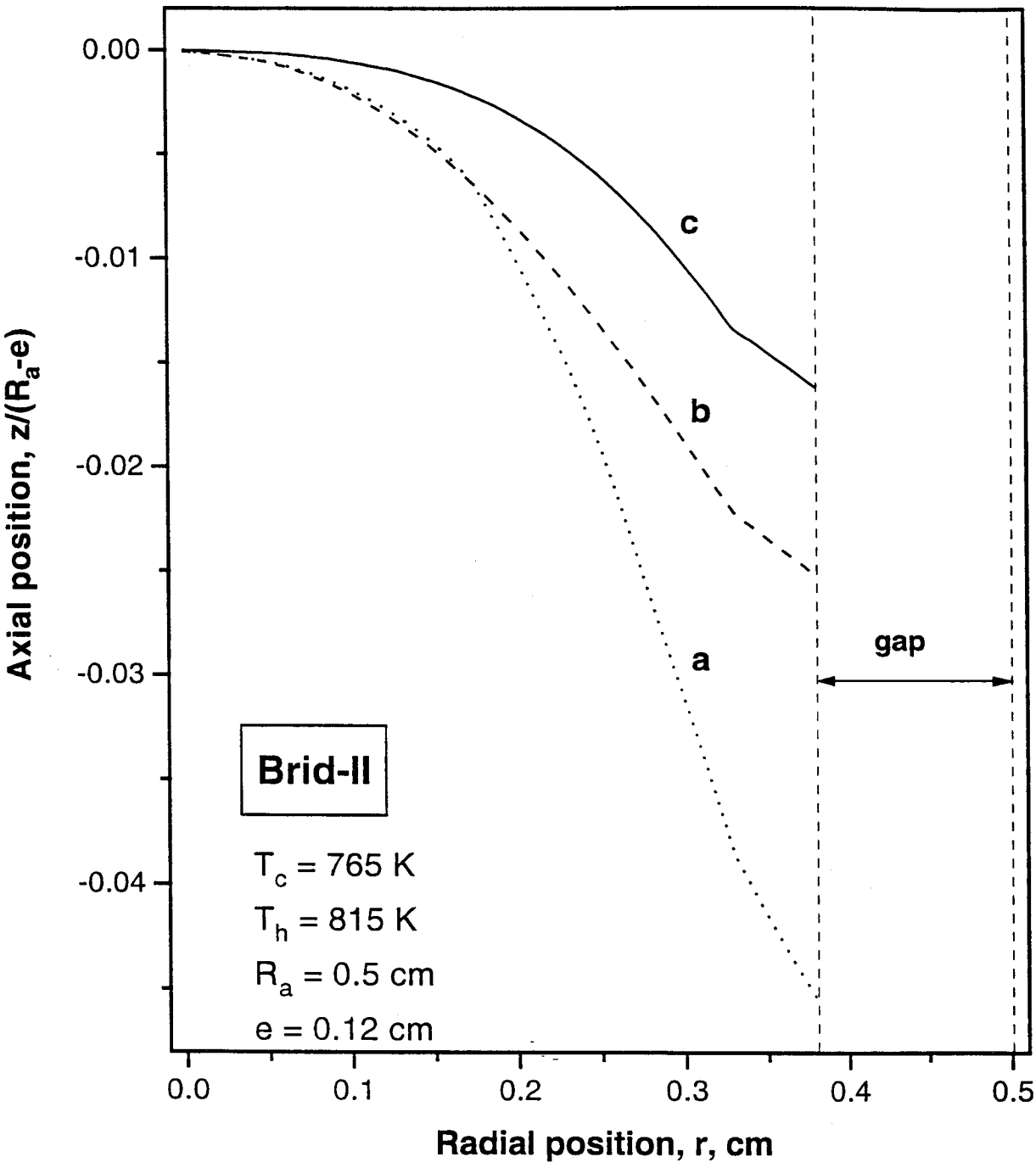
0.00
-0.01
-0.02
-0.03
-0.04
Axial position, z/(Ra-e)
c
b
a
gap
Brid-II
Tc = 765 K
Th = 815 K
Ra = 0.5 cm
e = 0.12 cm
0.0
0.1
0.2
0.3
0.4
0.5
Radial position, r, cm

Brid-l

$g = 10^{-5}\ g_0$

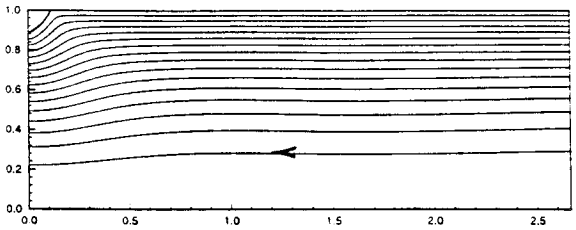

$g = 10^{-4}\ g_0$

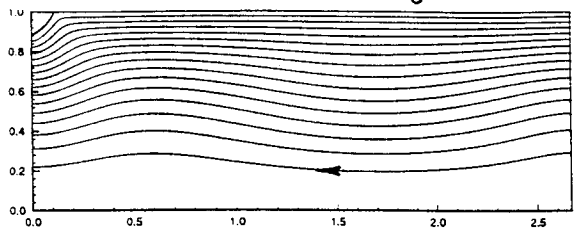

$g = 2*10^{-4}\ g_0$

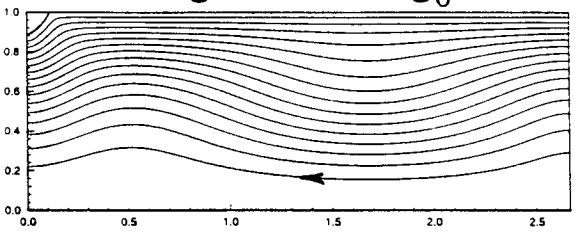

$g = 5*10^{-4}\ g_0$

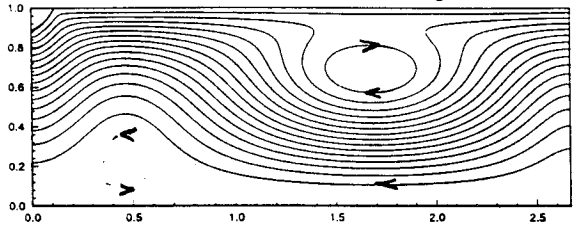

$g = 10^{-3}\ g_0$

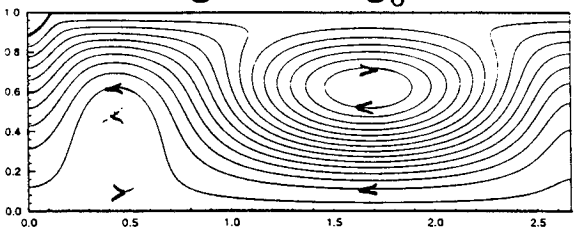

$g = 2*10^{-3}\ g_0$

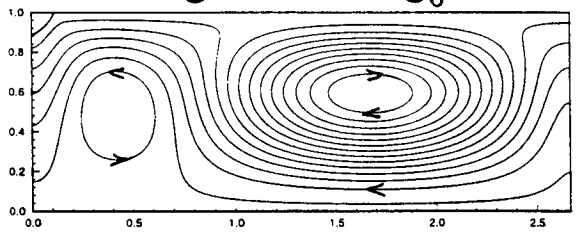

$g = 5*10^{-3}\ g_0$

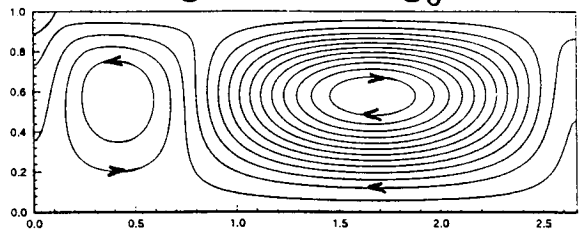

$g = 10^{-2}\ g_0$

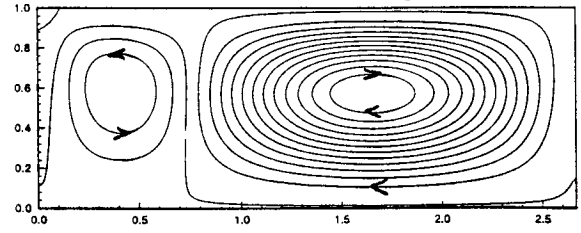

Fig 12

Brid-II

$g = 10^{-5}\, g_0$

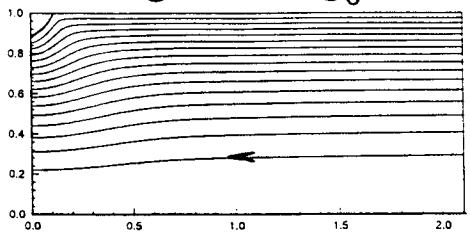

$g = 10^{-4}\, g_0$

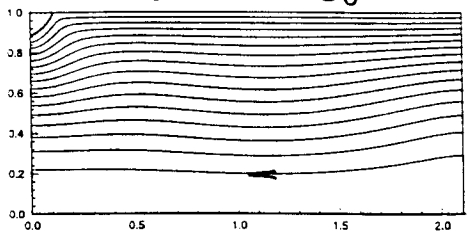

$g = 2*10^{-4}\, g_0$

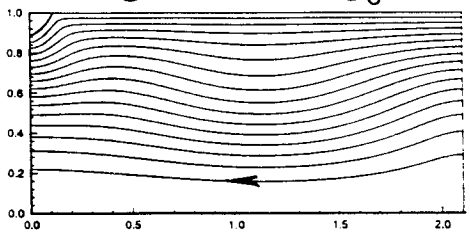

$g = 5*10^{-4}\, g_0$

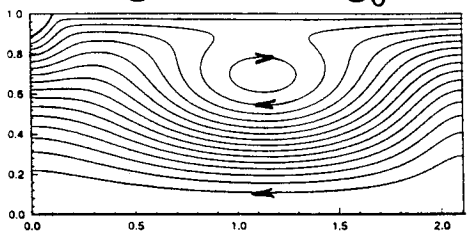

$g = 10^{-3}\, g_0$

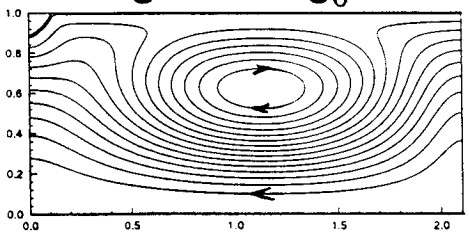

$g = 2*10^{-3}\, g_0$

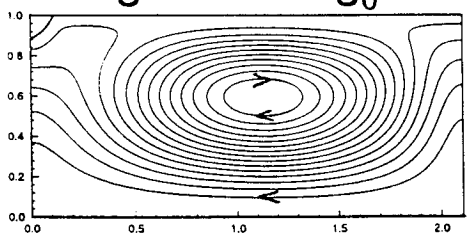

$g = 5*10^{-3}\, g_0$

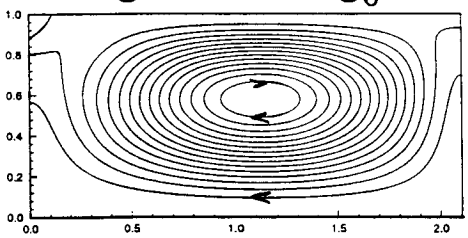

$g = 10^{-2}\, g_0$

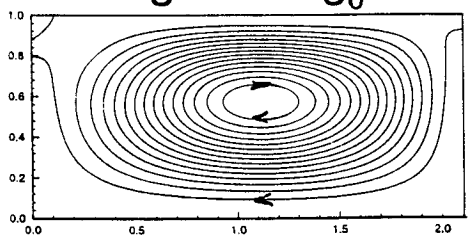

Fig 13

Brid-I

$g = 10^{-5}\ g_0$

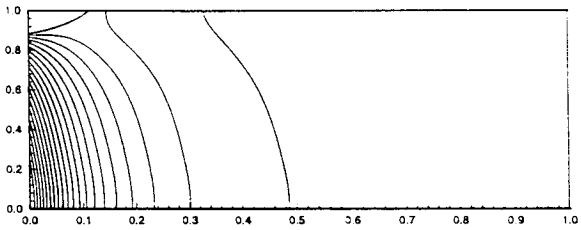

$g = 10^{-4}\ g_0$

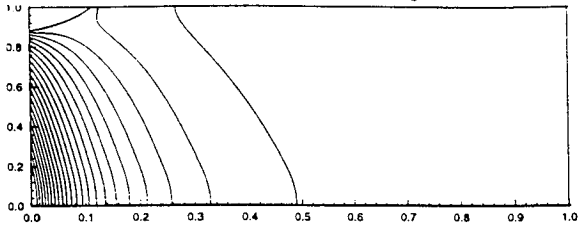

$g = 2*10^{-4}\ g_0$

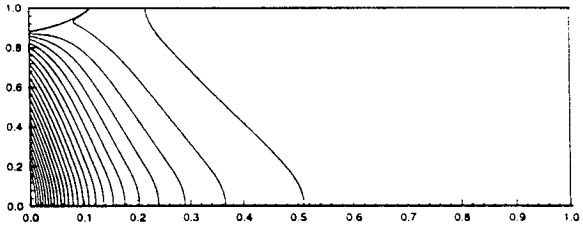

$g = 5*10^{-4}\ g_0$

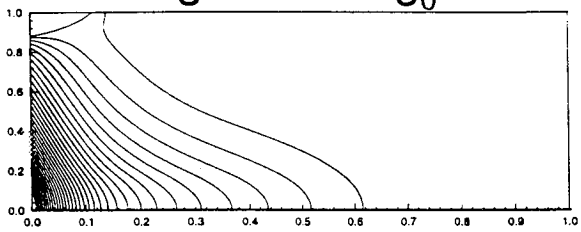

$g = 10^{-3}\ g_0$

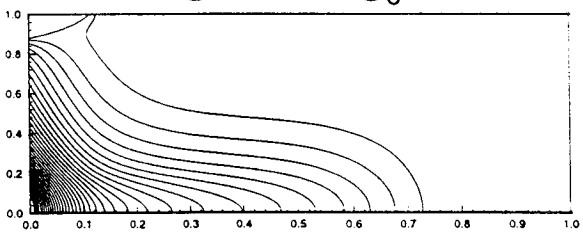

$g = 2*10^{-3}\ g_0$

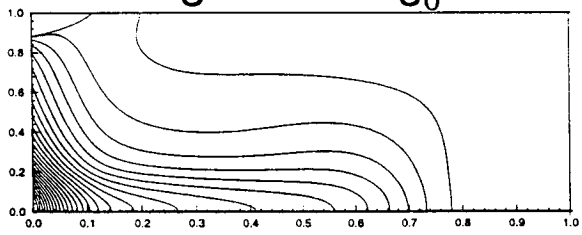

$g = 5*10^{-3}\ g_0$

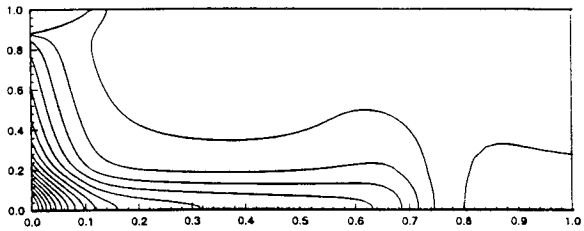

$g = 10^{-2}\ g_0$

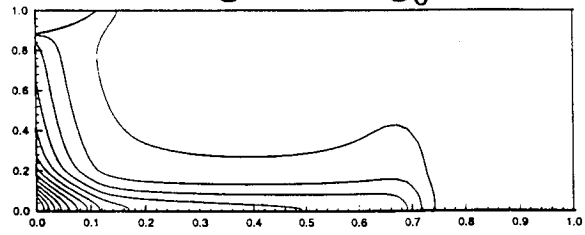

Fig 14

Brid-II

$g = 10^{-5}\ g_0$

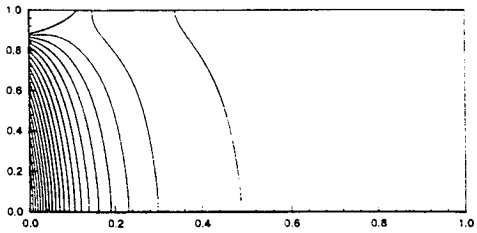

$g = 10^{-4}\ g_0$

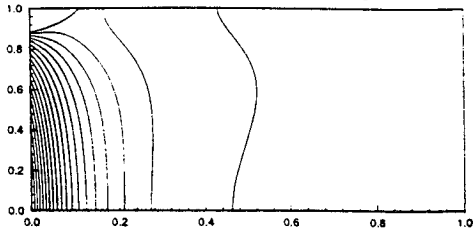

$g = 2*10^{-4}\ g_0$

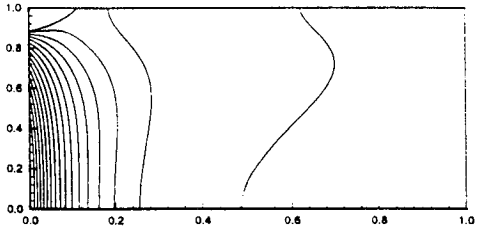

$g = 5*10^{-4}\ g_0$

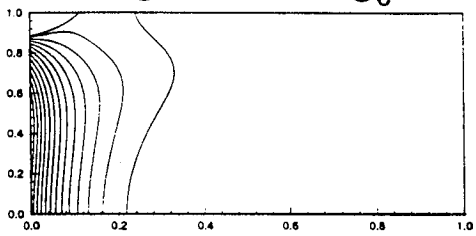

$g = 10^{-3}\ g_0$

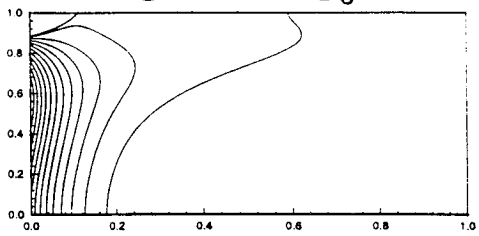

$g = 2*10^{-3}\ g_0$

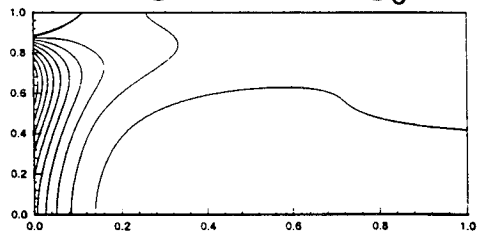

$g = 5*10^{-3}\ g_0$

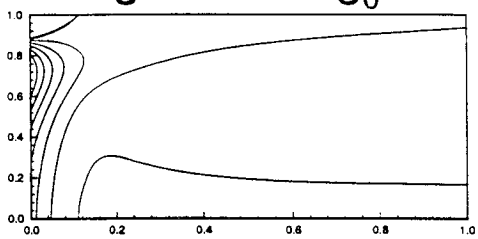

$g = 10^{-2}\ g_0$

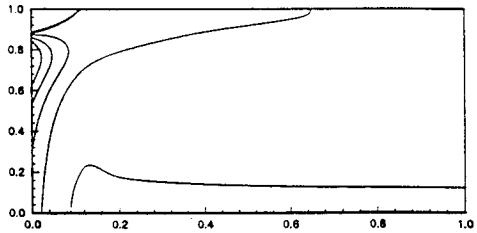

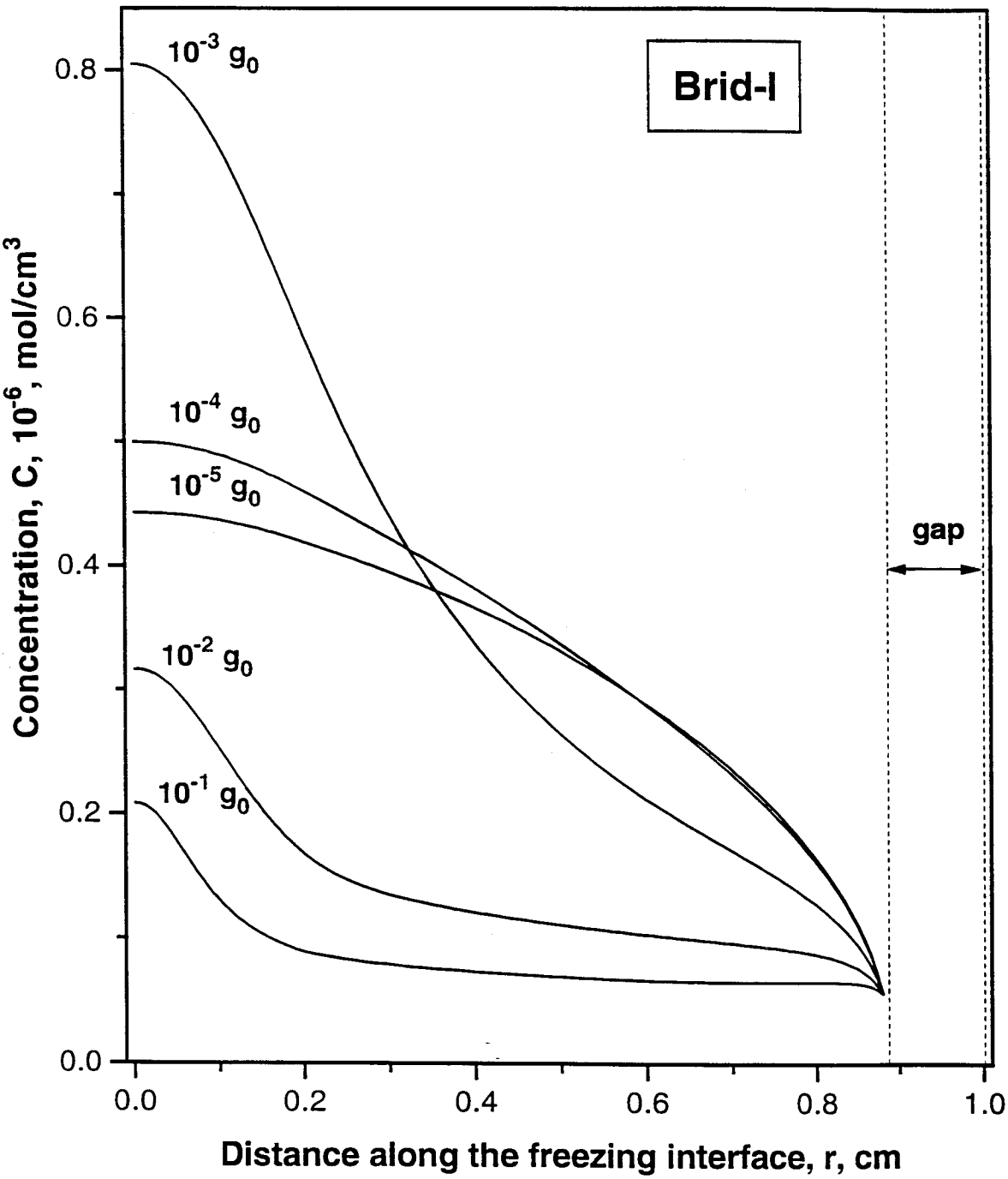
Brid-I
10^{-3} g_0
10^{-4} g_0
10^{-5} g_0
10^{-2} g_0
10^{-1} g_0
gap
Concentration, C, 10^{-6}, mol/cm^3
Distance along the freezing interface, r, cm
0.0
0.2
0.4
0.6
0.8
1.0

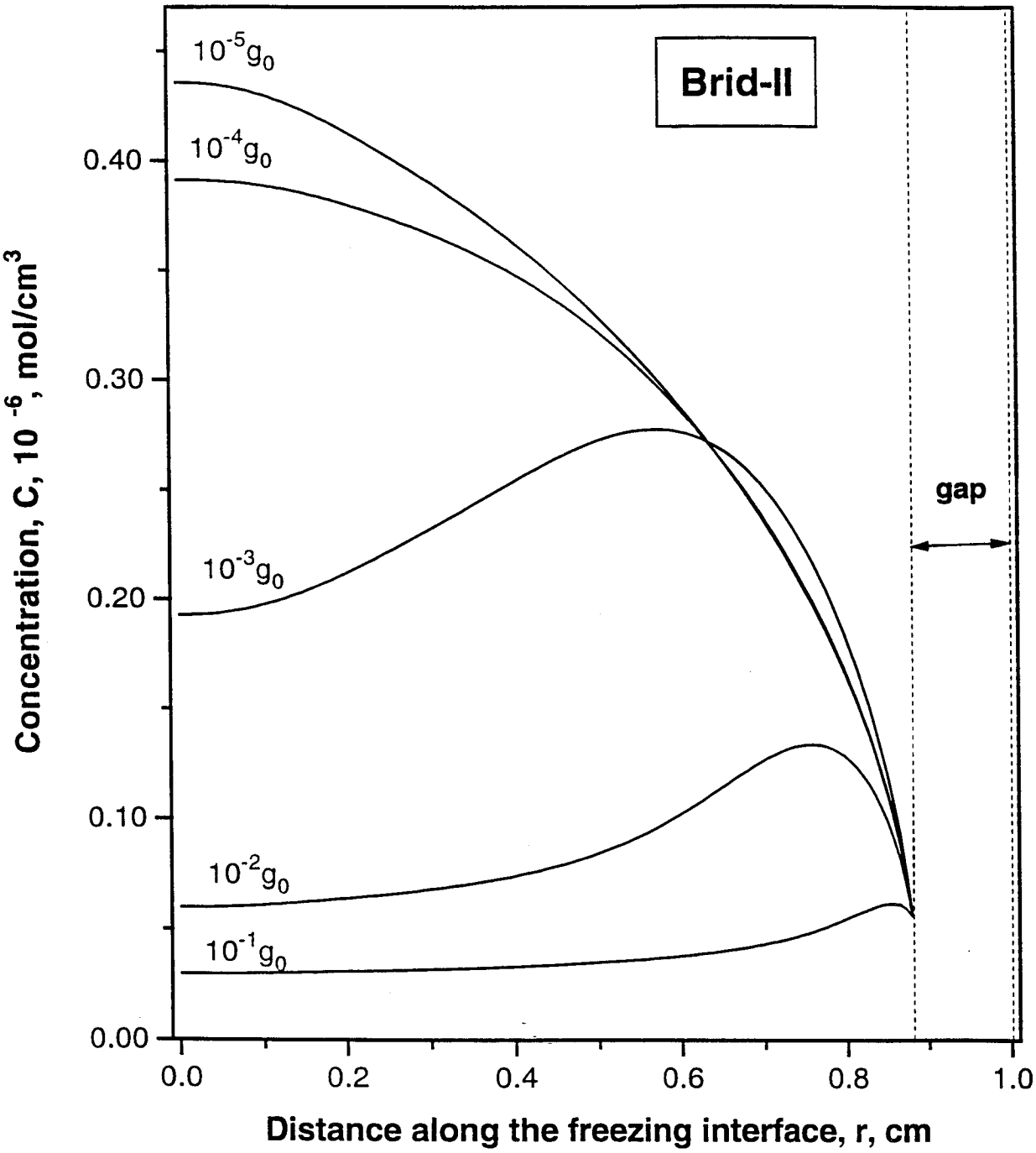
Brid-II
$10^{-5}g_0$
$10^{-4}g_0$
$10^{-3}g_0$
$10^{-2}g_0$
$10^{-1}g_0$
gap
Concentration, C, 10^{-6}, mol/cm^3
0.00
0.10
0.20
0.30
0.40
0.0
0.2
0.4
0.6
0.8
1.0
Distance along the freezing interface, r, cm

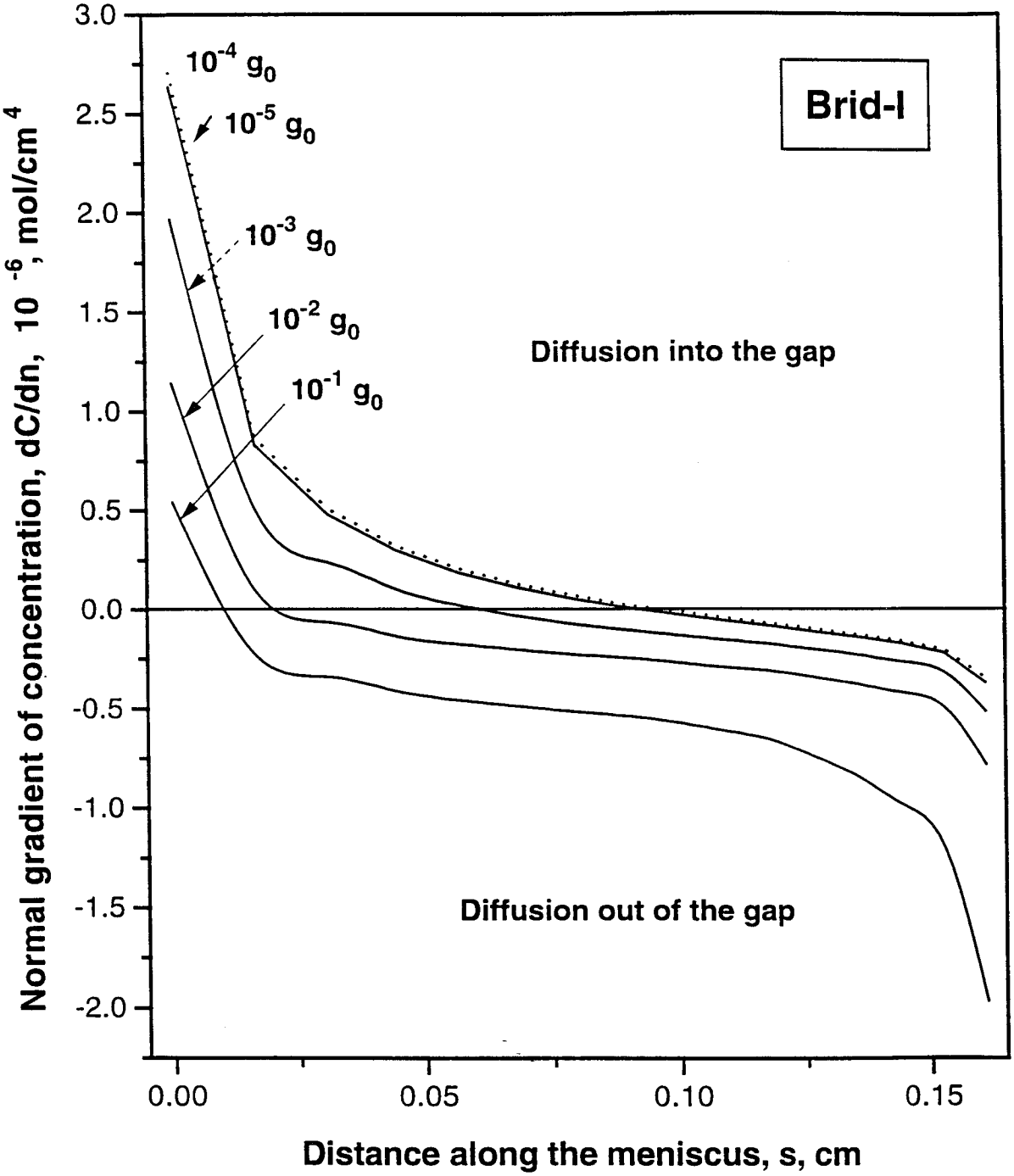
Brid-I
10^{-4} g_0
10^{-5} g_0
10^{-3} g_0
10^{-2} g_0
10^{-1} g_0
Diffusion into the gap
Diffusion out of the gap
Normal gradient of concentration, dC/dn, 10^{-6}, mol/cm^4
Distance along the meniscus, s, cm
3.0
2.5
2.0
1.5
1.0
0.5
0.0
-0.5
-1.0
-1.5
-2.0
0.00
0.05
0.10
0.15

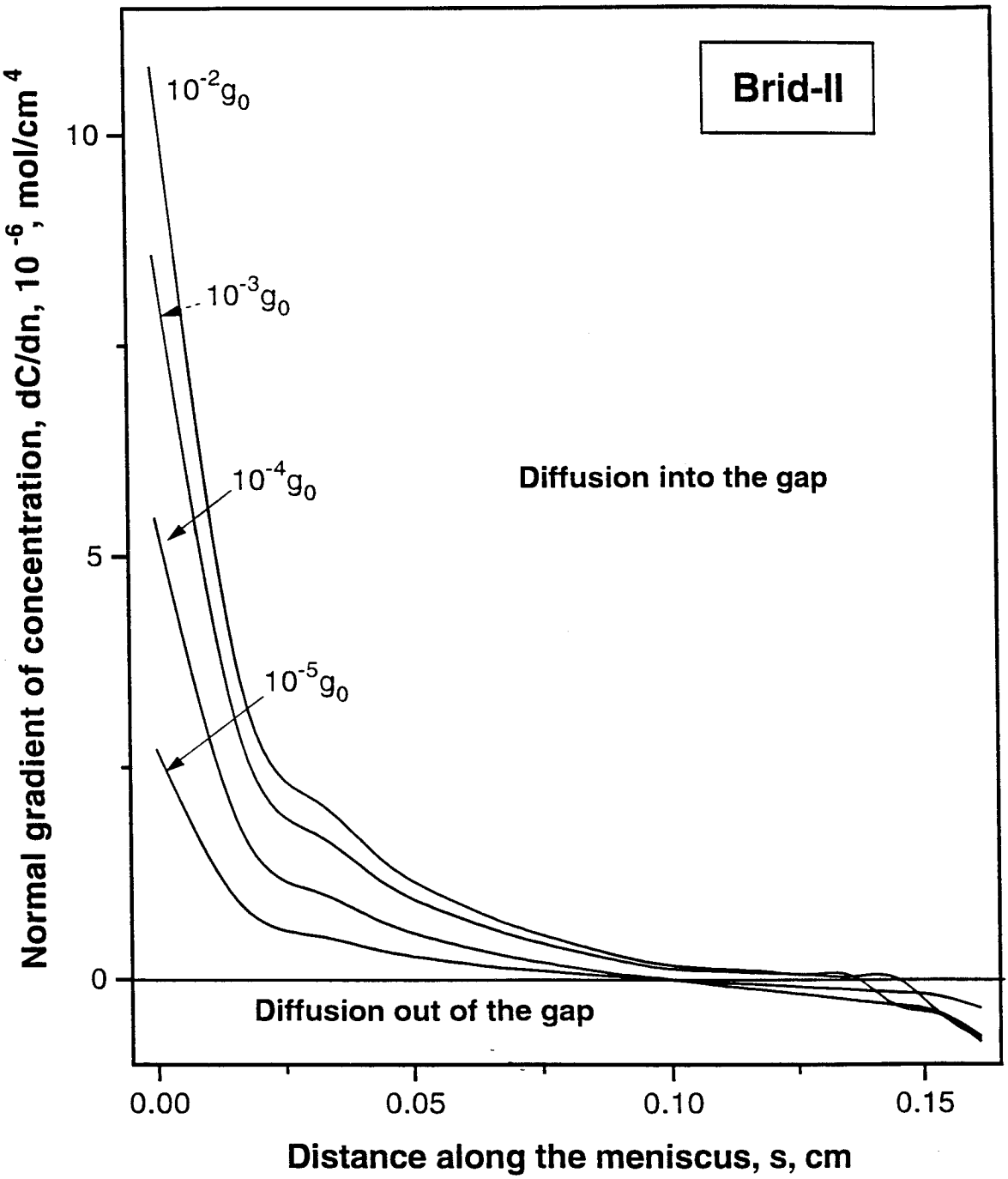
Brid-II
$10^{-2}g_0$
$10^{-3}g_0$
$10^{-4}g_0$
$10^{-5}g_0$
Diffusion into the gap
Diffusion out of the gap
Normal gradient of concentration, dC/dn, 10^{-6}, mol/cm^4
10
5
0
0.00
0.05
0.10
0.15
Distance along the meniscus, s, cm

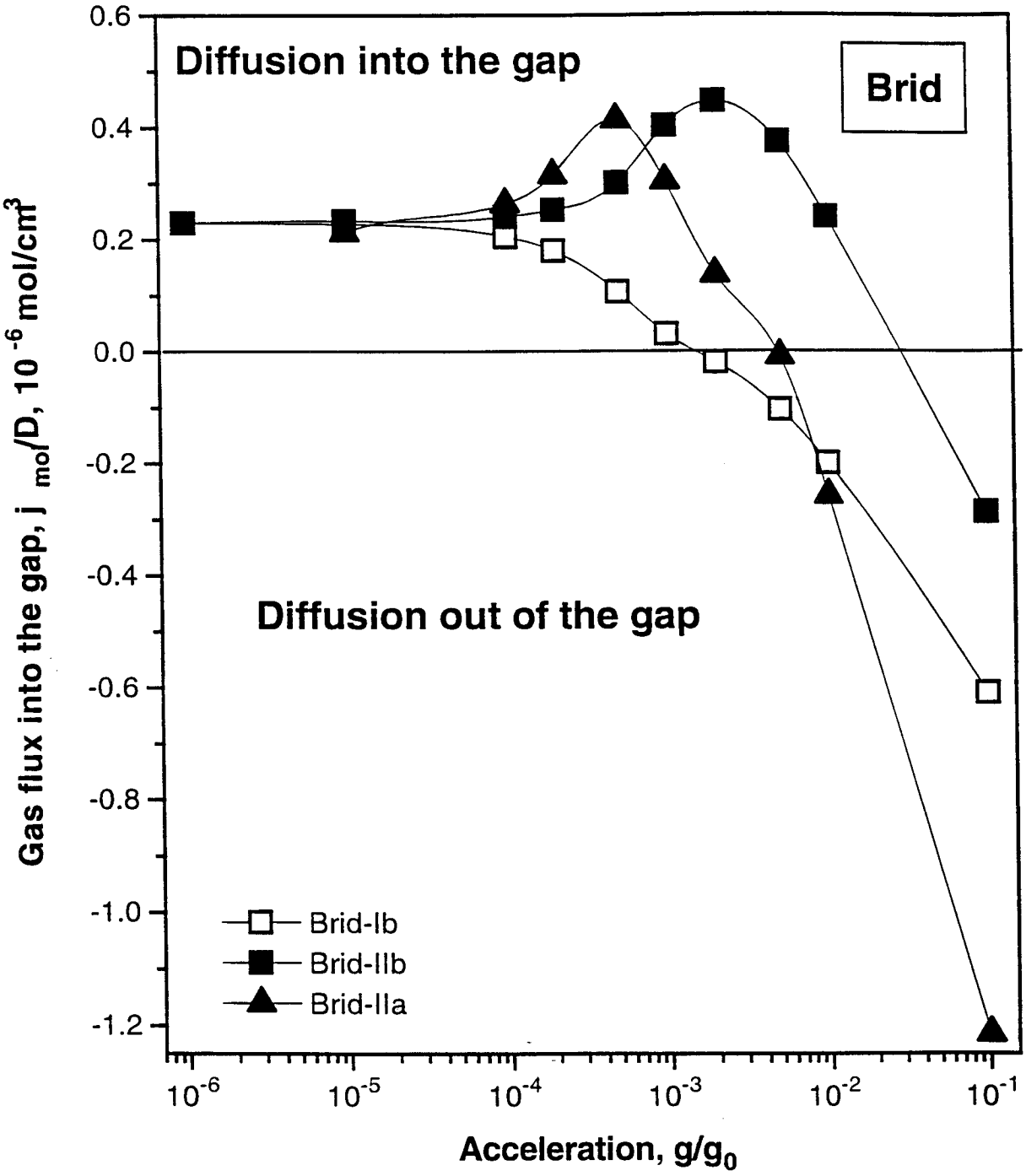
Diffusion into the gap
Brid
Diffusion out of the gap
Brid-Ib
Brid-IIb
Brid-IIa
0.6
0.4
0.2
0.0
-0.2
-0.4
-0.6
-0.8
-1.0
-1.2
10^{-6}
10^{-5}
10^{-4}
10^{-3}
10^{-2}
10^{-1}
Gas flux into the gap, j_{mol}/D, 10^{-6} mol/cm^3
Acceleration, g/g_0

Fig. 17